Modelling, fault detection and active vibration control of rotor dynamic systems with applications in machine tools

by

Rajiv Kumar Vashisht

A Thesis submitted to the Faculty of Graduate Studies of
The University of Manitoba
in partial fulfillment of the requirements of the degree of

Doctor of Philosophy

Department of Mechanical Engineering
University of Manitoba
Winnipeg, Manitoba
Canada

Abstract

Rotors are extensively used to transfer energy from one part to other parts of a mechanical system. During the service life of the rotors, they are subjected to different faults like the rotor crack, coupling misalignment, rotor bow, rotor-stator rubbing and unbalance. One of the important aspects of these faults is their interconnection. Presence of one fault can accelerate the growth of the other. If these faults are not identified timely, costly breakdown of the rotor system can occur. The presence of these faults changes the overall nature of the system dynamics from the linear to nonlinear one. This aspect can be used to identify the presence of these faults. Various system components like ball bearings and journal bearings also make the overall dynamics of a healthy rotor system nonlinear. Hence, it is not easy to detect the presence of faults based on the vibration signal. Transient response-based crack detection technique has been developed and verified using simulation techniques.

Rotor dynamics with transverse crack, coupling miss-alignment and rotor-stator rubbing can be represented using ordinary differential equations with time-periodic coefficients and intermittently varying coefficients. A new fault detection strategy based on short time Fourier transformation has been developed to detect the presence of crack and rotor stator rubbing even if the both coexist simultaneously. Due to the presence of unbalance, rotor systems with constant spinning speed are subjected to steady-state vibrations that can accelerate the crack growth or chances of rotor/stator rubbing action. During changes of the spinning speed, transient vibrations corresponding to resonance frequencies are also generated. To compensate both types of vibrations, a hybrid controller is successfully developed. Electromagnetic actuators are used to

generate required control forces. From the spectrum of the control signal, rotor faults like transverse crack and coupling miss-alignment can be efficiently diagnosed.

Applications of rotor dynamics can also be seen in machine tools. The spindle and ball screw drives are important examples of their applications. In the spindle, transverse and torsional vibrations are produced. However, in the ball screw drives, axial vibrations are generated. For precision control of the drives, a hybrid controller is proposed to increase command tracking efficiency and reduce the dynamic deflection of the carriage during metal cutting process. Experimental verification of the proposed controller has been done to verify its effectiveness. The dynamics of cutting tools is represented in the form of time-delay systems. Different time-domain algorithms are used to identify stable regions of machining operations. To improve the depth of cut, the active chatter control of turning and boring operations is carried out. Experimental results verify the effectiveness of the proposed active chatter control strategies. Based on the relative motion between the workpiece and cutting tool (during boring operation), cutting operations can be divided into different categories. The dynamics of such systems is represented using delay differential and time-periodic delay differential equations. Feasibility of active chatter control for each category is analyzed in detail. The effect of eccentricity and workpiece ovality on the dynamics of boring operations is thoroughly investigated. Linear Parameter Varying controllers are proposed to compensate for the changing dynamics of the system due to continuous metal removal in turning operations. Fractional-order proportional derivative controllers are designed using response optimization techniques and implemented in boring operations. Experimental results verify that these controllers save the control energy in active chatter control applications.

Machine learning techniques are used for online chatter detections in milling operations. Various chatter indicators are proposed. Improved dynamic equations are proposed for milling

operations to find the behaviour of vibrations during chatter conditions. Simulated data are used to train Convolutional Neural Networks that are then used to detect chatter in an online manner. Experimental results verify the effectiveness of the proposed technique.

Acknowledgments

I would like to take this opportunity to express my sincerest thanks to my supervisor, Professor Qingjin Peng, for his motivation, academic support, and guidance through this work. Without his support, this work would not have been possibly done. Many thanks are also directed to the advisory committee members, Professors Nan Wu and Babak Mehran for their constructive advice. This research has been supported by the University of Manitoba Graduate Fellowship (UMGF) and the Discovery Grants from the Natural Sciences and Engineering Research Council (NSERC) of Canada. I would also like to express my appreciation to awards from the Faculty of Graduate Studies and Faculty of Engineering as follows.

- Edward R. Toporeck Graduate Fellowship in Engineering for years 2017 and 2018
- Faculty of Graduate Studies research complete scholarship for year 2019
- Philip and Marjorie Eckman Scholarship in Engineering for year 2020

I am thankful to Professor S P Singh in the Department of Mechanical Engineering, Indian Institute of Technology, New Delhi, India for his kind support in conducting the experimental work in his laboratory. I would also like to thank my dear friends in the Indian Institute of Technology New Delhi for helping me to conduct the experiments.

I would also like to thank my dear friends in Virtual Manufacturing Laboratory at the University of Manitoba for the happy time we had together.

Dedication

To my dear parents, and my dear wife!

Table of Contents

Abstract ii
Acknowledgments v
Dedication vi
Table of Contents vii
List of Tables x
List of Figures xi
List of Abbreviations xv
Copyright Notices xvii
1. Introduction 1
1.1. Introduction to rotor dynamic systems 1
1.2. Faults in rotor dynamic systems 1
1.3. Active vibration control of rotor dynamic systems 3
1.4. Applications of rotor dynamic systems in machine tools 4
1.5. Research problems 7
1.6. Research objectives and methods 8
1.7. Connectivity of various parts of the dissertation 9
1.8. Structure of the dissertation 10
2. Literature Review 13
2.1. Overview 13
2.2. Faults in rotor dynamic systems 13
2.3. Active vibration control of rotor dynamic systems 17
2.4. Applications of rotor dynamic systems in machine tools 19
2.5. Research gaps and directions 28
3. Modelling and fault detection in rotodynamic systems 30
3.1. Overview 30
3.2. Mathematical Modelling 31
3.3. Conventional crack detection techniques based on the steady-state dynamic response 45
3.4. Proposed Crack Detection Technique based on Transient Response 45

3.5. Active Vibration Control using Robust Control Methodology 49
3.6. Switching Control Strategy 50
3.7. Application of Switching Control and STFT based Spectrum 54
3.8. Concluding remarks 55
4. Modelling and detection of rotor stator rubbing action 57
4.1. Overview 57
4.2. Mathematical Modelling 58
4.3. Simulation model 63
4.4. Detection of transverse crack and rubbing action 64
4.5. Effect of different factors on rotor/stator rubbing action 65
4.6. Concluding remarks 72
5. Active vibration control of rotor dynamic systems 74
5.1. Overview 74
5.2. Mathematical modelling of a rotor system 74
5.3. Mu-synthesis using D-K iterations 78
5.4. Conventional Adaptive Feedforward Control with an internal estimation of frequency 79
5.5. External Frequency estimation 81
5.6. Results with conventional Adaptive Feedforward controller 82
5.7. Proposed Hybrid controller with an external estimation of frequency 85
5.8. Experiment 90
5.9. Results 92
5.10. Concluding remarks 96
6. Precision control of ball screw drives 97
6.1. Overview 97
6.2. Mathematical Modelling 98
6.3. Design and Implementation of Hybrid Controller 104
6.4. Experiment 107
6.5. Theoretical and experimental results 108
6.6. Concluding remarks 116
7. Active chatter control of turning operations 118
7.1. Overview 118
7.2. Active chatter control using an electromagnetic actuator 118

7.3. Dynamic modelling for turning of the stepped shaft 121
7.4. Linear parameter varying controller design 134
7.5. Results and Discussion 134
7.6. Concluding remarks 138
8. Active chatter control of boring operations 139
8.1. Overview 139
8.2. Mathematical Modelling of stationary bar boring operation 140
8.3 Mathematical modelling of rotating bar boring operation 146
8.4. Simulation model and formulation of delay equations 147
8.5. Active chatter control of stationary bar boring operation 150
8.6. Active chatter control for rotating bar boring operation 162
8.7. Concluding remarks 166
9. Chatter detection in milling operations using Neural Networks 167
9.1. Overview 167
9.2. Dynamic modelling of milling operations 167
9.3. Comparison of simulation results with literature and experimental results 171
9.4 The amplitude of tool vibrations and tool forces during chatter 178
9.5. Presence of multiple chatter frequencies 180
9.6. Chatter indicators 182
9.7. Online chatter identification based on Convolutional Neural Networks 190
9.8. Concluding remarks 193
10. Research conclusions, contributions and future recommendations 195
10.1. Conclusions 195
10.2 Research contributions 198
10.3 Further recommendations 199
Papers published/submitted from dissertation 201
Bibliography 203
Appendix A i

List of Tables

Table 3-1 Physical parameters and mechanical properties of the rotor bearing system 34
Table 3-2 Damping parameters of the discrete mass representation of rotor bearing system 35
Table 3-3 The comparison of natural frequencies 39
Table 3-4 Geometric properties of 6014 Ball Bearing (Tiwari and Gupta, 2000)..... 43
Table 5-1 The physical parameters and mechanical properties of the rotor bearing system..... 78
Table 5-2 Physical Parameters of Electromagnetic actuator 92
Table 6-1 Important parameters of the ball screw drive 102
Table 7-1 Physical Parameters of Electromagnetic actuator used 120
Table 7-2 Parameters of the flexible shaft 122
Table 8-1 Physical Parameters of Electromagnetic actuator 151
Table 8-2 Comparison of theoretical and experimental results 152
Table 9-1 Confusion matrix for STFT based detection……...190
Table 9-2 Confusion matrix for tool locus-based detection…….191

List of Figures

Figure 1-1 Rotor with crack (Lalanne and Ferraris, 1990) 2
Figure 1-2 Rotor/stator rubbing 2
Figure 1-3 Schematic of the experimental setup for AMB 4
Figure 1-4 Conventional applications of rotor dynamic systems and applications in machine tools 5
Figure 1-5 Schematic diagram of the ball screw drive 5
Figure 1-6 Conventional turning operation 6
Figure 1-7 Active chatter control in boring operation 7
Figure 1-8 Connectivity of different parts of the dissertation 10
Figure 3-1 Schematic of the finite element model of a rotor-bearing system 33
Figure 3-2 Equivalent physical model of the discrete mass model of the rotor bearing system in one plane (not to scale) 36
Figure 3-3 Phenomenological model of the discrete mass model of the rotor bearing system in one plane (not to scale) 37
Figure 3-4 Bode plot for the different modeling techniques at Disk1 and 2 39
Figure 3-5 Ball bearing system 41
Figure 3-6 Cracked Rotor model 42
Figure 3-7 Horizontal and vertical responses of the rotor bearing (Healthy and Cracked) system at disks 1 and 2 46
Figure 3-8 Spectrogram of the rotor-bearing system with rigid bearing support (at disk2) 47
Figure 3-9 Spectrogram of the rotor Ball Bearing system with flexible bearing support (at disk1) 48
Figure 3-10 Open and closed-loop responses of the 40% Cracked rotor with the robust controller 49
Figure 3-11 Spectrogram of the healthy rotor and 10% cracked rotor with ball bearings at disk 1 (closed-loop response) (in region II) 50
Figure 3-12 Frequency domain response of the rotor ball bearing system at disk 1 (in region II) using negative velocity feedback controller as a function of crack severity 51
Figure 3-13 Architecture of the switched control 52
Figure 3-14 Response of the 10% cracked flexible rotor with active and switching control 53
Figure 3-15 Spectrogram of the healthy rotor and 5% cracked rotor with ball bearings at disk 1 (closed-loop response) (in region II) using switching control strategy 54
Figure 3-16 Spectrogram of the healthy rotor and 30% cracked rotor with ball bearing at disk 1 (closed loop response) (in region II) 55
Figure 4-1 Schematic of the 2-DOF rotor stator system (Front view) 60
Figure 4-2 Schematic of the 2-DOF rotor stator system (side view) 60
Figure 4-3 Cracked rotor model 61
Figure 4-4 Comparison of vibration characteristics at different rotor spin frequencies for vertical and horizontal rotors 65

Figure 4-5 Effect of gravity and presence of crack on vibration characteristics of the horizontal rotor (spin frequencies above the resonance) 67
Figure 4-6 Effect of gravity and presence of crack on vibration characteristics of the horizontal rotor (spin frequency below the resonance) 67
Figure 4-7 Vibration characteristics of the vertical rotor during coasting up as varied clearance amplitudes 69
Figure 4-8 Vibration characteristics of the horizontal rotor during coasting up as varied clearance amplitudes 69
Figure 4-9 Vibration characteristics of the cracked horizontal rotor during coasting up as varied clearance amplitudes (part 1) 71
Figure 4-10 Vibration characteristics of the cracked horizontal rotor during coasting up as varied clearance amplitudes (part 2) 71
Figure 5-1 Rotor/bearing/coupling system 76
Figure 5-2 Comparison of conventional and proposed control architecture 83
Figure 5-3 Time domain response by conventional Adaptive Feedforward Control at 20 Hz Spinning speed 83
Figure 5-4 Time domain response by Adaptive Feedforward Control with time varying frequency component applied to rotor system 84
Figure 5-5 Comparison of actual and estimated frequencies by Adaptive Notch Filter at sampling frequency of 200 Hz 84
Figure 5-6 Flow chart for proposed adaptive feedforward controller 87
Figure 5-7 Frequency response function of different systems 88
Figure 5-8 Robust stability, performance and other parameters 89
Figure 5-9 Multi-harmonic hybrid control architect 90
Figure 5-10 Experimental setup for active vibration control for rotor system 91
Figure 5-11 Comparison of Mu- controller and Derivative controller for Disk 2 93
Figure 5-12 Response of rotor system with the proposed hybrid controller (Experimental) 94
Figure 5-13 The response of the rotor system with coupling misalignment using proposed controller (Experimental) 95
Figure 6-1 Two-dimensional representation of the ball screw drive 99
Figure 6-2 Simplified model of the ball screw drive 100
Figure 6-3 Effect of location and mass of the carriage on the first natural frequency (with bearing clearance) 103
Figure 6-4 Simulink implementation of Hybrid controller 107
Figure 6-5 Experimental setup for ball screw drive 108
Figure 6-6 Loop sensitivity with different controllers 109
Figure 6-7 Loop magnitude with different controllers and loop shaping factor 110
Figure 6-8 Time domain analysis for command tracking with different controllers (Simulation results) 112
Figure 6-9 Performance of various controllers during metal cutting (Experimental results) 114
Figure 6-10 Comparison of performance with LPV and other controllers (Simulation results) 116

Figure 7-1 Active chatter control architecture for flexible stepped shaft 119
Figure 7-2 Schematic of the overall control system for turning operation 121
Figure 7-3 Mode shapes of flexible stepped shaft 123
Figure 7-4 Natural frequencies of the flexible stepped shaft as a function of tool location and pass number 124
Figure 7-5 Stiffness and critical depth of cut as a function of tool location for the stepped flexible shaft 125
Figure 7-6 Nomenclature and schematic of the cutting tool 126
Figure 7-7 Stability lobe diagram as a function of tool location 130
Figure 7-8 First natural frequency as a function of the number of cutting passes and tool location 131
Figure 7-9 Frequency domain presentation of the perturbed system with LPV controller 135
Figure 7-10 Time-domain performance of the perturbed system (the 10th pass of the tool) with the nominal H-inf and LPV controller 136
Figure 7-11 Performance of the perturbed system with a gain scheduled/LPV controller with sensor and actuator in the loop 137
Figure 7-12 Performance of the perturbed system with a gain-scheduled/LPV controller with sensor and actuator in the loop (feedrate 400 microns/second) 137
Figure 8-1 Different types of boring operations 139
Figure 8-2 Schematic of the overall boring operation 142
Figure 8-3 Analysis of ovality and eccentricity 144
Figure 8-4 Forces during revolving bar boring (not to scale) 146
Figure 8-5 Physical schematic for active chatter control 150
Figure 8-6 Design parameters and frequency response of the loop shaping design procedure controller 152
Figure 8-7 Simulink presentation of the control system 155
Figure 8-8 Flowchart for fractional order PD^{λ} control system synthesis 156
Figure 8-9 Closed loop response of the boring process with fractional order PD controller (λ=0.2) (simulations) 157
Figure 8-10 Comparison of the semi-discretization approach and Pseudo spectral approach ... 158
Figure 8-11 Open-loop Stability lobe diagram for boring without and with ovality 159
Figure 8-12 Closed loop response the boring process with eccentricity using PD controller (experimental) 160
Figure 8-13 Performance of Fractional order PD^{λ} controller at 20 microns/rev feed rate (experimental) 161
Figure 8-14 Open-loop Stability lobe diagram for boring with revolving bar 163
Figure 8-15 Closed loop response of the boring operation (with revolving bar) using PD control 164
Figure 8-16 Closed loop response of the boring operation (with revolving bar) using PD^{λ} controller 164

Figure 8-17 Closed-loop response of the boring operation using switching control and time-varying feedback (with revolving bar) 165
Figure 9-1 Geometric parameter representation of the milling tool 169
Figure 9-2 Geometric parameters of the cutting surface when the tool leaves the workpiece ... 169
Figure 9-3 Schematic of the milling process with corresponding sensors 173
Figure 9-4 Stability lobe diagram for a specified range 175
Figure 9-5 Comparison of simulation results with experimental results at 3300 rpm 176
Figure 9-6 Comparison of simulation results with experimental results at 3650 rpm. 177
Figure 9-7 Stability lobe diagram for the system under analysis 178
Figure 9-8 Amplitude of vibration (in x-direction i.e. feed direction) at a different spinning speed of milling tool 179
Figure 9-9 Chatter frequencies as a function of spinning speed of milling cutter 182
Figure 9-10 Instantaneous frequencies as a function spinning speed of milling tool (axial depth of cut is 4 mm) 184
Figure 9-11 Effect of noise on instantaneous frequencies 185
Figure 9-12 STFT as a function of spinning speed of milling tool (at 4 mm axial depth of cut) 186
Figure 9-13 Effect of noise on power spectral density 187
Figure 9-14 Effect of noise on Spectrogram 187
Figure 9-15 Milling tool locus as a function spinning speed of milling tool (noise free cases) . 189
Figure 9-16 Effect of noise on locus of milling tool at different spinning speeds 189
Figure 9-17 Architecture of convolutional Neural Networks 190
Figure 9-18 Training points for simulation assisted deep learning 191

List of Abbreviations

AMB	Active magnetic bearing
BSD	Ball screw drive
CNC	Computer Numerical Control
LPV	Linear parameter varying
PD	Proportional derivative
VC	Varying compliance
AHE	Auxiliary harmonic excitations
HHT	Hilbert-Huang Transformations
FFT	Fast Fourier transform
STFT	Short time Fourier transform
FAR	Full annular rub
PFW	Partial forward whirl
PBW	Partial backward whirl
WHIP	Dry whip
PID	Proportional derivative control
ANF	Adaptive notch filter
DOF	Degree-of-freedom
ACC	Active chatter control
DFA	Detrended fluctuation analysis
HMM	Hidden Markov models
ANN	Artificial neural networks
SB	Stationary bar
RB	Rotating bar
DSMDM	Discrete mass-spring damper element-based model
FEM	Finite element model
MSE	Multi sine excitation

MHG	Multiple harmonics generation
MP	Multi period
AFFC	Adaptive feedforward controller
DFT	Discrete Fourier transformation
EA	Electromagnetic Actuator
VA	Voltage amplifier
IGSLS	Interpolating gain scheduled loop shaping
LSDP	Loop shaping design procedure
ODE	Ordinary differential equations
FOPD	Fractional order proportional derivative
PS	Pseudo spectral
CNN	Convolutional neural network
DWT	Discrete wavelet transformations
SLD	Stability lobe diagrams

Copyright Notices

1. With kind permission from Elsevier Publishers:

- Rajiv Kumar Vashisht, Qingjin Peng, Crack detection in the rotor ball bearing system using switching control strategy and Short Time Fourier Transform, 2018, Elsevier Publication, Journal of Sound and Vibration 432, 502-529.
- Rajiv Kumar Vashisht, Qingjin Peng. Efficient active chatter mitigation for boring operation by electromagnetic actuator using optimal fractional order PD-λ controller. Elsevier publication, Journal of Material Processing Technology. 276 (2020) 116423.

2. With kind permission from the American Society of Mechanical Engineering (ASME):

- Rajiv Kumar Vashisht, Qingjin Peng, Nonlinear dynamic modelling of the cracked rotor ball bearing system with emphasis on damage detection capabilities, 2018, ASME Publication, Journal of Vibration and Acoustics, 140, pp 041018-10.
- Rajiv Kumar Vashisht, Model based determination of size and location of a crack in a rotor system using wavelet transformation and pattern search optimization. ASME 2019 International Design Engineering Technical Conferences and Computers and Information in Engineering Conference, IDETC2019-97072.
- Rajiv Kumar Vashisht, Qingjin Peng. Dynamic modelling and diagnosis of transverse crack and rotor/stator rub in a flexible rotor system. ASME 2019 International Design Engineering Technical Conferences and Computers and Information in Engineering Conference, DETC2019-97047.
- Rajiv Kumar Vashisht, The effect of gravity and rotor configuration on dry friction whip and safe rotor/stator clearance. ASME 2019 International Design Engineering Technical Conferences and Computers and Information in Engineering Conference, DETC2019-97048.

3. With kind permission from Sage Publishers:

- Rajiv Kumar Vashisht, Qingjin Peng, Adaptive hybrid control of unbalanced vibrations of a rotor/active magnetic bearing system with coupling misalignment using low cost instrumentation, 2019, Sage Publication, Journal of Vibration and Control. pp. 1-24.

4. With kind permission from Springer Publishers:

- Rajiv Kumar Vashisht, Qingjin Peng. Improving the cutting rate in turning operations of flexible stepped shafts with a linear parameter varying controller using the electromagnetic actuator, 2019, Springer Publication, International Journal of Advanced Manufacturing Technology,104, pp. 1-16.
- Rajiv Kumar Vashisht, Qingjin Peng. Feasibility analysis of active chatter control for stationary and revolving bar boring operations based on magnitude of control forces using Fractional order PD-λ controller. 2020, Springer Publication, International journal of Advanced Manufacturing Technology, 106, pp.3957–3974.

Chapter 1
Introduction

1.1. Introduction to rotor dynamic systems

Rotors are machine elements transferring torque and power from one component to the other. They are integrated with components like bearings, couplings, belts and pulleys. The rotor in combination with other components is called a rotor system. Rotors are subjected to torque and bending moments either constant in magnitude or time-varying. Due to the flexibility of rotors, they are subjected to vibrations. To find the rotor response at a particular point, modelling of the dynamic rotor system is necessary. Analytical, semi-analytical and numerical techniques are generally used to set up dynamic governing equations of motion of the system. Normally, the dynamics of healthy rotor systems can be represented using ordinary differential equations.

1.2. Faults in rotor dynamic systems

Due to the cyclic nature of the applied torque or bending moment, certain types of cracks are developed in rotors. Dynamic torque produces ‘Slant’ cracks while dynamic bending moments cause ‘Transverse’ cracks. Rotor bearing systems are generally encountered with ‘Transverse’ cracks. With the passage of time, these cracks propagate and pose other instability problems as shown in Figure 1.1. This is the first type of faults in rotating machinery. However, there can be other faults like rotor/stator rub, coupling misalignment, rotor bow and bearing malfunctions. For the purpose of condition monitoring, different techniques are applied to detect the presence of various faults. However, vibration signal-based condition monitoring is best suitable due to its online nature. Due to the presence of these faults, the dynamics of rotor systems become nonlinear.

In the presence of multiple faults, it becomes difficult to detect the type of faults. The dynamics of the cracked rotor can be represented using ordinary differential equations with time-periodic coefficients.

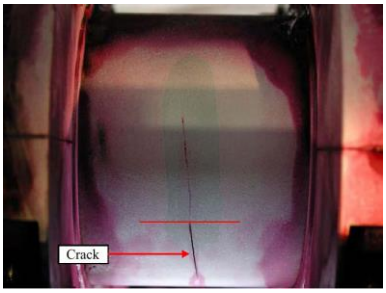

Figure 1.1 Rotor with crack (Lalanne and Ferraris, 1990)

The clearance between the rotor and stationary housing or stator should be reduced to increase the efficiency and leakage prevention in rotating machinery. Unbalanced masses are unavoidable in the rotating machinery. This raises the chances of contacts between the rotor and housing (stator), which is called rotor-stator rubbing. This is the second main fault in rotating machinery as shown in Figure 1.2. Depending on the type and severity of rubbing, the amount of damage can vary from cosmetic damage to the full destruction of the equipment.

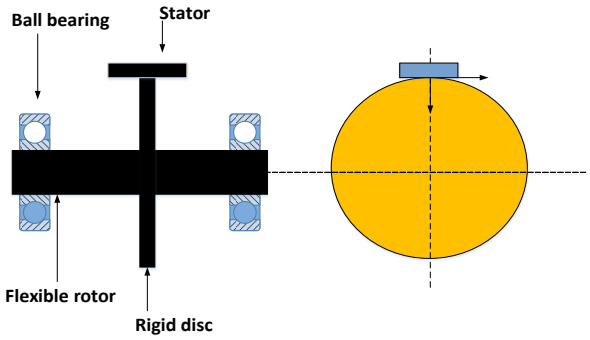

Figure 1.2 Rotor/stator rubbing

There are different states associated with the rubbing viz. damped, divergent and self-maintained actions. In the first kind, the contact disappears with the passage of time. In the

divergent mode (second kind), the amplitude of vibration increases constantly with time. In the self-maintained mode, the contact does not disappear with time. When the clearance between the rotor and stator is fixed and the rotor spins at different frequencies, different characteristics are observed. There is a need for early detection of rotor/stator rub if it occurs. Dynamics of the rotor in the presence of rub must be thoroughly studied. The dynamics of the rotor system under these conditions is represented as a piecewise linear or hybrid system. There is a strong need to develop rub identification strategies based on the vibration response of the rotor dynamic system.

1.3. Active vibration control of rotor dynamic systems

For safety as well as service life considerations, it is important to reduce the vibration level of any rotor-bearing system. The most common cause of the rotor vibrations is the unbalanced mass which remains up to a certain extent even with precision balancing. The application of damping at rotor supports acts, as a mean of reducing the rotor vibration. Active as well as passive damping techniques have been reported in the literature to reduce the vibration level. In passive techniques flexible damped supports, squeeze-film dampers and viscoelastic bearing supports are common.

Active magnetic bearing (AMB) supports a load using the magnetic levitation. AMB supports moving parts without physical contacts as shown in Figure 1.3. For instance, the moving parts are able to levitate a rotating shaft and permit relative motion with very low friction and no mechanical wear. Magnetic bearings support the highest speed of all kinds of bearings. Apart from supporting the load, they reduce rotor vibrations to some extent. In these conditions, they work like electromagnetic actuators.

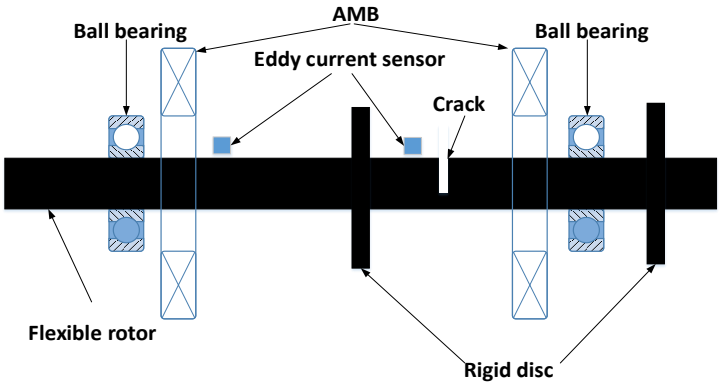

Figure 1.3 Schematic of the experimental setup for AMB

AMBs are used in industrial applications such as the electrical power generation, petroleum refinement, machine tool operation and natural gas handling. They are also used in the Zippe-type centrifuge, for uranium enrichment and in turbomolecular pumps, where oil-lubricated bearings would be a source of contamination. In case of the active vibration control, transient as well as steady-state vibrations can be reduced quickly in amplitude.

1.4. Applications of rotor dynamic systems in machine tools

Flexible rotors are also applied in machining operations. Principles of rotor dynamics are applicable for modelling and design of these systems (Figure 1.4). The dynamics of these systems can be represented in the form of time-delay systems.

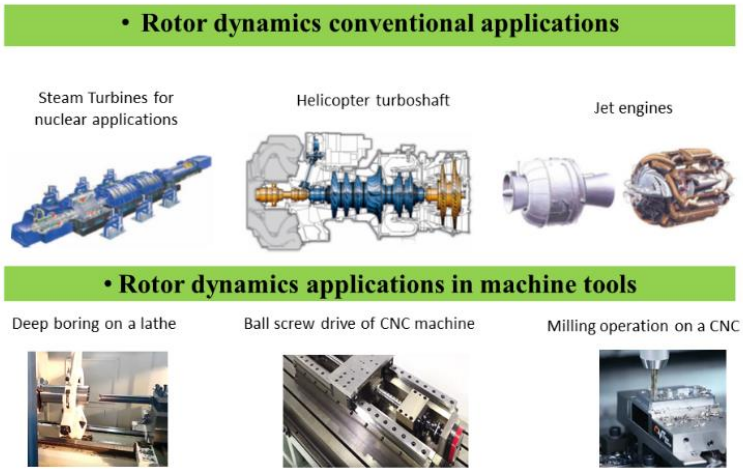

Figure 1.4 Conventional applications of rotor dynamic systems and applications in machine tools

1.4.1. Applications in ball screw drives of Computer Numerical Control (CNC) machines

CNC machines are extensively used in the manufacturing industry. Ball screw drives (BSD) and spindle units are the main components of CNC machines. BSD is used to convert the rotary motion to the linear motion. Due to the finite stiffness of ball bearings and driving shafts, axial vibrations reduce the command tracking efficiency of BSD (Figure 1.5). When designing controllers for this application, the axial flexibility of the driving shaft must be considered.

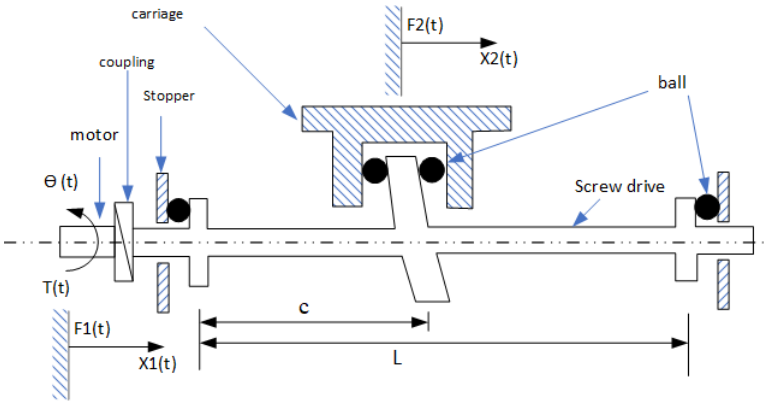

Figure 1.5 Schematic diagram of the ball screw drive

1.4.2. Active chatter control in turning operations

While turning flexible shafts, the flexibility of the cutting tool and shaft (i.e. workpiece) plays an important role (Figure 1.6). Due to this flexibility, for certain combinations of spinning speed of the shaft and depth of cut, self-excited vibrations of the tool and workpieces are produced. This phenomenon is called chatter. It can significantly reduce the surface finish of the workpiece and reduce the useful life of the cutting tool. Hence active as well passive chatter prevention techniques are applied to get rid of the problem.

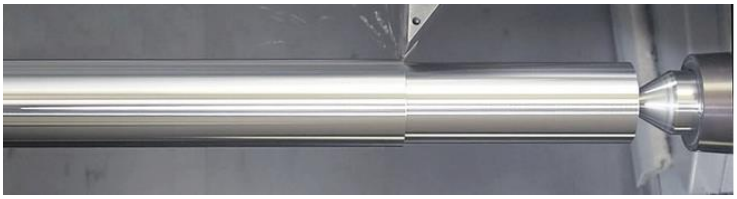

Figure 1.6 Conventional turning operation

1.4.3. Active chatter control in boring operations

Chatter vibrations reduce the depth of cut at a particular spindle speed of machine tools and hence the machining efficiency. Figure 1.7 shows an application of electromagnetic actuators for actively controlling self-excited vibrations produced during machining in boring operations. The dynamics of the boring operation can be represented using ordinary differential equations with time delay. If the eccentricity or ovality is taken into consideration, these systems are changed into time-periodic time-delay systems.

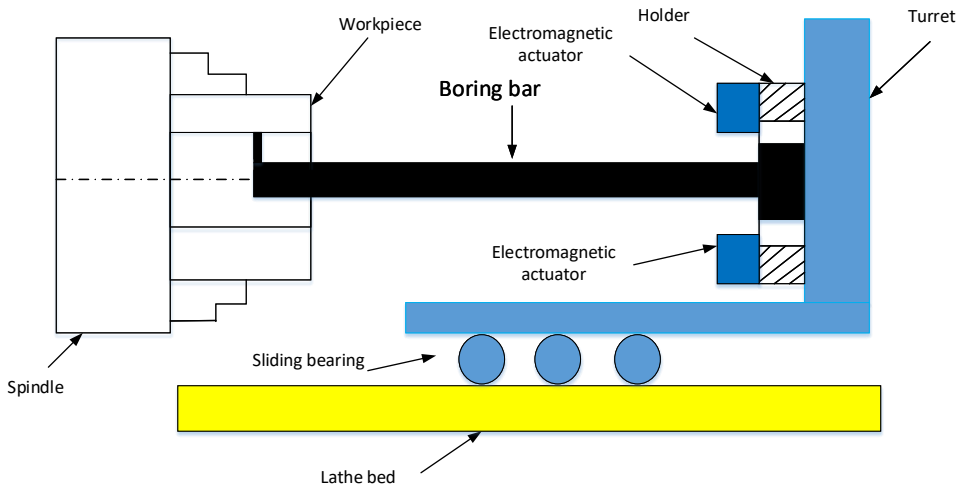

Figure 1.7 Active chatter control in boring operation

1.4.4. Chatter detection in milling operations

In milling operations, due to the intermittent nature of cutting forces, forced vibrations are always present in the system. Suitable online techniques are desirable to detect the presence of chatter. Once chatter is detected, suitable measures can be taken to move the system into the chatter-free zone from chatter conditions. In the past, different online and offline chatter detection techniques have been developed to enhance the productivity of milling operations.

1.5. Research problems

Following research problems are identified to form the research objectives.

I. There is a lack of improved techniques for the modelling of transverse rotor crack and robust online crack detection strategies in case of rotor systems. The multiple harmonics are generated in the presence of rotor faults when the rotor is spinning at a particular rotor spin frequency. It becomes difficult to pin point the type of the fault based on these steady state vibrations. There are no techniques available to differentiate between rotor crack and

other rotor faults (like rotor/stator rubbing action and coupling mis-alignment) based on this vibration response.

II. It is known that feedback controllers are partially effective in suppression of harmonic steady state vibrations in rotor systems, but there are very few control design techniques for suppressing these vibrations.

III. High control forces are required to impart active damping in case of active chatter control applications. There are no active chatter suppression techniques which require small size actuators to be used with the low energy consumption.

IV. There are very less online chatter detection strategies available for milling operation to increase the productivity. Machine learning techniques are not applied for these types of applications.

V. There is a lack of applying concepts of rotor dynamics to machine tools and metal cutting dynamics for the precision control of machine operations and improvement of machining efficiency. There is a lack of control design strategies for robust, energy efficient and precision control of machine tools (like ball screw drive unit of the CNC machines).

1.6. Research objectives and methods

Research objectives and methods of this thesis are as follows.

I. Modeling of transverse cracks and rotor/stator rubbing, and development of a crack detection strategy for rotor systems based on vibration signals. A switching control strategy in combination with short time Fourier transform (STFT) will be investigated for the crack detection.

II. Development of a hybrid controller that combines feedback and feed forward controls to reduce the transient and steady state rotor vibrations. Mu-synthesis based robust control technique will be applied to obtain the robust stability and robust performance.

III. Controllers based on H-infinity control theory, interpolation of controllers at the grid points (i.e. Linear Parameter Varying controller) and fractional calculus will be developed for active chatter controls of the metal cutting processes.

IV. Development of an online chatter detection strategy using machine learning techniques to improve the workpiece surface finish and tool life.

V. Development of high precision and energy efficient control of machine tools (ball screw drive unit of the CNC machines).

1.7. Connectivity of various parts of the dissertation

Figure 1.8 shows the connectivity of different parts of the dissertation. The modelling, fault detection and active vibration control of rotor systems were investigated under classical applications of rotor dynamic systems. These applications are high-end applications and can be seen in the power generation, jet engines and other aerospace structures. However, applications of rotor dynamic systems can also be found in machine tools. The spinning cutting tool of a milling or boring machine represents a rotor dynamic system with cutting forces acting on the tip of an over-hanging rotor. The dynamics of such a rotor system can be represented with time-delay differential equations. To enhance the material removal rate during metal cutting operations, active damping needs to be imparted in the form of active chatter control. The control forces are provided using electromagnetic actuators. Apart from transverse vibrations, sometimes axial vibrations are also generated in rotor systems. The ball screw drive of CNC machines is an important example

in this regard. For precise command tracking, the active vibration control of these resonant axial modes is required.

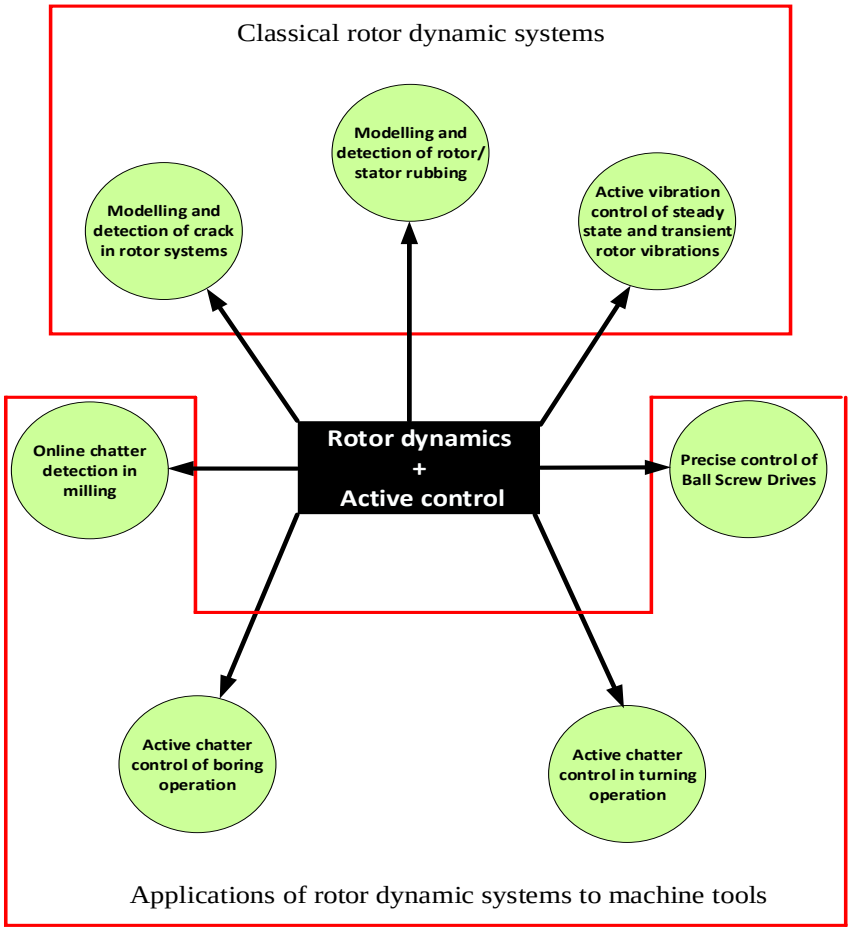

Figure 1.8 Connectivity of different parts of the dissertation

1.8. Structure of the dissertation

The dissertation contains 10 chapters. Chapter 1 introduces the research background and highlights the importance of the research, objectives and research deliverables.

Chapter 2 discusses the literature survey on various aspects of rotor dynamics and applications in machine tools. The research directions based on the literature review are then presented.

Chapter 3 introduces modelling of rotor dynamic systems along with various faults like transverse cracks. The modelling of ball bearings is also presented.

Chapter 4 presents modelling of rotor systems in rotor/stator rubbing actions. Various signal processing techniques are investigated to detect the presence of rotor/stator rubbing actions based on the vibration response.

Chapter 5 presents the active vibration control of rotor systems for coupling faults as well as rotor cracks. The amplitude of vibrations is reduced in case of transient and steady-state vibrations. The Mu-synthesis based robust control technique is proposed along with the feed-forward cancellation technique.

Chapter 6 discusses the hybrid (LPV+PPI) control of ball screw drives of CNC machines. The experimental apparatus and controller synthesis are explained in detail.

Chapter 7 describes the active chatter control of turning operations. An LPV controller is developed to obtain robust stability for the total span of the shaft.

Chapter 8 introduces the active chatter control of the boring process using fractional order PD controllers. It can significantly reduce control forces compared to robust controllers. Small-sized electromagnetic actuators are proposed to maintain closed-loop stability. The effect of eccentricity and ovality on the stability lobe diagrams is investigated. Feasibility of active chatter controls for revolving boring bar systems is verified.

Chapter 9 presents the online chatter detection in milling operations using machine learning techniques. An automatic spindle speed adjustment algorithm is designed and implemented to drag the system from chatter to chatter-free conditions.

Chapter 10 summarizes this research and outlines possible extensions for further research.

Chapter 2
Literature Review

2.1. Overview

Rotors are used to transmit the mechanical energy from one part of the system to the other. A rotor system consists of bearings and couplings along with rotors. In this chapter, literature is reviewed regarding different faults in rotor systems, active vibration control of rotor systems and applications of rotor systems in machine tools. Gaps in the literature are presented with research directions for this dissertation.

2.2. Faults in rotor dynamic systems

In the last three decades, researchers have developed different crack detection techniques. Chen and Zhang (2011) presented a comprehensive introduction to this subject. Wauer (1990), Gasch (1993) and Dimarogonas (1996) analyzed the nonlinear dynamics of rotor systems with fatigue cracks. It was observed that nonlinear vibrations are produced in rotors in the presence of a transverse crack. The permanently open cracks represent asymmetrical rotor and pose stability problems. These types of cracks are generally found in rotors with the low weight. Under the weight dominance, the crack opens as well as closes repeatedly representing a breathing crack. Hinge models of the cracked rotor were reviewed (Gasch, 1993). Breathing crack model of the flexible rotor was proposed in the early time (Jun et al., 1992). The comparison of these two models is available in papers by Patel and Darpe (2008a, 2008b) and Cheng et al. (2011). In case of a cracked rotor system, the stability of periodic motion was used to detect the presence of cracks (Sinou, 2007, Chen et al. 2007, Han and Chu, 2012, Collins et al., 1991, Babu et al., 2008). Apart

from simple two-DOF systems used to model the rotors, various analytical, semi-analytical techniques, as well as finite element techniques have been used to model rotors with cracks.

In double row angular contact ball bearings, the restoring forces are a function of quadratic terms of displacement. Ishida et al. (1990) investigated forced oscillations of rotor-bearing systems in the presence of these nonlinearities. A simple Jeffcott type of rotors was considered in this work and experimental results validated theoretical results regarding the shape of resonance curves. A detailed model of the ball bearing system considering the parametric excitation effect was however considered. Ji et al. (1998) used perturbation methods for the analysis of transient and steady-state vibrations of the nonlinear rotor-bearing system. A nonlinear model of restoring forces generated by bearings was considered. However, parametric excitation considerations and other important modelling aspects of ball bearings were not studied in this work.

Chen (2009) studied an ideal Jeffcott rotor considering three nonlinear factors of ball bearing systems. First is the nonlinear Hertzian contact force between balls and races, second is the clearance of bearings, and third is the varying compliance (VC) vibrations. Villa et al. (2008) studied the stability of nonlinear systems in the frequency domain. A finite element method was used to discretize equations of the motion. In the above study, the steady-state behaviour of nonlinear systems with a very large number of the degrees-of-freedoms was studied using condensation techniques. However, no attention was paid to calculate the transient response of the overall system.

Hou et al. (2016) studied the dynamics of a simple Jeffcott rotor mounted on ball bearings in the presence of a transverse crack. In case of a Jeffcott rotor, bearings are mounted on the shaft/rotor edges, giving less contribution of nonlinear bearing effects to the overall dynamics of the system. This is probably the most recent paper in the field of rotor dynamics, investigating the

combined effect of bearing nonlinearities and rotor cracks. It is also observed that the Jeffcott rotor does not represent the real rotor-bearing system with multiple rigid disks, couplings, flexible bearing supports and centrally located ball bearings. All these parameters demand a high order model of the system to represent the exact dynamics of the real rotor.

The presence of cracks in a revolving rotor converts a linear system into a nonlinear system with varying system parameters due to the parametric excitation. Historically, the 2X (where X is the critical or resonance frequency) response of a revolving rotor system in sub-harmonic and super-harmonic regions has been used to detect the presence of cracks. This process can be used in both frequency and time domains. Markert et al. (2001) applied the same approach in the time domain to identify a crack and its location in a flexible rotor. In this regard, Kulesza et al. (2011) designed a set of observers to find out the presence and location of a crack in a rotor. Sawicki et al. (2011a) used auxiliary harmonic excitations (AHE) to detect the presence of cracks in the rotors. They observed the dynamic response of the rotor under sinusoidal excitation. They noticed that the spectrum of vibration response of a cracked rotor contains multiple frequencies. These frequencies are a function of the rotor spin speed and external excitation frequency. The parametric excitation effect caused by rotor cracks is responsible for the generation of these frequencies. This is a form of nonlinearity. The same concept was used by the authors and their co-workers in other publications (Sawícki et al., 2011, Kulesza, 2014). These methods are quite recent and are being used frequently. Some of the researchers detected the rotor crack based on the transient response of the revolving rotor. Darpe et al. (2004b) studied the transient vibration behaviour of a cracked Jeffcott rotor while crossing the critical or resonance speed. They studied the orbit plots near sub-harmonic resonances to analyze the effect of critical speeds on the orbit orientation. Babu et al. (2008) applied Hilbert-Huang Transformations (HHT) to analyze the transient response of the

cracked Jeffcott rotor. They emphasized that HHT gives better results compared to the continuous wavelet transform and Fast Fourier transform (FFT) for crack detection in a rotor based on the transient response. The main emphasis was on the transient response of the rotor when passing through a critical frequency. Silani et al (2013) investigated the ability of the short-time Fourier transform (STFT) to detect the presence of small cracks based on the transient response calculations. Yang et al. (2015) investigated the role of Empirical Mode Decomposition for analyzing cracks based on the transient response. The existing research in references (Babu et al., 2008, Silani et al., 2013, Yang et al., 2015) is mainly based on the application of STFT for the response in resonance regions. This high amplitude in resonance regions can increase the crack propagation speed. However, working in pre-resonance regions (where the vibration amplitude is much less than the amplitude in resonance regions) is advantageous.

The rubbing of the rotor and stationary stator is also a common fault in rotating machinery. In this concern, Jacquet-Richardet et al. (2013) presented a detailed literature survey on the rotor/stator rub phenomena. Elastic collision theory and impact energy models are quite helpful in the analysis of rotor/stator rub. Based on that, Cong et al. (2011) evaluated the severity of the rub impact fault. Some researchers presented numerical simulations along with experimental results and established the correlation between them (Torkhani et al., 2012). Light, medium and heavy rub conditions were analyzed theoretically and experimentally in their work. Behzad et al. (2013) also used contact mechanics principles in modelling rotor/stator contact. Ma et al. (2013, 2015) modelled a rotor-bearing system by using the Lagrange Multiplier method for the contact formation. Ma et al. (2014, 2015) extended his previous work and modelled the rotor-stator rub under different loading conditions and stator configurations. Recently, Varney et al. (2015) investigated a two-degree-of-freedom asymmetrically supported rotor-stator contact system under

the effect of gravity. They obtained the various type of vibration responses including periodic, quasi-periodic and chaotic behaviours.

There are other physical phenomena related with the rotor/stator rub like jump phenomena, synchronous full annular rub (FAR), partial forward whirl (PFW), partial backward whirl (PBW), chaotic response and dry whip (WHIP) (Jiang and Ulbrich, 2004). In a WHIP, the frequency remains constant and the amplitude increases dramatically. This is a dangerous state of affairs and harmful to the equipment.

It has been observed that WHIP can be initiated without the external stimulus if the right combination of rotor spin frequency and unbalanced mass is achieved. Shang et al. (2011) studied analytically the global vibration characteristics of rotor/stator rubbing systems. Patel and Darpe (2008b) investigated rotor-stator rubbing in a cracked rotor using a full spectral analysis. Lee and Han (1998) used the concept of planar motion to diagnose the rubbing induced faults. Patel et al. (2009) and Zhao et al. (2012) studied the application of Hilbert-Huang transformations and wavelet transformations to vibrations produced during coasting up of a rotor with rotor/stator rub. Generally, the rub phenomena are reproduced by simulations without considering the effect of gravity. The effect of gravity needs to be studied in full detail along with the presence of a transverse breathing crack. Also, there is an urgent need to derive new techniques of diagnosing cracks and rubbing faults based on the vibration response, even if these two faults coexist.

2.3. Active vibration control of rotor dynamic systems

Due to the absence of frictional contacts, active magnetic bearings (AMB) have a long service life. These bearings are robust in nature and require very less maintenance. Hence, they are used in many areas like flywheels (Park 2014; Ren et al. 2013; Fang et al. 2013a, 2013b), control moment gyros and turbopumps (Abrahamsson et al. 2014; Yi et al. 2008). The optimal control is

an important technique of feedback controllers. An optimal solution was obtained in terms of control energy and error (Jastrzębski et al. 2009). However, system uncertainties were not considered in the design of the controller. Robust control techniques like H_∞ and μ-synthesis are worth considering when designing the controller for an uncertain system (Mushi et al. 2012). Stability properties of the closed-loop system with such controllers are better than that with optimal controllers. Proportional – Integral – Derivative (PID) controllers tuned using the multi-objective optimization were also used (Wei et al. 2016).

A gain phase modifier was used to adaptively suppress vibrations caused by the unbalance (Fang et al. 2013a). This method was capable of handling the trouble created by low pass characteristics of the power amplifier. Chen et al. (2015) used a double loop compensation method to suppress unbalanced vibrations.

Zheng et al. (2016) presented an unbalanced vibration reduction scheme using the PID controller for a magnetically suspended centrifugal compressor. An adaptive notch filter (ANF) was used for the frequency estimation. Other methods of the frequency estimation include adaptive observer structures, frequency locked loop (Rodriguez et al. 2011), marginal median discrete Fourier Transform (Djurovic, 2007), and neural network theory. Adaptive Notch Filter is well known in the field due to its simple structure and small computational burden (Mojiri et al. 2004). The biggest advantage of this technique is that its efficiency remains intact even in the presence of power system disturbances (Yazdani et al. 2009; Chu et al. 2011). Yazdani et al. (2009) and Chu et al. (2011) used ANF for reducing the unbalanced vibrations of magnetically levitated rigid rotors.

2.4. Applications of rotor dynamic systems in machine tools

2.4.1. Control ball screw drives of CNC machines

CNC machines have three important units: i) ball screw drives (BSDs) for the linear motion of the table or carriage, ii) spindle units for giving rotary motion to cutting tools, and iii) control unit for the overall control of the CNC machine. In BSDs, the rotary motion of the motor is converted into a linear motion of the carriage by a ball screw nut system. The BSD shaft is mounted on ball bearings. It can be preloaded to avoid any backlash. Due to axial flexibility of the shaft and finite stiffness of balls of the nut and bearings, axial vibrations are generated in the BSD system. The coupling between the motor and shaft also contributes to these vibrations. These are also called structural resonances. Structural resonances inhibit the performance of BSD in many ways (Altintas et al., 2011, Varanasi and Nayfeh, 2004, Pritschow and Croon, 2013). Mainly, they lower the bandwidth of the control system by lowering the gain and phase margins of the overall system (Gordon and Erkorkmaz, 2013). The particular shape of the required reference motion trajectories excites these flexible structural modes. The ultimate goal of a servo control system is to dampen these flexible modes and to increase the bandwidth of the overall system (Kamalzadeh and Erkorkmaz, 2007).

Different active, as well as passive techniques, are available to reduce the structural resonance. In passive techniques, the main approach is to reduce the excitation of flexible modes by aggressive motion commands. The reference trajectories are optimized and pre-filtered to generate desirable frequency contents (Sencer et al., 2015). Input pre-shaping is an important passive damping technique to reduce undesirable structural vibrations (Singhose et al., 1996). In this technique, smooth trajectory commands are generated to reduce undesirable structural vibrations. Optimal reference commands can be generated using filtered B-splines (Duan et al., 2018). The

robustness of the overall system can also be enhanced by optimizing the frequency spectrum of reference commands in a particular band (Sencer and Tajima, 2016).

In active techniques, active damping can be provided to dampen flexible modes. For such systems, a pole placement control strategy provided quite favourable results (Gordon and Erkorkmaz, 2013). The sliding mode control strategy was used to control the rigid body and flexible mode of the BSD system (Kamalzadeh and Erkorkmaz, 2007, Sencer and Tajima, 2016). In addition, the sophisticated LPV control strategy was used to compensate time-varying dynamics generated due to removal of mass during metal cutting (Sepasi et al. 2012). Combination of the pole placement and loop shaping was used (Hanifzadegan and Nagamune, 2015) to safeguard the performance of a closed-loop system against disturbances caused by cutting loads. An LPV controller was implemented for the stiffness variation and mass removal due to cutting.

Feedforward control is another control strategy used for the control of ball screw drives. A zero-phase error tracking controller (ZPETC) is widely used for this purpose (Tomizuka, 1987). In this direction, Chen et al. (2006) used a hybrid controller made by combining the ZPETC controller with cross-coupling controller. Erkorkmaz and Altintas (2001) used a controller made by the combination of disturbance estimator, friction compensator and a ZPETC. The main problem with feedforward controllers is that the plant dynamics must be known with certainty. This problem was solved by Uchiyama (2008). He used an adaptive two-DOF controller to feed tool drives. The system parameters were updated to achieve desired performance in the presence of uncertain reference signals. To compensate for position-dependent dynamics of the ball screw drive, a controller composed of modal characteristic modifier and adaptive tuning algorithm was used (Liu et al., 2017a, 2017b). Artificial neural networks were used for adaptive tuning. It is

obvious from the above work that hybrid controllers are better suitable for satisfying multiple requirements.

Although robust H_∞ controllers require no special hardware for the control implementation, they have not gained wide acceptance in the industry. In industry, a cascade PPI controller is normally used (Sun et al., 2016). Here P is the proportional controller and I is the integral controller. PI controller is implemented in the motor speed loop and P controller is implemented in a table position loop. Pritschow et al. (2003) modified this controller by additional acceleration feedback. A semi-active damper between the table and machine bed was used to enhance the closed-loop performance (Verl and Frey, 2012). A feed drive mechanism with soft axial bearing and strong parallel damper was used to enhance the performance (Pritschow and Croon, 2013). Using the concept proposed in references (Pritschow et al., 2003, Verl and Frey, 2012, Pritschow and Croon, 2013), the increased bandwidth was obtained but additional sensors or actuators were required. Very recently, Sun et al. (2018) increased the bandwidth of the position loop without using any additional actuator, with the help of a disturbance observer. Li et al. (2018) used a feedforward compensation method for dynamic mechanical tracking errors. A dynamic model was proposed to offset position commands given to the controller. Dumanli et al. (2018) used the acceleration and jerk feedback to improve the bandwidth of controllers. Linear Quadratic Regulator was used to position poles at certain specified positions.

2.4.2. Active chatter control in turning operation

Merritt (1965) described the basics of the regenerative chatter (Marui et al., 1983, Kato and Marui, 1974). Jen et al. (1996) described the dynamic interaction of workpiece and lathe structure. In this work, the flexibility of the cutting tool and workpiece was studied in combination to generate stability lobe diagrams. Shawky et al. (1998) used a model predictive control-based

strategy for enhancing the accuracy of bar turning. They used the Kalman filter-based state estimation with online measurements. Yu et al. (2008) conducted the stability analysis of flexible shafts (uniform and stepped). They emphasized on the location-dependent stiffness of the shafts and related it with the stability lobe diagrams of stepped shafts. Normally the cutting dynamics is represented as a single-DOF system. However, the two and three-DOF systems are more suitable to represent the cutting dynamics of flexible shafts. Rao et al. (1999) used a 3-DOF model to represent the dynamics of the turning process. This analysis was more suitable than that presented by Wang and Cleghorn (2002). The work on stability analysis of turning of a long slender shaft was extended by Li et al. (2012). In certain circumstances, the flexibility of workpiece and cutting tools need to be considered. In this case, the compliance between the two was considered by Otto et al. (2015). Recently, the stability analysis of long flexible shafts was also presented by Stepan et al. (2017).

Active chatter control (ACC) for turning operations was presented by Ganguli et al. (2007). They used frequency-domain methods for checking the stability of turning operations. To validate theoretical results, experiments were conducted and presented (Ganguli et al., 2005). The concept of an active dynamic absorber was introduced by Tewani et al., (1995). Apart from turning operations, the ACC of the boring process has undergone tremendous progress. Recently magnetic actuators were used in ACC of the boring process (Lu et al., 2014). ACC for the turning process with the experimental validation is reported by Shiraishi et al. (1991) to implement an optimal control method. A combination of frequency and time domain methods was used to study the stability of cutting systems (Mei et al., 2005, Lu et al., 2018). Ma et al. (2017) emphasized that it is difficult to measure the structural parameters of the cutting system. With the passage of time, these parameters are bound to change also. They used an Adaptive Sliding Mode Control for ACC.

They theoretically proved the stability of the proposed controller and experimentally validated the effectiveness of the controller. These show state of the art of techniques for chatter prevention in turning operations.

There is a trend in combining passive and active techniques to enhance the overall efficiency of the process. Meng et al. (2015) used a sinusoidal spindle speed variation in the combination with a state feedback controller. After the thorough study, it was observed that the ACC control has been implemented for preventing chatter for fixed-parameter systems. The dynamics of stepped shafts with the location-dependent flexibility is quite complicated. As the material is removed, natural frequencies of the shaft change drastically. Hence, the ACC designed for one particular set of parameters loses stability for another set of parameters.

2.4.3. Active chatter control in boring operation

From time to time several passive techniques were devised to enhance the depth of cut without chatter in boring operations. The research of Klein et al. (1975) provided the theoretical foundation for enhancing the chatter stability by means of the active chatter control strategy. Tanaka et al. (1994) used piezoelectric actuators for enhancing the chatter stability of boring operations. Wang et al. (2001) used electrorheological fluids for actively controlling the chatter in boring operations. Pratt et al. (2001) investigated theoretically and experimentally the stability of a slender boring bar under regenerative chatter conditions. Andréne et al. (2003) installed a piezo actuator into a turning tool holder for vibration control. Chen et al. (2014) used magnetic actuators for controlling the chatter in boring bars. Mei et al. (2009) used a magnetorheological fluid controlled boring bar for reducing the chatter.

Experimental results were also discussed (Ganguly et al., 2005). Parameters of machines are subjected to change during their service life. Designed controllers must be robust enough to bear

these uncertainties. In this regard, Sliding Mode Control (SMC), Linear Quadratic Regulators (LQR) and H_∞ controllers have been applied for active control applications (Tewani et al., 1995). Ma et al. (2017) observed that in designing all these controllers, the proper estimation of machine tool parameters is required, which is difficult to measure. Considering these limitations, an adaptive SMC was implemented in their work.

2.4.4. Chatter detection in milling operation

The sensor cost is decreasing day-by-day giving a push to online chatter detection technology. Researchers have developed methods for online chatter detection using vibration, sound and power signals obtained from different types of sensors.

Rahman and Ito (1986) diagnosed the onset of chatter based on the horizontal deflection of the cutting tool. Liao and Young (1996) proposed the spindle speed regulation to control chatter when it has just started. They collected the dynamic cutting force signal from the dynamometer. They used fast Fourier transform of collected signals to determine the new spindle speed. (During chatter, due to the interaction of cutting tool and workpiece, a particular sound is generated. A microphone is a good sensor to catch that sound. Delio et al. (1992) used the audio signal for detection and control of chatter. Schmitz et al. (2001) extended this idea because microphones are economical compared to dynamometers, displacement probes and accelerometers. In their work (Schmitz et al. 2002, 2003), they worked on the once per revolution audio signal variance as an indicator of chatter. They also worked on the statistical evaluation of the audio signal. The energy of the measured sound signal, when exceeds a certain threshold level, can be considered as an indicator of chatter (Weingaertner et al., 2006). Ismail and Ziaei (2002) worked on a 5-axis milling machine. They conducted a sound analysis of the machining process in combination with offline scheduling of process parameters and online spindle ramping. Tsai et al. (2009, 2010) worked on

the signal obtained from acoustic sensors and proposed a spindle speed compensation technique. Okuma (2006) presented a commercial chatter detection solution. They used microphones that were connected to NC machines through a USB port to give acoustic feedback. He also presented a software downloadable tool to NC machines, which can suggest the new spindle speeds for online adaption. However, the limitation of the audio-based signal techniques is that the sound from other machines can interact with the machine under consideration.

Faassen et al. (2006) used accelerometers for the detection of chatter in machine tools. Doppenberg et al. (2006) used the algorithm proposed by Faassen et al. (2006) to adjust the spindle speed to move the system into a chatter-free zone. Tansel et al. (2012) worked on the chatter detection on a milling machine with index-based reasoning using a torque-based signal from a rotary dynamometer. They used a lookup table approach for classification of input signals. The chatter detection in case of turning is easy compared to milling operations. For the turning operation chatter detection, Tangjitsitcharoen and Moriwaki (2008), and Tangjitsitcharoen (2009) proposed the use of power spectral density of the tool deflection. Kuljanic et al. (2008, 2009) developed a multi-sensor chatter detection system. They compared the sensitivity of displacement sensors, accelerometers and dynamometers for chatter detection applications. Vela et al. (2010) used a detrended fluctuation analysis (DFA) technique adopted for the time-frequency domain to detect chatter instabilities from data obtained from accelerometer sensors. DFA has additional advantages over the traditional spectrum analysis. These can deal with nonstationary and nonlinear signals efficiently. Yao et al. (2010) used wavelets and support vector machines for chatter detection. Zhang et al. (2010) used a combination of hidden Markov models (HMM) and artificial neural networks (ANN) for chatter monitoring. In their work, HMM were used for temporal modelling of features extracted from time-varying signals and ANN were used for integrating

inputs. Eppel et al. (2010) used optical sensors for measuring the milling tool deflection. Based on the signal obtained, they developed a technique for differentiating between chatter and non-chatter conditions.

Cao et al. (2013) combined wavelet packets and Hilbert Huang Transformations (HHT) for the chatter identification in end milling operations. Wavelets were used to denoise the signal and HHT were used to analyse the time-frequency distribution of the signal obtained from accelerometers mounted on the spindle unit of the milling machine. Wang et al. (2009) emphasized that Fourier transform is not capable of differentiating transition in non-stationary signals, hence is not suitable for online detection of chatter onset. They presented a statistical chatter detection algorithm based on the statistical analysis of discrete wavelet transforms. Choi and Shin (2003) presented a wavelet-based maximum likelihood parameter estimation technique for the chatter identification in turning and milling operations. Yoon and Chin (2005) emphasized that detailed coefficients in the wavelet transform can give some indications of the chatter in milling operations.

The use of accelerometers and other sensors increases the cost and complexity of CNC machines. Hence researchers have tried to detect the chatter based on the signal obtained from the servo system of the spindle unit. Kakinuma et al. (2011) used disturbance observer theory to detect the self-excited and forced vibrations developed during chatter. Shimoda et al. (2017) also used disturbance observer theory to detect the presence of chatter from the signal obtained from the drive unit (i.e. linear encoders) of CNC machines. In these techniques, they used bandpass filters to detect chatter frequency. With this method, it becomes easy to isolate the structural dynamics of the cutting tool. However, the chatter frequency is not known a priory and hence it is difficult to determine the cut-off frequencies of these filters. Manual intervention becomes necessary based on cutting conditions. This is however detrimental to online chatter detections. To overcome this

difficulty, frequency domain chatter detection techniques were developed to use the total spectrum of the available signal from sensors (Liu et al. 2018). Recently, Aslin and Altintas (2018) used the machine tool drive unit current obtained from a servo system for the detection of chatter. They removed the forced vibration component and used a Fourier Transform of the remaining signal to detect the presence of chatter.

For applications of machine learning in machine health monitoring, Hoang et al. (2019) presented a thorough survey of applications of deep learning techniques for the roller bearing fault diagnosis. For more detail, references therein can be referred to Zhao et al. (2019). They discussed the applicability of different machining learning methods for machine health monitoring. They considered the gearbox fault detection, induction motor fault detection and tool wear prediction of CNC milling machines. They used statistical, frequency domain and time-frequency domain results in the analysis. Oleaga et al. (2018) proposed a machine learning-based solution for chatter prediction in a heavy-duty milling machine. They used regression trees for prediction of the chatter frequency. However, they emphasized on prediction instead of detection, especially on an online basis. It is a known fact that collecting experimental data is a costly affair. Bearing this in mind, Sobie et al. (2018) used a simulation-driven machine learning approach for bearing fault classification. They used data collected from high-resolution dynamic simulations of ball bearings. These data were used to train machine learning algorithms. They used convolutional neural networks for the bearing fault classification. After an extensive search, it was realized that the literature available in the field of chatter detections using the machine or deep learning is scant.

2.5. Research gaps and directions

Based on the literature survey, following gaps are noticed and research directions are identified.

- There is a need to show the impact of the ball bearings in the rotor system on the efficiency of crack detection techniques based on the steady-state vibration response.
- There is a need to devise a transverse crack detection strategy, which can be used in the presence of ball bearings in the rotor system.
- There is a need to identify and quantify these faults simultaneously.
- The effect of gravity needs to be studied in full detail along with the presence of a transverse breathing crack for rotor/stator rubbing. Also, there is an urgent need to derive new techniques of diagnosing cracks and rubbing faults based on the vibration response, even if these two faults coexist.
- An effort should be made such that the fault detection can be done in an online manner.
- There is a need to apply hybrid controllers (a combination of feedback and adaptive feedforward cancellation) to reduce the amplitude of steady-state as well as transient vibrations. The control strategy should also be capable of identifying the rotor system faults (like rotor crack and coupling misalignment) using the power spectral density of applied control inputs.
- There is a great need to implement principles of rotor dynamics to machine tools. There is a need for applying hybrid controllers to enhance the command tracking efficiency as well as the performance of the BSD during metal cutting operations.
- There is a need to apply Linear Parameter Varying (LPV) controllers for updating controller parameters during the total span of the shaft during turning operations.

- Due to the flexibility of the boring bar in all directions, there is a need for the 3D model for the cutting process in case of boring operations. Heavy forces are required to maintain stability during active chatter control applications. There is a need for controllers to require small control forces for ACC applications. There is also a need to consider the effect of ovality of the workpiece as well as the eccentricity of the boring bar during the modelling process so that stability lobe diagrams can be constructed accurately.
- There is a need to derive the dynamic model for stationary bar (SB) and rotating bar (RB) boring operations and to investigate the difference between the two. Feasibility analysis of ACC for RB boring operations must also be carried out.
- There is strong need of developing an online chatter detection technique for turning, boring and milling operations. An algorithm is required for the automatic spindle speed regulation so that a system can be dragged to the chatter-free zone from chatter conditions (without using ACC).

Based on the gaps found in literature and identified research directions, research has been conducted. Following chapters will introduce theoretical as well as experimental work done in this thesis to fill these gaps.

Chapter 3

Modelling and fault detection in rotodynamic systems

3.1. Overview

In case of simple Jeffcott rotors, bearings lie on edges of the rotors, hence bearing nonlinearities are not properly absorbed in the dynamic response. Real rotors containing multiple disks, flexible bearing supports, centrally located ball bearings and couplings are far more complex in terms of their dynamic response than simple Jeffcott rotors. Nonlinear dynamic modelling of the flexible rotor with centrally located ball bearing has been developed along with transverse crack and used for simulation purposes. It has been observed that crack detection techniques based on the steady-state vibration response work well for simple Jeffcott rotors only. The presence of ball bearings and other system nonlinearities inhibit the direct application of steady-state dynamic response-based crack detection techniques for real rotor-bearing systems condition monitoring. However, transient response-based crack detection techniques can be successfully applied to work in the presence of system nonlinearities. Crack propagation is enhanced during high amplitude vibrations, hence, instead of working in the resonance region, working in pre-resonance regions is advantageous due to lower vibration amplitudes. Switching control strategy based on a combination of active vibration control and Short Time Fourier Transform is proposed in this work. The proposed technique basically operates on the signal in pre-resonance regions (with low vibration amplitude) hence avoids chances of the crack propagation. This technique can be used to detect the presence of even small cracks and works well in the presence of bearing nonlinearities and flexible bearing supports that are inherently present in real rotor-bearing systems and qualitatively change dynamics of the overall system.

3.2. Mathematical Modelling

Many techniques are available for mathematical modelling of cracked flexible rotors. Analytical techniques are slightly difficult to apply; however, the generated mathematical models are low in the order. They can only be applied to simple geometries. Finite element methods can be applied to complex geometries, but the resulted models are high in the order. In this research, a discrete mass spring damper element-based model (DMSDM) of the real rotor system is developed compared to the finite element model (FEM). To obtain better accuracy, parameters of the low order DMSDM are fine-tuned to match its results with a high order FEM. The resulted model is then used for simulation purposes.

3.2.1. Finite Element Model of flexible Rotor systems

A shaft is discretized into several finite elements. Each element contains two nodes with 4 degrees-of-freedom at each node. For discretization, Timoshenko beam elements are used. Elemental governing equations of the motion are as follows (Lalanne and Ferraris, 1990, Vashisht et al., 2018)

$$\left(\mathbf{M_T^e} + \mathbf{M_R^e}\right)\ddot{\mathbf{x}}_\mathbf{i}^\mathbf{e} + \left(\mathbf{C_R^e} - \Omega_{\text{Rotor}}\,\mathbf{G_R^e}\right)\dot{\mathbf{x}}_\mathbf{i}^\mathbf{e} + \mathbf{K_B^e}\mathbf{x}_\mathbf{i}^\mathbf{e} = \mathbf{Q_i^e} \tag{3.1}$$

where $\mathbf{M_T^e}$ and $\mathbf{M_R^e}$ are translational and rotary elemental mass matrices. $\mathbf{C_R^e}$, $\mathbf{G_R^e}$ and $\mathbf{K_B^e}$ are elemental damping, gyroscopic, and stiffness matrices respectively. $\mathbf{Q_i^e}$ defines a gravity force vector for the element. $\mathbf{x_i^e}$ is the displacement vector for the element. Ω_{Rotor} is the rotor spin frequency. For the sake of simplicity, classical damping is considered by using Rayleigh's expression: $\mathbf{C_R^e} = \alpha(M_T^e + M_R^e) + \beta K_B^e$, where α and β are constants. The dynamic model of the rigid discs is given by the following relations (Lalanne and Ferraris, 1990).

$$\left(\mathbf{M_T^d} + \mathbf{M_R^d}\right)\ddot{\mathbf{x}}_\mathbf{i}^\mathbf{d} + \left(-\Omega_{\text{Rotor}}\,\mathbf{G_R^d}\right)\dot{\mathbf{x}}_\mathbf{i}^\mathbf{d} = \mathbf{Q_i^d} + \mathbf{F_i^d} \tag{3.2}$$

where $\mathbf{M_T^d}$, $\mathbf{M_R^d}$ and $\mathbf{G_R^d}$ are the translational mass, rotary mass, and gyroscopic matrices, respectively. $\mathbf{Q_i^d}$ and $\mathbf{F_i^d}$ are the weight of the disk and the unbalance forces respectively. The unbalanced mass is attached to the disk 2. The bearings are mounted on flexible bearing supports as shown in Figure 3.1 (Sections A and B). A coupling shown in Section C of Figure 3.1 is located at the right extreme of the flexible shaft. Bearing supports are modelled as two-node linear elastic spring elements. These bearing supports considerably change the dynamics of the overall system and are formulated in the form of following equations of motion (Lalanne and Ferraris, 1990, Vashisht et al., 2018).

$$\mathbf{M^s}\ddot{\mathbf{x}}_i^{\mathbf{s}} + \mathbf{K^s x_i^s} = \mathbf{F_i^s} \tag{3.3}$$

where $\mathbf{M^s}$, $\mathbf{K^s}$ and $\mathbf{F_i^s}$ are the elemental mass matrix, stiffness matrix, and external load vector, respectively. The effect of bearing stiffness is accommodated by placing the stiffness coefficients at appropriate locations. The global dynamics of the complete rotor system is represented in the matrix form as follows.

$$(\mathbf{M_T} + \mathbf{M_T^d} + \mathbf{M^s} + \mathbf{M_R} + \mathbf{M_R^d})\,\ddot{\mathbf{x}} + \left(\mathbf{C_R} - \Omega_{Rotor}\ (\boldsymbol{G}_R + \boldsymbol{G}_R^d)\right)\dot{\mathbf{x}} + (\mathbf{K_B} + \mathbf{K^s})\,\mathbf{x} = (\mathbf{Q} + \mathbf{Q^d} + \mathbf{F^d} + \mathbf{F^s}) \tag{3.4}$$

The system of equations can be presented in a compact form:

$$\mathbf{M}\,\ddot{\mathbf{x}} + \left(\mathbf{C} - \Omega_{\mathrm{Rotor}}\,\mathbf{G}\right)\dot{\mathbf{x}} + \mathbf{K}\,\mathbf{x} = \mathbf{F_Q} + \mathbf{F_W} \tag{3.5}$$

where **M** and **G** are the global mass and gyroscopic matrices respectively. The global damping and stiffness matrices are represented by **C** and **K** respectively. The global vector of the gravity and imbalance forces are represented by $\mathbf{F_Q}$ and $\mathbf{F_W}$ respectively.

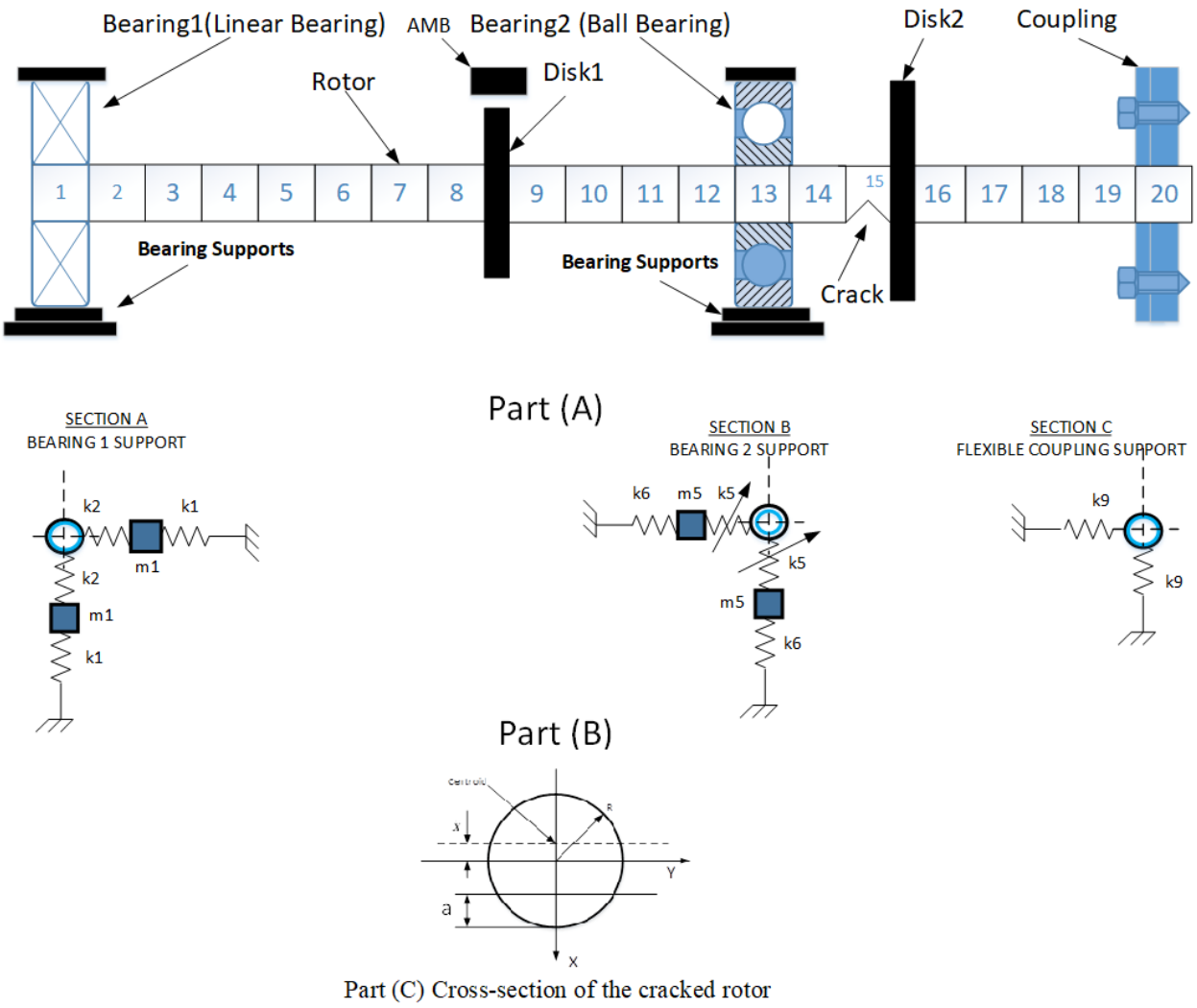

Figure 3.1 Schematic of the finite element model of a rotor-bearing system

Equations (3.1-3.5) are used in this work to obtain the FEM of a rotor system. The rotor is lying horizontally and has two rigid disks. The effect of gravity is given due consideration. The rotor is divided into 20 discrete elements. The bearings, disks and coupling are assumed to be located on nodes. However, due to the purpose of clarity, some of these components cover some of the elements in Figure 3.1. The overall length and diameter of the rotor are 1478 mm and 40 mm respectively. The mass of the Disk 1 is 5 Kg and Disk 2 is 19.4 Kg (Figure 3.2). The rotor is mounted on two bearings. A flexible coupling connects the rotor at the right-hand side. Left-hand

side bearing support contains a linear bearing with stiffness $7x10^8$ N/m with a mass of the bearing pedestal or support as 6 Kg. The stiffness of the bearing support is $3.8x10^6$ N/m. Right-hand side bearing support contains a ball bearing with bearing stiffness $4.6x10^7$ N/m and a mass of the bearing pedestal as 6 Kg having the same stiffness of the bearing as the left-hand side support. The rotor-bearing system is assumed being made of various spring-mass dampers connected. Figure 3.2 represents the equivalent discrete spring-mass system and shows various physical parameters of the rotor-bearing system. This figure represents these connected elements in one plane. The important physical parameters of the complete system along with mechanical properties are shown in Table 3.1 (Villa et al., 2008).

Table 3.1 Physical parameters and mechanical properties of the rotor bearing system

Notation	Description	Value
D	Shaft Diameter of the shaft	0.04 m
L	Shaft Length of the shaft	1.478 m
ρ	Density	7800 Kg/m^3
E	Young's modulus of elasticity	210 x 10^9 N/m^2
α	First Rayleigh damping coefficient	1.36
β	Second Rayleigh damping coefficient	1.75 x 10^{-5}
ϵ	Eccentricity of the mass unbalance	0.2 m
m	Imbalance mass	3 x 10^{-3} Kg

Table 3.2 Damping parameters of the discrete mass representation of rotor bearing system

Notation	Description	Value
c_1	Damping coefficient of the first bearing support	90 Ns/m
c_2	Damping coefficient of the first bearing element	90 Ns/m
c_3	Damping coefficient of length section L_2	12 Ns/m
c_4	Damping coefficient of length section L_3	12 Ns/m
c_5	Damping coefficient of second bearing element	90 Ns/m
c_6	Damping coefficient of second bearing support	90 Ns/m
c_7	Damping coefficient of length section L_4	12 Ns/m
c_8	Damping coefficient of length section L_5	12 Ns/m
c_9	Damping coefficient of coupling	90 Ns/m

3.2.2. Discrete Mass spring damper element-based Model

The DMSDM has reduced order with high computational efficiency. Figure 3.3 represents the DMSDM of the overall system in the horizontal direction. For the vertical direction, a similar system can be generated. Equations of motions can be derived using the force method or energy method.

In this research, the energy method is used. The kinetic energy T and potential energy U subjected to lateral vibrations in the horizontal direction can be written as follows (Lalanne and Ferraris, 1990, Vashisht et al., 2018).

$$T = \frac{1}{2}\left[m_1\ \dot{u}_1^2 + m_2\ \dot{u}_2^2 + m_3\ \dot{u}_3^2 + m_4\ \dot{u}_4^2 + m_5\ \dot{u}_5^2 + m_6\ \dot{u}_6^2 + m_7\ \dot{u}_7^2 \right] \tag{3.6}$$

$$U = \frac{1}{2}\begin{bmatrix} k_1\ (u_1)^2 + k_2\ (u_1 - u_2)^2 + k_3\ (u_2 - u_3)^2 + k_4\ (u_3 - u_4)^2 + k_5\ (u_4 - u_5)^2 \\ + k_6\ (u_5)^2 + k_7\ (u_4 - u_6)^2 + k_8\ (u_6 - u_7)^2 + k_9\ (u_7)^2 \end{bmatrix} \tag{3.7}$$

The kinetic and potential energy in the vertical direction can be obtained in a similar manner. Using the Lagrange method, equations of motions in horizontal and vertical directions can be calculated. Lagrangian (L) is defined as follows (Lalanne and Ferraris, 1990, Vashisht et al., 2018).

$$L = T - V \tag{3.8}$$

The Euler-Lagrange equation is given as follows (Lalanne and Ferraris, 1990, Vashisht et al., 2018).

$$\frac{d}{dt}\left(\frac{\partial L}{\partial \dot{q}}\right)=\frac{\partial L}{\partial q} \tag{3.9}$$

Using this equation and incorporating the appropriate damping (shown in Table 3.2), the following equations of the motion are derived:

$$\begin{aligned}
&m_1\ddot{u}_1+(c_1+c_2)\dot{u}_1-c_2\dot{u}_2+(k_1+k_2)u_1-k_2u_2=F_{u_1}\\
&m_2\ddot{u}_2-c_2\dot{u}_1+(c_2+c_3)\dot{u}_2-c_3\dot{u}_3-k_2u_1+(k_2+k_3)u_2-k_3u_3=F_{u_2}\\
&m_3\ddot{u}_3-c_3\dot{u}_2+(c_3+c_4)\dot{u}_3-c_4\dot{u}_4-k_3u_2+(k_3+k_4)u_3-k_4u_4=F_{u_3}\\
&m_4\ddot{u}_4-c_4\dot{u}_3+(c_4+c_5+c_7)\dot{u}_4-c_5\dot{u}_5-c_7\dot{u}_6-k_4u_3+(k_4+k_5+k_7)u_4-k_5u_5-k_7u_6=F_{u_4}\\
&m_5\ddot{u}_5-c_5\dot{u}_4+(c_5+c_6)\dot{u}_5-k_5u_4+(k_5+k_6)u_5=F_{u_5}\\
&m_6\ddot{u}_6-c_7\dot{u}_4+(c_7+c_8)\dot{u}_6-c_8\dot{u}_7-k_7u_4+(k_7+k_8)u_6-k_8u_7=F_{u_6}\\
&m_7\ddot{u}_7-c_8\dot{u}_6+(c_8+c_9)\dot{u}_7-k_8u_6+(k_8+k_9)u_7=F_{u_7}
\end{aligned} \tag{3.10}$$

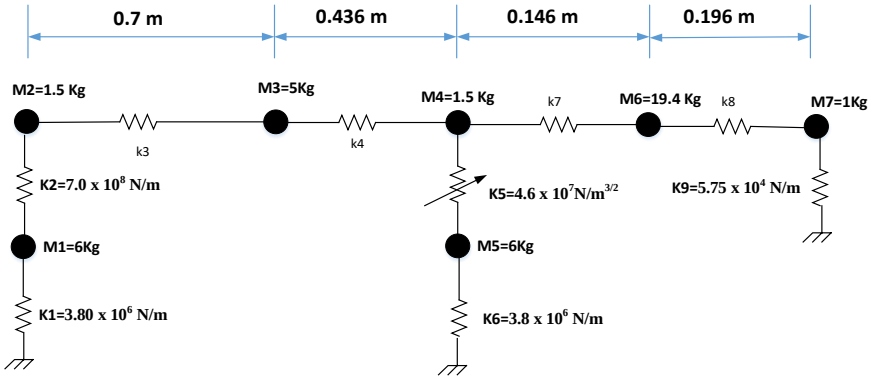

Figure 3.2 Equivalent physical model of the discrete mass model of the rotor bearing system in one plane (not to scale)

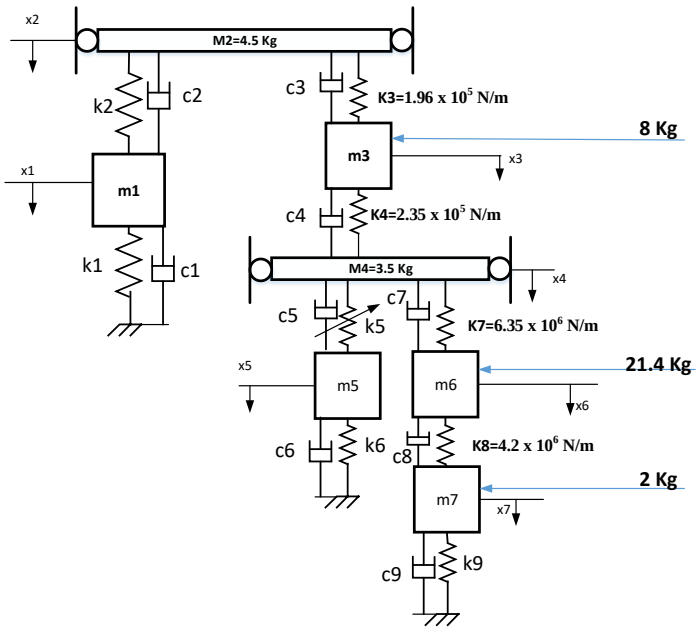

Figure 3.3 Phenomenological model of the discrete mass model of the rotor bearing system in one plane (not to scale)

where *us* are deflections, *cs* are damping coefficients, *ks* are the stiffness's and F_u s are the forces acting in the horizontal direction. The equations of motion in the vertical direction are given as follows.

$$
\begin{aligned}
&m_1\ddot{v}_1+(c_1+c_2)\dot{v}_1-c_2\dot{v}_2+(k_1+k_2)v_1-k_2v_2=F_{v_1}\\
&m_2\ddot{v}_2-c_2\dot{v}_1+(c_2+c_3)\dot{v}_2-c_3\dot{v}_3-k_2v_1+(k_2+k_3)v_2-k_3v_3=F_{v_2}\\
&m_3\ddot{v}_3-c_3\dot{v}_2+(c_3+c_4)\dot{v}_3-c_4\dot{v}_4-k_3v_2+(k_3+k_4)v_3-k_4v_4=F_{v_3}\\
&m_4\ddot{v}_4-c_4\dot{v}_3+(c_4+c_5+c_7)\dot{v}_4-c_5\dot{v}_5-c_7\dot{v}_6-k_4v_3+(k_4+k_5+k_7)v_4-k_5v_5-k_7v_6=F_{v_4}\\
&m_5\ddot{v}_5-c_5\dot{v}_4+(c_5+c_6)\dot{v}_5\ -k_5v_4+(k_5+k_6)v_5=F_{v_5}\\
&m_6\ddot{v}_6-c_7\dot{v}_4+(c_7+c_8)\dot{v}_6-c_8\dot{v}_7-k_7v_4+(k_7+k_8)v_6-k_8v_7=F_{v_6}\\
&m_7\ddot{v}_7-c_8\dot{v}_6+(c_8+c_9)\dot{v}_7-k_8v_6+(k_8+k_9)v_7=F_{v_7}
\end{aligned}
\qquad (3.11)
$$

where *vs* are deflections in the vertical direction and F_v s are forces acting at individual masses in the vertical direction. Equations (3.10-3.11) are used to construct the DMSDM of the rotor-bearing system used in this research. To match the modal parameters of the full and reduced order model, the genetic algorithm-based multi-objective optimization is performed. If $\hat{\omega}_r(\mathbf{x})$ and $\hat{\phi}_r(\boldsymbol{x}) \in R^{N_0}$

(for r=1…H) are modal frequencies and mode shape components at the N_0^{th} degrees-of-freedom respectively (for the first *H* modes), corresponding to parameter ***x***, we need to solve following eigenvalue problem (Lalanne and Ferraris, 1990, Vashisht et al., 2018).

$$[\boldsymbol{K}(\boldsymbol{x}) - \hat{\omega}_r^2(\boldsymbol{x})\boldsymbol{M}(\boldsymbol{x})]\ \hat{\phi}_r(\boldsymbol{x}) = \mathbf{0} \tag{3.12}$$

where $\mathbf{K}(\boldsymbol{x})$ and $\mathbf{M}(\boldsymbol{x})$ represent the stiffness and mass matrices respectively of the reduced-order DMSDM with parameter ***x***. The optimization problem can be set up to minimize the following objective function.

$$\Psi(\boldsymbol{x}) = \{\Psi_1(\boldsymbol{x}), ...\Psi_n(\boldsymbol{x})\} \tag{3.13}$$

where $\Psi_i(\boldsymbol{x}) = \dfrac{\left\|\hat{\omega}_i(\boldsymbol{x}) - \tilde{\omega}_i\right\|^2}{\left\|\tilde{\omega}_i\right\|^2} + \dfrac{\left\|\hat{\phi}_i(\boldsymbol{x}) - \tilde{\phi}_i\right\|^2}{\left\|\tilde{\phi}_i\right\|^2}, i = 1, ..., H$. Here $\|z\|^2 = z^T z$ is the usual Euclidian norm. *H* is the number of modes considered. The modal frequencies and mode shapes for the i^{th} mode of the full order system are represented by $\tilde{\omega}_i$ and $\tilde{\phi}_i$, respectively. The original shaft stiffness parameters were calculated using the strength of material formulas. These modified coefficients are available in Figure 3.3. Figure 3.4 shows the frequency response functions of both models at Disks 1 and 2 for the vertical response. It is evident that only the first two modes are sufficient to calculate the overall response of the system. The contribution of higher modes is negligible. Table 3.3 shows the comparison of un-damped natural frequencies of both models. The first two frequencies match well and are of interest.

Table 3.3 The comparison of natural frequencies

Mode	Finite Element Model	Discrete Mass Model
1	35.2 Hz	34.7 Hz
2	46.2 Hz	45.5 Hz
3	89.0 Hz	98.3 Hz
4	150.3 Hz	169.0 Hz
5	232.5 Hz	244.0 Hz

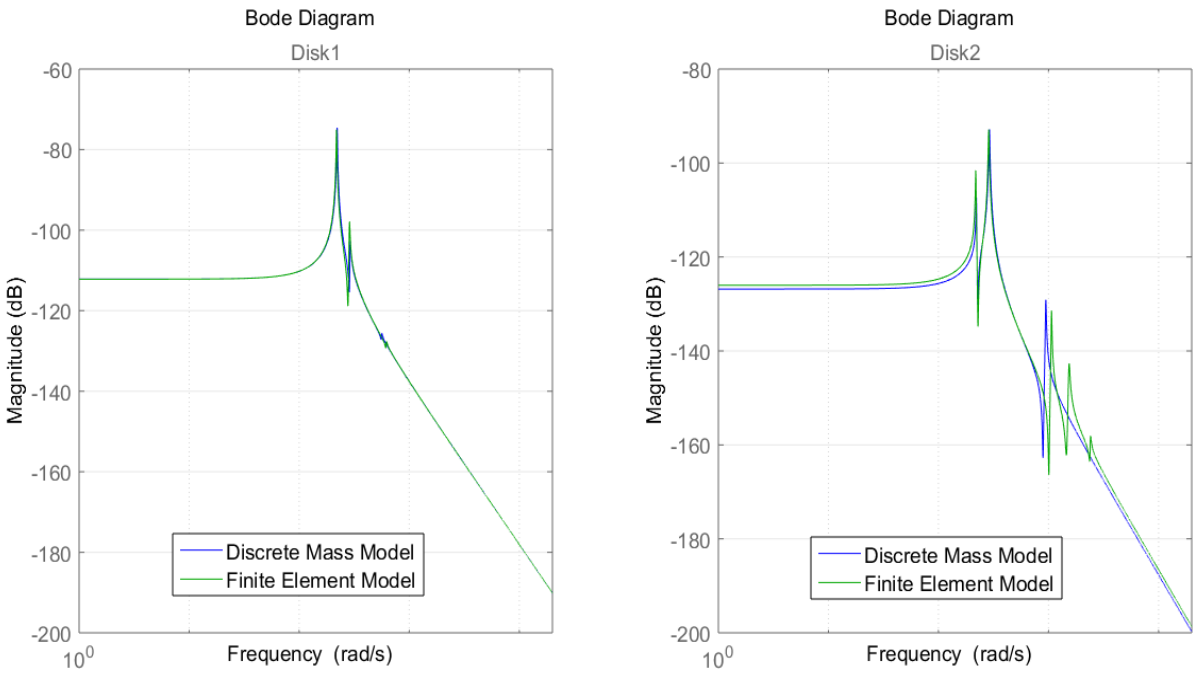

Figure 3.4 Bode plot for the different modeling techniques at Disk1 and 2

3.2.3. The Ball Bearing Model

Figure 3.5 shows a ball bearing. Ball-bearing 6014 is used in this work. Table 3.4 shows the parameters of the ball bearing. The ball bearing is modelled as a two-degrees-of-freedom system (one in horizontal and the other in the vertical direction) with the radial clearance and Hertz contact between races and spherical balls. While formulating the dynamical equations of motion it was assumed that the outer race of the ball bearing is fixed to the flexible bearing support. However, it is assumed that the inner race is fixed to the flexible rotor. The rotor and cage rotate at different

frequencies. The purpose of the cage is to maintain a constant separation between balls. The relation between the cage rotational velocity and shaft rotational velocity is given by the following relation (Harsha et al., 2004, Tiwari and Gupta, 2000).

$$\Omega_{\mathbf{cage}} = \Omega_{\mathbf{rotor}} \left(\frac{R_i}{R_i + R_o} \right) \tag{3.14}$$

where R_i and R_o represent the inner and outer cage radius of the ball bearing respectively. Ω_{rotor} is the rotor spin velocity. Ω_{cage} is the spinning velocity of the cage. N_b is the number of balls in the bearing. The angular space between two balls is equal to $\Delta\theta = \frac{2\pi}{N_b}$. The angle between balls is given by the following relation (Harsha et al., 2004, Tiwari and Gupta, 2000, Vashisht et al., 2018a).

$$\theta_k = \frac{2\pi}{N_b}(k-1) + \Omega_{cage} t, \qquad \text{k=1,....,N}_\text{b} \tag{3.15}$$

The relative radial distance Θ_k between the inner and the outer races at the k^{th} ball position can be expressed as follows (Harsha et al., 2004, Tiwari and Gupta, 2000, Vashisht et al., 2018a).

$$\Theta_k = (u_0 - u_i)\cos(\theta_k) + (v_i - v_0)\sin(\theta_k) \qquad k=1,....,N_b \tag{3.16}$$

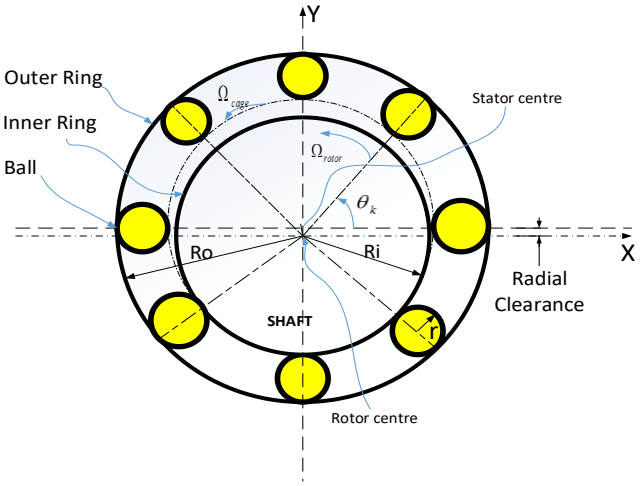

Figure 3.5 Ball bearing system

The horizontal and vertical displacements of the inner and outer races are given by u_i, u_0, v_i and v_0 respectively. θ_k is the position at the k^{th} ball. Based on the position of each ball and the local Hertzian contact, the restoring force can be estimated by using the following relation (Harsha et al., 2004, Tiwari and Gupta, 2000).

$$\Lambda_k = \begin{cases} Z(\Theta_k - \delta)^n & \Theta_k \geq \delta \\ 0 & \Theta_k < \delta \end{cases} \tag{3.17}$$

where δ is the radial clearance between races and balls. Z is the effective stiffness. It can be obtained by combining the effects of all the balls. It shows in Figure 3.5 that the ball bearing stiffness Z actually represents stiffness k_5 as follows (Harsha et al., 2004, Tiwari and Gupta, 2000).

$$Z = \frac{1}{\frac{1}{K_i^{3/2}} + \frac{1}{K_o^{3/2}}} \tag{3.18}$$

Global bearing reaction forces can be calculated by adding the individual restoring force from each ball of bearings. Afterwards, the total restoring force components Υ_u and Υ_v in X and Y directions can be represented respectively as follows (Harsha et al., 2004, Tiwari and Gupta, 2000).

$$\Upsilon_u = -\sum_{k=1}^{N_b} \Lambda_k \cos(\theta_k) \tag{3.19}$$

$$\Upsilon_v = -\sum_{k=1}^{N_b} \Lambda_k \sin(\theta_k) \tag{3.20}$$

Equations of the motion for the DMSDM in the horizontal direction are modified as follows.

$$\begin{aligned} &m_4\ddot{u}_4 - c_4\dot{u}_3 + (c_4 + c_5 + c_7)\dot{u}_4 - c_5\dot{u}_5 - c_7\dot{u}_6 - k_4u_3 + (k_4 + k_7)u_4 + Z\ (\Upsilon_u) - k_7u_6 = F_{u_4} \\ &m_5\ddot{u}_5 - c_5\dot{u}_4 + (c_5 + c_6)\dot{u}_5 + k_6u_5 + Z\ (\Upsilon_u) = F_{u_5} \end{aligned} \tag{3.21-3.22}$$

with $\Theta_k = (u_4 - u_5)\cos(\theta_k) + (v_4 - v_5)\sin(\theta_k)$ k=1,....,N_b

Similarly, equations of motion of the DMSDM in the vertical direction are modified as follows.

$$\begin{aligned} &m_4\ddot{v}_4 - c_4\dot{v}_3 + (c_4 + c_5 + c_7)\dot{v}_4 - c_5\dot{v}_5 - c_7\dot{v}_6 - k_4v_3 + (k_4 + k_7)v_4 + Z\ (\Upsilon_v) - k_7v_6 = F_{v_4} \\ &m_5\ddot{v}_5 - c_5\dot{v}_4 + (c_5 + c_6)\dot{v}_5 + k_6v_5 + Z\ (\Upsilon_v) = F_{v_5} \end{aligned} \tag{3.23-3.24}$$

with $\Theta_k = (u_4 - u_5)\cos(\theta_k) + (v_4 - v_5)\sin(\theta_k)$ k=1,....,N_b. Equations (3.21-3.24) are used to accommodate the presence of ball bearings in the overall rotor-bearing system.

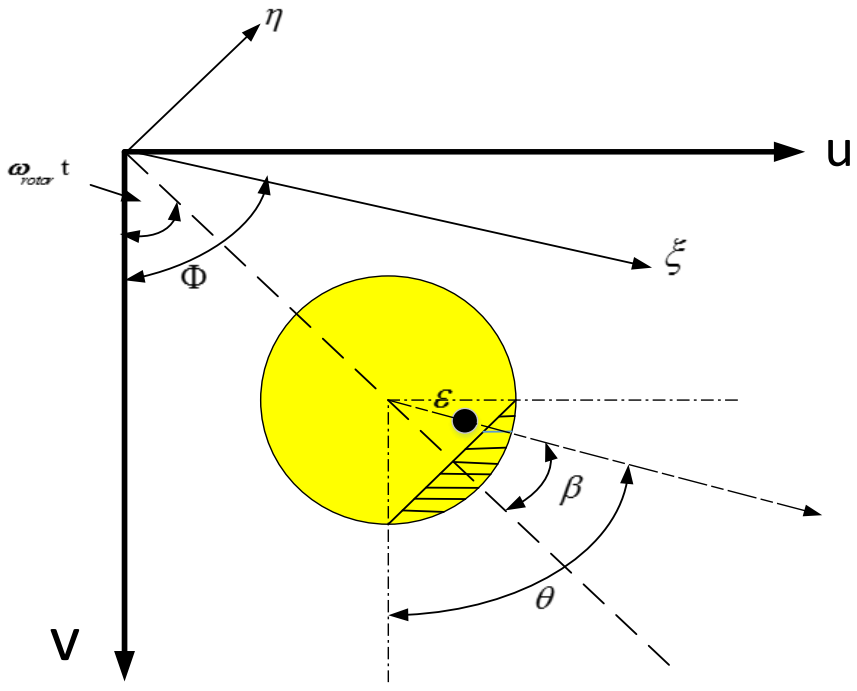

Figure 3.6 Cracked Rotor model

Table 3.4 Geometric properties of 6014 Ball Bearing (Tiwari and Gupta, 2000)

Notation	Description	Value
R_d	Ball radius	5.953 mm
R_o	Outer race radius	38.993 mm
N_b	Number of balls	16
δ	Radial clearance	20 μm
m_2, m_4	Bearing-element mass	1.5 Kg
$Z=k_5$	Load–deflection factor for contact point	$4.6x10^7$ N/$m^{3/2}$

3.2.4. Cracked rotor model compatible with Discrete Mass Spring Damper based model

Equations of motions of a rotor system with the two-degree-of-freedom in stationary Cartesian coordinates can be written as follows (Mayes and Davies, 1984).

$$\begin{bmatrix} m & 0 \\ 0 & m \end{bmatrix}\begin{Bmatrix} \ddot{u} \\ \ddot{v} \end{Bmatrix}+\begin{bmatrix} c & 0 \\ 0 & c \end{bmatrix}\begin{Bmatrix} \dot{u} \\ \dot{v} \end{Bmatrix}+\boldsymbol{K}(t)\begin{Bmatrix} u \\ v \end{Bmatrix}=m\ \varepsilon\ \Omega_{rotor}^2\begin{Bmatrix} \cos(\Omega_{rotor}t+\beta) \\ \sin(\Omega_{rotor}t+\beta) \end{Bmatrix}+\begin{Bmatrix} F_u \\ F_v \end{Bmatrix} \quad (3.25\text{-}3.26)$$

where u and v are displacements of the disc in the horizontal and vertical directions, respectively, in a stationary coordinate system. The stiffness matrix of the cracked shaft is represented as $\boldsymbol{K}$(t). 'm', 'c', 'ε' and 'β' are the equivalent mass of the system, viscous damping coefficient, eccentricity and attitude angle of the disc imbalance force vector, respectively. 'Ω_{rotor}' represents the rotational speed of the rotor system. Figure 3.6 shows all these parameters. When a cracked rotor rotates slowly under its own weight, the crack will open and close once periodically. Therefore, the stiffness matrix of the shaft $\boldsymbol{K}$ (t) varies periodically during the operation due to the crack presence. The stiffness matrix $\boldsymbol{K}$ (t) in the inertial coordinates reads as follows (Mayes and Davies, 1984, Vashisht et al., 2018).

$$\boldsymbol{K}(t)=\begin{bmatrix} k_{uu} & k_{uv} \\ k_{vu} & k_{vv} \end{bmatrix} \quad (3.27)$$

In rotating coordinates, the stiffness matrix for a cranked shaft can be written as follows (Mayes and Davies, 1984).

$$\boldsymbol{K_R}(t)=\begin{bmatrix} k & 0 \\ 0 & k \end{bmatrix}- f(\Omega_{rotor}\ t)\begin{bmatrix} \Delta k_{\zeta} & 0 \\ 0 & \Delta k_{\eta} \end{bmatrix} \tag{3.28}$$

where *k*, represents the stiffness of the uncracked rotor. Variations of the rotor stiffness in ζ and η directions can be represented as Δk_{ζ} and Δk_{η} respectively (Figure 3.6). The crack function $f(\Omega_{rotor}t)$ depends on the angular orientation of the crack as follows (Mayes and Davies, 1984).

$$f(t)=\frac{1+\cos(\Omega_{rotor}t+\beta)}{2} \tag{3.29}$$

The stiffness matrix **K** (t) in the inertial coordinates reads as follows (Mayes and Davies, 1984).

$$\boldsymbol{K}(t)=\boldsymbol{T}\ \boldsymbol{K}_R(t)\boldsymbol{T}^{-1},\quad \boldsymbol{T}=\begin{bmatrix} \cos(\Omega_{rotor}t) & -\sin(\Omega_{rotor}t) \\ \sin(\Omega_{rotor}t) & \cos(\Omega_{rotor}t) \end{bmatrix}. \tag{3.30}$$

By incorporating the appropriate element into the overall system, the dynamic equations are given as:

$$m_4\ddot{u}_4-c_4\dot{u}_3+(c_4+c_5+c_7)\dot{u}_4-c_5\dot{u}_5-c_7\dot{u}_6-k_4u_3+k_4u_4+Z\ (\Upsilon_u)+k_{uu}(u_4-u_6)+k_{uv}(v_4-v_6)=F_{u_4}$$
$$m_6\ddot{u}_6-c_7\dot{u}_4+(c_7+c_8)\dot{u}_6-c_8\dot{u}_7+k_8u_6-k_8u_7-k_{uu}(u_4-u_6)+k_{uv}(v_4-v_6)=F_{u_6}$$

(3.31-3.32)

Similarly, the dynamic equations of motion in the vertical direction are given as follows.

$$m_4\ddot{v}_4-c_4\dot{v}_3+(c_4+c_5+c_7)\dot{v}_4-c_5\dot{v}_5-c_7\dot{v}_6-k_4v_3+k_4v_4+Z\ (\Upsilon_v)+k_{vv}(v_4-v_6)+k_{vu}(u_4-u_6)=F_{v_4}$$
$$m_6\ddot{v}_6-c_7\dot{v}_4+(c_7+c_8)\dot{v}_6-c_8\dot{v}_7+k_8v_6-k_8v_7-k_{vv}(v_4-v_6)-k_{vu}(u_4-u_6)=F_{v_6}$$

(3.33-3.34)

Equations (3.31-3.34) are used to accommodate the effect of cracks on the overall dynamics of the rotor-bearing system. The purpose to construct the DMSDM is that theoretical results should well match experimental results while maintaining the low order of the overall system. This low order model will be useful for obtaining the transient response of the system in Section 3.4. The

effect of ball bearing nonlinearities is accurately absorbed in this low order model. Results presented in Section 3.4 are obtained by simulating this reduced-order model.

3.3. Conventional crack detection techniques based on the steady-state dynamic response

By using certain excitation signals externally and observing the produced response, various conceptual conclusions can be drawn. These techniques are discussed in Appendix A. The negative effect of the presence of ball bearing on the crack detection efficiency is also discussed in detail.

3.4. Proposed Crack Detection Technique based on Transient Response

The steady-state response of flexible bearings can be affected by ball bearing nonlinearities. Transient response methods provide better crack detection capabilities without losing performance in the presence of ball bearing nonlinearities. The torque is applied to the rotor system starting from rest conditions in such a manner that it provides a particular acceleration to the rotor. In this study, the rotor spin frequency is increased from zero to 60 Hz in 15 seconds. This acceleration can be varied depending upon the transient response of the system. When the system starts at zero initial conditions, due to the presence of gravity, the system vibrates in the vertical direction. It comes to a certain lower amplitude in a certain time interval depending on the inherent damping of the system. For convenience, the total time period of 15 seconds is divided into three regions. The first region (denoted as Region I) is that a portion in which initial transients die in 0 to ≈ 4 seconds. The second region (Region II) is that a portion in which the average excitation frequency covers half the first and second critical frequency of the overall system. This region is also termed as a pre-resonance region (≈ 4 to 7.5 seconds). The third region is the resonance region in which the system vibrates at its first and second critical frequencies. This region is denoted as Region III (≈ 7.5 to 15 seconds). Since the present system contains the first two closely spaced modes (34.75 Hz and 45.54 Hz), region II should cover half of these critical frequencies. Region III covers the

first two critical frequencies. Figure 3.7(c) shows these regions on the timescale. It is also obvious from the figure that when the spin frequency of the rotor passes through half of the critical frequencies (Region II), the vertical amplitude of the system increases (in case of the cracked rotor only). However, the amplitude in the horizontal direction remains constant (for both healthy and cracked rotors). It is also obvious that, in the resonance region, the vibration amplitude of the cracked rotor is much more than the amplitude of the healthy rotor. The figure is self-explanatory.

Silani et al., (2013) shows the application of STFT for the vertical response at Disk 1 or 2. First of all the STFT of the signal for Disk 2 (with the rigid bearing supports) is presented in Figure 3.8.

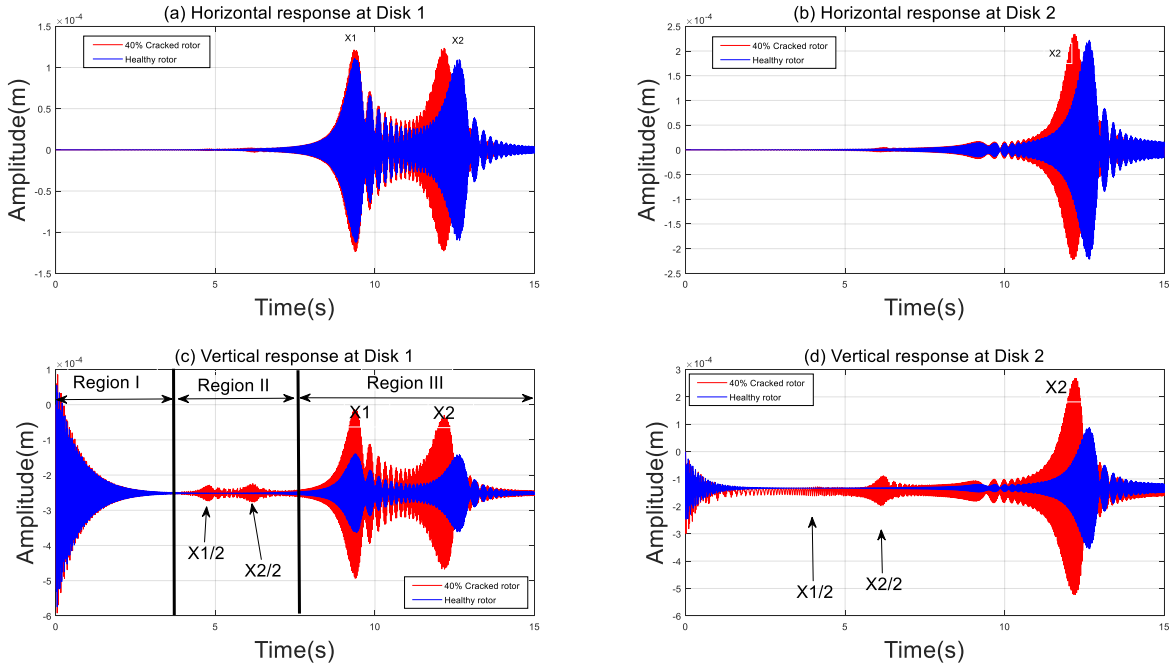

Figure 3.7 Horizontal and vertical responses of the rotor bearing (Healthy and Cracked) system at disks 1 and 2

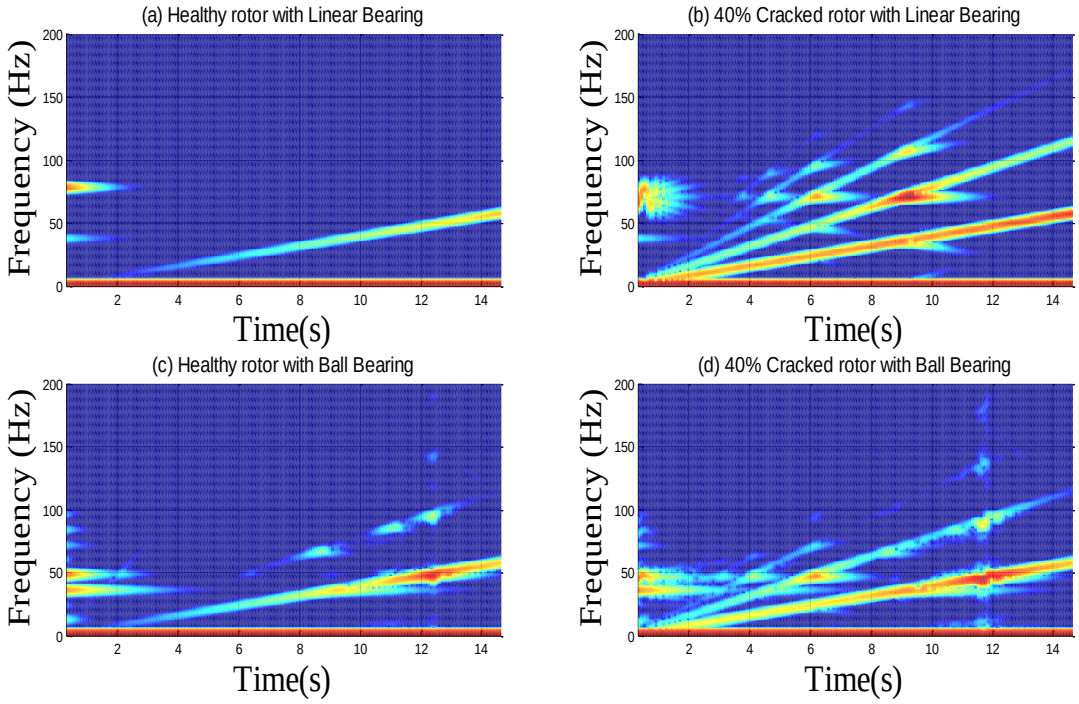

Figure 3.8 Spectrogram of the rotor-bearing system with rigid bearing support (at disk2)

The reason for this is that the crack is near Disk 2 and the rigid bearing supports have been considered so that our rotor nearly represents the Jeffcott rotor. The healthy bearing shows a single inclined line in the spectrogram. Figure 3.8 represents the system response corresponding to the linearly varying rotor spin frequency. In case of a cracked rotor, multiple such lines are observed (Part b). The findings of this work are matched that of reference (Silani et al., 2013). However, Part (c) shows that an additional line is also observed due to the presence of bearing nonlinearities. But that line is not continuous. For the cracked rotor with ball bearings, two additional lines are observed (Part d). For the cracked rotor, the number of inclined lines is decreased. The intensity of the lines is also decreased. This shows the negative effect of the bearing nonlinearity on the crack detection capability based on transient response also. This problem can be partially tackled by considering the response at Disk 1 instead of Disk 2 which contains fewer distortions caused by ball bearings (although not shown for the purpose of brevity).

To further enhance the crack detection capability, the segmented approach is used in this work. As discussed earlier, the total response has been divided into three different regions. Now, to minutely study the system response, we draw the spectrum by using STFT for the data pertaining to region II as shown in Figure 3.9. For a healthy rotor, there are two lines: one corresponding to the linearly varying rotor spin frequency and the other line showing the prolonged effect of initial transients excited due to initial conditions of the system. To clearly see the response due to the cracked rotor, this must be eliminated.

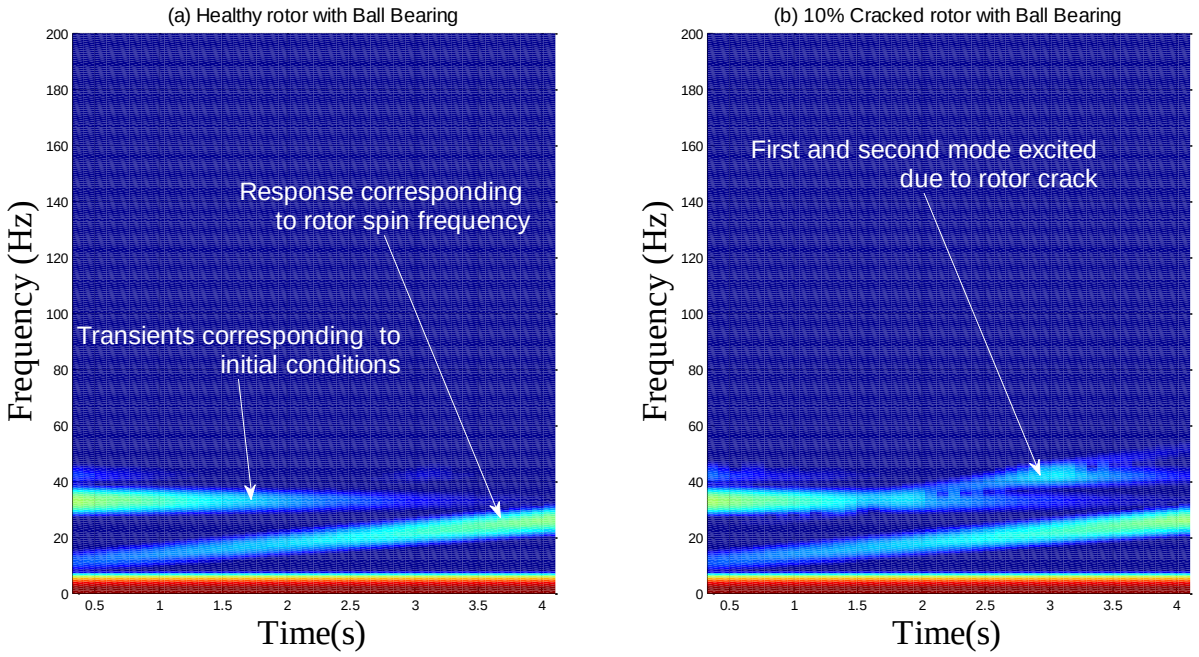

Figure 3.9 Spectrogram of the rotor Ball Bearing system with flexible bearing support (at disk1)

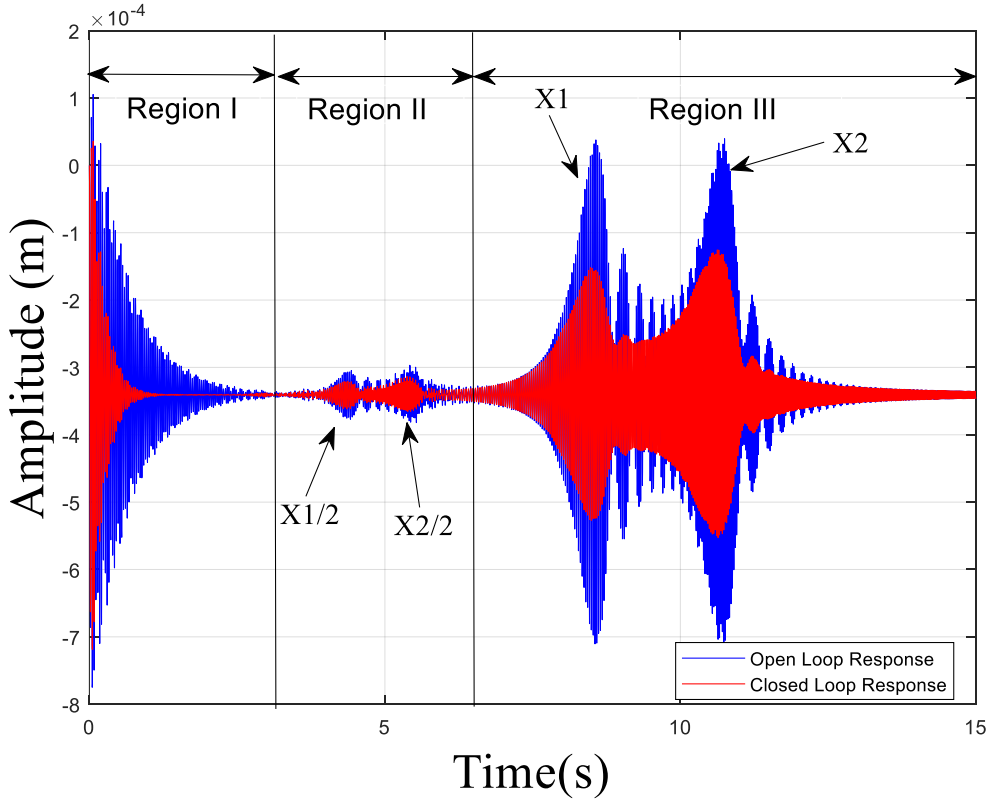

Figure 3.10 Open and closed-loop responses of the 40% Cracked rotor with the robust controller

Figure 3.10 shows the time response of the 40% cracked rotor during the run-up. To reduce the amplitude and vibrations in horizontal and vertical directions, a controlled signal through AMB is applied on Disk 1. In this study, a simple 'Robust Feedback Controller' is applied.

3.5. Active Vibration Control using Robust Control Methodology

Due to the presence of nonlinearities caused by ball bearings and rotor cracks, the overall system is not purely linear. There is a need to apply the robust control theory to compensate for these weak nonlinearities.

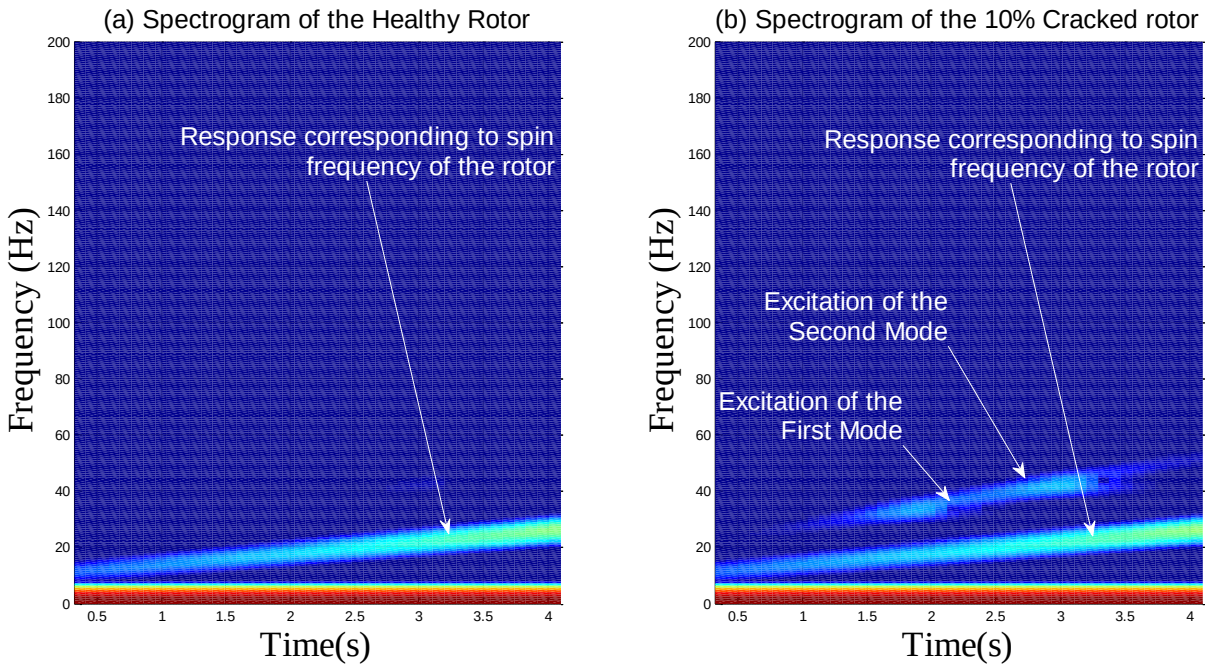

Figure 3.11 Spectrogram of the healthy rotor and 10% cracked rotor with ball bearings at disk 1 (closed-loop response) (in region II)

3.6. Switching Control Strategy

By applying the robust controller and increasing the speed of the rotor progressively, it is observed that the initial transients die out quickly. The spectrum of the system in region II is shown in Figure 3.11. A single line corresponding to the spin frequency of the rotor is shown for the healthy rotor. For a 10% cracked rotor, an additional line is observed that shows the excitation of first and second modes when the spin frequency passes through half of the first and second critical frequencies. The frequency response spectrum of the vertical vibration response of Disk 1 (in region II) is obtained by using the simple Fourier Transform of data as shown in Figure 3.12. The system nonlinearities are obvious in this figure. The dominant part of the graph represents the rotor spin frequency. The second mode excitation is more predominant during the less percentage of the crack depth in the rotor system. However, with the increase in the crack percentage, both the modes get equally affected.

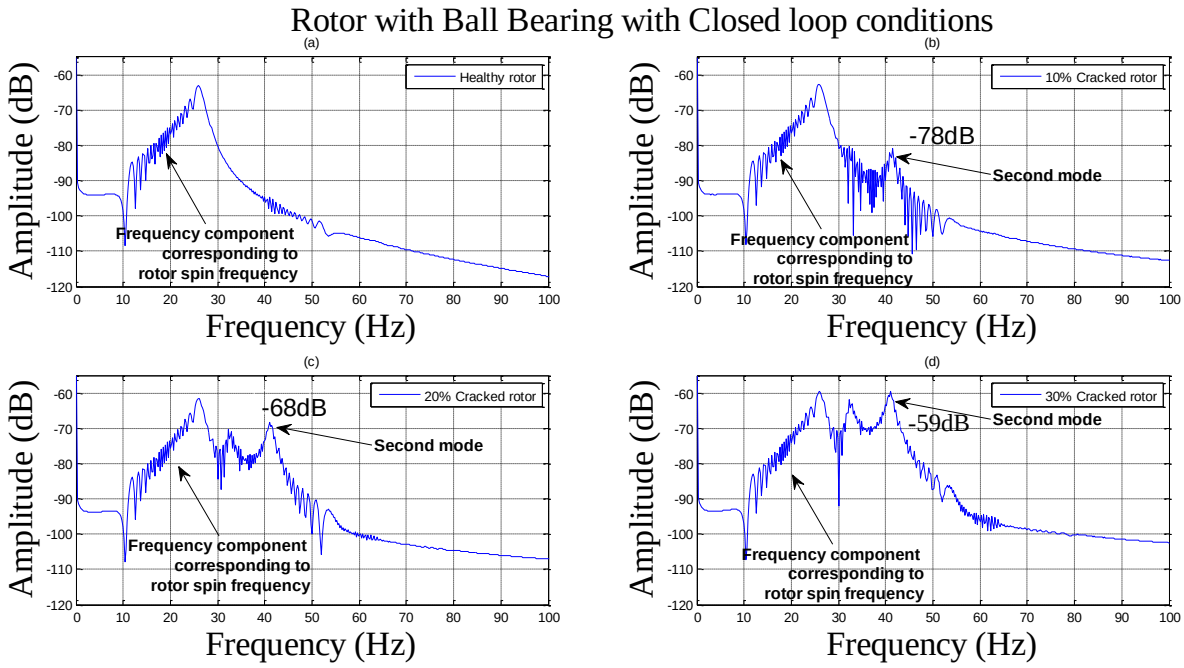

Figure 3.12 Frequency domain response of the rotor ball bearing system at disk 1 (in region II) using negative velocity feedback controller as a function of crack severity

This excitation of the first and second modes can be further enhanced by the reverse application of a closed-loop controller. In normal conditions, we use a 'negative feedback controller'. The purpose is to reduce the vibration amplitude. By converting this 'negative feedback controller' to 'positive feedback controller', instead of suppressing the amplitude of vibrations in region II, these modes get excited. To do this, a switching controller concept is used. According to this concept, the same 'negative feedback controller' used in regions I and III is converted to 'positive feedback controller' in region II. The important thing worth mentioning is that, for the healthy rotor, no signal is generated in region II, hence the feedback controller is not effective at all i.e. it does not excite the system.

Figure 3.13 shows a flowchart of the switching controller. For a given set of mass, stiffness and damping matrices, the system is simulated using 'ode45' command of MATLAB. The relative and absolute tolerances are settled as $1x10^{-9}$ for obtaining the accurate numerical results.

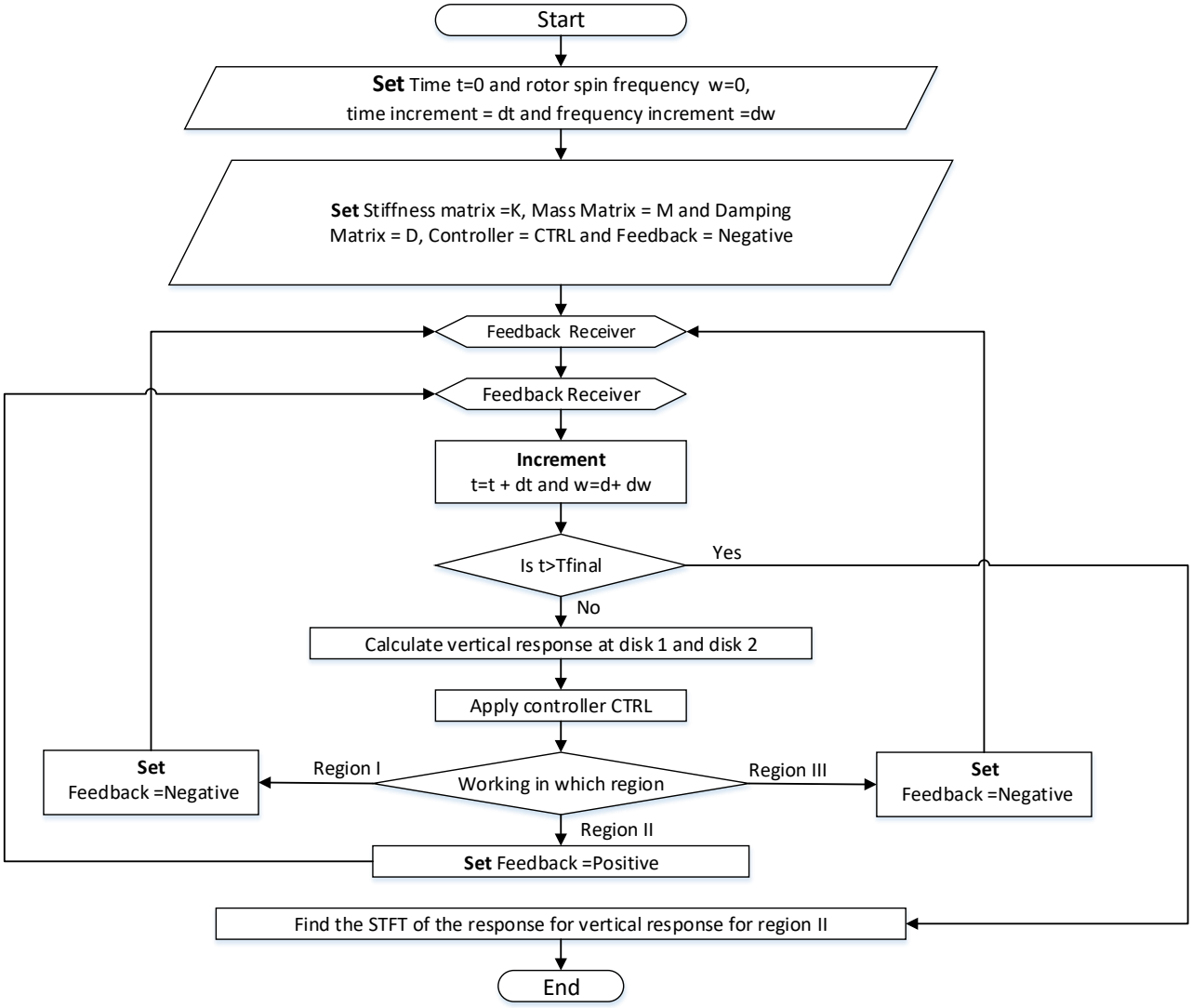

Figure 3.13 Architecture of the switched control

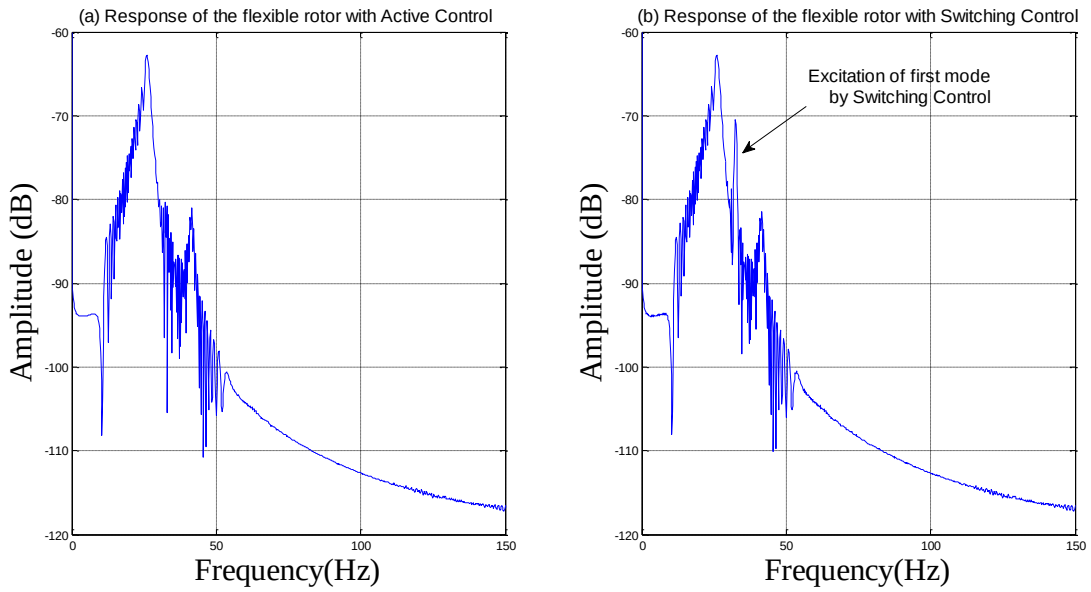

Figure 3.14 Response of the 10% cracked flexible rotor with active and switching control

The gyroscopic matrix is not considered in the system as it works on very low spinning speeds. As time passes, the rotor spin frequency is linearly increased as a function of time in the form of a linear chirp. The rotor acceleration term is chosen in such a manner to obtain the well-separated regions I, II and III. Data are analyzed for different rotor accelerations. However, these parameters have a negligible effect on results as long as all the three regions are well separated. A robustly designed controller using 'negative feedback' is applied to the system. The maximum simulation time is settled as 15 seconds for the well-separated regions I, II and III. For regions, I and III, a 'negative feedback controller' is applied to suppress vibrations. For region II, a 'positive feedback controller' obtained by reversing the sign of the 'negative feedback controller' is applied. Here instead of suppressing vibrations, the controller excites the system based on the vibration amplitude in this region. It is worth noting that the 'positive feedback controller' only excites the system in this region for a cracked rotor. In case of a healthy rotor, no vibrations are produced in this region hence no excitation of the system takes place. This fact makes the difference.

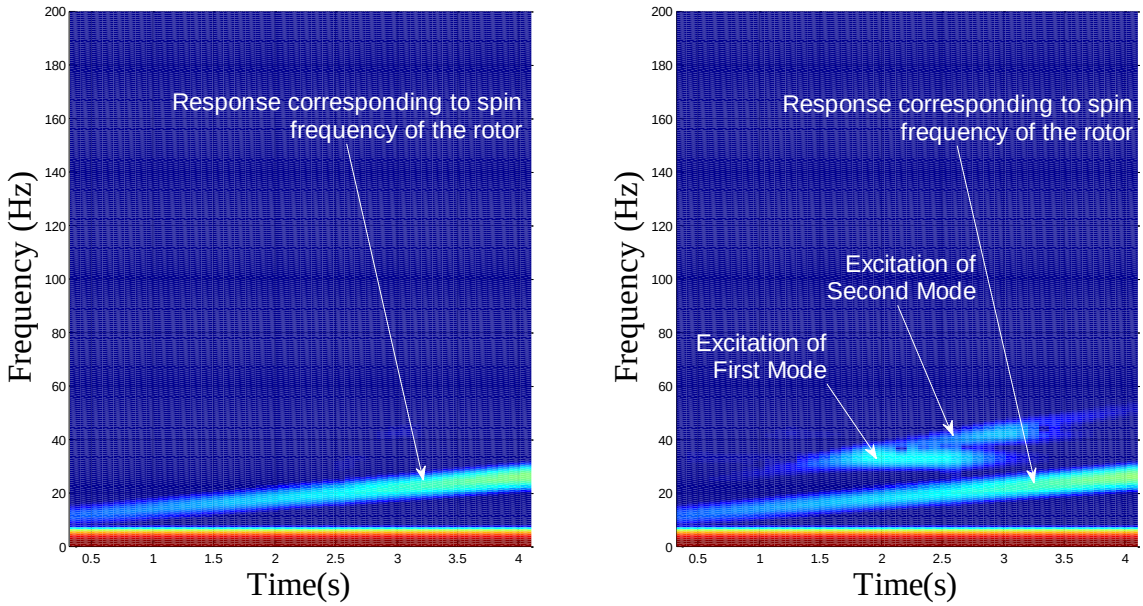

Figure 3.15 Spectrogram of the healthy rotor and 5% cracked rotor with ball bearings at disk 1 (closed-loop response) (in region II) using switching control strategy

3.7. Application of Switching Control and STFT based Spectrum

With the application of active control, the amplitude of vibration decreases in the pre-resonance region. However, with the application of switching control strategy, the vibration amplitude increases in the pre-resonance regions. Figure 3.14 shows the comparison of the vibration response of the 10% cracked rotor with the application of active control and with switching control. It is obvious that the vibration amplitude at the first mode is enhanced with the switching control strategy. This increase is obvious in the STFT based spectogram also.

Generally, the measurement signal is corrupted by the noise that is made up of a high-frequency signal. Using a low pass filter with a certain cutoff frequency, the required signal can be made noise-free for analysis. Figure 3.15 shows the spectrum of a 5% cracked rotor. Initial transients are suppressed in region I. In region II, the cracked rotor system is excited. First and second modes get more excited revealing the presence of a small crack. The first and second mode excitation is obvious in the STFT based spectrum. For a healthy rotor, this effect is not obtained. Results show

in Figure 3.16 with a 30% crack depth (with switching control strategy). The third inclined line also appears in the picture although faint. The colour of the lines depends upon the amplitude of vibrations. For a lower amplitude, the blue colour is dominated. As the amplitude increases, the colour changes from blue to white and then to yellow. Based on these colours, the amount of crack depths can be estimated easily.

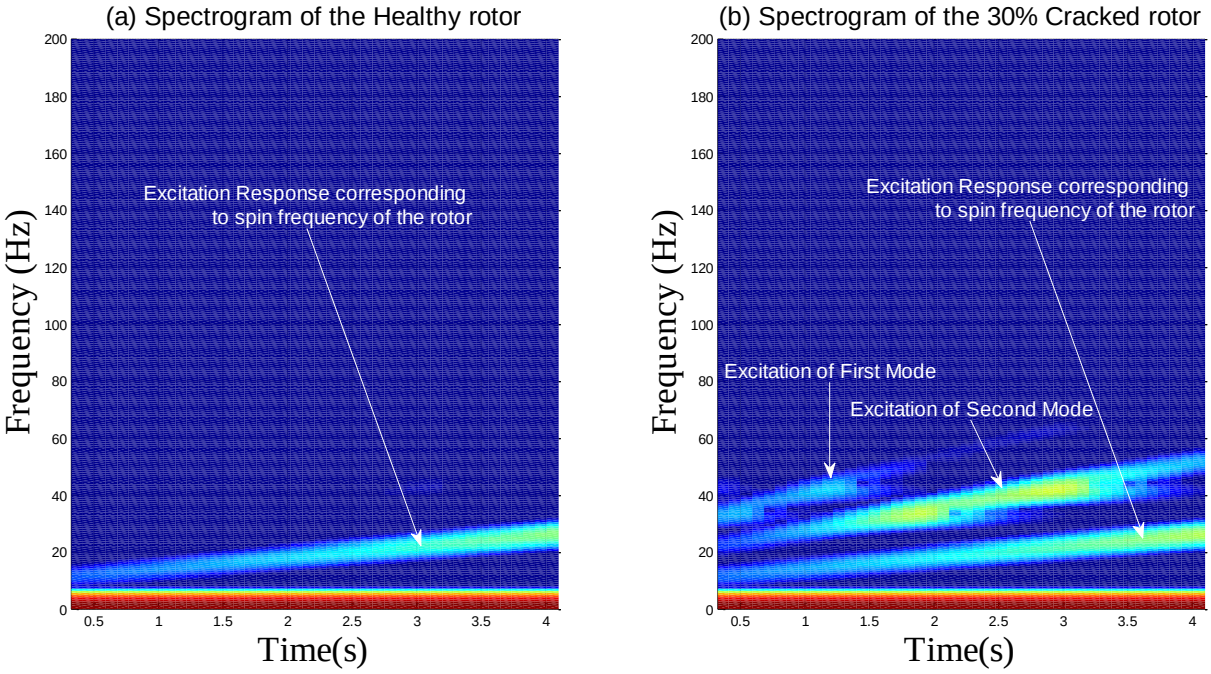

Figure 3.16 Spectrogram of the healthy rotor and 30% cracked rotor with ball bearing at disk 1 (closed loop response) (in region II)

3.8. Concluding remarks

A Jeffcott rotor mounted on bearings with the linear restoring force characteristics differs significantly in the dynamic response from real rotors. The real rotors have multiple sources of nonlinearity like ball bearings, rotor-stator rub, rotor bow and misalignment. By modelling the ball bearing nonlinearities as an integral part of the system dynamics and then simulating the overall system, follows are concluded.

- Ball bearings or other system nonlinearities inhibit the direct application of crack detection techniques based on a steady-state dynamic response for real rotor-bearing systems.
- Flexible bearing supports negatively affect the crack detection capabilities of the AHE and MSE based techniques (see Appendix A).
- Transient dynamic response-based crack detection techniques are more suitable compared to steady-state dynamic response-based techniques in the presence of different system nonlinearities.
- If the rotor spin frequency is varied from zero to resonance frequencies, certain amazing characteristics are observed in the vertical dynamic response of the flexible rotor system. Different time-frequency analysis techniques like Short Time Fourier Transform have a great potential for detecting the interesting characteristics hidden in a frequency varying signal.
- Dynamic characteristics related to cracks can be enhanced by applying a switching control strategy.

It is obvious that there is a need to investigate the practical utility of the proposed technique. Also, there is a strong need to develop other signal processing techniques working on the signal in pre-resonance regions to reveal another interesting dynamic characteristic related to the cracked rotor. To practically implement the proposed methodology on a real-life rotor, the experiment is required. Measurement of noise is inevitable in an experimental setup. Also, there is a possibility of steady-state direct current components in the signal. The use of High-Pass and Low-Pass filters can eliminate this problem.

Chapter 4

Modelling and detection of rotor stator rubbing action

4.1. Overview

Due to unbalance present in a rotating machinery, fluctuating stresses are generated leading to the formation of transverse cracks in rotors. The cracks propagate with the passage of time and increase the amplitude of vibration. High vibration amplitudes can produce rotor/stator rubs. During the rubbing phase, the crack propagation gets enhanced due to the interconnected nature of these faults. If left unattended, these faults can cause the premature failure of machine components. Hence, there is a need to develop fault detection mechanisms based on the vibration response so that these faults can be diagnosed during initial stages. The effect of gravity and the presence of cracks significantly change vibration characteristics of the rotor, which is thoroughly investigated in this research for a two-degrees-of-freedom Jeffcott rotor. It has been observed that during rubbing, higher harmonics are excited. These harmonics are integer multiple of the rotor spin frequency. A similar type of response is also observed due to the presence of a transverse rotor crack. It is difficult to distinguish the type of faults based on the steady-state dynamic response only. Instead of working on a steady-state vibration response, the transient vibration response during coasting up of the rotor is considered. During coasting up of the rotor, high harmonics are excited for both the crack as well as rotor/stator rubbing. The excitation of higher harmonics starts at much earlier stage in the spectrogram of the vertical response for the cracked rotor compared to that of rubbing. This fact is used in the development of a fault diagnosis technique based on Short Time Fourier Transform of the vibration response. The proposed technique can efficiently distinguish different types of faults even if multiple faults coexist.

Unbalance is not avoidable even in a very precise rotating machinery. During the service life of revolving machinery, it is prone to the development of other faults like cracks and rotor-stator rubs. The cracks are generated due to fatigue stresses caused by fluctuating bending moments. Faults in rotating machinery are inter-related and the generation of one may lead to the development of the other fault. Unbalanced mass tries to enhance these defects. For example, if a crack is developed, the vibration amplitude increases and rubbing action between the rotor and stator start due to the limited amount of clearance between rotating parts and the stationary housing. The rubbing action in some cases can dramatically increase the vibration amplitude which facilitates the crack growth. The other type of faults in rotating machinery are coupling misalignment and rotor bow. The existence of these faults cannot be denied. It is important to study the dynamics of a system in the presence of multiple faults simultaneously.

4.2. Mathematical Modelling

4.2.1. Modelling of rotor-stator rub

A flexible rotor supported on rigid supports is shown in Figure 4.1. The rotor position is represented by two degrees-of-freedom, i.e. horizontal displacement x and vertical displacement y. The shaft rotates at a rotor spin frequency n. Governing equations of the motion of such a system are given as follows (Varney and Green, 2015)

$$M\ddot{x} + c\dot{x} + k_{xx}x = m\varepsilon n^2 \cos(nt) \tag{4.1}$$

$$M\ddot{y} + c\dot{y} + k_{yy}x = m\varepsilon n^2 \sin(nt) - Mg \tag{4.2}$$

where M is the mass of the rigid disk on a flexible massless rotor, m is the unbalanced mass lying at a distance ε from the central axis, c is the damping coefficient, k_{xx} is the stiffness in the x-direction and k_{yy} is the stiffness in the y-direction and g is the acceleration due to gravity. There

is a stationary housing called stator covering the rotor with a clearance δ . The rotor/stator contact occurs when the rotor deflection $r = \sqrt{x^2 + y^2}$ exceeds the clearance. When the contact occurs, two forces are generated. One being the normal force F_N and other is tangential frictional force F_T. The normal force is given as follows (Varney and Green, 2015).

$$F_N = \begin{cases} 0 & \text{if } r < \delta \\ k_S(r-\delta) & \text{if } r > \delta \end{cases} \tag{4.3}$$

where k_s is the stiffness of the stator. The frictional force is as follows.

$$F_T = \mu F_N \tag{4.4}$$

Consulting Figure 4.2, it is obvious that

$$\cos(\theta) = \frac{x}{r} \tag{4.5}$$

$$\sin(\theta) = \frac{y}{r} \tag{4.6}$$

Decomposing tangential and normal forces in x and y-directions as follows (Varney and Green, 2015).

$$F_x = F_T \sin(\theta) - F_N \cos(\theta) \tag{4.7}$$

$$F_y = -F_T \cos(\theta) - F_N \sin(\theta) \tag{4.8}$$

Considering Equations (4.5-4.8), it is obvious:

$$F_x = k_S \frac{r-\delta}{r}(\mu y - x) \tag{4.9}$$

$$F_y = k_S \frac{r-\delta}{r}(-y - \mu x) \tag{4.10}$$

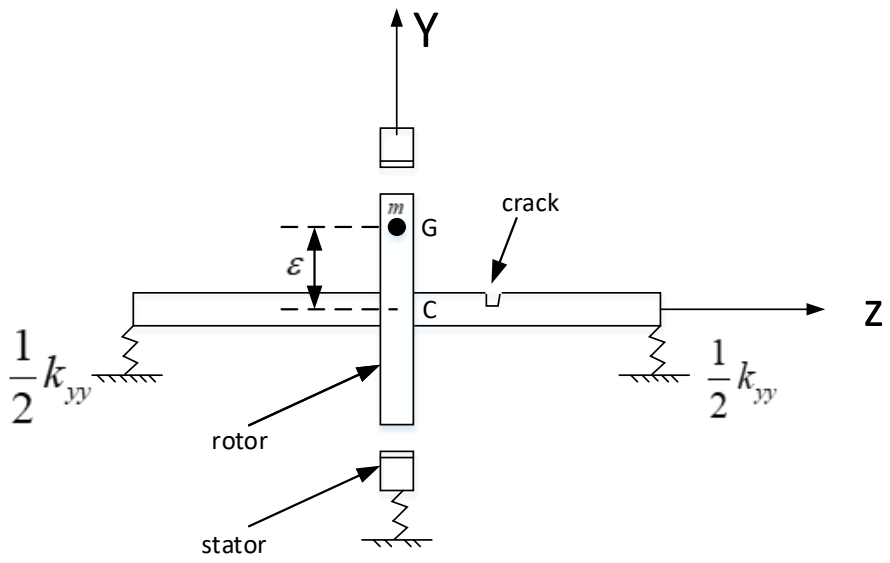

Figure 4.1 Schematic of the 2-DOF rotor stator system (Front view)

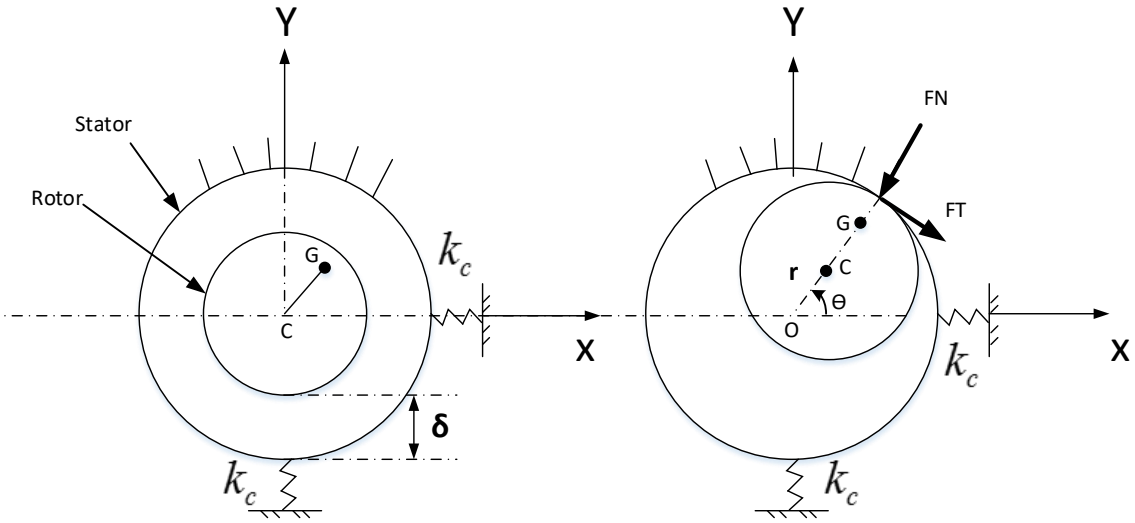

Figure 4.2 Schematic of the 2-DOF rotor stator system (side view)

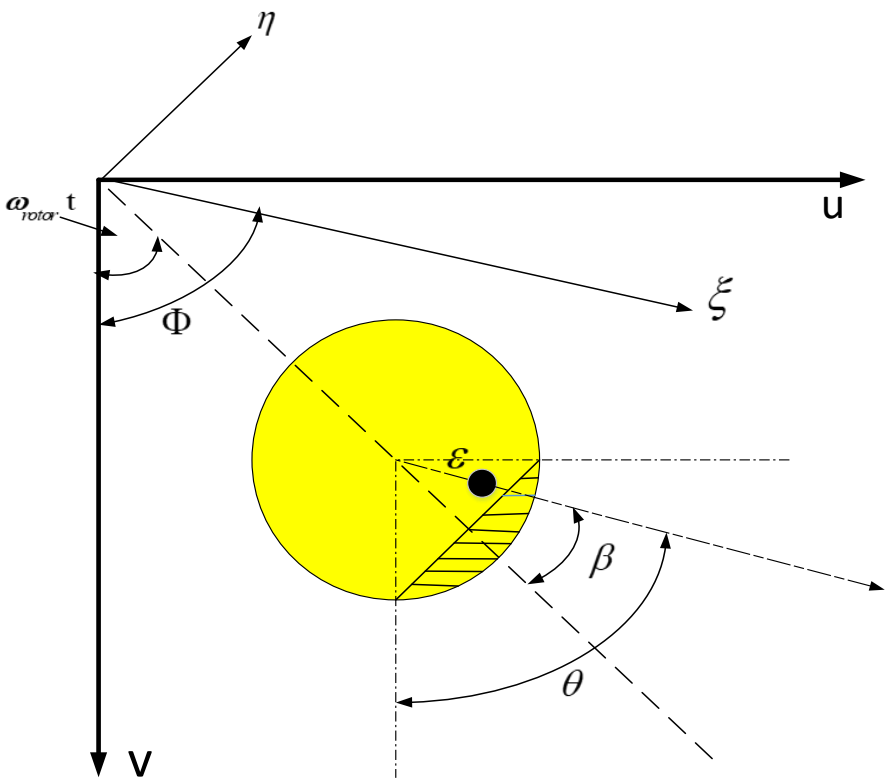

Figure 4.3 Cracked rotor model

where k_s is the stiffness of the stator. By considering Eqs. (4.1-4.10), we obtain (Varney and Green, 2015):

$$M\ \ddot{x}+c\ \dot{x}\ +k_{xx}x+k_S\frac{r-\delta}{r}(x-\mu y)=m\ \varepsilon\ n^2\cos(nt) \tag{4.11}$$

$$M\ \ddot{y}+c\ \dot{y}\ +k_{yy}y+k_S\frac{r-\delta}{r}(y+\mu x)=m\ \varepsilon\ n^2\sin(nt)-M\ g \tag{4.12}$$

Since we have to consider the dry friction backward whirling and whip phenomena, the governing equations of self-excited vibrations are given as follows (Jiang and Ulbrich, 2004, Vashisht et al., 2019b).

$$M\ \ddot{x}+c\ \dot{x}\ +k_{xx}x+k_S\frac{r-\delta}{r}(x-\mu\ sign(v_{rel})y)=m\ \varepsilon\ n^2\cos(nt) \tag{4.13}$$

$$M\ \ddot{y}+c\ \dot{y}\ +k_{yy}y+k_S\frac{r-\delta}{r}(y+\mu\ sign(v_{rel})x)=m\ \varepsilon\ n^2\sin(nt)-M\ g \tag{4.14}$$

where $v_{rel} = n\, r_{disk} + n_w r$ with $r = \sqrt{x^2 + y^2}$ is the relative velocity between the disk and stator at the contact point. r_{disk} is the radius of the disk and n_w is the whirling frequency of the rotor. This frequency is positive when the rotor whirls in the forward direction and negative when whirls in the backward direction. In some cases, the relative velocity can even become negative. During this stage, the direction of frictional force changes. In case of a dry friction backward whirl, the rotor whirls at a constant backward whirl frequency. The supplied rotational energy will be continuously transferred to the rotor in the form of the energy required for the lateral vibration of the rotor. In this case, the amplitude of the rotor response increases to a high value. This stage is dangerous and can damage the equipment.

4.2.2. Modelling of 2-DOF cracked rotor

In case of a cracked rotor, equations of the motion of the rotor system in stationary Cartesian coordinates can be written as follows (Mayes and Davies, 1984, Vashisht et al., 2018).

$$\begin{bmatrix} M & 0 \\ 0 & M \end{bmatrix} \begin{Bmatrix} \ddot{x} \\ \ddot{y} \end{Bmatrix} + \begin{bmatrix} c & 0 \\ 0 & c \end{bmatrix} \begin{Bmatrix} \dot{x} \\ \dot{y} \end{Bmatrix} + \boldsymbol{K}(t) \begin{Bmatrix} x \\ y \end{Bmatrix} = m\, \varepsilon\, n^2 \begin{Bmatrix} \cos(nt+\beta) \\ \sin(nt+\beta) \end{Bmatrix} + \begin{Bmatrix} 0 \\ -Mg \end{Bmatrix} \tag{4.15}$$

In the above expression, x and y represent horizontal and vertical displacements of the disc in the stationary coordinate system. **K** (t) is the time-varying stiffness matrix of the cracked rotor. Parameter β represents the angle of the disc imbalance force (Figure 4.3). The crack opens and closes periodically under the effect of gravity and behaves like a breathing crack. Therefore, the stiffness matrix of the shaft (i.e. **K** (t)) varies periodically due to the crack effect. The stiffness matrix **K** (t) in the stationary coordinates is given as follows (Mayes and Davies, 1984, Vashisht et al., 2018).

$$\boldsymbol{K}(t) = \begin{bmatrix} k_{xx} & k_{xy} \\ k_{yx} & k_{yy} \end{bmatrix} \tag{4.16}$$

The stiffness matrix of a cracked shaft, in rotating coordinates, can be written as follows [30].

$$\boldsymbol{K_R}(t) = \begin{bmatrix} k_{xx} & 0 \\ 0 & k_{yy} \end{bmatrix} - f(nt) \begin{bmatrix} \Delta k_{\zeta} & 0 \\ 0 & \Delta k_{\eta} \end{bmatrix} \tag{4.17}$$

where diagonal elements in the first matrix represent the stiffness of the uncracked rotor in horizontal and vertical directions. Diagonal elements in the second matrix represent variations in rotor stiffness $k_\zeta \; and \; k_\eta \;\; in \; \zeta \; and \; \eta$ directions, respectively (Figure 4.3). Function $f(nt)$ is a crack function. Its value depends on the angular orientation of the crack as follows.

$$f(nt) = \frac{1+\cos(nt+\nu)}{2} \tag{4.18}$$

where ν represents the crack orientation. Its value is taken as zero in this research. Stiffness matrix **K** (t) in the stationery coordinates is as follows (Mayes and Davies, 1984, Vashisht et al., 2018).

$$\boldsymbol{K}(t) = \boldsymbol{T}\, \boldsymbol{K}_R(t) \boldsymbol{T}^{-1}, \boldsymbol{T} = \begin{bmatrix} \cos(nt) & -\sin(nt) \\ \sin(nt) & \cos(nt) \end{bmatrix} \tag{4.19}$$

4.3. Simulation model

For a two-degree-of-freedom rotor system, it is assumed that the 5 Kg mass disk is supported by a massless rotor of stiffness $1x10^5$ N/m. An eccentric (unbalanced) mass of $3x10^{-3}$ Kg lies on the disk at a distance of 150 mm from the centroid. The damping coefficient of the system is 225 Ns/m. The stiffness of the stator is 10 times that of the rotor. The clearance of $15x10^{-6}$ m (δ) is provided between the rotor and stator. The natural frequency of the rotor is 22.5 Hz. When the rotor and stator are in contact with each other, the natural frequency of the combined rotor/stator system is 71.17 Hz. In this way, the rotor stiffness varies as a function of time. These systems are called hybrid systems. The dynamics of these systems is inherently nonlinear in nature.

4.4. Detection of transverse crack and rubbing action

Responses of the system are evaluated at rotor spin frequencies of 30 Hz, 37 Hz, 47 Hz and 61 Hz. There is no frequency below the natural frequency of the rotor. Figure 4.4 shows the spectrum and locus of the rotor at these frequencies. When the rotor is in the vertical position, the effect of gravity is not considered. At 30 Hz of the rotor spin frequency, the response is forward annular rub (FAR). The spectrum shows a single frequency in the spectrum i.e. the rotor spin frequency. At 37 Hz, the response changes to partial forward whirl (PFW). The response contains two frequencies, the rotor spin frequency and other components of 62 Hz (whirling frequency). This frequency component changes with the rotor spin frequency. At 47 Hz, the spectrum contains two frequencies i.e. the rotor spin frequency and 58 Hz (whirling frequency) component. The amplitude of the system is moderate at this rotor spin frequency. This is a case of the partial backward whirl (PBW).

At 61 Hz, the amplitude increases dramatically. The system vibrates solely at a frequency of 73 Hz, near the natural frequency of the combined rotor/stator system. This is a dangerous state as a dry whip (WHIP) is very harmful to the equipment due to its high amplitude vibrations characteristics.

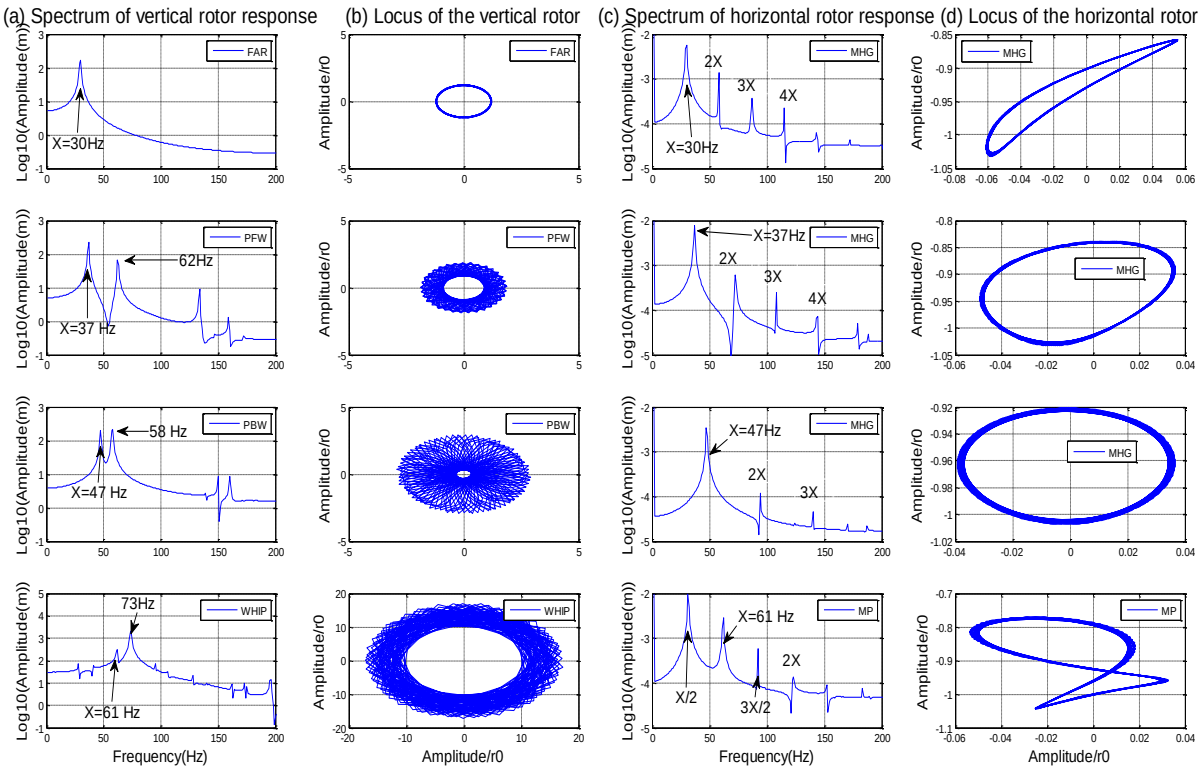

Figure 4.4 Comparison of vibration characteristics at different rotor spin frequencies for vertical and horizontal rotors

4.5. Effect of different factors on rotor/stator rubbing action

4.5.1. Effect of gravity on whirling and whip

The primary aim of this work is to establish the effect of gravity and rotor cracks on the vibration characteristics of the overall system. Due to the presence of gravity, there is a static deflection of $490\text{x}10^{-6}$ m. For the analysis of the rotor/stator system, $\delta = 490\text{x}10^{-6}\,\text{m} + 15\text{x}10^{-6}\,\text{m}$ is taken for the system. It has been observed through simulations that responses of the system at 30 Hz to 47 Hz rotor spin frequencies contain multiple harmonics that are an integer multiple of the rotor spin frequency. We have named this state as the multiple harmonics generation (MHG). If X is the spin frequency of the rotor, the spectrum of the horizontal rotor contains X, 2X, 3X…, frequency components. Column (d) in Figure 4.4 shows the locus of the rotor. However, at 61 Hz,

the response of the system changes to multi-periodic (MP). At this rotor spin frequency, the response appears not only at X, 2X, 3X…, frequencies but at $\frac{X}{2}, \frac{3X}{2} \ldots,$ frequencies also. It produces a period 2 vibration response.

4.5.2. Effect of breathing crack on dry friction whirling and whip

A breathing crack model is considered in this work. This action takes place in a situation where weight dominance is present. The 30% crack depth is taken for the analysis. Again, the vibration characteristics are investigated at 28 Hz, 47 Hz and 61 Hz rotor spin frequencies as shown in Figure 4.5. All the frequencies are above the resonance frequency. At 28 Hz, the system behaves as MP with the period 2 vibration. However, as it moves away from the resonance i.e. (22.5 Hz), this behaviour diminishes and gradually converts into MHG. At 61 Hz rotor spin frequency, the crack presence converts the vibration characteristics from MP to MHG as shown in Figure 4.5 with the presence of gravity only. For results in Figures 4.6, the clearance was settled as 15×10^{-6}m, however, the vertical static deflection was considered.

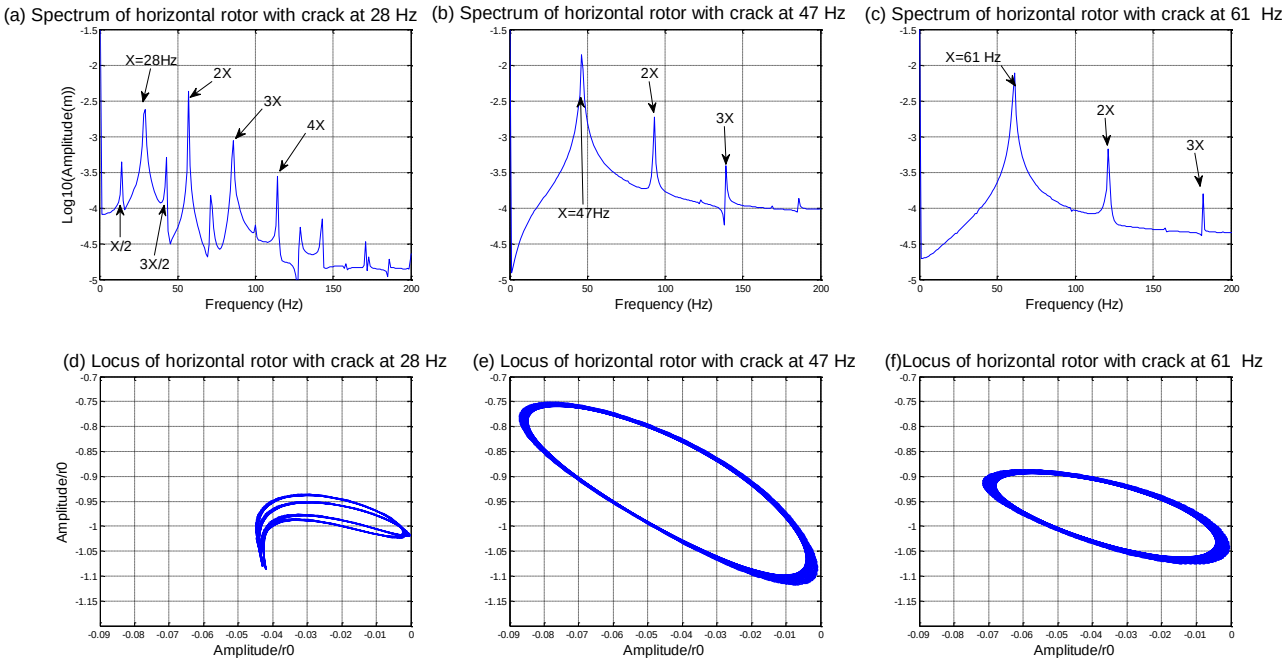

Figure 4.5 Effect of gravity and presence of crack on vibration characteristics of the horizontal rotor (spin frequencies above the resonance)

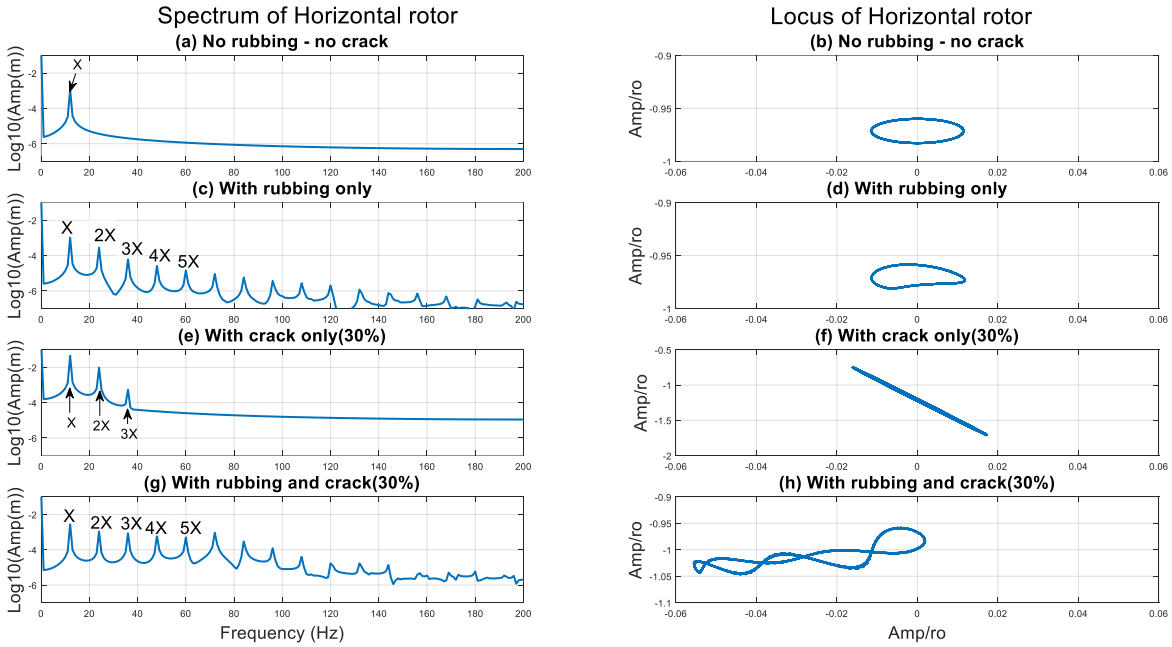

Figure 4.6 Effect of gravity and presence of crack on vibration characteristics of the horizontal rotor (spin frequency below the resonance)

Below the resonance frequency, for clearance of $15x10^{-6}$m, different types of responses are possible for the horizontal rotor in the presence of a breathing crack and rubbing. The rotor was spun at a frequency of 12 Hz. With the presence of rubbing, the response of the system is MHG with a significant amplitude at first 6 harmonics as the integer multiple of rotor spin frequency (Figure 4.6, c and d). With a breathing crack but no rubbing, MHG takes place as shown in Figures 4.6e and 4.6f. However, the first two harmonics have a significant amplitude. Under the effect of both rubbing and transverse crack, the response is shown in parts g and h.

The secondary aim of this research is to develop a crack and rub diagnosing system based on signal processing technology. Time-frequency analysis is an important part of the vibration analysis for non-stationary signals (whose parameters vary with time). Short-Time Fourier Transform is one of the methods used for the time-frequency analysis to present the signal (transient response) in a graphical format as a function of time. Normally, this graph is called the spectrogram.

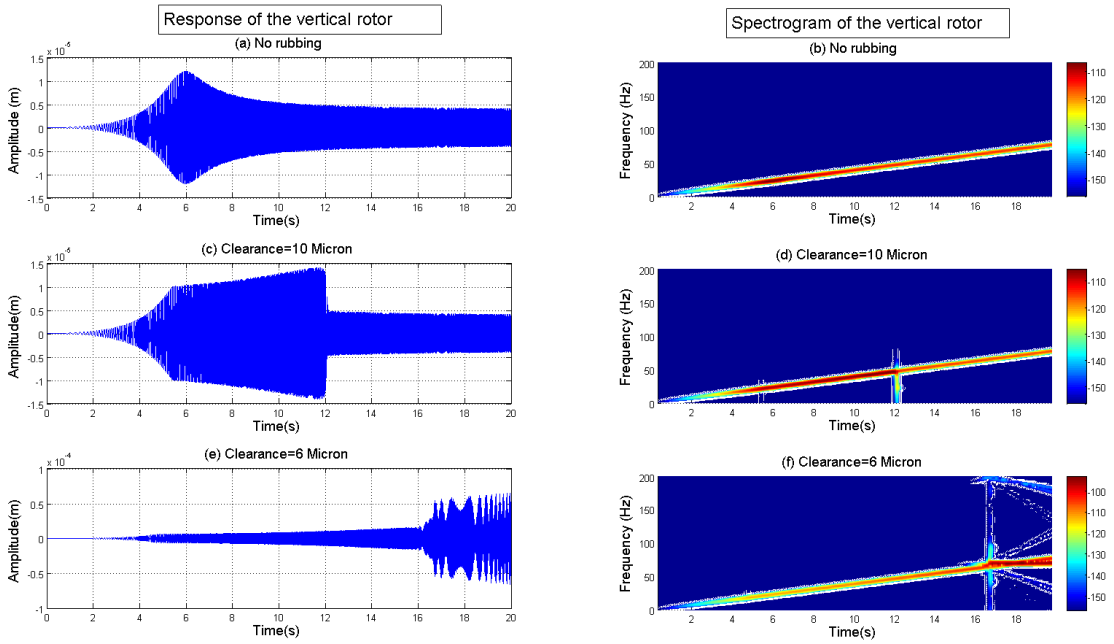

Figure 4.7 Vibration characteristics of the vertical rotor during coasting up as varied clearance amplitudes

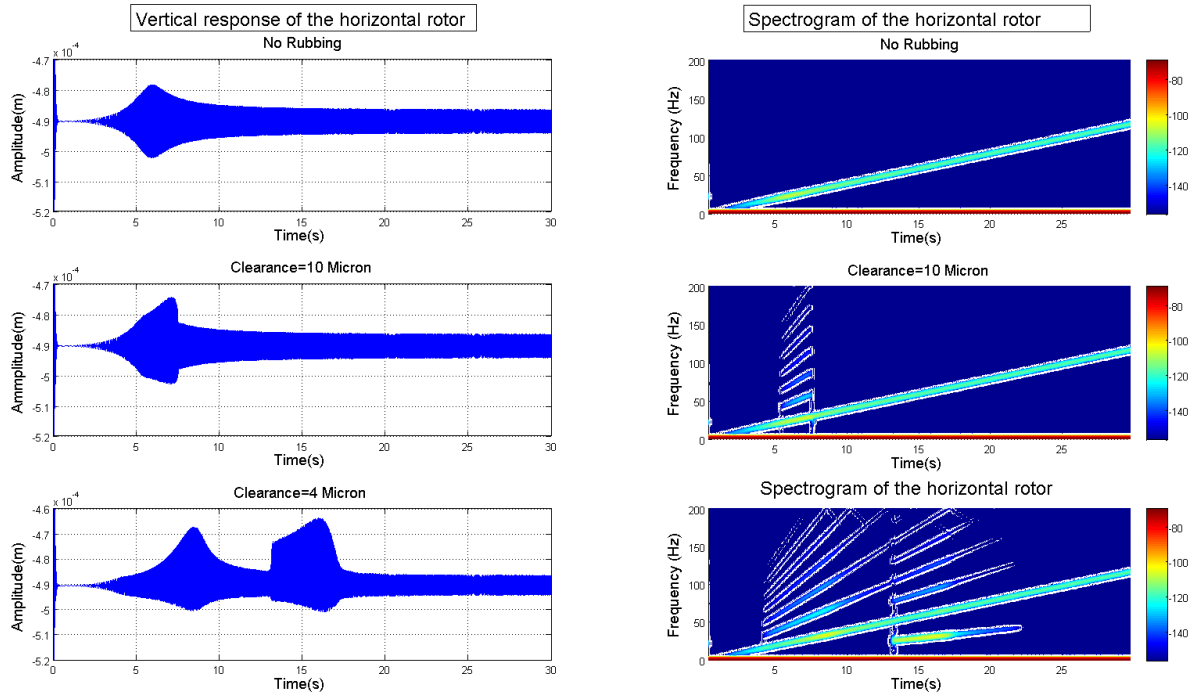

Figure 4.8 Vibration characteristics of the horizontal rotor during coasting up as varied clearance amplitudes

Figure 4.7 shows the response, as well as spectrogram of the vertical rotor (without considering gravity) during coasting up. With a 10-microns clearance, the vibration amplitude increases during the time period of 6 to 12 seconds as shown in parts c and d of Figure 4.7. However, by further reducing the clearance level to 6 microns, the vibration response converts into WHIP as shown in parts e and f of Figure 4.7. The spectrogram of the response shows that after 16 seconds, the whirling frequency of 72 Hz comes into picture and system vibrates at this frequency only, independent of the rotor spin frequency.

For the vertical response of the horizontal rotor without cracks, the effect of gravity comes into the picture shown in Figure 4.8. It is obvious that even with 10- and 4-microns clearance, the system response never turns into a WHIP. Here the static deflection is considered due to gravity. The system response is MHG and the higher harmonics at 2X, 3X.., appear in the system response, which is obvious in the form of inclined lines (acute angle) in the spectrogram. These inclined lines start appearing in the spectrogram at 4 seconds and remain up to 7 seconds for the 10 microns clearance. By further reducing the clearance to 4 microns, these lines are available up to 23 seconds.

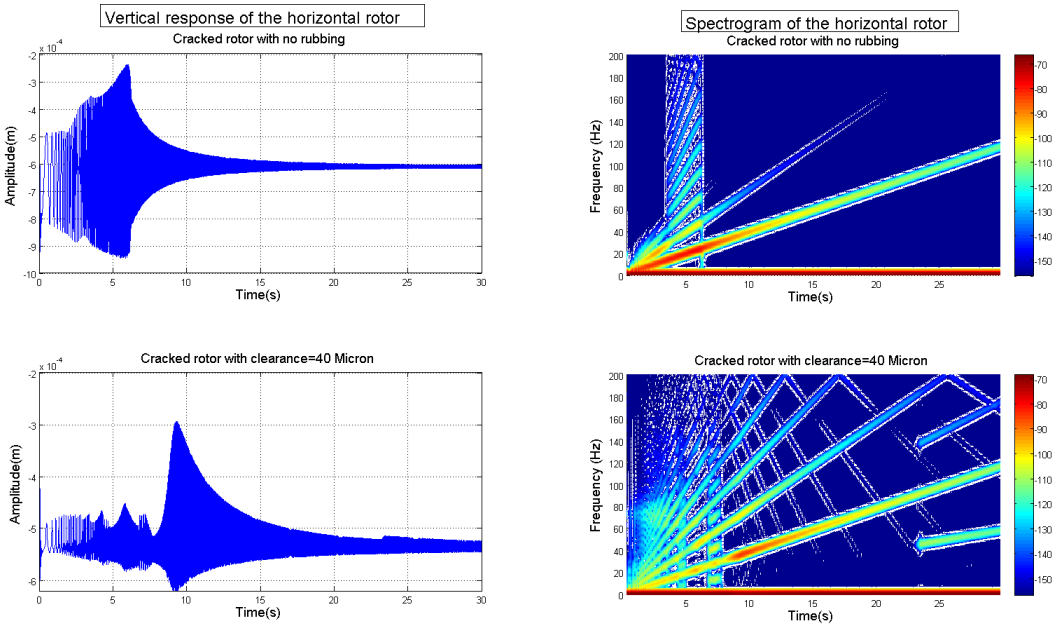

Figure 4.9 Vibration characteristics of the cracked horizontal rotor during coasting up as varied clearance amplitudes (part 1)

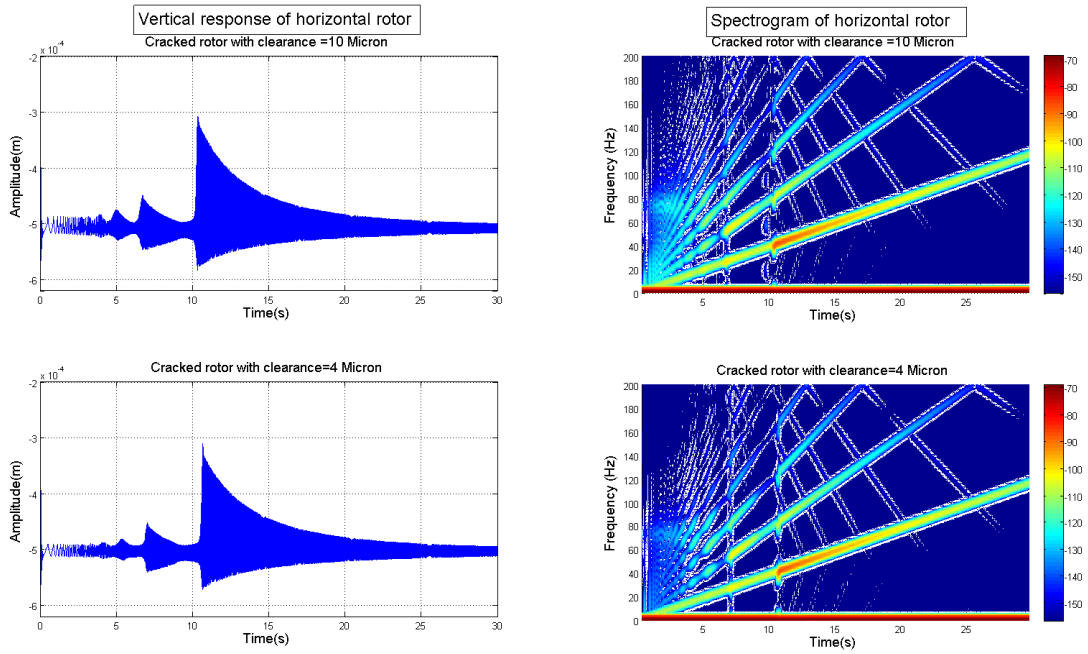

Figure 4.10 Vibration characteristics of the cracked horizontal rotor during coasting up as varied clearance amplitudes (part 2)

Figure 4.9 shows the response of the system with a breathing crack. In the first row of this figure, the rubbing is absent. MHG takes place from the time period 4 to 7 seconds. Multiple inclined lines appear in the spectrogram. This response appears similar to that obtained from rubbing. However, there is a difference. The first few inclined lines start from zero in case of a cracked rotor. If both the crack and rubbing, with a 40-microns clearance, are present in the system, more and more inclined lines start from the origin. For the cracked rotor, if the clearance level is further reduced to 10 and 4 microns (Figure 4.10), the number of the inclined lines further increases. Apart from inclined lines at an acute angle, inclined lines at an obtuse angle with respect to the horizontal also appear in the spectrogram in case the crack and rubbing co-exist. This aspect can be used as a diagnostic tool for crack and rub identification.

4.6. Concluding remarks

Based on the simulated results, the following conclusions has been drawn.

- The dry whip phenomena can easily be generated in the absence of gravity through simulations but it is difficult to produce under the effect of gravity (even with extremely high unbalanced mass).
- Generation of the multiple harmonics is quite general in case of rotor/stator rubbing for a wide range of rotor spin frequencies and clearance levels under the effect of gravity. Hence this aspect can be used to detect the presence of rotor/stator rub in case of a healthy rotor based on the steady-state response of the flexible rotor.
- In the presence of a breathing crack, multiple harmonics are also generated in the vertical response of a flexible horizontal rotor. But this feature is also very common in the presence of rotor/ stator rub. Hence, the steady-state response of the system alone cannot be used to distinguish between the two types of faults and there is a strong need to work on the analysis of

the transient response of a flexible rotor under coasting up, the situation in which the rotor spin frequency is increased at a constant acceleration.

- The Short-Time Fourier Transformation based time-frequency analysis of the transient vibrations (during coasting up) presents several diagnosis features, which can be used to detect the presence of multiple types of faults in rotating machinery. Multiple inclined lines starting from **zero time** appear in the spectrogram of the vertical response of the cracked flexible rotor.
- Multiple offset lines inclined with respect to the horizontal axis, starting at **large distances from zero time**, appear in the spectrogram for the vertical response of the horizontal rotor in which rotor/stator rubbing takes place.
- In case of a cracked real rotor, when the rotor spin frequency reaches half of the resonance frequency, the corresponding mode gets excited. This particular phenomenon is beautifully captured in the spectrogram of the vertical response of the flexible rotor. An inclined line with respect to the horizontal at roughly 60^0 appears in the spectrogram.
- There is a need to improve the model by considering the Hertzian contact and viscous friction (as well as the nonlinear friction model) between the rotor and stator in future. The inherent nature of the considered system is the multi-physics and multi-scale. It involves dynamical and thermo-mechanic responses, effects of a high speed of rotation and strong coupling between dynamics and tribological characteristics. There is also a need to integrate the coupling of thermal, mechanical and wear components. Although experimental results for simple Jeffcott rotors have been compared to theoretical results through simulations, it is necessary to extend the experimental results to real rotor/stator systems.

Chapter 5

Active vibration control of rotor dynamic systems

5.1. Overview

An adaptive hybrid controller is proposed for reducing the unbalanced vibration response of a flexible rotor/active magnetic bearing system. It is observed that conventional adaptive feedforward controller (AFFC) normally used in the active noise control are very sensitive in performance for changes in rotor spin frequencies. Although frequency updating is a part of their architecture, a small variation in the rotor spin frequency can reduce its effectiveness drastically. A smart combination of the adaptive notch filter and Goertzel filter is proposed for the frequency estimation. During changes of the rotor spin frequency, fundamental harmonics of the flexible rotor are excited. By using a hybrid controller that combines feedback control and AFFC, the amplitude of these fundamental harmonics is reduced significantly. By applying the multi-harmonic hybrid control, the multiple harmonics generated due to coupling misalignment are compensated efficiently. Fourier Transform of the control signal is further used to detect the presence of the coupling misalignment.

5.2. Mathematical modelling of a rotor system

A flexible rotor system contains multiple rigid disks, multiple bearings with flexible bearing supports (Figure 5.1a). Geometrical and physical parameters are described in Table 5.1. The structure consists of certain discrete elements, 16 elements in the present case. The global mass matrix (**M**) and stiffness matrix (**K**) for the structure of the rotor system can be derived based on the geometry of the structure (Villa et al. 2008). The damping matrix (**C**) can be derived from mass and stiffness matrices. The effect of rotational spin frequency (Ω) of the rotor can be considered

via gyroscopic matrix (**G**). Dynamic equations of motion of the complete system are as follows (Vashisht et al., 2019c)

$$\mathbf{M\ddot{x}} + (\mathbf{C} - \Omega\mathbf{G})\mathbf{\dot{x}} + \mathbf{Kx} = \mathbf{F_u} + \mathbf{F_{AMB}} + \mathbf{F_{Coupling}} \quad (5.1a)$$

where $\mathbf{x}$, $\mathbf{\dot{x}}$ and $\mathbf{\ddot{x}}$ are global vectors of displacement, velocity and acceleration. $\mathbf{F_u}$, $\mathbf{F_{AMB}}$ and $\mathbf{F_{Coupling}}$ are vectors of forces generated by unbalanced masses, by active magnetic bearings and at misaligned coupling, respectively. These coupling forces are as follows (Jalan et al. 2009).

$$\mathbf{F_{coupling}} = \begin{bmatrix} \vdots \\ 0 \\ FX\ \sin(\Omega\ t) + FX\ \sin(2\Omega\ t) + FX\ \sin(3\Omega\ t) \\ FX\ \cos(\Omega\ t) + FX\ \cos(2\Omega\ t) + FX\ \cos(3\Omega\ t) \\ 0 \\ \vdots \end{bmatrix} \quad (5.1b)$$

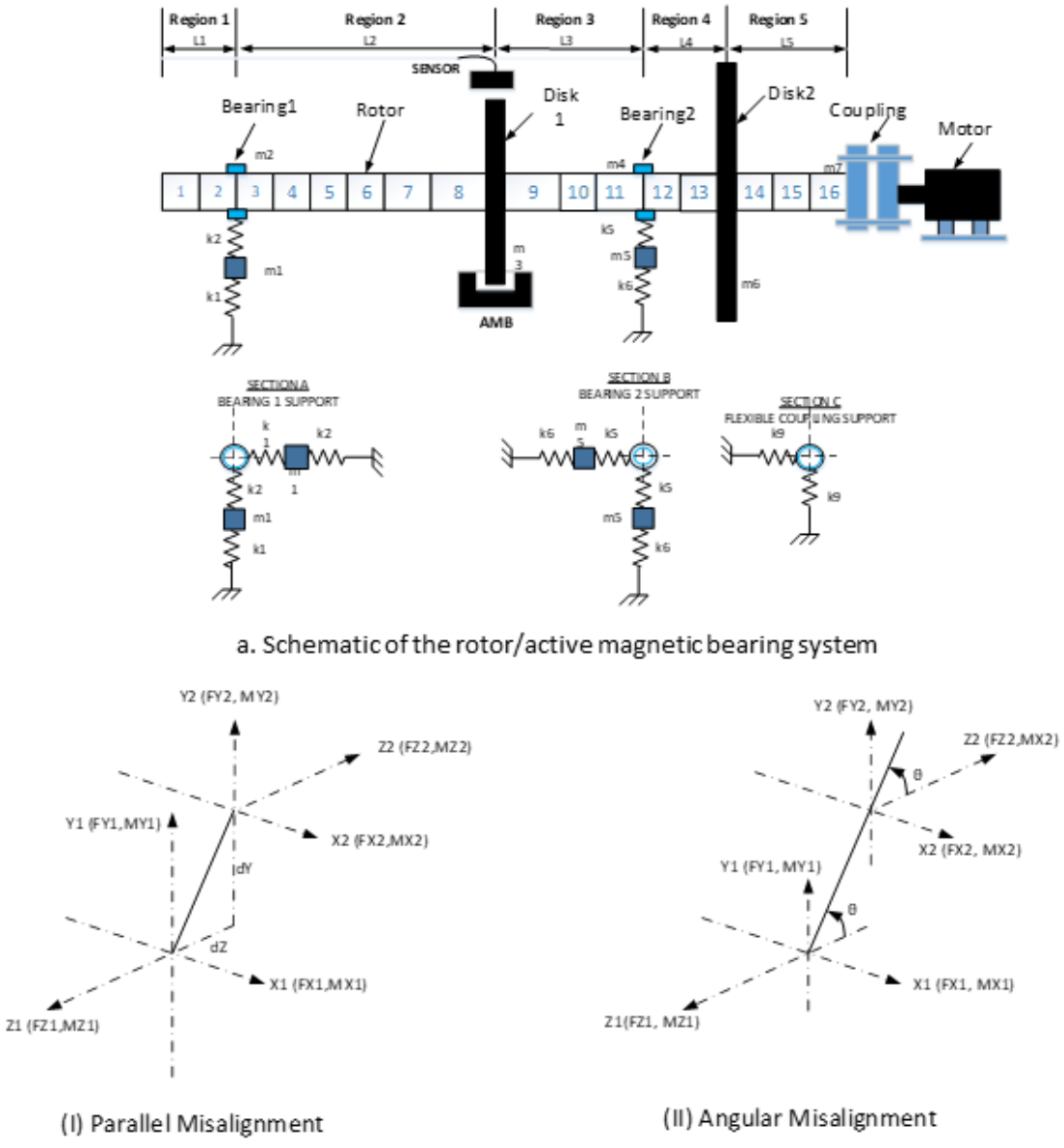

Figure 5-1 Rotor/bearing/coupling system

Details of these forces can be found in reference (Jalan et al. 2009 and Vashisht et al., 2019c). Figure (5.1b) shows the parallel and angular misalignment in coupling. In this work, it is assumed that mixed-coupling misalignment (a combination of parallel and angular misalignment) is present in the system. Apart from coupling misalignment, there are other parameters of the system which

can be changed during the service life of the rotor-bearing system. For example, the bearing support stiffness plays an important role (parameters k_1 and k_6 in table 5.1, for the detailed model, refer to chapter 3). The bolt looseness is an important factor which can reduce the bearing support stiffness. With this, the natural frequencies of the rotor system are subject to change. So, there is a need to use a robust controller which is suitable for a range of parameters.

Finite element models are of large order. To reduce the order of the overall system, modal analysis is carried out. Equation (5.1) can be reduced into the following form.

$$\widetilde{\mathbf{M}}\,\ddot{\mathbf{q}} + \left(\widetilde{\mathbf{C}} - \Omega\,\widetilde{\mathbf{G}}\right)\dot{\mathbf{q}} + \widetilde{\mathbf{K}}\,\mathbf{q} = \mathbf{\Phi}^{\mathbf{T}}\left(\mathbf{F_u} + \mathbf{F_{AMB}} + \mathbf{F_{Coupling}}\right) \tag{5.2}$$

$$\mathbf{x} = \mathbf{\Phi}\,\mathbf{q} \tag{5.3}$$

where $\widetilde{\mathbf{M}} = \mathbf{\Phi}^{\mathbf{T}}\mathbf{M}\,\mathbf{\Phi}$, $\widetilde{\mathbf{C}} = \mathbf{\Phi}^{\mathbf{T}}\mathbf{C}\,\mathbf{\Phi}$, $\widetilde{\mathbf{G}} = \mathbf{\Phi}^{\mathbf{T}}\mathbf{G}\,\mathbf{\Phi}$, $\mathbf{\Phi}$ is the modal matrix obtained during the modal analysis. By considering the first 'r' modes, Equation (5.2) in the absence of gyroscopic effect (for a small variation of spinning speed, the change in gyroscopic effect is negligible) can be written as follows.

$$\begin{bmatrix} 1 & \cdots & 0 \\ \vdots & \ddots & \vdots \\ 0 & \cdots & 1 \end{bmatrix}\ddot{\mathbf{q}} + \begin{bmatrix} 2\xi_1\omega_1 & \cdots & 0 \\ \vdots & \ddots & \vdots \\ 0 & \cdots & 2\xi_r\omega_r \end{bmatrix}\dot{\mathbf{q}} + \begin{bmatrix} \omega_1^2 & \cdots & 0 \\ \vdots & \ddots & \vdots \\ 0 & \cdots & \omega_r^2 \end{bmatrix}\mathbf{q} = \begin{bmatrix} \phi_1^1 & \cdots & 0 \\ \vdots & \ddots & \vdots \\ 0 & \cdots & \phi_n^r \end{bmatrix}\left(\mathbf{F_u} + \mathbf{F_{AMB}} + \mathbf{F_{Coupling}}\right) \tag{5.4}$$

$$\begin{bmatrix} x_1 \\ x_2 \\ \vdots \\ x_m \end{bmatrix} = \begin{bmatrix} \phi_1^1 & \phi_1^2 & \ldots & \phi_1^r \\ \phi_1^1 & \phi_1^1 & \ldots & \phi_2^r \\ \vdots & \vdots & \ddots & \vdots \\ \phi_m^1 & \phi_m^1 & \ldots & \phi_m^r \end{bmatrix}\begin{bmatrix} q_1 \\ q_2 \\ \vdots \\ q_m \end{bmatrix} \tag{5.5}$$

In the above matrices, there are 'm' number of sensors and 'n' number of actuators. ω_r is the r^{th} natural frequency, ζ_r is the r^{th} damping ratio and ϕ_n^r is the mode shape for the r^{th} mode and n^{th} location.

Table 5.1 The physical parameters and mechanical properties of the rotor bearing system

Notation	Description	Value
D	Shaft Diameter of the shaft	0.04 m
L	Shaft Length of the shaft	1.7 m
L_1	First length section of the shaft	0.222 m
L_2	Second length section of the shaft	0.7 m
L_3	Third length section of the shaft	0.436 m
L_4	Fourth length section of the shaft	0.146 m
L_5	Fifth length section of the shaft	0.196 m
ρ	Density	7800 Kg/m^3
E	Young's modulus of elasticity	210 x 10^9 N/m^2
α	First Rayleigh damping coefficient	1.36
β	Second Rayleigh damping coefficient	1.75 x 10^{-5}
m_3	Mass of left-hand side rigid disk	5 Kg
m_6	Mass of right-hand side rigid disk	19.4 Kg
ϵ	Eccentricity of the mass unbalance	0.2 m
m_2	First bearing-element mass	1.5 Kg
k_2	First bearing-element stiffness	7.0 x 10^8 N/m
m_4	Second bearing-element mass	1.5 Kg
K_H	Load–deflection factor for point contact	4.6 x $10^7 N/m^{3/2}$
m_1	First bearing support mass	6 Kg
k_1	First bearing support stiffness	3.80 x 10^6 N/m
m_5	Second bearing support mass	6 Kg
k_6	Second bearing support stiffness	3.8 x 10^6 N/m
m_7	Flexible coupling mass	1.0 kg
k_9	Flexible coupling stiffness	5.75 x 10^4 N/m

5.3. Mu-synthesis using D-K iterations

For any structured uncertainty Δ, the stability of the overall system and the performance should obey the following conditions (Gu et al., 2005, Vashisht et al., 2019c).

- Robust Performance $\Leftrightarrow \left\|\boldsymbol{M}\right\|_{\mu} < 1$ for uncertainty Δ (5.6)
- Robust Stability $\Leftrightarrow \left\|\boldsymbol{M}_{11}\right\|_{\mu} < 1$ for uncertainty Δ (5.7)
- Nominal Performance $\Leftrightarrow \left\|\boldsymbol{M}_{22}\right\|_{\infty} < 1$ (5.8)

- Nominal Stability $\Leftrightarrow$ **M** is internally stable

For the robust stability and robust performance, it is required to find a stabilizing controller **K** such that:

$$\sup_{\omega \in R} \mu \left\| \boldsymbol{M}(\boldsymbol{P}, \boldsymbol{K})(j\omega) \right\| < 1 \tag{5.9}$$

A D-K iteration method for μ-synthesis is used (Gu et al. 2005). It is based on solving the final optimization problem for a stabilizing controller **K** and diagonal scaling matrix **D.**

$$\inf_{\boldsymbol{K}(s)} \sup_{\omega \in R} \inf_{\mathrm{D}} \bar{\sigma} \left\| \boldsymbol{D}\, \boldsymbol{M}(\boldsymbol{P}, \boldsymbol{K})\, \boldsymbol{D}^{-1}(j\omega) \right\| \tag{5.10}$$

The **D**-**K** iteration method for μ-synthesis is as follows (Gu et al., 2005).

1. Start with an initial value of **D**=**I**, where **I** is the identity matrix.
2. Fix **D** and solve for **K** using the H-infinity optimization $\boldsymbol{K} = \inf_{\boldsymbol{K}(s)} \left\| F_l(\boldsymbol{P}, \boldsymbol{K}) \right\|_\infty$
3. Fix **K** and solve the following convex optimization problem

   $\boldsymbol{D}(j\omega) = \inf_{\mathrm{D}} \bar{\sigma} \left\| \boldsymbol{D} F_l(\boldsymbol{P}, \boldsymbol{K}) \boldsymbol{D}^{-1}(j\omega) \right\|$
4. Curve fit $\boldsymbol{D}(j\omega)$ to get a stable minimum phase **D**(s). Go to step 2 and repeat until a pre-specified convergence tolerance is achieved.

5.4. Conventional Adaptive Feedforward Control with an internal estimation of frequency

Effect of impulsive disturbances can be reduced using a feedback type of controllers. In the case of periodic disturbances, feedforward controllers are suitable. Let m be the mass of the unbalanced part, ε be the distance of the unbalanced mass from the centre of rotation and ω_1 is rotational frequency of the rotor in radian per second, the unbalanced force is given by:

$$F = m\, \varepsilon\, \omega_1^2 \tag{5.11}$$

This force will be acting in the horizontal as well as vertical directions with phase angle θ such that in discrete-time it can be presented as follows (Shimada et al. 1999, Vashisht et al., 2019c).

$$d(n) = \alpha(n)\cos\left(\frac{\omega_1 n}{F_s}\right) + \beta(n)\sin\left(\frac{\omega_1 n}{F_s}\right) \tag{5.12}$$

where F_s is the sampling frequency and n is the instant of time. If u(n) is the control force, the system output in terms of error signal e(n) is given by:

$$e(n) = G(z)\big(u(n) - d(n)\big) \tag{5.13}$$

where G(z) is the transfer function in z-domain. The error signal will be zero when the estimate of d(n) is equal to $u(n)$ i.e. $u(n) = \hat{d}(n)$, $\hat{d}(n)$ is the estimate of disturbing force as follows.

$$\hat{d}(n) = \hat{\alpha}(n)\cos\left(\frac{\omega_1 n}{F_s}\right) + \hat{\beta}(n)\sin\left(\frac{\omega_1 n}{F_s}\right) \tag{5.14}$$

For updating coefficients, the instantaneous cost function $J = e(n)^2$ is used. If w(n) at time n is defined as $w(n) = \begin{bmatrix} \hat{\alpha}(n) & \hat{\beta}(n) \end{bmatrix}^T$ the gradient of the cost function J becomes (Shimada et al. 1999):

$$\nabla(n) = \frac{\partial J}{\partial w(n)} = \begin{bmatrix} 2e(n)\cos\left(\frac{\omega_1 n}{F_s}\right) \\ 2e(n)\sin\left(\frac{\omega_1 n}{F_s}\right) \end{bmatrix} \tag{5.15}$$

Such that

$$\begin{aligned} \hat{\alpha}(n) &= \hat{\alpha}(n-1) - 2\mu_{\alpha\beta}e(n)\cos\left(\frac{\omega_1 n}{F_s} + \phi\right) \\ \hat{\beta}(n) &= \hat{\beta}(n-1) - 2\mu_{\alpha\beta}e(n)\sin\left(\frac{\omega_1 n}{F_s} + \phi\right) \end{aligned} \tag{5.16}$$

where $\mu_{\alpha\beta}$ is the updating coefficient and ϕ is the phase angle of the flexible rotor system at frequency ω_1. In case the frequency ω_1 is not certain or time-varying, it must be updated at each instant of time. Parameter updating equations are modified as follows (Shimada et al. 1999, Vashisht et al., 2019c)

$$\begin{aligned}\hat{\alpha}(n) &= \hat{\alpha}(n-1) - 2\mu_{\alpha\beta} e(n)\cos\left(\Omega(n-1)+\phi\right)\\ \hat{\beta}(n) &= \hat{\beta}(n-1) - 2\mu_{\alpha\beta} e(n)\sin\left(\Omega(n-1)+\phi\right)\end{aligned} \tag{5.17}$$

$$\omega_1(n) = \omega_1(n-1) - 2\mu_{\omega_1}\left(\frac{e(n)}{F_s}\right)\left(-\hat{\alpha}(n)\sin\left(\Omega(n-1)+\phi\right) + \hat{\beta}(n)\cos\left(\Omega(n-1)+\phi\right)\right) \tag{5.18}$$

$$\Omega(n) = \Omega(n-1) + \frac{\omega_1(n)}{F_s} \tag{5.19}$$

$$u(n) = \hat{\alpha}(n)\cos\left(\Omega(n-1) + \frac{\omega_1(n)}{F_s} + \phi\right) + \hat{\beta}(n)\sin\left(\Omega(n-1) + \frac{\omega_1(n)}{F_s} + \phi\right) \tag{5.20}$$

5.5. External Frequency estimation

Adaptive Notch Filter (ANF) is a second-order adaptive filter used to estimate the frequency of a sinusoidal signal. Dynamic equations of the filter are as follows (Yoon et al. 2017)

$$\ddot{x}(t) + 2\xi\omega_1(t)\,\dot{x}(t) + \omega_1^2(t)x(t) = 2\xi\omega_1^2(t)e(t) \tag{5.21}$$

$$\dot{\omega}_1(t) = \gamma\, x(t)[2\,\xi\,\omega_1^2(t)\,e(t) - 2\,\xi\,\omega_1(t)\,\dot{x}(t)] \tag{5.22}$$

where *x(t)* is the filter state, $\omega_1(t)$ is the natural frequency of the filter or the frequency to be estimated for the signal e(t), ξ is the damping ratio of the filter, γ is the estimation gain. The estimated frequency $\omega_1(t)$ converges to a fixed value when the right-hand side of Equation (5.22) becomes zero. This presentation is for a continuous-time system. However, for the real-life implementation, it must be discretized using bilinear transformations.

5.6. Results with conventional Adaptive Feedforward controller

Section 5.4 explains conventional AFFC. The schematic is shown in Figure 5.2 (a). Figure 5.3 shows the response of the system with AFFC. The rotor spin frequency is fixed at 10 Hz. Equation (5.16) is used to apply AFFC. If the rotor spin frequency is kept at 19.995 Hz, the performance of the closed-loop system deteriorates. If the rotor spin frequency is further changed to 19.95 Hz, the control effectiveness becomes nearly zero (not shown for the purpose of brevity). This aspect shows that the effectiveness of AFFC is fully dependent on the frequency. If the frequency tracking capability of AFFC is activated by using Equations (5.17-5.20), the control effectiveness is regenerated. If the frequency gap is increased i.e. the difference between the actual frequency and starting frequency, convergence takes a lot of time. Up to a certain extent, convergence speed can be improved by increasing the value of adaptation coefficients. By arbitrarily increasing these values, the closed-loop system becomes unstable.

Based on the real-life scenario, the rotor spin frequency is increased from 20 Hz to 25 Hz. This increase in value starts at 20 second and ends at 30 second. The conventional AFFC with high adaptation coefficients is used. It is obvious that the conventional AFFC cannot cope up such a big change (i.e. 5 Hz) (Figure 5.4).

Obviously, the next choice is to use frequency estimators in combination with conventional AFFC. Adaptive Notch Filters are best suited for the frequency estimation. However, they have limitations in case of the low-cost instrumentation where low sampling rates are available. At higher sampling frequencies (in several kHz), the error is virtually zero. However, at 200 Hz, the error in estimation is quite large especially at higher frequencies as shown in Figure 5.5.

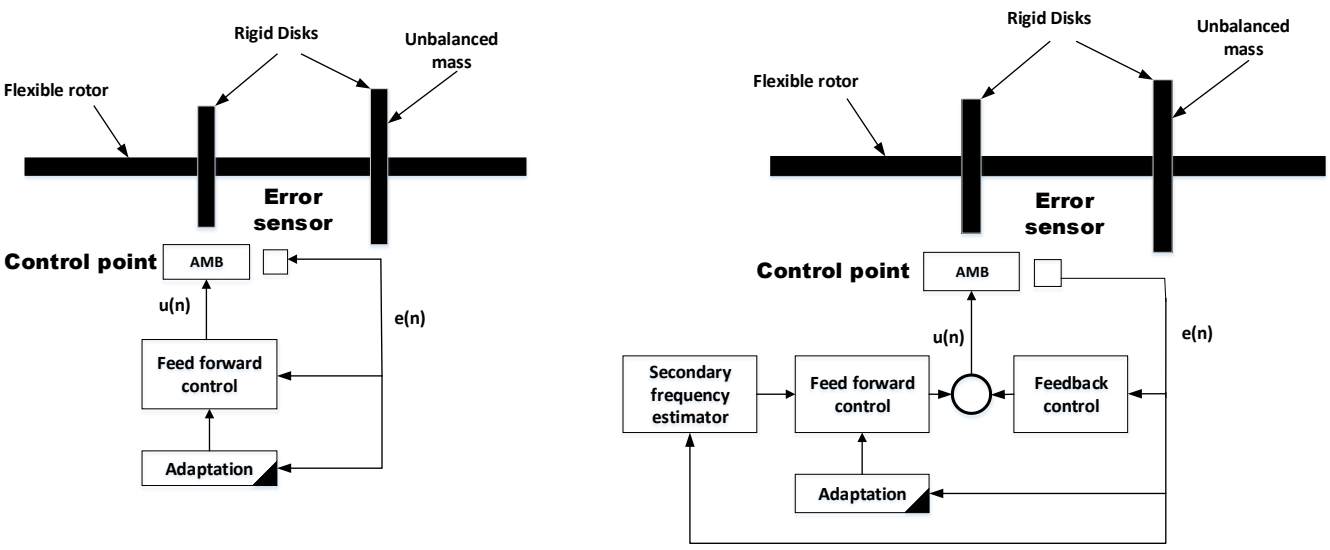

(a) Conventional adaptive feed forward control

(b) Proposed hybrid control

Figure 5.2 Comparison of conventional and proposed control architecture

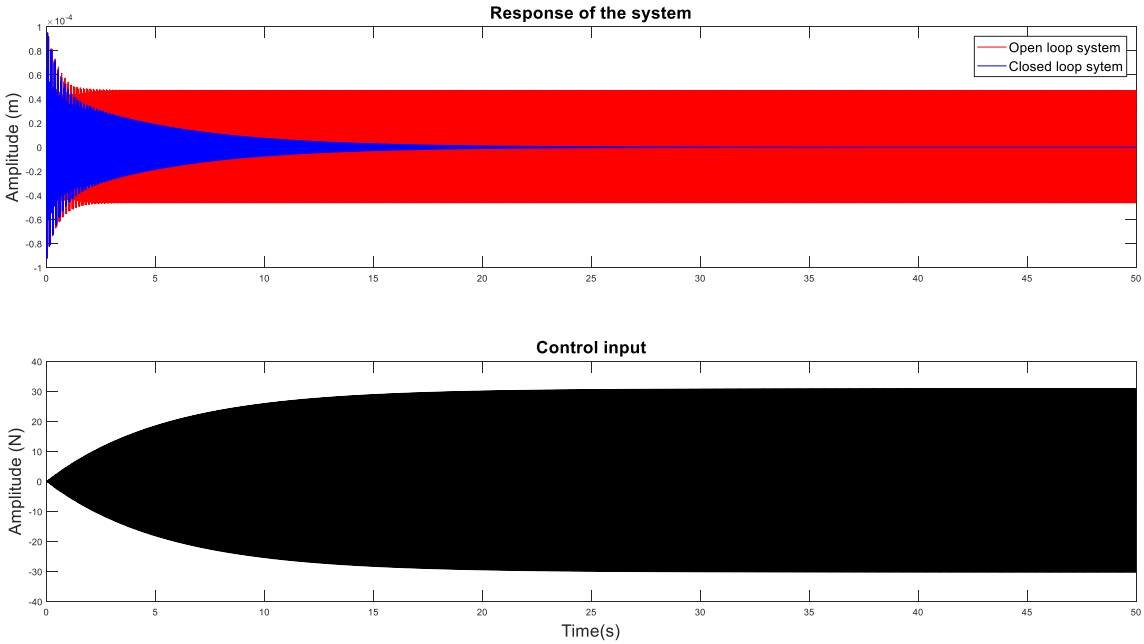

Figure 5.3 Time domain response by conventional Adaptive Feedforward Control at 20 Hz Spinning speed

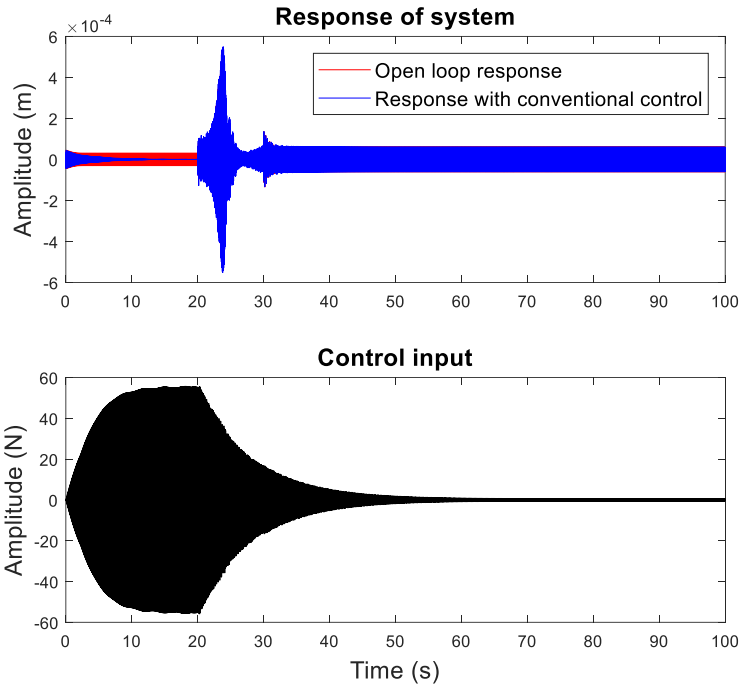

Figure 5.4 Time domain response by Adaptive Feedforward Control with time varying frequency component applied to rotor system

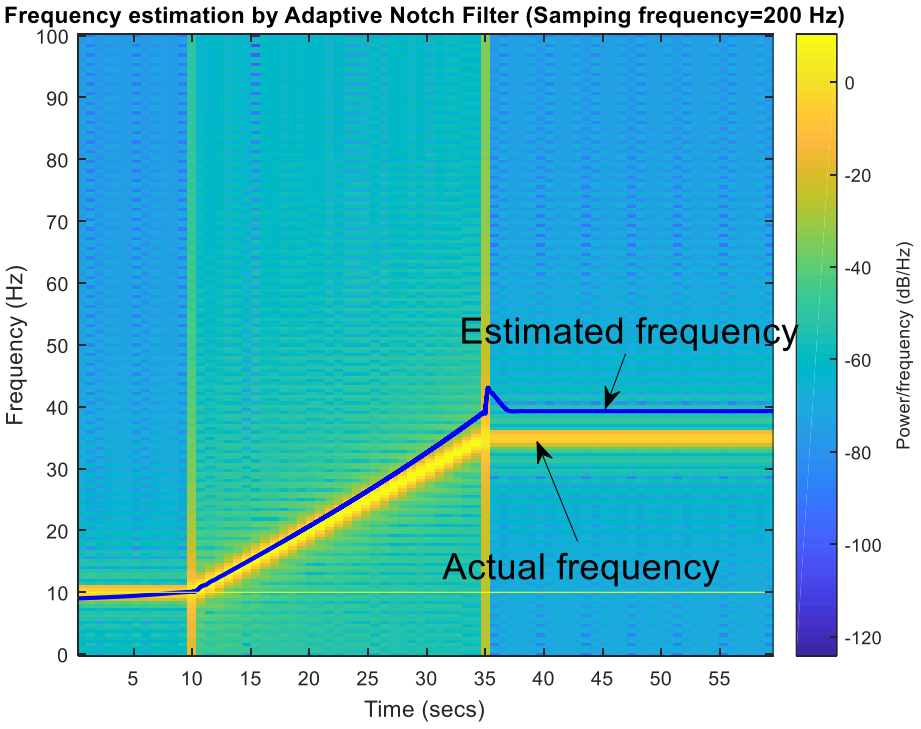

Figure 5.5 Comparison of actual and estimated frequencies by Adaptive Notch Filter at sampling frequency of 200 Hz

The Goertzel filter-based computation of Discrete Fourier Transform (DFT) is free from these errors. Very accurate estimation is made with this filter. Based on the sequence length of the signal, the desired resolution in the frequency domain is possible. An online version of the Goertzel filter is also available (Manngård et al. 2017). However, the computational load of these filters is quite heavy. They are not suitable for the online frequency estimation with low sampling rates (e.g. 200 Hz). The combination of ANF and Goertzel filter is beneficial in this situation. Hence both the frequency estimators are used to design the proposed AFFC.

5.7. Proposed Hybrid controller with an external estimation of frequency

From Figure 5.4 it is obvious that when the frequency of a signal changes (although at a moderate rate), the fundamental harmonics are excited. Their amplitude is much higher than the steady-state amplitude at non-resonant frequencies. Hence feedback controllers are required to reduce these high amplitudes of vibration.

5.7.1. Adaptive Feedforward Control

The proposed AFFC uses the ANF and Goertzel filter (Figure 5.2b). The flowchart shown in Figure 5.6 describes the complete architecture of the proposed controller. ANF is used for online frequency estimation. If the rotor spin frequency of the flexible rotor is changed, ANF can detect this change. There is a steady-state error in the estimation of the frequency but the frequency change can be well detected. The number of time steps N is fixed based on the general experience. If frequency variations are frequent, N is small and vice-a-versa. During frequency changes, AFFC is totally useless in terms of vibration reduction. Hence, the controller is switched off during periods of the frequency variation.

If the frequency variation continues, the controller remains switched off and data points are collected. ANF is used to detect the frequency variation and rough frequency estimation only.

When the frequency variation is ceased, the Goertzel filter roughly estimates the current frequency of the signal (in the vicinity of the estimate made by ANF). When the rough estimate is completed, the resolution of the Goertzel frequency can be refined. Discrete Fourier transformation (DFT) coefficients are calculated in the vicinity of the rough estimate made by the Goertzel filter. Not all of the DFT coefficients need to be calculated. This reduces the computational burden. After the refined estimate of the current frequency is done, this frequency can be used as an initial point for conventional AFFC. Now the AFFC controller is switched on.

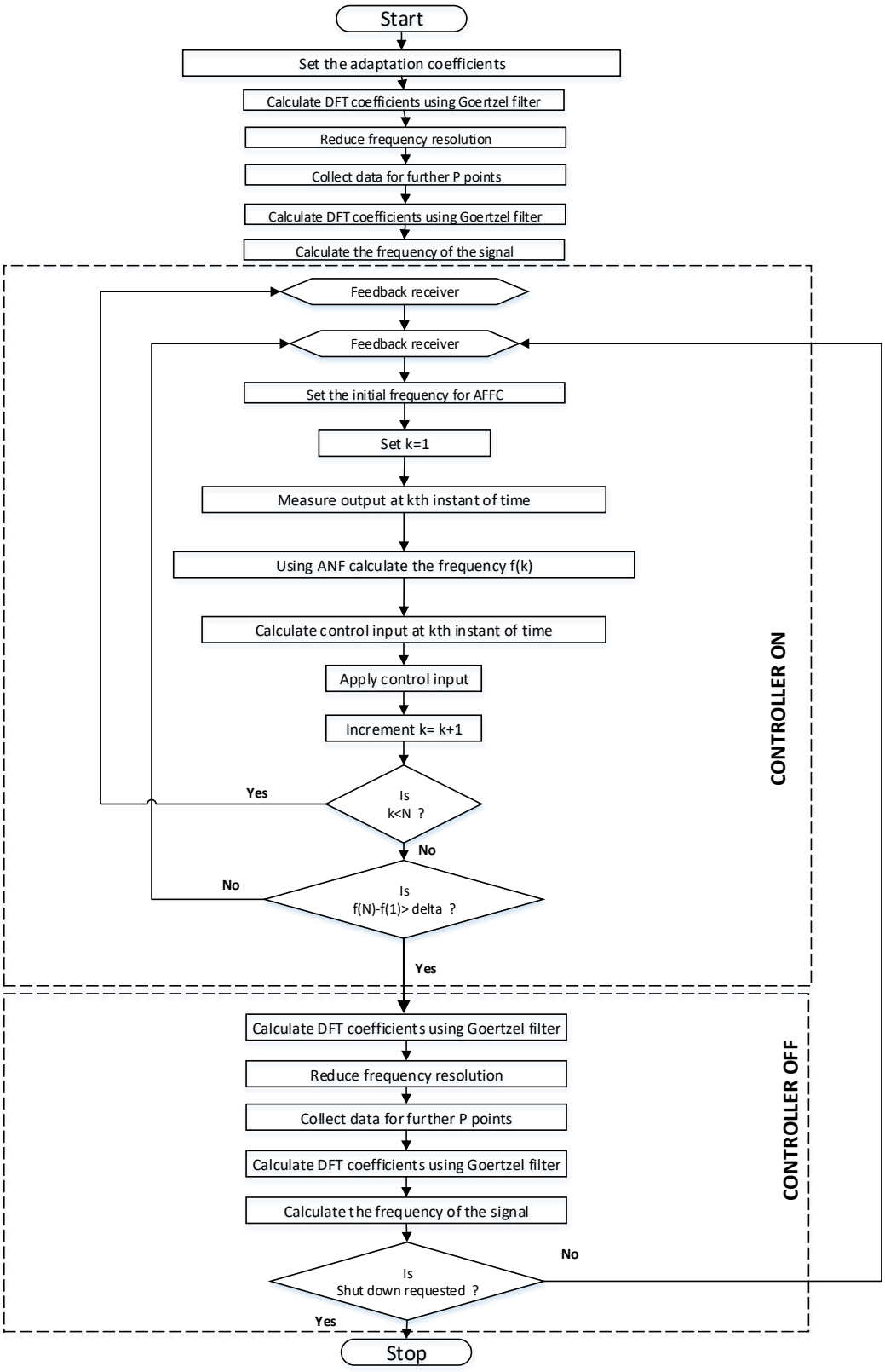

Figure 5.6 Flow chart for proposed adaptive feedforward controller

5.7.2. Mu-synthesis based Robust Feedback Control

To achieve the desired performance of the disturbance rejection, it is necessary to satisfy inequality $\left\| w_p \left(I + GK \right)^{-1} \right\|_\infty < 1$. Singular values of sensitivity function $\left(I + GK \right)^{-1}$ over the frequency range must lie below $\frac{1}{w_p}$ (Gu et al., 2005). This is achieved by using MATLAB's Robust control toolbox. From the frequency response function of the flexible rotor system, it is obvious that the first two modes are dominant. Figure 5.7 shows the frequency response of the nominal system, required model of the system, control weighting function and performance weighting function. Singular values of the closed loop system are shown in Figure 5.8. It is obvious that the closed loop system achieves the nominal performance as well as robust performance (Figure 5.8). Controller order reduction is completed before implementation. The order of the full system is 29 compared to the reduced system with order 10.

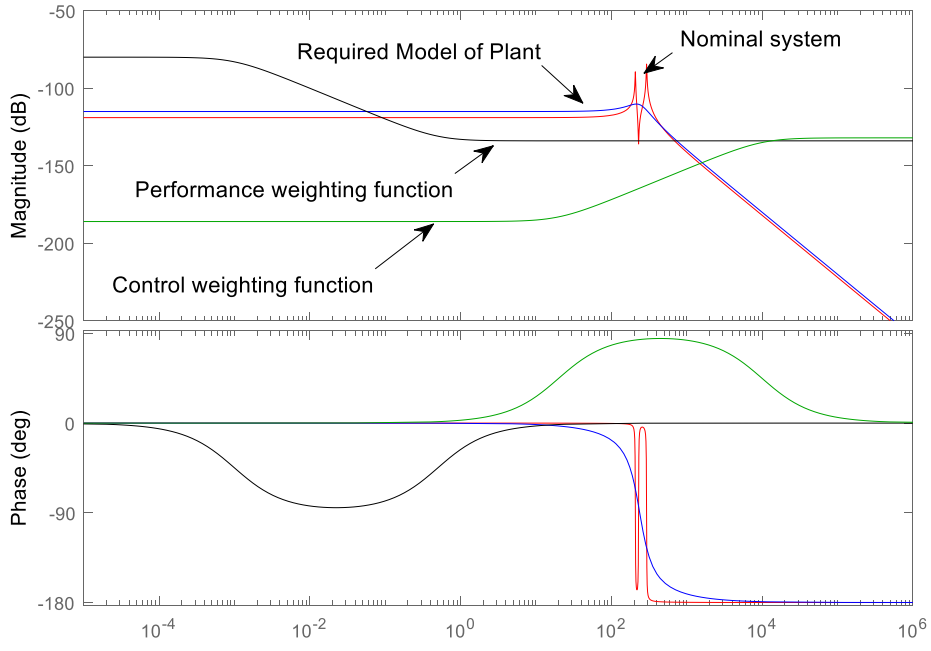

Figure 5.7 Frequency response function of different systems

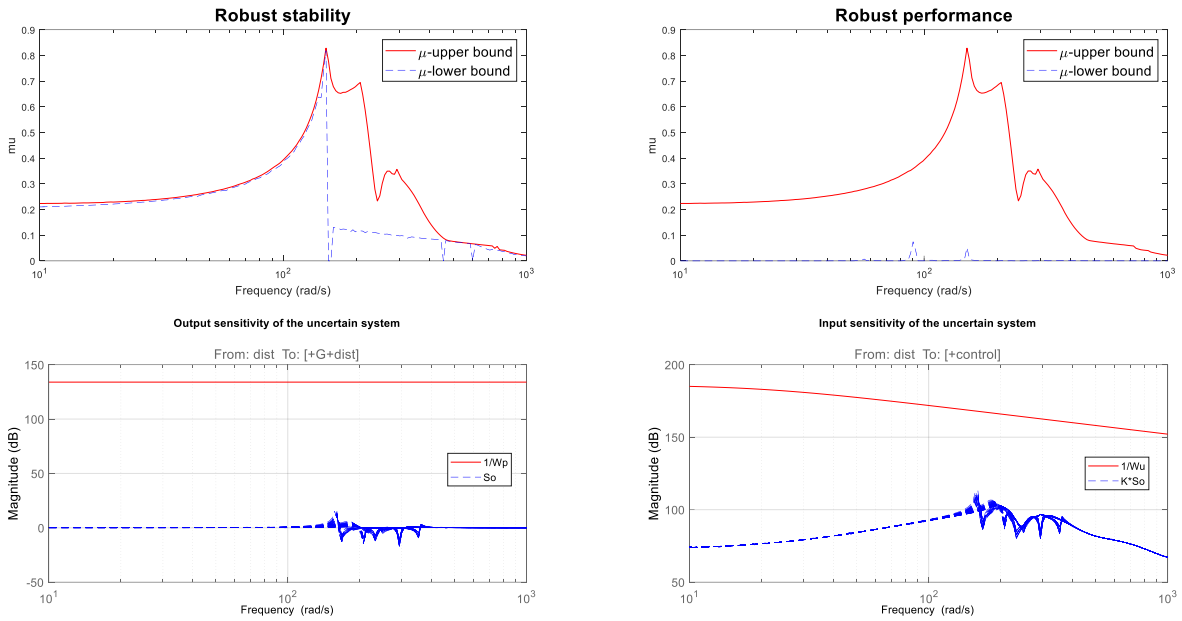

Figure 5.8 Robust stability, performance and other parameters

5.7.3. Hybrid controller

The hybrid controller is shown in Figure 5.2 (b) is used in this work. The proposed controller is a combination of the feedback and AFFC controller. The proposed controller can attenuate multiple harmonics at a time. In the case of coupling misalignment, multiple harmonics that are integer multiple of rotor spin frequency are developed. The proposed hybrid controller shown in Figure 5.9 is used for the desired task.

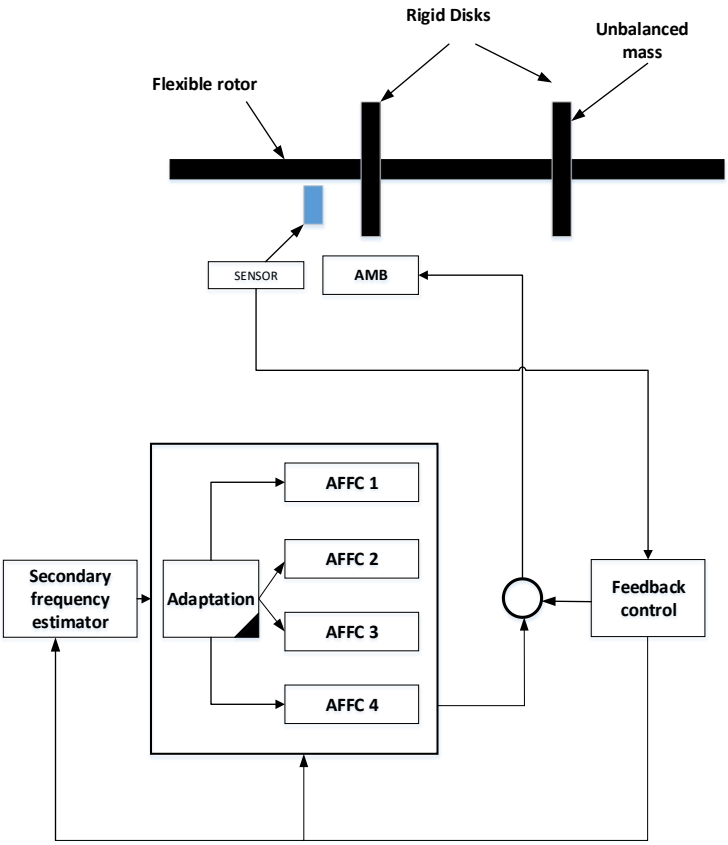

Figure 5.9 Multi-harmonic hybrid control architect

5.8. Experiment

The experimental setup contains the following parts as shown in Figure 5.10.

- For acquiring data, a USB based card NI-USB-6212 from National Instruments is used. It is compatible with software LabView to acquire data as well as signal generation. Its input and output ranges are from -10 volts to +10 volts. For acquiring the data only, the sampling rate of a few kHz can be easily obtained. However, for the controller implementation and calculating the control signal, a certain time is consumed. This restricts the sampling rate to lower values. In this research, the 200 Hz sampling rate is fixed. All the calculations for the controller implementation are processed in this period of time. However, using real-time engines, much higher sampling rates can be obtained but the high cost of these real-time

engines restricts their applications. The cost of National Instruments based PXI- Real-time engines varies from 10 to 15 times for the NI-USB-6212 data acquisition card.

- Eddy current probes from Bently Nevada are used as sensors. The gap up to a few microns can be easily measured with this sensor system. It has 8 volts voltage drop per millimetre of gap.
- An AC amplifier is used to increase the amplitude of current signals emerged from the computer.
- For generating control forces, a home-made electromagnetic actuator is used. Details are available in next sub-section.

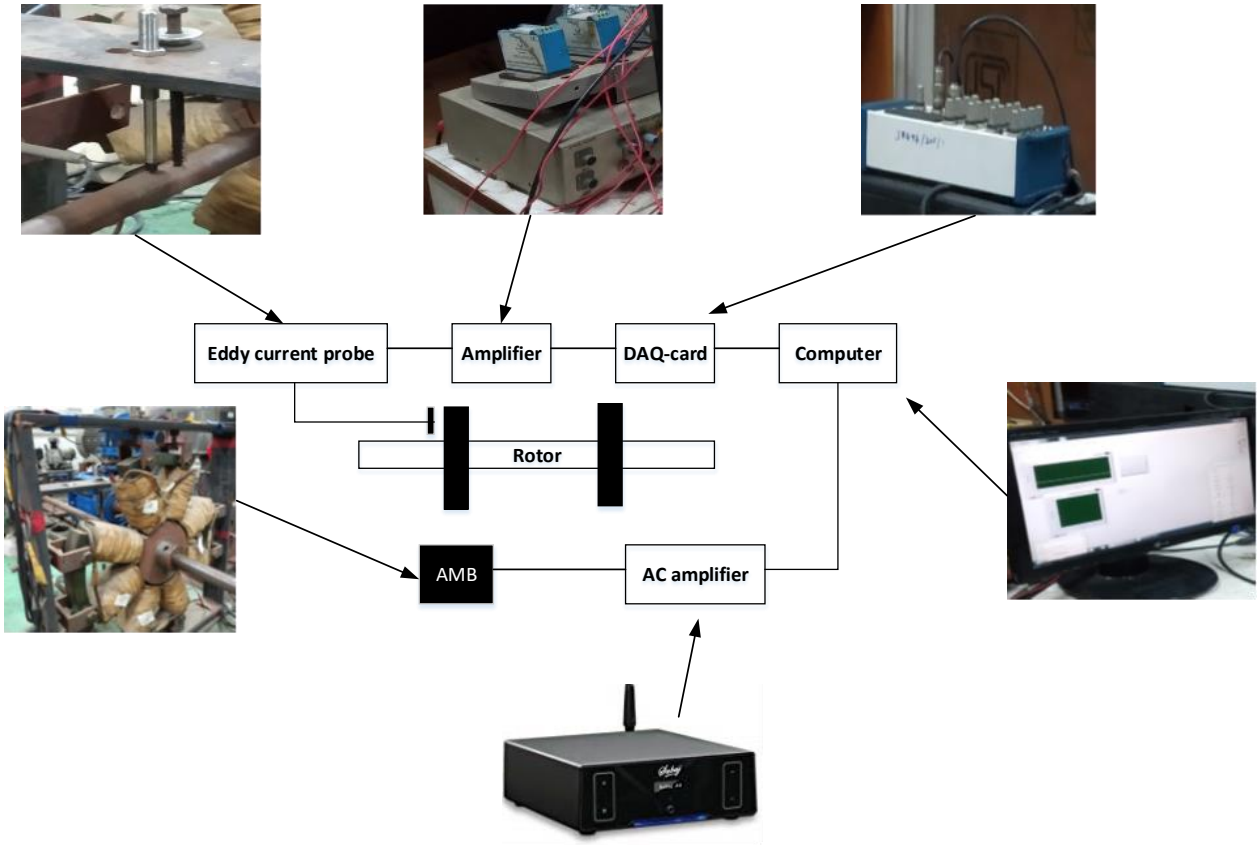

Figure 5.10 Experimental setup for active vibration control for rotor system

Here i_0 represents the bias current and i is the control current. The force produced by this current is given by:

$$F_{AMB} = k\left[\frac{(i+i_0)^2}{(gap-x)^2} - \frac{(i-i_0)^2}{(gap+x)^2}\right] \quad (5.23)$$

where x is the displacement of the workpiece from the equilibrium position, 'gap' is the distance between the core and the workpiece under equilibrium conditions. The value of the coefficient k is given by:

$$k = \frac{1}{4}\,\mu_0\, n^2 A \quad (5.24)$$

where μ_0 is the permeability of the air, n is the number of winding turns and projected area of the core. The value of different parameters of electromagnetic actuators is given in Table 5.2.

Table 5.2 Physical Parameters of Electromagnetic actuator

Sr	Parameter	Notation	Value
1	Permeability of air	μ_0	1.256×10^{-6} N/A^2
2	Area of iron core	A	40 mm x 40mm
3	Number of winding turns	n	500
4	Nominal air gap	gap	4 mm
5	Bias current	i_0	3 A

5.9. Results

It was observed that Proportional-Integral-Derivative (PID) based feedback controllers have extensively used to remove the steady-state vibrations from literature. However, this technique did not work in the present rotor system. A proportional and simple derivative controller is proposed to reduce the steady-state vibrations in the present rotor system with multiple flexible modes. This technique works well for rigid rotors as well as simple Jeffcott rotor system with the single dominant mode. However, in the presence of multiple modes, the efficiency reduces drastically.

The next question arises regarding the application of advanced robust control techniques like Loop Shaping and Mu-synthesis controller. The performance comparison is done between Mu-synthesis and a derivative type feedback controller. If the high gain derivative controller was applied, the requirement of control forces raises to a high value. The value of gain is chosen in such a way that the response with this controller matches exactly with that obtained by Mu-controller. If the low gain derivative controller is used, the control force requirement is comparatively less. However, with this controller, there is an initial rise in response.

Another advantage of using the Mu-controller is that the vibration response at Disk 2 (notice that control actuator is applied at Disk 1) is less than that obtained by using a derivative type feedback controller (Figure 5.11). At lower gains, the amplitude difference is quite significant (**30%** fall). These factors prove the superiority of the Mu-controller compared to Derivative feedback controller. The same trend follows for PID type feedback controllers. Using robust spatial control techniques, this superiority can be further enhanced.

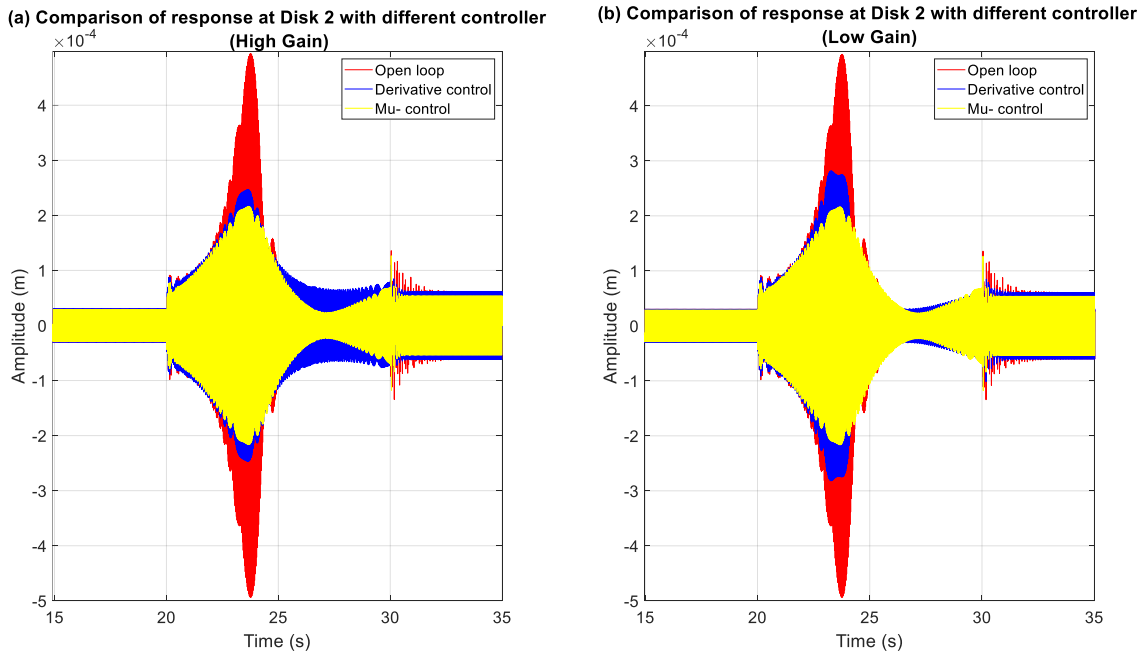

Figure 5.11 Comparison of Mu- controller and Derivative controller for Disk 2

For the application of the proposed hybrid controller, simulation results show open and closed-loop responses of the rotor system rotating at 20 Hz frequency. At 20 s, the spinning speed starts increasing and it increases up to 25 Hz in next 10 s. From 20-30 s, the transient vibrations take place. Figure 5.12 shows the experimental response of the rotor system along with control forces in terms of amplified control voltages. Since AC voltage amplifier is used, it becomes easy to measure the control voltage. With the change of temperature, parameters of the electromagnetic actuator (EA), as well as voltage amplifier (VA), are subjected to change. One of the biggest advantages of the AFFC controller is that it can take care of changing parameters of EA and VA.

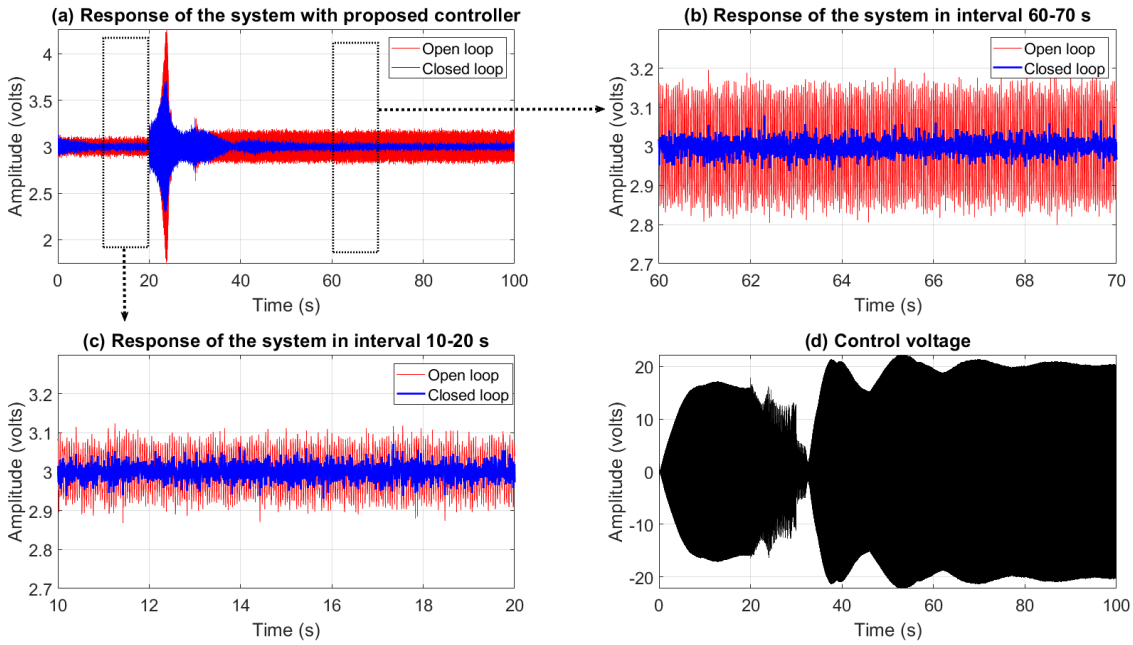

Figure 5.12 Response of rotor system with the proposed hybrid controller (Experimental)

The AFFC controller is efficient for a particular rotor spin frequency. In the case of coupling misalignment, multiple frequency components (an integer multiple of the rotor spin frequency) appear in the spectrum. The multi-harmonic hybrid controller shown in Figure 5.13 is used for this purpose. The frequency of the first harmonic is estimated only. Figure 5.13 shows the open and closed-loop responses of the rotor system with coupling misalignment at 20 Hz rotor spin

frequency. The response contains 40 Hz and 60 Hz signals also. With applications of the proposed controller, the amplitude at all the harmonics reduces considerably (Figure 5.13 (a)). Figure 5.13 (b) shows the spectrum of applied control signals. It clearly shows three harmonics i.e. 20 Hz, 40 Hz and 60 Hz.

It is obvious that the feedback controller is nearly useless at other frequencies (i.e. other than natural frequencies). AFFC is suitable for these frequencies. By using the combination of multi-harmonic AFFC and robust feedback control (i.e. hybrid control), the magnitude reduction at natural as well as at other frequencies is possible.

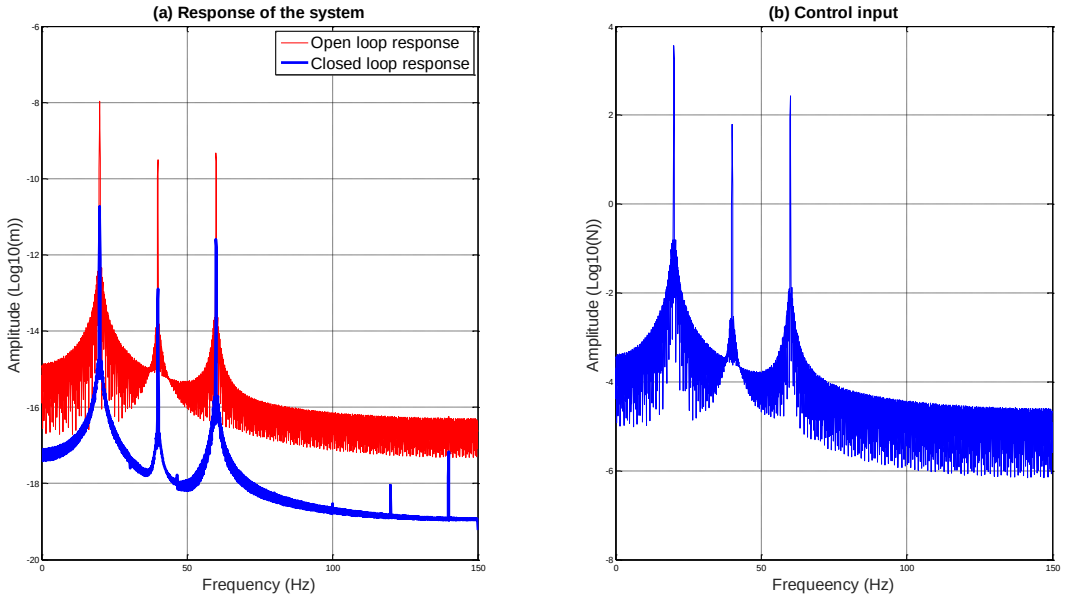

Figure 5-13 The response of the rotor system with coupling misalignment using proposed controller (Experimental)

5.10. Concluding remarks

An adaptive hybrid controller is proposed and implemented. Simulation and experimental results have authenticated the superiority of the proposed method. Based on the results following conclusions are drawn.

- Conventional AFFC cannot tolerate sharp rotor spin frequency changes. External frequency estimators need to be applied for improving the performance of these controllers.
- ANF provides unacceptable results at low sampling rates, however, it can be used to indicate that frequency changes are occurring in the system.
- Goertzel filter is computationally demanding, however, it can be used efficiently when a small number of DFT coefficients is needed for computation.
- Combination of ANF and Goertzel filter can be used efficiently to estimate changing rotor spin frequencies.

Chapter 6

Precision control of ball screw drives

6.1. Overview

This chapter presents a hybrid controller by combining the interpolating gain scheduled loop shaping (IGSLS) controller and cascade PPI controller. It achieves active vibration damping as well as high bandwidth disturbance rejection for a ball screw drive system (BSD). The IGSLS controller is designed based on loop shaping principles for the non-collocated system from the motor torque to carriage/table position. It is observed that by increasing gains of controllers, the closed-loop stability margins are reduced although the command tracking efficiency increases. High gain controllers also cause a large variation in motor torque when BSD is used in the machining process. From time and frequency domain analysis, it is found that the proposed hybrid controller has high command performance efficiency along with better performance during the machining process. For machine drives in the absence of pre-loading, the system parameters vary over a large range, depending upon the carriage/table mass and location. The BSD system can be modelled as a linear parameter varying (LPV) system using the mass and location of the carriage as scheduling parameters. It is also observed that fixed gain robust controllers cannot maintain the closed-loop stability for the total range of system parameters of the BSD. Based on the transient response, the carriage mass can be estimated online with sufficient accuracy. Using this information and table location, IGSLS controllers can be implemented in real-time using interpolation techniques. Simulations and experimental results confirm the performance of the proposed controller in command tracking, the variation of motor torque during machining and disturbance rejection.

6.2. Mathematical Modelling

The ball screw drive is actuated by a servo motor. The torque is applied through the flexible coupling. The rotary motion of the ball screw is converted into translational motion of the carriage. The flexibility of the carriage plays an important role in the overall dynamics of the system.

6.2.1. Modelling of ball screw drives

Figure 6.1 shows a two-dimensional representation of the ball screw drive. The balls and the lead screw are flexible. The stiffness of the ball near the left-hand side stopper has a stiffness k_{b1} and stiffness of the ball near the right-hand side stopper k_{b2}. The stiffness of the coupling is k_c. The stiffness of the carriage balls is k_n. The total length of the lead screw is *L*. The lead of the lead screw is *l*. If $\theta(t)$ is the actual angle of rotation of the motor ($x_1(t)$ is the virtual displacement), *T(t)* is the actual torque applied at the motor ($F_1(t)$ is the virtual force), they are related to each other with the following expressions as shown in Figure 6.1 (Varanasi and Nayfeh, 2004).

$x_1(t) = (l/2\pi)\theta(t)$ (see Figure 6.1) (6.1)

$F_1(t) = (2\pi/l)T(t)$ (see Figure 6.1) (6.2)

Figure 6.1 represents the various stiffnesses related to the ball screw drive. The equivalent stiffness of the overall system is given as follows (Varanasi and Nayfeh, 2004).

$$k_t = \left[\frac{1}{k_1 + k_2} + \frac{1}{k_n} + \left(\frac{l}{2\pi} \right)^2 \left(\frac{1}{k_c} + \frac{c}{GJ} \right) \right]^{-1} \tag{6.3}$$

where *c* is the distance of the carriage from the left-hand side stopper, *G* is the modulus of rigidity, *J* is the polar moment of inertia, k_n is the stiffness of balls near the carriage (on the left and right of the carriage) and:

$$k_1 = \left[\frac{c}{EI} + \frac{1}{k_{b1}} \right]^{-1} \tag{6.4}$$

$$k_2 = \left[\frac{L-c}{EI} + \frac{1}{k_{b2}} \right]^{-1} \tag{6.5}$$

where E is the modulus of elasticity, I is the bending moment of inertia, k_{b1} and k_{b2} are the stiffnesses of balls on the left and right sides of the ball screw system. The details of modelling can be seen in reference (Varanasi and Nayfeh, 2004). This modelling uses a distributed parameter approach for the LPV representation.

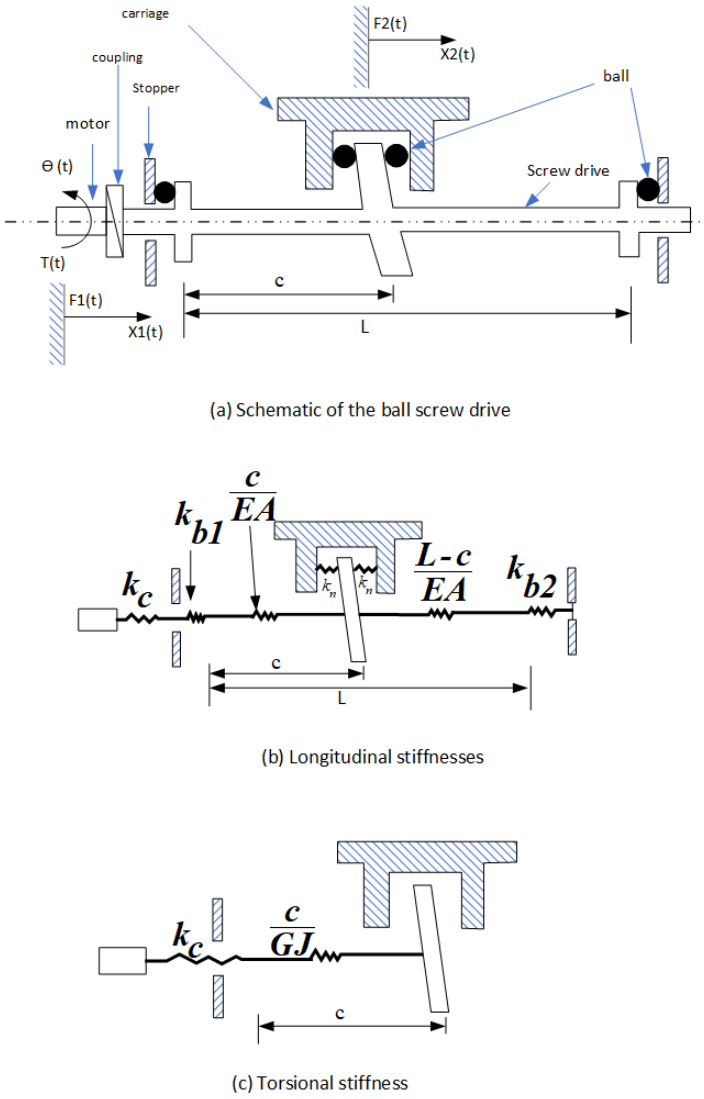

Figure 6.1 Two-dimensional representation of the ball screw drive

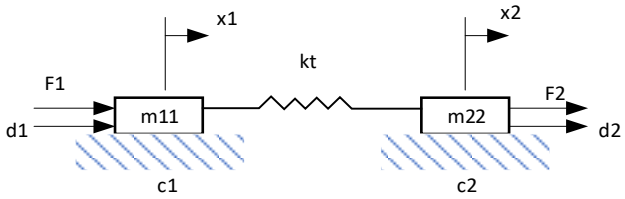

Figure 6.2 Simplified model of the ball screw drive

Let $X_2(t)$ be the displacement of the carriage and $F_2(t)$ be forces acting on the carriage, using the Galerkin type weighted residual method (Varanasi and Nayfeh, 2004), the dynamic equations of motion are represented as follows.

$$\boldsymbol{M}\begin{Bmatrix}\ddot{x}_1(t)\\ \ddot{x}_2(t)\end{Bmatrix}+\boldsymbol{C}\begin{Bmatrix}\dot{x}_1(t)\\ \dot{x}_2(t)\end{Bmatrix}+\boldsymbol{K}\begin{Bmatrix}\dot{x}_1(t)\\ \dot{x}_2(t)\end{Bmatrix}=\begin{Bmatrix}F_1(t)\\ F_2(t)\end{Bmatrix} \tag{6.6}$$

Where

$$\boldsymbol{M}=\begin{bmatrix}m_{11} & m_{12}\\ m_{21} & m_{22}\end{bmatrix} \tag{6.7}$$

With

$$\begin{aligned} m_{11} &= n^2(J+J_{11})+m\\ m_{12} &= n^2J_{12}-m\\ m_{21} &= m_{12}\\ m_{22} &= n^2J_{22}+m+m_c \end{aligned} \tag{6.8}$$

where J is the second polar moment of the screw, m_c is the mass of the carriage and the value of other parameters can be found in reference (Varanasi and Nayfeh, 2004). The damping matrix of the system is as follows.

$$\boldsymbol{C}=\begin{bmatrix}n^2C_1 & 0\\ 0 & C_2\end{bmatrix}=\begin{bmatrix}c_1 & 0\\ 0 & c_2\end{bmatrix} \tag{6.9}$$

Where C_1 is the motor damping and C_2 is the damping coefficient between slides and the carriage. The stiffness matrix is given by Varanasi and Nayfeh (2004)

$$\boldsymbol{K} = k_t \begin{bmatrix} 1 & -1 \\ -1 & 1 \end{bmatrix} \tag{6.10}$$

It is obvious that the overall stiffness of the ball screw system is dependent on parameter c. Hence the dynamic system represented by Equation (6.6) is dependent on parameter c. In the transfer function of the system dynamics can be represented as follows (Figure 6.2) in the form of a discrete mass system for controller design purpose as follows.

$$\begin{bmatrix} x_1(s) \\ x_2(s) \end{bmatrix} = \begin{bmatrix} G_{11}(s) & G_{12}(s) & G_{13}(s) \\ G_{21}(s) & G_{22}(s) & G_{23}(s) \end{bmatrix} \begin{bmatrix} F_1(s) \\ d_1(s) \\ d_2(s) \end{bmatrix} \tag{6.11}$$

Where

$$\begin{aligned} G_{11}(s) &= \frac{x_1(s)}{F_1(s)} = G_{12}(s) = \frac{x_1(s)}{d_1(s)} = \frac{m_{22}s^2 + c_2 s + k_t}{\Delta(s)} \\ G_{13}(s) &= \frac{x_1(s)}{d_2(s)} = \frac{k_t}{\Delta(s)} \\ G_{21}(s) &= \frac{x_2(s)}{F_1(s)} = G_{22}(s) = \frac{x_2(s)}{d_1(s)} = \frac{k_t}{\Delta(s)} \\ G_{23}(s) &= \frac{x_2(s)}{d_2(s)} = \frac{m_{11}s^2 + c_1 s + k_t}{\Delta(s)} \end{aligned} \tag{6.12}$$

$$\begin{aligned} \Delta(s) &= m_{11}m_{22}s^4 + a_1 s^3 + a_2 s^2 + a_3 s \\ a_1 &= m_{11}c_2 + m_{22}c_1 \\ a_2 &= c_1 c_2 + (m_{11} + m_{22})k_t \\ a_3 &= (c_1 + c_2)k_t \end{aligned} \tag{6.13}$$

6.2.2. Simulation model

Parameters in Table 6.1 are used for conducting simulations as well as experiments. The material of the ball screw is steel with Modulus of Elasticity $210x0^9$ N/m^2, Modulus of Rigidity

$78x0^9$ N/m^2 and density 7850 Kg/m^3. The carriage mass is allowed to vary from 25 Kg to 45 Kg. The damping coefficients C_1 and C_2 are measured experimentally as 0.001 and 0.01, respectively.

Table 6.1 Important parameters of the ball screw drive

No.	Parameter	Symbol	Value
1	Ball screw average diameter	d	16 mm
2	Ball screw lead	l	5 mm
3	Ball screw length between bearing supports	L	920 mm
4	Stiffness of the balls near the carriage	k_n	260 MN/m
5	Left hand side ball stiffness at the start of ball screw	k_{b1}	50 MN/m
6	Right hand side ball stiffness at the end of ball screw	k_{b2}	50 MN/m
7	Torsional stiffness of the coupling	k_c	690 Nm
8	Motor inertia	J	8 x 10^{-5} Kg m^2
9	Carriage mass	m_c	25-45 Kg

Based on Equation (6.6), the state-space model of the system can be expressed as follows.

$$\begin{Bmatrix} \dot{x}_1 \\ \dot{x}_2 \\ \ddot{x}_1 \\ \ddot{x}_2 \end{Bmatrix} = \boldsymbol{A} \begin{Bmatrix} x_1 \\ x_2 \\ \dot{x}_1 \\ \dot{x}_2 \end{Bmatrix} + \boldsymbol{B} \begin{Bmatrix} F_1 \\ F_2 \end{Bmatrix}$$

$$\begin{Bmatrix} x_1 \\ x_2 \\ \dot{x}_1 \\ \dot{x}_2 \end{Bmatrix} = \boldsymbol{C} \begin{Bmatrix} x_1 \\ x_2 \\ \dot{x}_1 \\ \dot{x}_2 \end{Bmatrix} \qquad (6.14 \text{ a, b})$$

where $\boldsymbol{C}$ is a unity matrix. F_1 and F_2 are control forces at the motor and carriage. $\boldsymbol{A}$ and $\boldsymbol{B}$ are system matrices as follows.

$$A = \begin{bmatrix} 0 & I \\ -M^{-1}K & -M^{-1}C \end{bmatrix}$$

$$B = \begin{bmatrix} 0 \\ M^{-1} \end{bmatrix} \qquad (6.15\ a, b)$$

6.2.3. The framework of LPV modelling

As the carriage load is increased, the first resonance frequency of the BSD is decreased. Under certain circumstances, the preload applied to the BSD may vanish also. The ball bearing clearance plays a major role in this regard. If the clearance on the right-hand side ball bearing increases, there is a drastic change in the resonance frequency of the BSD as shown in Figure 6.3 (because now it is in the form of a fixed free bar instead of a fixed-fixed bar). As the carriage mass changes, the resonance frequency of the BSD also varies significantly.

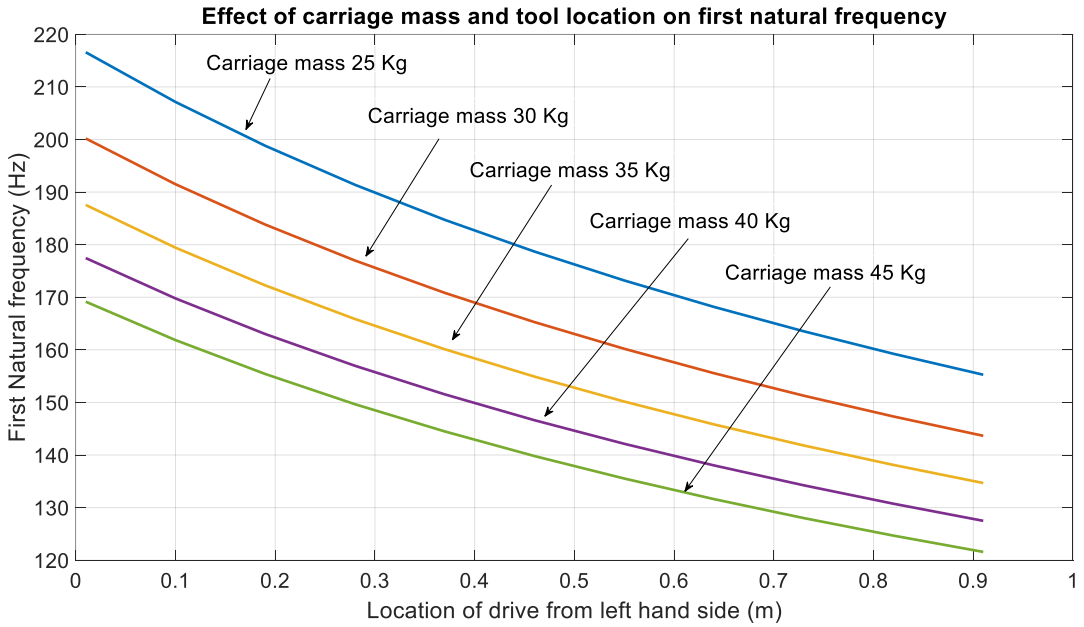

Figure 6.3 Effect of location and mass of the carriage on the first natural frequency (with bearing clearance)

Equation (6.6) shows the dynamic model of the BSD. Elements of the mass and stiffness matrix vary as a function of location and mass of the carriage. It is obvious that the dynamics of the overall system can be represented as an LPV system as follows.

$$\begin{Bmatrix} \dot{x}_1 \\ \dot{x}_2 \\ \ddot{x}_1 \\ \ddot{x}_2 \end{Bmatrix} = \boldsymbol{A}(m_{BSD}, l_{BSD}) \begin{Bmatrix} x_1 \\ x_2 \\ \dot{x}_1 \\ \dot{x}_2 \end{Bmatrix} + \boldsymbol{B}(m_{BSD}, l_{BSD}) \begin{Bmatrix} F_1 \\ F_2 \end{Bmatrix}$$
$$\begin{Bmatrix} x_1 \\ x_2 \\ \dot{x}_1 \\ \dot{x}_2 \end{Bmatrix} = \boldsymbol{C} \begin{Bmatrix} x_1 \\ x_2 \\ \dot{x}_1 \\ \dot{x}_2 \end{Bmatrix} \qquad (6.16 \text{ a, b})$$

where m_{BSD} and l_{BSD} are the mass and location of carriage from the left-hand side respectively, and $\boldsymbol{C}$ is a unity matrix. Matrices $\boldsymbol{A}(m_{BSD}, l_{BSD})$ and $\boldsymbol{B}(m_{BSD}, l_{BSD})$ are as follows.

$$\boldsymbol{A}(m_{BSD}, l_{BSD}) = \begin{bmatrix} \boldsymbol{0} & \boldsymbol{I} \\ -\boldsymbol{M}(m_{BSD}, l_{BSD})^{-1} \boldsymbol{K}(m_{BSD}, l_{BSD}) & -\boldsymbol{M}(m_{BSD}, l_{BSD})^{-1} \boldsymbol{C} \end{bmatrix}$$
$$\boldsymbol{B}(m_{BSD}, l_{BSD}) = \begin{bmatrix} \boldsymbol{0} \\ \boldsymbol{M}(m_{BSD}, l_{BSD})^{-1} \end{bmatrix} \qquad (6.17 \text{ a, b})$$

The next section shows that any fixed-gain controller cannot meet stability requirements for this LPV system. Hence, an LPV controller (in this case it is IGSLS controller) is designed and implemented to obtain robust stability and robust performance.

6.3. Design and Implementation of Hybrid Controller

There are different techniques for tracking the desired trajectory. Robust control, adaptive control and model-free control techniques can be used for desired trajectory tracking. In the next sub-sections, we will explain cascaded PPI controllers, fixed-gain loop shaping and IGSLS controllers.

6.3.1. Cascaded PPI controller

It is a model-free controller (not in the strict sense). Here P is the proportional controller and I is the integral controller. P controller is applied for the carriage position feedback. Combination of P and I controllers is applied for the motor speed feedback. The efficiency of PPI can be further

enhanced with a table/carriage velocity feedback. This idea has been implemented recently and is state of the art in case of model-free controllers. The main disadvantage of such a control system is that there is a need for additional sensors. Even then, these controllers are extensively used in the industry. These controllers are extremely robust. However, there is a limit to the performance of these model-free controllers. Model-based controllers are rich in terms of performance, but their robustness is limited in case of large plant/system parameter variations. Coefficient K_{p1} for the carriage position feedback is $12x10^6$. Coefficients K_{p2} and K_i for the motor velocity feedback are 34000 and 1000 respectively. The coefficients are determined by optimization in the frequency domain. Details have been omitted for the purpose of brevity.

6.3.2. Fixed gain loop shaping controller

Practical systems deviate considerably from the nominal model derived using system physics. There are uncertainties entering the nominal system. These uncertainties enter the nominal system in the form of additive perturbations, inverse additive perturbations, multiplicative uncertainties etc. Uncertainties may be structured (parametric) as well as unstructured (complex). To maximize the robust stability of a closed-loop system, one must minimize follows (Gu et al., 2005).

$$\gamma = \left\| \begin{bmatrix} \boldsymbol{K(I-GK)^{-1}M^{-1}} \\ \boldsymbol{(I-GK)^{-1}M^{-1}} \end{bmatrix} \right\|_{\infty} \tag{6.18}$$

Theoretical details for synthesizing the controller can be found in reference (Gu et al., 2005).

6.3.3. Hybrid Controller Design and Implementation

In the present analysis, the weight of the carriage is assumed to vary from 25 Kg to 45 Kg with grid points [25, 30, 35, 40, 45] Kg. The carriage travel length varies from 20 mm to 920 mm with grid points [20, 100, 200, 300, 400, 500, 600, 700, 800, 920] mm. Overall 5 *x* 10 =50 grid points are generated at which the Loop shaping controller is designed. The compensator with

transfer function $1x10^7 \frac{2s+1}{0.9s+0.1}$ is chosen for the low gain controller and $1x10^8 \frac{2s+1}{0.9s+0.1}$ is chosen for the high gain controller. For convenience, $1x10^8$ is termed as a loop shaping factor in the rest of the chapter. Now a general procedure is described for interpolation of the controller. Any linear parameter varying *(i.e. IGSLS)* system for interpolation can be represented as follows.

$$\boldsymbol{G}(\alpha) = \left[\begin{array}{c|c} \boldsymbol{A}(\alpha) & \boldsymbol{B}(\alpha) \\ \hline \boldsymbol{C}(\alpha) & \boldsymbol{D}(\alpha) \end{array}\right] \tag{6.19}$$

where $\boldsymbol{A}(\alpha)$, $\boldsymbol{B}(\alpha)$, $\boldsymbol{C}(\alpha)$ and $\boldsymbol{D}(\alpha)$ are system matrices. These matrices are parameterized using a homogeneous polynomial of degree g. Here α is taken as time-varying scheduling parameter. Details can be found in reference (Gu et al., 2005). The above algorithm is implemented in MATLAB/SIMULINK block LPV. The interpolating controller is implemented as shown in Figure 6.4. There are two scheduling parameters viz. the mass and location of the carriage. The carriage mass can be identified from the transient response of the system.

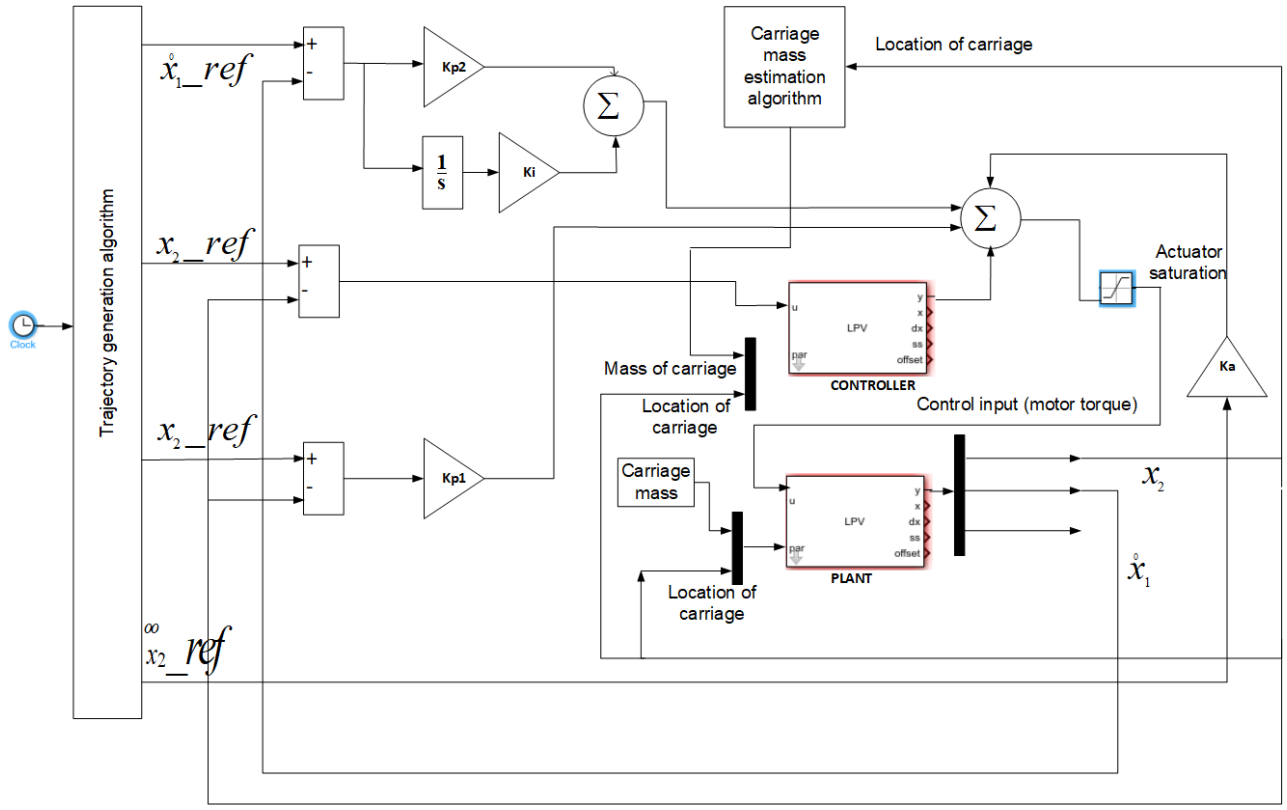

Figure 6.4 Simulink implementation of Hybrid controller

6.4. Experiment

A single-stage ball screw drive shown in Figure 6.5 is used. A home-made ball screw with 16 mm pitch and 950 mm length is used. Guideways are used to support the carriage. The servo motor is driven by a pulse width modulator amplifier. The carriage position is measured by a linear encoder with a resolution of 100 nm. An analog DC accelerometer (PCB 3711E1110G) with a bandwidth of 1000 Hz is attached to the carriage acceleration. In addition, a rotor encoder with resolution 0.001 degrees is used to measure the angle of rotation. A DSpace board DS-1103 is used to implement the controller. The stiffness of balls of the bearing and carriage nut is calculated using the process in reference (Gu et al., 2005)

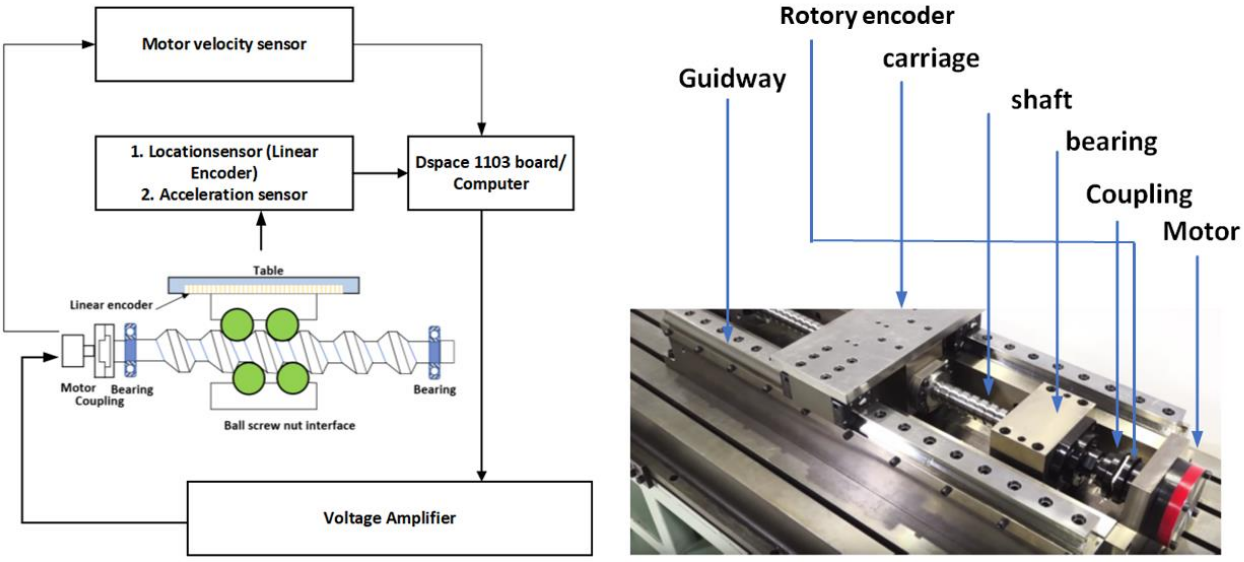

(a) Schematic of experimental setup *(b) Photograph of the setup*

Figure 6.5 Experimental setup for ball screw drive

6.5. Theoretical and experimental results

To verify the efficiency of the proposed control strategy, simulations, as well as experimentations, are conducted. The performance of the BSD system for various control techniques is discussed in the following sections.

6.5.1. Performance comparison of fixed gain loop shaping design procedure (LSDP) controller with Cascaded PPI controller

Frequency domain analysis plays a vital role in accessing the stability of any closed-loop system. The loop transfer function, Nyquist stability criteria, sensitivity function and cross-over frequency can be used to design controllers based on frequency-domain results. For a fair comparison between LSDP and PPI controllers, these controllers are tuned to possess similar stability margins. In the industry, this limit is normally held between 1.5-2. Figure 6.6 shows the sensitivity magnitude with different controllers. This figure is also used to represent the bandwidth of the overall system with a particular controller.

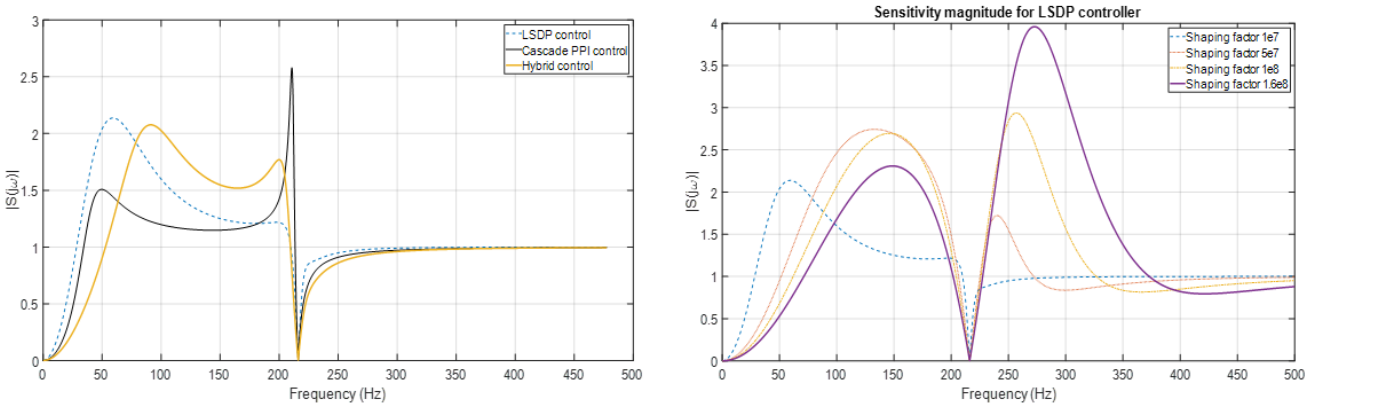

(a) Sensitivity function with different controllers (b) Sensitivity function with LSDP control different shaping factors

Figure 6.6 Loop sensitivity with different controllers

With the PPI controller, disturbances at the motor input can be effectively suppressed from 0-40 Hz and >220 Hz. The LSDP controller can suppress input disturbances from 0-35 Hz and >220 Hz. However, with the hybrid controller, the limit is increased up to 0-55 Hz and >220 Hz (Figure 6.6 a). This means the hybrid controller has more overall bandwidth than the other counterparts.

However, disturbances at input get amplified above 230 Hz if the shaping factor is increased above $1x10^7$ (Figure 6.6b). It can reduce input disturbances above 375 Hz only (this limit varies based on shaping factor used). Although by increasing the shaping factor above $1x10^7$, its bandwidth increases for lower frequencies i.e. 0-70 Hz only, disturbances at input get amplified in the range 240-375 Hz. It can reduce or mitigate input disturbances above 375 Hz only. Hence, controller gains cannot be increased beyond a certain limit.

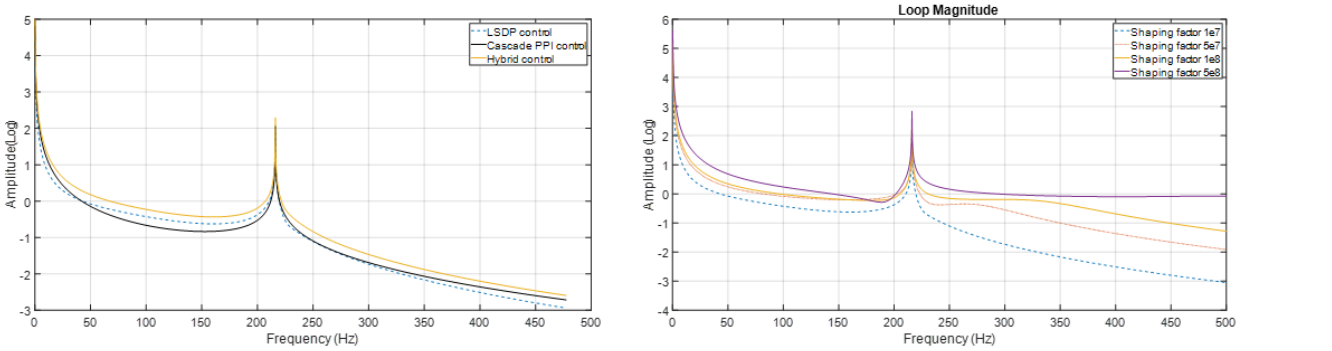

(a) Loop magnitude with different controllers (b) Loop magnitude with LSDP controller with different shape factors

Figure 6.7 Loop magnitude with different controllers and loop shaping factor

The loop transfer function for the PPI controlled system is given by:

$$L = \frac{K_{p2}s + K_i}{s}\left(G_{11}(s)s + G_{21}(s)K_{p1}\right) \tag{6.20}$$

Based on the loop magnitude results shown in Figure 6.7a, it is clear that the tracking ability of LSDP is better than PPI controller due to higher low-frequency gains. The cross-over frequencies are the same (40 Hz-230 Hz). This means the controllers can actively damp the axial vibrations of the BSD in the same range. The hybrid controller has high crossover frequencies i.e. 75 Hz-230 Hz as well as high gains of the low frequency.

There is a limit to the performance of PPI controlled systems (even after controller parameter optimization). But this limit can be extended in case of the LSDP controlled system by increasing the loop shaping factor (Figure 6.7b). However, additional problems are developed by increasing the shaping factor as will be seen shortly during a metal cutting operation, i.e. when the dynamic cutting forces are applied at the table/carriage as shown in Figure 6.9.

One thing worth mentioning here is that as the carriage is moving away from the motor, the axial resonance frequency of the BSD decreases. The PPI controller is robust in terms of the closed-loop stability for a large range of parameters. However, LSDP is less robust in terms of

closed-loop stability. The stability of the LSDP controller is also dependent on the loop shaping factor. For higher loop shaping factor values, the LSDP controller is less stable (in terms of the frequency range where input disturbances get mitigated) (Figure 6.7b).

The open-loop transfer function from table disturbances d_2 to carriage position x_2 is given by transfer function G_{23} (s). The closed-loop disturbance transfer function for the system with the PPI controller is given as follows.

$$G_{d_2 \to x_2} = \frac{G_{23} + \left(K_{p_2} s + K_i\right)\left(G_{11}G_{23} - G_{13}G_{21}\right)}{1 + L} \tag{6.21}$$

The hybrid controller is best in achieving lower level amplitude of vibrations for the external disturbances acting at the carriage (normally the cutting forces). For the time domain command tracking performance of different controllers, Part a of Figure 6.8 shows the reference trajectory to be achieved. From this figure, it is obvious that there is an abrupt start. This type of trajectory is intentionally chosen to quantify the effectiveness of the different control algorithms for non-smooth trajectories. With the PPI controller, there is a less transient error at the start. The movement of the carriage is 150 mm from the start (from the motor end). Hence there is very less change in system parameters up to this carriage movement. Although model base controllers are high in performance for the robust stability, parameters of the system should remain within a tolerable limit. For example, the mass of the carriage varies based on the mass of the workpiece mounted on it. As discussed earlier, the dynamics of the system depends on the location of the carriage also. Based on these factors, it is a general practice in the industry to use model-free controllers like cascaded PPI controllers that are robustly stable for very large values of carriage/table mass and location. To compare the performance of the model-free controllers with model-based controllers, the trajectory is designed in such a way that the carriage remains near the

motor side (maximum amplitude 150 mm). In this way, the effect of change of dynamics with the carriage location is minimized.

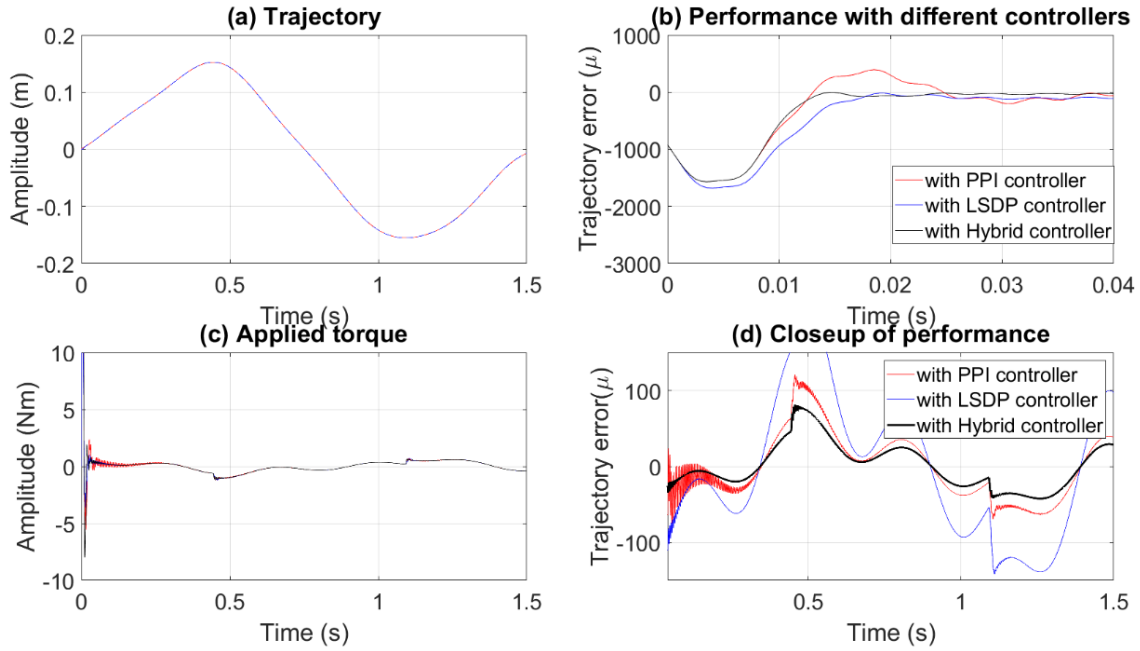

Figure 6.8 Time domain analysis for command tracking with different controllers (Simulation results)

The maximum error between the reference and achieved trajectory is 115 microns (after initial transient errors are over) with the PPI controller. With the low gain LSDP (if used alone), the error is much more. However, with the hybrid controller, the error is 73 microns (Figure 6.8). By using a high gain LSDP controller, the trajectory error further reduces to a small value. But, as discussed earlier, higher controller gains are not suitable when BSD is undergoing the metal cutting process.

In the above figures, the efficiency of the controllers is tested in the absence of metal cutting forces (i.e. rapid movement of the BSD). For testing the efficiency of the controller during the metal cutting process, a milling process was performed. A milling cutter of diameter 19.04 mm was used for metal cutting. The spinning speed of the milling tool was fixed at 2150 r.p.m. The milling tool has only one tooth to avoid the problem of runout. The feed rate of the BSD was fixed at 3.58 mm/s. The tooth pass frequency of 2150/60=35.8 Hz was realized during experimentation.

Multiple harmonics that are integer multiple of tooth pass frequency are present in the spectrum. Figure 6.9 shows the performance of various controllers. Parts a, b and c represent the table position error, motor velocity and torque applied at the motor respectively with low gain LSDP controller (with shaping factor $1x10^7$). The performance of the LSDP controller and cascaded PPI controller is almost the same in terms of table position error, motor velocity variation and applied torque (Parts d, e and f). With the hybrid controller, the table position error is relatively low and motor velocity variation is minimum (Parts g, h and i). The table position error was also a minimum.

Parts j, k and l (Figure 6.9) show that if a high gain LSDP controller is used (with shaping factor $1x10^8$), the table position error is maximum, motor velocity variation is maximum as well as applied torque amplitude varies between extreme limits. The torque amplitude variation is 4 times as compared to the low gain LSDP controller (with shaping factor $1x10^7$).

The variation is harmful to the motor life. The energy efficiency also decreases with an increase in torque amplitude variation. Hence, there is a limit for increasing the shaping factor (in other words the controller gains). It is obvious that to increase the overall efficiency (i.e. BSD motion during metal cutting and rapid movements), a combination of cascade PPI and low gain LSDP is the best alternative.

Afterwards, to check the robustness of PPI and LSDP controllers in the time domain, both controllers are applied to the BSD when the starting point of the reference trajectory is 350 mm from the start (i.e. motor side). The PPI controller maintains closed-loop stability under the changing dynamics. However, The LSDP controller becomes unstable. There is the continuous chattering of the carriage around some nominal points. The magnitude of chattering depends upon

the saturation limit of the motor. Here the need of the IGSLS controller arises i.e. the system should remain stable for the large variation in system parameters.

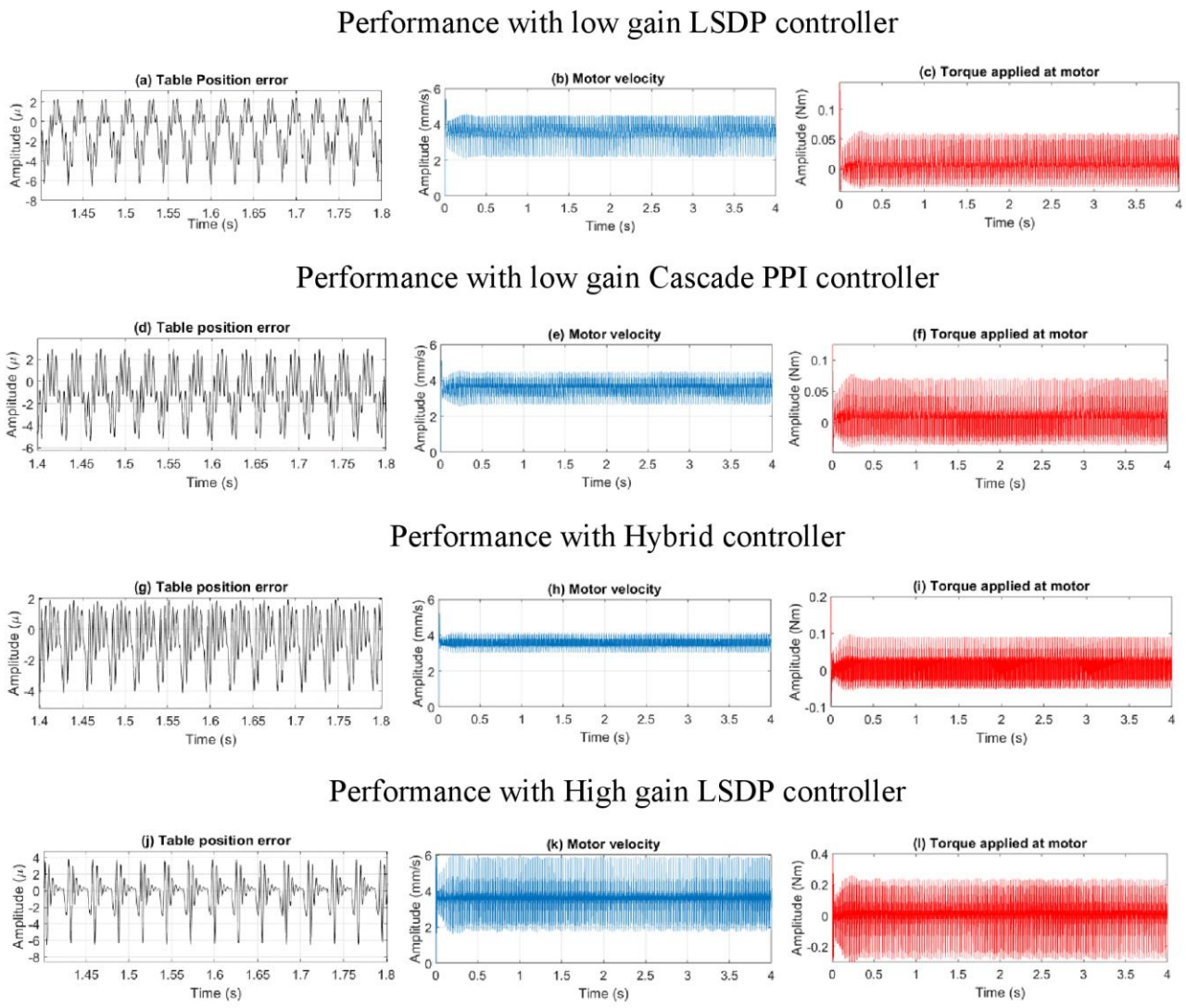

Figure 6.9 Performance of various controllers during metal cutting (Experimental results)

6.5.2. Comparison of fixed gain LSDP controller with IGSLS controller

It is obvious that as gains of the controller are increased (i.e. using a high loop shaping factor), the stability margins of the closed-loop system for the total range of system parameters are

decreased. However, the system performance improves with gains of the controller (for rapid movement of BSD). The stability of the closed-loop system also depends on various other factors. These factors include the unmodelled dynamics, accuracy with which the system parameters are modelled and the actuator nonlinearities. Depending on the accuracy limit of the carriage/table mass estimation, the loop shaping factor plays an important role. In the present work, $1x10^7 \frac{2s+1}{0.9s+0.1}$ is fixed as the loop shaping factor for the controller design. The closed-loop stability is retained even if the carriage mass is estimated as 30 Kg instead of 25 Kg (i.e. exact value).

In the next simulation, the carriage or table is moved from the extreme left to extreme right (l=920 mm). To prevent sudden acceleration, the desired trajectory was filtered out by curve fitting. The curve fitting was done by 7^{th} order sinusoidal such the displacement as a function of time. Figure 6.10 shows the performance of different controllers. The carriage mass of 25 Kg was taken for the analysis. The PPI controller is stable for the total travel of the carriage. However, the performance is not satisfactory as a large difference between reference and obtained trajectory. With the PPI controller, the maximum trajectory error is 66 microns (after the transients are over for 0-0.08 seconds). With the IGSLS controller (if used alone), the error is high and with the hybrid controller, the error is 43 microns, i.e. 54% increase in the command tracking efficiency.

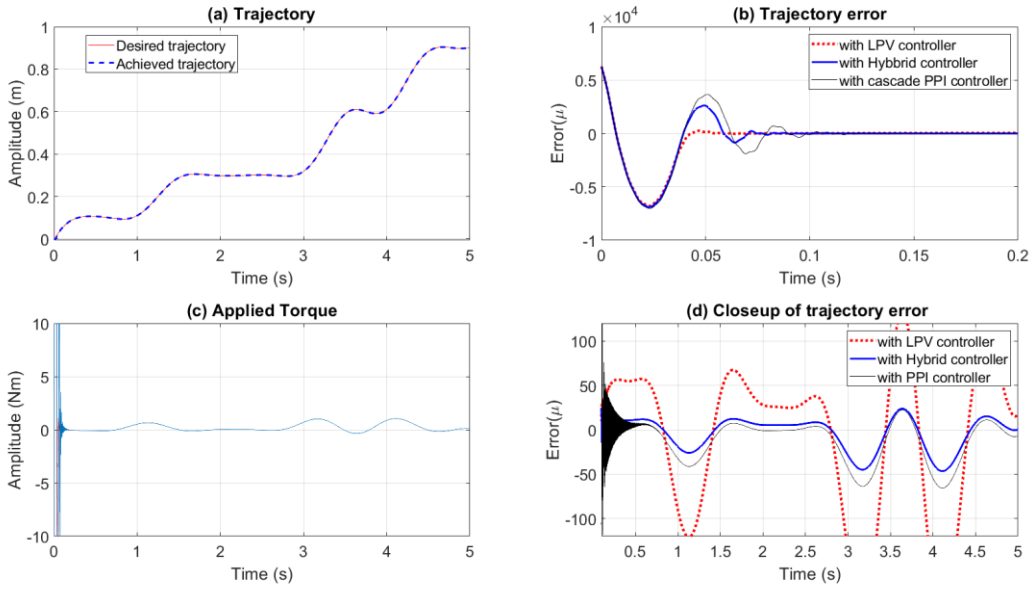

Figure 6.10 Comparison of performance with LPV and other controllers (Simulation results)

6.6. Concluding remarks

Based on time and frequency domain results following conclusions can be drawn.

- Robust stability of LSDP controllers cannot be maintained for a large variation of system parameters.
- Cascaded PPI controllers are robustly stable; however, their command tracking performance is limited, and bandwidth is smaller than high gain LSDP controllers.
- High gain LSDP controllers cause large variations in the motor velocity and torque applied at the motor. This factor reduces the useful life of the motor and enhances energy losses at the motor. Hence controller gains cannot be increased arbitrarily. The only option left to increase the command tracking performance (during rapid movement of BSD) and decrease torque variation (during metal cutting operation) is to use hybrid controllers. Command tracking performance of the hybrid controller made by joining PPI and LSDP controllers in parallel is much better than the case when they are used individually.

- The bandwidth and performance (during rapid movement and metal cutting) of the hybrid controller is much higher than PPI and LSDP controllers (if used alone).
- Using interpolation-based IGSLS controllers, the closed-loop stability and performance can be maintained for the complete range of parameters. The performance and bandwidth are further enhanced by connecting the PPI controller in parallel with the IGSLS controller (i.e. using a hybrid controller).

Chapter 7

Active chatter control of turning operations

7.1. Overview

The stability requirement in turning operations limits the cutting depth. The common trend is to generate stability lobe diagrams to avoid chatter regions. However, flexibility of shaft results in the low material removal rate due to the limited stable depth of cut. Normally the workpiece is considered rigid and active chatter control techniques are applied to reduce vibrations of flexible cutting tools. In this work, both the workpiece and cutting tool are considered flexible in appropriate directions. The novelty of the work is the combination of theory and practical applications. As the material is removed during cutting, natural frequencies of the shaft are changed. Fixed parameter controllers lose their effectiveness under these changing conditions. Linear Parameter Varying controller is designed and implemented so that the cutting stability can be maintained in the total range of parameters. Due to the non-contact nature of electromagnetic actuators, control forces can be applied from a distance and hence stability can be maintained. Theoretical solutions are investigated for the feasibility of the control process through simulations. The results are verified experimentally. The productivity is improved as the cutting depth is increased from 72 microns to 250 microns in a case study.

7.2. Active chatter control using an electromagnetic actuator

7.2.1. Schematic for active chatter control

For active chatter controls, additional damping has to be provided to the system. In the active control nomenclature, this is called electronic damping. An electromagnetic actuator (EA) is used for applying control forces. Figure 7.1 shows a general case for the flexible shaft processed by a

lathe machine. The EA is installed on the tool post of the lathe machine along with the cutting tool. An eddy current probe which acts as the sensor is also applied near the actuator for a collocated sensor/actuator system. Figure 7.2 shows a schematic of the overall system.

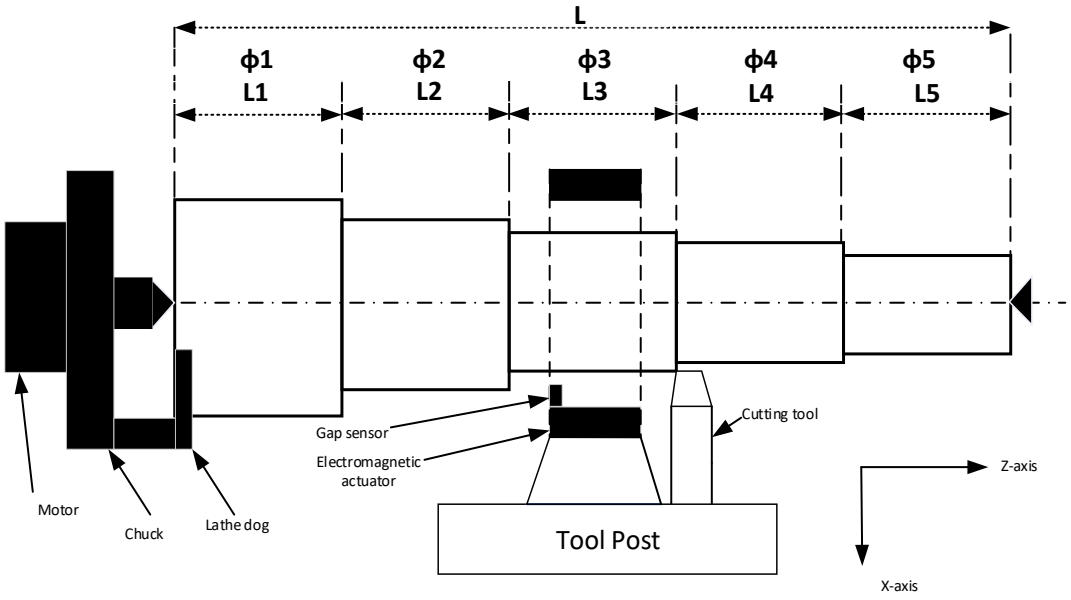

Figure 7.1 Active chatter control architecture for flexible stepped shaft

7.2.2. Dynamics of the electromagnetic actuator

In the case of an EA, control forces are related to the actuator current as follows (Vashisht et al., 2019d).

$$F_{EA} = k\left[\frac{(i+i_0)^2}{(\Delta - x)^2} - \frac{(i-i_0)^2}{(\Delta + x)^2}\right] \tag{7.1}$$

where Δ represents the gap between the shaft and EA in the equilibrium position, x is the distance between the core of the EA and flexible shaft. The instantaneous current is represented as i and the bias current is represented by i_0. The constant k is given as follows.

$$k = \frac{1}{4}\mu_0 n^2 A \tag{7.2}$$

In the above relation μ_0 is the permeability of the air, n is the number of winding turns and A is the area of the shoe on which winding is attached. Table 7.1 shows the properties of the EA.

Table 7.1 Physical Parameters of Electromagnetic actuator used

No.	Parameter	Notation	Value
1	Permeability of air	μ_0	1.256×10^{-6} N/A^2
2	Area of iron core	A	20 mm x 10mm
3	Number of winding turns	n	500
4	Nominal air gap	Δ	3 mm
5	Bias current	i_0	3 A

Electric resistance R and inductance L can be measured for the circuit. The voltage applied v to the EA bears the following relation with the current i.

$$v = R\, i + L \frac{di}{dt} \tag{7.3}$$

The control voltage generated from the computer can be stepped up using the voltage amplifier so that high voltage and hence the high current can be applied for generation of control forces.

7.2.3. Schematic of the experiment

The experimental setup contains the following hardware components (Figure 7.2). The detail of the components is introduced in Chapter 5.

The force generated by the electromagnetic actuator depends on the applied current as well as gap between the shaft and actuator. To approximate this nonlinear phenomenon (i.e. the relation between applied current and the generated force), artificial neural networks (ANN) are used. The input layer of the ANN contains 2 neurons, the output layer contains one neuron and the hidden layer contains 20 neurons. After training, the ANN is used as a Simulink block.

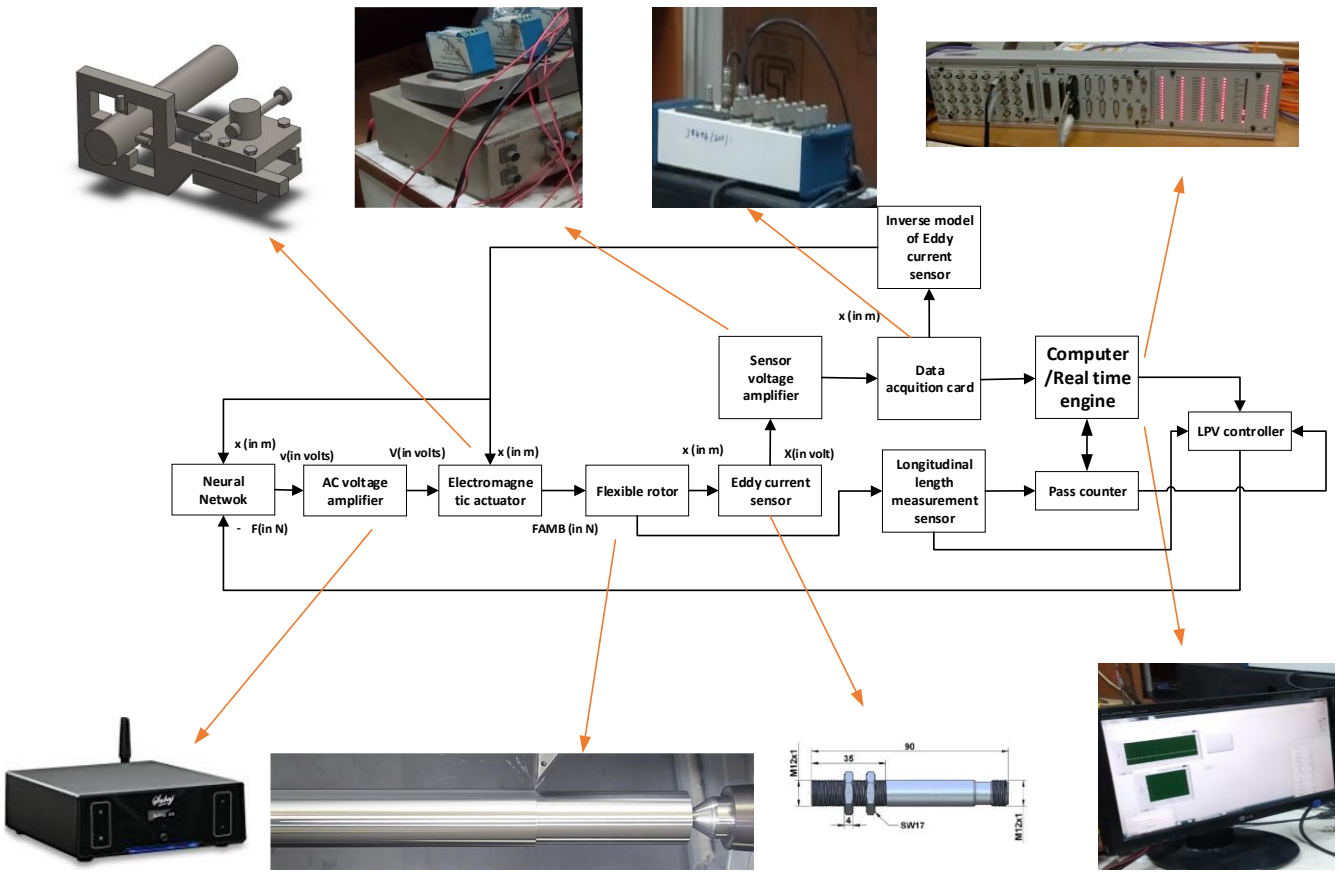

Figure 7.2 Schematic of the overall control system for turning operation

7.3. Dynamic modelling for turning of the stepped shaft

7.3.1. Structural dynamics of the stepped shaft

Let F_x, F_y and F_z are forces acting in x, y and z axes, respectively on the cutting tool, displacements caused by these forces are given as follows (in Laplace domain).

$$\begin{bmatrix} x(s) \\ y(s) \\ z(s) \end{bmatrix} = \begin{bmatrix} \phi_{xx}(s) & \phi_{xy}(s) & \phi_{xz}(s) \\ \phi_{yx}(s) & \phi_{yy}(s) & \phi_{yz}(s) \\ \phi_{zx}(s) & \phi_{zy}(s) & \phi_{zz}(s) \end{bmatrix} \begin{bmatrix} F_x(s) \\ F_y(s) \\ F_z(s) \end{bmatrix} \tag{7.4}$$

where $\phi_{xx}(s)$ is the transfer function of the structural system from input $F_x(s)$ to output x(s). It is expressed as $\phi_{xx}(s) = \sum_{i=1}^{m} \frac{\Psi_{ai}\Psi_{si}}{s^2 + 2\xi_i\omega_i s + \omega_i^2}$, where m are the number of modes considered, Ψ_{ai} is the mode shape at the actuator location, Ψ_{si} is the mode shape at the sensor location, ξ_i and ω_i are damping ratio and natural frequency for the i^{th} mode considered. Similarly, the transfer function in other directions can be formulated. Forces F_x, F_y *and* F_z also act on the workpiece. If the workpiece is flexible, the corresponding deflections will be experienced by the workpiece. In this work, it is assumed that the cutting tool has enough rigidity along x-axis and y-axis (see Figure 7.1). The movement of the cutting tool is possible only along the z-axis. However, the shaft is considered flexible with the shaft movement along x-axis and y-axis due to limited rigidity. The finite element method is used to determine dynamic equations of motion of the flexible shaft as below.

$$\mathbf{M}\,\ddot{\mathbf{z}}(t) + \mathbf{C}\,\dot{\mathbf{z}}(t) + \mathbf{K}\,\mathbf{z}(t) = \mathbf{f}(t) \qquad (7.5)$$

where $\mathbf{f}(t)$ is the applied nodal force and $\mathbf{z}(t)$ is the nodal displacement vector. **M, C** and **K** are global mass, damping and stiffness matrix of the flexible shaft respectively. Using the modal analysis, natural frequencies and modes of the flexible shaft can be determined. Initial dimensions of the stepped shaft are given in Table 7.2.

Table 7.2 Parameters of the flexible shaft

Parameter	Value	Parameter	Value
ϕ_1	35 mm	L_1	100 mm
ϕ_2	30 mm	L_2	100 mm
ϕ_3	25 mm	L_3	100 mm
ϕ_4	20 mm	L_4	100 mm
ϕ_5	15 mm	L_5	100 mm

The desired diametral dimensions after machining are [30 25 20 15 15] mm. Figure 7.3 shows the first mode shape of the flexible stepped shaft. As the tool moves from one cutting location to the other, natural frequencies of the flexible shaft change due to subsequent material removal. At the same time, the whole material cannot be cut in a single pass. At each pass, some material is cut and the systems natural frequencies change. If 0.25 mm material is cut in a single pass, the final dimensions are reached after 10 passes.

Figure 7.4 shows natural frequencies as a function of the tool location and number of tool passes. To generate this figure, the cut depth is assumed as 1 mm.

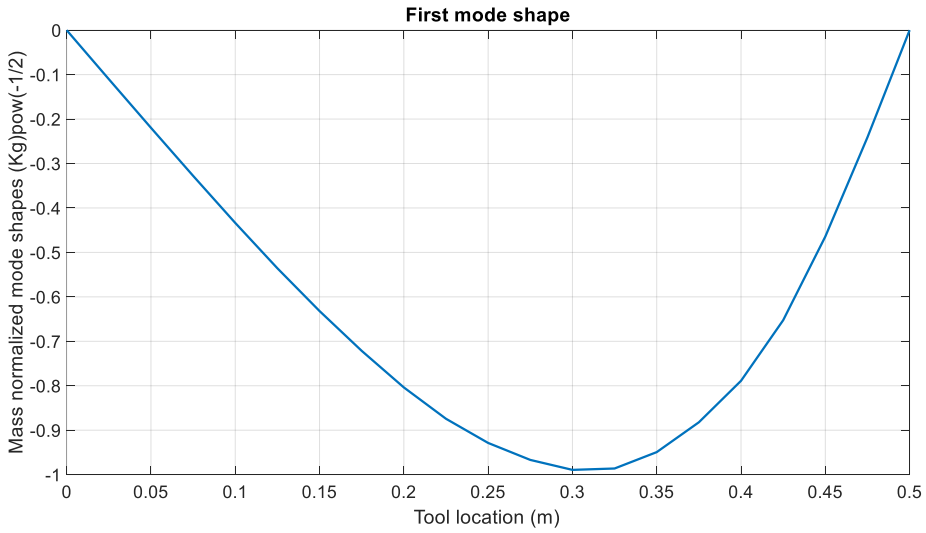

Figure 7.3 Mode shapes of flexible stepped shaft

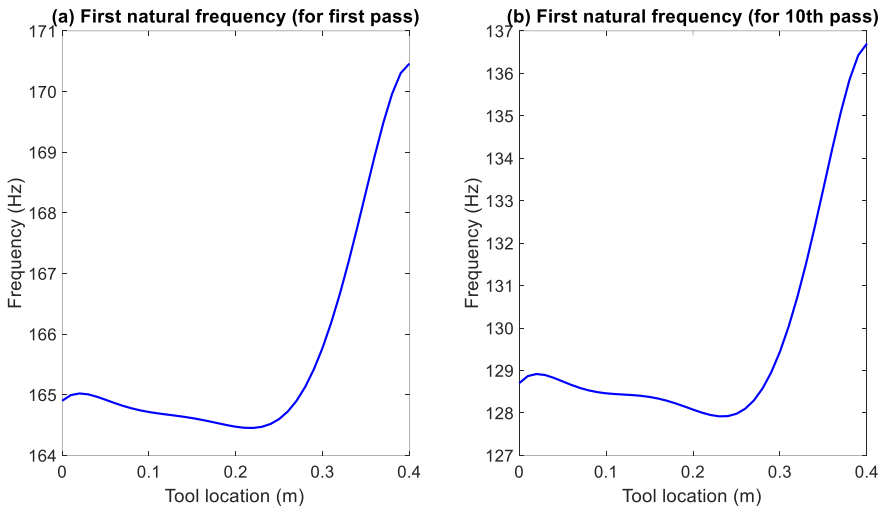

Figure 7.4 Natural frequencies of the flexible stepped shaft as a function of tool location and pass number

7.3.2. Location dependent stiffness of the stepped shaft

From the configuration of the stepped shaft, it is obvious that the shaft stiffness is location-specific. It is minimum near the centre. Hence the critical depth of cut is minimum near the centre as shown in Figure 7.5. The critical depth of cut ranges from 70 to 370 microns. Hence, we cannot design a single controller for the whole range of parameters.

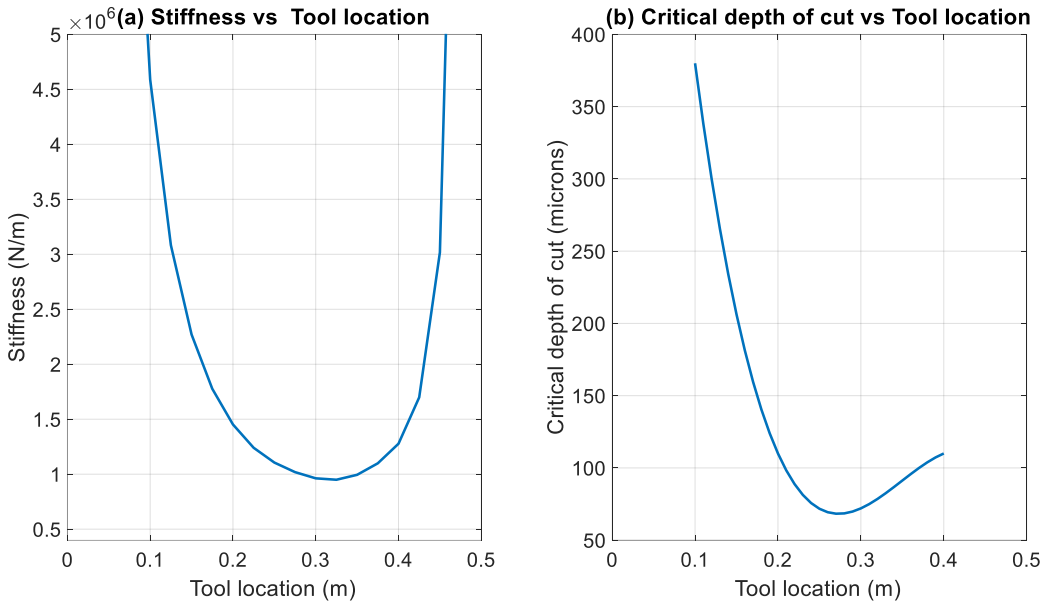

Figure 7.5 Stiffness and critical depth of cut as a function of tool location for the stepped flexible shaft

7.3.3. Nomenclature for the cutting system

To design a controller based on parameters of the system, dynamics of the cutting process need to be understood. For the turning of the flexible shaft, a single point cutting tool is used. The nomenclature of the tool is discussed as follows.

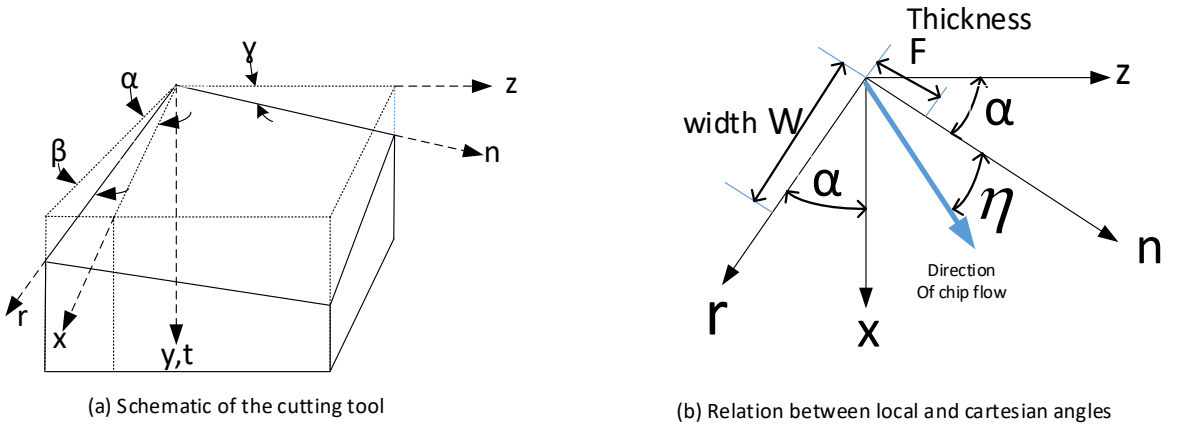

(a) Schematic of the cutting tool

(b) Relation between local and cartesian angles

Figure 7.6 Nomenclature and schematic of the cutting tool

Figure 7.6 (a) shows the general schematic of a cutting tool with various angles. There are two types of coordinate axis viz. global (i.e. x, y and z-axis) and local (r, n and t). The tool geometry can be represented using certain angles of the tool. These angles include the approach angle(α), inclination angle (β) and normal rake angle (γ). The depth of cut (W) and thickness of the chip (F) are also shown along the local coordinate axis. The feed rate per revolution (f_0) is along the negative z-axis. The actual width or depth of cut (b) is along the x-axis. The chip flows on the plane (r-n) in an angle (η) with the local n-axis. It is called the chip flow angle. The force acting along local coordinate axes (r, n and t) can be calculated accordingly.

7.3.4. Regenerative chip model along with cutting forces

It is obvious that the tool moves along the z-axis at a certain angle. The chip thickness (F) and width of cut (W) are the major parameters. Cutting forces along the local coordinate system are given by the following linear relationship.

$$[F_n(t) \quad F_r(t) \quad F_t(t)] = [K_n \quad K_r \quad K_t]\, W\, F \tag{7.6}$$

K_n , K_r and K_t are stiffness coefficients of the workpiece along the respective local coordinate system. The relation of W and F with other parameters is given by Figure 7.6 (b).

$$F = f_0 \cos(\alpha) - \left((z(t) \cos(\alpha) + x(t) \sin(\alpha)) - (z(t-T) \cos(\alpha) + x(t - T) \sin(\alpha)) \right) \tag{7.7}$$

$$W = b \cos(\alpha) \tag{7.8}$$

where $z(t)$ and $x(t)$ are the displacement of the tool at the instant of time (t) along z-axis and x-axis respectively. $z(t-T)$ and $x(t-T)$ are displacements of the tool in one revolution before i.e. delayed by time interval T. T is the time required to complete one revolution. The physical depth of cut (b) along the x-axis plays a major role.

In turning, the workpiece rotates at a certain spinning speed. Forces acting along the global coordinates are related to local coordinates by following relations.

$$\begin{bmatrix} F_z(t) \\ F_x(t) \\ F_y(t) \end{bmatrix} = \begin{bmatrix} \cos(\alpha) & 0 & \sin(\alpha) \\ 0 & 1 & 0 \\ -\sin(\alpha) & 0 & \cos(\alpha) \end{bmatrix} \begin{bmatrix} \cos(\beta) & -\sin(\beta) & 0 \\ \sin(\beta) & \cos(\beta) & 0 \\ 0 & 0 & 1 \end{bmatrix} \begin{bmatrix} 1 & 0 & 0 \\ 0 & \cos(\gamma) & \sin(\gamma) \\ 0 & -\sin(\gamma) & \cos(\gamma) \end{bmatrix} \begin{bmatrix} F_n(t) \\ F_r(t) \\ F_t(t) \end{bmatrix} \tag{7.9}$$

$$\begin{bmatrix} F_z(t) \\ F_x(t) \\ F_y(t) \end{bmatrix} = \begin{bmatrix} a_{11} & a_{12} & a_{13} \\ a_{21} & a_{22} & a_{23} \\ a_{31} & a_{32} & a_{33} \end{bmatrix} \begin{bmatrix} F_n(t) \\ F_r(t) \\ F_t(t) \end{bmatrix} \tag{7.10}$$

Let K_n, K_r and K_t be the stiffnesses of the workpiece along the local axes n, r, and t. Following relations are valid for connecting forces with material parameters.

$$F_n(t) = K_n F W \tag{7.11}$$

$$F_r(t) = K_r F W \tag{7.12}$$

$$F_t(t) = K_t F W \tag{7.13}$$

Putting the value of forces in the local coordinate system, we get:

$$F_n(t) = K_n \begin{pmatrix} b f_0 \cos^2(\alpha) + b \sin(\alpha) \cos(\alpha) x(t-T) + b \cos^2(\alpha) z(t-T) \\ -b \sin(\alpha) \cos(\alpha) x(t) - b \cos^2(\alpha) z(t) \end{pmatrix} \tag{7.14}$$

$$F_r(t)=K_r\begin{pmatrix} b\ f_0\ \cos^2(\alpha)+b\ \sin(\alpha)\cos(\alpha)x(t-T)+b\cos^2(\alpha)z(t-T) \\ -b\sin(\alpha)\cos(\alpha)x(t)-b\cos^2(\alpha)z(t)\end{pmatrix} \quad (7.15)$$

$$F_t(t)=K_t\begin{pmatrix} b\ f_0\ \cos^2(\alpha)+b\ \sin(\alpha)\cos(\alpha)x(t-T)+b\cos^2(\alpha)z(t-T) \\ -b\sin(\alpha)\cos(\alpha)x(t)-b\cos^2(\alpha)z(t)\end{pmatrix} \quad (7.16)$$

Putting the results in Equation (7.10), the global forces are given by:

$$F_z(t)=b\ f_0\ X_1\cos^2(\alpha)-b\ X_1 z(t)\cos^2(\alpha)+bX_1 z(t-T)\cos^2(\alpha)-b\ \sin(\alpha)X_1 x(t)\cos(\alpha) +b\ \sin(\alpha)X_1 x(t-T)\cos(\alpha) \quad (7.17)$$

$$F_x(t)=b\ f_0\ X_2\cos^2(\alpha)-b\ X_2 z(t)\cos^2(\alpha)+bX_2 z(t-T)\cos^2(\alpha)-b\ \sin(\alpha)X_2 x(t)\cos(\alpha) +b\ \sin(\alpha)X_2 x(t-T)\cos(\alpha) \quad (7.18)$$

$$F_y(t)=b\ f_0\ X_3\cos^2(\alpha)-b\ X_3 z(t)\cos^2(\alpha)+bX_3 z(t-T)\cos^2(\alpha)-b\ \sin(\alpha)X_3 x(t)\cos(\alpha) +b\ \sin(\alpha)X_3 x(t-T)\cos(\alpha) \quad (7.19)$$

Where,

$$X_1=\left(a_{11}K_n+a_{12}K_r+a_{13}K_t\right)$$
$$X_2=\left(a_{21}K_n+a_{22}K_r+a_{23}K_t\right)$$
$$X_3=\left(a_{31}K_n+a_{32}K_r+a_{33}K_t\right)$$

After simplifying,

$$F_z(t)=b\left(f_0\ g_{21}-\ z(t)\ g_{21}+\ z(t\text{-}T)\ g_{21}-\ g_{23}\ x(t)+g_{23}\ x(t\text{-}T)\right) \quad (7.20)$$

$$F_x(t)=b\left(f_0\ g_{41}-\ z(t)\ g_{41}+\ z(t\text{-}T)\ g_{41}-\ g_{43}\ x(t)+g_{43}\ x(t\text{-}T)\right) \quad (7.21)$$

$$F_y(t)=b\left(f_0\ g_{61}-\ z(t)\ g_{61}+\ z(t\text{-}T)\ g_{61}-\ g_{63}\ x(t)+g_{63}\ x(t\text{-}T)\right) \quad (7.22)$$

Where,

$$g_{21}=X_1\cos^2(\alpha),\qquad g_{41}=X_2\cos^2(\alpha),\qquad g_{61}=X_3\cos^2(\alpha)$$
$$g_{23}=X_1\sin(\alpha)\cos(\alpha),\qquad g_{43}=X_2\sin(\alpha)\cos(\alpha),\qquad g_{63}=X_3\sin(\alpha)\cos(\alpha)$$

Using these forces, the dynamics of the cutting system can be formulated.

7.3.5. Open-loop stability analysis

It is obvious from Figure 7.6 that forces in x-direction and z-direction are coupled. The workpiece material is considered as steel with K_m, K_r and K_t of 544×10^6 N/m^2, 124×10^6 N/m^2 and 2881×10^6 N/m^2, respectively (Eynian and Altintas, 2009). Values of tool angles α, β and γ are taken as 30^0 each. Values of m, c and k for the cutting tool is taken as 50 Kg, 2000 Ns/m and 2×10^7 N/m respectively (Meng et al., 2017). Using Equations (7.5) and (7.20-7.22), the total dynamics of the system can be represented in a state-space form with delay terms as follows.

$$\dot{\mathbf{X}}(t)=\mathbf{A}\,\mathbf{X}(t) + \mathbf{A}_d\,\mathbf{X}(t-T) + \mathbf{B}\,\mathbf{u}(t) \tag{7.23}$$

where,

$$\boldsymbol{A}=\begin{bmatrix} 0 & 1 & 0 & 0 & 0 & 0 \\ -\left(\frac{k}{m}\right)-\left(b\frac{g_{21}}{m}\right) & -\left(\frac{c}{m}\right) & -\left(\frac{bg_{23}\phi_1}{m}\right) & 0 & 0 & 0 \\ 0 & 0 & 0 & 1 & 0 & 0 \\ -bg_{41}\phi_1 & 0 & -\omega_x^2-bg_{43}\phi_1^2 & -2\xi\omega_x & 0 & 0 \\ 0 & 0 & 0 & 0 & 0 & 1 \\ -bg_{61}\phi_1 & -bg_{63}\phi_1^2 & 0 & 0 & -\omega_y^2 & -2\xi\omega_y \end{bmatrix}$$

$$\boldsymbol{A_d}=\begin{bmatrix} 0 & 0 & 0 & 0 & 0 & 0 \\ \left(b\frac{g_{21}}{m}\right) & 0 & \left(\frac{bg_{23}\phi_1}{m}\right) & 0 & 0 & 0 \\ 0 & 0 & 0 & 0 & 0 & 0 \\ bg_{41}\phi_1 & 0 & bg_{43}\phi_1^2 & 0 & 0 & 0 \\ 0 & 0 & 0 & 0 & 0 & 0 \\ bg_{61}\phi_1 & 0 & bg_{63}\phi_1^2 & 0 & 0 & 0 \end{bmatrix}, \quad \boldsymbol{B}=\begin{bmatrix} 0 \\ 0 \\ 0 \\ \phi_2 \\ 0 \\ 0 \end{bmatrix}$$

$$\boldsymbol{X}(t)=\begin{bmatrix} z(t) & \dot{z}(t) & q_x(t) & \dot{q}_x(t) & q_y(t) & \dot{q}_y(t) \end{bmatrix}^T$$

$$\boldsymbol{X}(t-T)=\begin{bmatrix} z(t-T) & \dot{z}(t-T) & q_x(t-T) & \dot{q}_x(t-T) & q_y(t-T) & \dot{q}_y(t-T) \end{bmatrix}^T$$

where q's are modal displacements and $\dot{q}$'s are modal velocities, ϕ_1 is the mode shape value at the tool location. Matrix **B** is composed of mode shapes where the actuator is located. ϕ_2 is the mode shape value at the EA location. By using Equation (7.23), the stability lobe diagrams can be generated. Pseudo-Spectral methods are used to generate these diagrams. Figure 7.7 shows the stability boundary from 400-2400 rpm at different tool locations. Different flexibility of the workpiece at different locations plays a major role in terms of critical depth of cut.

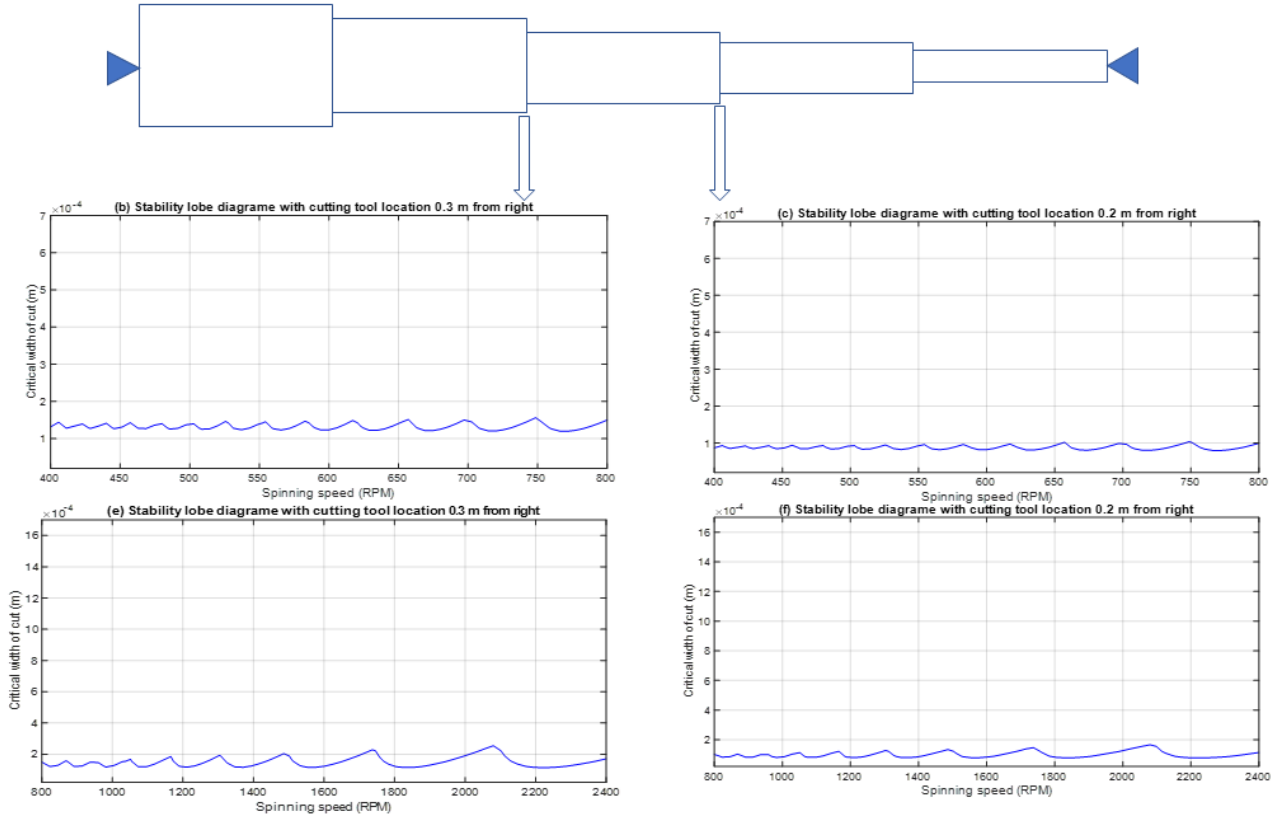

Figure 7.7 Stability lobe diagram as a function of tool location

7.3.6. Linear parameter varying system-based representation of the stepped shaft

From Figure 7.4 it is obvious that the natural frequency of the flexible shaft is a function of both the tool location and number of passes of the cutting tool. Figure 7.8 shows this dependency. Let q_1 and q_2 represent tool pass and tool location parameters respectively.

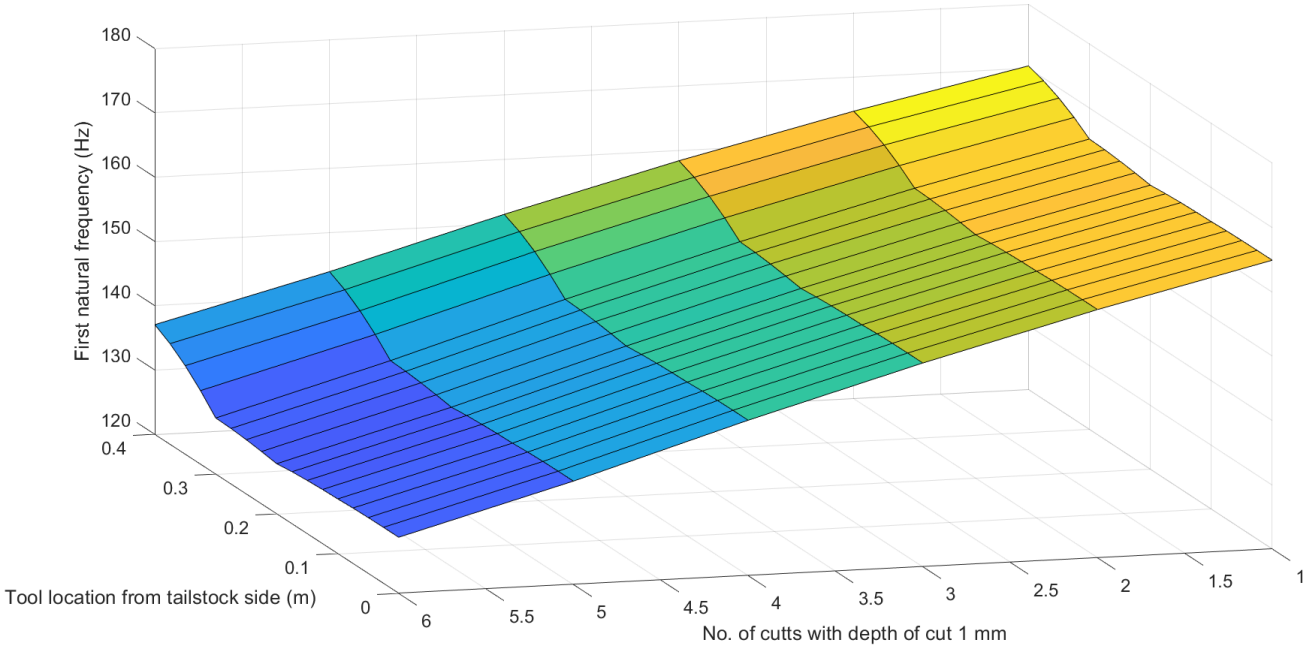

Figure 7.8 First natural frequency as a function of the number of cutting passes and tool location

Dynamics of an open-loop system can be written in the following form.

$$\begin{aligned} \dot{\mathbf{X}}(t) &= \mathbf{A}(q_1, q_2)\mathbf{X}(t) + \mathbf{B}(q_1, q_2)\mathbf{u}(t) \\ \mathbf{y}(t) &= \mathbf{C}(q_1, q_2)\mathbf{X}(t) \end{aligned} \tag{7.24a}$$

or

$$\begin{aligned} \dot{\mathbf{X}}(t) &= \mathbf{A}(\alpha)\mathbf{X}(t) + \mathbf{B}(\alpha)\mathbf{u}(t) \\ \mathbf{y}(t) &= \mathbf{C}(\alpha)\mathbf{X}(t) \end{aligned} \tag{7.24b}$$

With

$$\boldsymbol{A}(\alpha)=\boldsymbol{A}(q_1,q_2)=\begin{bmatrix} 0 & 1 & 0 & 0 & 0 & 0 \\ -\frac{k}{m} & -\frac{c}{m} & 0 & 0 & 0 & 0 \\ 0 & 0 & 0 & 1 & 0 & 0 \\ 0 & 0 & -f_1(q_1,q_2)^2 & -2\xi f_1(q_1,q_2) & 0 & 0 \\ 0 & 0 & 0 & 0 & 0 & 1 \\ 0 & 0 & 0 & 0 & -f_1(q_1,q_2)^2 & -2\xi f_1(q_1,q_2) \end{bmatrix}$$

$$\boldsymbol{B}(\alpha)=\boldsymbol{B}(q_1,q_2)=\begin{bmatrix} 0 & 0 & 0 & 0 \\ \frac{1}{m} & 0 & 0 & 0 \\ 0 & 0 & 0 & 0 \\ 0 & f_2(q_1,q_2) & 0 & f_3(q_1,q_2) \\ 0 & 0 & 0 & 0 \\ 0 & 0 & f_2(q_1,q_2) & 0 \end{bmatrix}$$

$$\boldsymbol{C}(\alpha)=\boldsymbol{C}(q_1,q_2)=\begin{bmatrix} 1 & 0 & 0 & 0 & 0 & 0 \\ 0 & 0 & f_2(q_1,q_2) & 0 & 0 & 0 \\ 0 & 0 & 0 & 0 & f_2(q_1,q_2) & 0 \\ 0 & 0 & f_3(q_1,q_2) & 0 & 0 & 0 \end{bmatrix}$$

Parameter varying functions are given as follows (see Figure 7.8).

$$f_1(q_1,q_2) = p_{00} + p_{10}q_1 + p_{01}q_2 + p_{20}q_1^2 + p_{11}q_1q_2 + p_{02}q_2^2 + p_{30}q_1^3 + p_{21}q_1^2q_2 + p_{12}q_1q_2^2 + p_{03}q_2^3 \tag{7.25}$$

$$f_2(q_1,q_2) = r_{00} + r_{10}q_1 + r_{01}q_2 + r_{20}q_1^2 + r_{11}q_1q_2 + r_{02}q_2^2 + r_{30}q_1^3 + r_{21}q_1^2q_2 + r_{12}q_1q_2^2 + r_{03}q_2^3 \tag{7.26}$$

$$f_3(q_1,q_2) = s_{00} + s_{10}q_1 + s_{01}q_2 + s_{20}q_1^2 + s_{11}q_1q_2 + s_{02}q_2^2 + s_{30}q_1^3 + s_{21}q_1^2q_2 + s_{12}q_1q_2^2 + s_{03}q_2^3 \tag{7.27}$$

When cutting forces are included, ordinary differential equations (ODE) are changed in delay differential equations. Using the following second-order Pade's approximation:

$$e^{-T\,s} \approx \frac{T^2s^2\text{-}6Ts+12}{T^2s^2+6Ts+12} \tag{7.28}$$

Delay differential equations can be again converted into ODEs. The time-varying system can be represented in a state-space form as below (Gu et al., 2005).

$$\boldsymbol{G}(.,\alpha)=\begin{cases}\dot{\boldsymbol{x}}=\boldsymbol{A}(\alpha)\boldsymbol{x}+\boldsymbol{B}_1(\alpha)\boldsymbol{w}+\boldsymbol{B}_2(\alpha)\boldsymbol{u}\\ \boldsymbol{z}=\boldsymbol{C}_1(\alpha)\boldsymbol{x}+\boldsymbol{D}_{11}(\alpha)+\boldsymbol{D}_{12}(\alpha)\boldsymbol{u}\\ \boldsymbol{y}=\boldsymbol{C}_2\boldsymbol{x}+\boldsymbol{D}_{21}\boldsymbol{w}+\boldsymbol{D}_{22}\boldsymbol{u}\end{cases} \tag{7.29}$$

where $\alpha(t)=\left(q_1(t),q_2(t),....q_m(t)\right)$ with $q_m(t)\in\left[q_{1m},q_{um}\right]$. Parameter vector $\alpha(t)$ takes values in a box with corner $\prod_i$ with i =1,2, …, q, and $q=2^m$. The system matrix becomes (Gu et al., 2005):

$$\boldsymbol{G}(.,\alpha)=\left[\begin{array}{c|cc}\boldsymbol{A}(\alpha) & \boldsymbol{B}_1(\alpha) & \boldsymbol{B}_2(\alpha)\\ \hline \boldsymbol{C}_1(\alpha) & \boldsymbol{D}_{11}(\alpha) & \boldsymbol{D}_{12}(\alpha)\\ \boldsymbol{C}_2 & \boldsymbol{D}_{21} & \boldsymbol{D}_{22}\end{array}\right] \tag{7.30}$$

With ranges in a matrix polytope with vertices $G\left(\prod_i\right)$. Decomposing the parameter vector

$\alpha(t)=p_1\prod_1+....+p_q\prod_q$ with $p_i\geq 0$ and $\sum_{i=1}^{q}p_i=1$ over the corners $\prod_i$ of the parameter box, the system matrix $\mathbf{G}(\alpha)$ is given as follows.

$$\mathbf{G}(\alpha)=p_1\mathbf{G}\left(\prod_1\right)+p_2\mathbf{G}\left(\prod_2\right)+....+p_q\mathbf{G}\left(\prod_q\right) \tag{7.31}$$

7.4. Linear parameter varying controller design

A Linear Parameter Varying (LPV) controller is designed using the Linear Matrix Inequality technique (Gu et al., 2005) for LPV systems represented by Equation (7.29). The linear parameter varying controller for this system is given by:

$$\boldsymbol{K}(.,\alpha)=\begin{cases}\dot{\boldsymbol{\zeta}}=\boldsymbol{A_K}(\alpha)\boldsymbol{\zeta}+\boldsymbol{B}_K(\alpha)\boldsymbol{y}\\ \boldsymbol{u}=\boldsymbol{C_K}(\alpha)\boldsymbol{\zeta}+\boldsymbol{D_K}(\alpha)\boldsymbol{y}\end{cases} \tag{7.32}$$

It can be represented in a polytopic form as follows.

$$\begin{bmatrix}\boldsymbol{A_K}(\alpha) & \boldsymbol{B_K}(\alpha)\\ \boldsymbol{C_K}(\alpha) & \boldsymbol{D_K}(\alpha)\end{bmatrix}=\sum_{i=1}^{q}p_i\begin{bmatrix}\boldsymbol{A_K}(\prod_i) & \boldsymbol{B_K}(\prod_i)\\ \boldsymbol{C_K}(\prod_i) & \boldsymbol{D_K}(\prod_i)\end{bmatrix} \tag{7.33}$$

Such that interpolating gain-scheduled controller is given by:

$$\begin{aligned}\mathbf{A}_k(\alpha)&=p_1\mathbf{A}_k\left(\prod_1\right)+....+p_q\mathbf{A}_k\left(\prod_q\right)\\ \mathbf{B}_k(\alpha)&=p_1\mathbf{B}_k\left(\prod_1\right)+....+p_q\mathbf{B}_k\left(\prod_q\right)\\ \mathbf{C}_k(\alpha)&=p_1\mathbf{C}_k\left(\prod_1\right)+....+p_q\mathbf{C}_k\left(\prod_q\right)\\ \mathbf{D}_k(\alpha)&=p_1\mathbf{D}_k\left(\prod_1\right)+....+p_q\mathbf{D}_k\left(\prod_q\right)\end{aligned} \tag{7.34}$$

This interpolation scheme yields smooth scheduling of the controller for parameter $\alpha(t)$. Details can be seen in reference (Gu et al., 2005).

7.5. Results and Discussion

As the natural frequency varies in a range, the Bode plot for all the systems (in an open loop) is shown in Figure 7.9 (a). The LPV controller has a Bode plot given by part (b) of this figure. The comparison of open and closed loop systems is represented by part (c) of this figure.

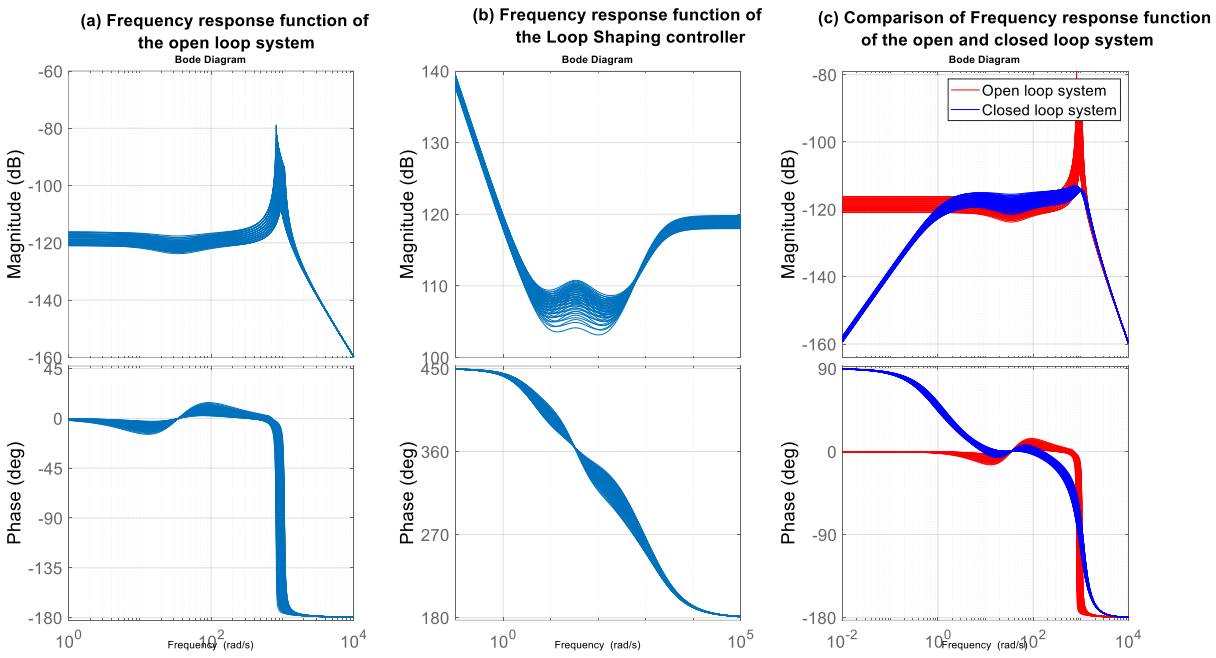

Figure 7.9 Frequency domain presentation of the perturbed system with LPV controller

To calculate the time domain response, simulations are conducted in the SIMULINK/ MATLAB environment. In the case study, the open-loop critical depth of cut (for tool location 0.2 m from right) is 72 microns. To enhance the cutting rate, it is decided to increase the depth of cut to 250 microns. For this LPV system, an H_∞ LPV controller is synthesised and applied. The feed rate is settled as 100 microns/revolution. The spinning speed of the shaft is fixed as 600 rpm. This corresponds to a time delay of 0.1 seconds. During the first tool cuts the workpiece in dimensions of [35 30 25 20 15] mm, the response shows the control forces required to overcome the chatter as shown in Figures 7.10 (a) and (b). The comparison is done with the velocity feedback controller. It is obvious that the H_∞ controller has better noise tolerance. However, if this controller (H_∞ controller) is applied during the10^{th} tool pass when dimensions of the shaft are [30 25 20 15 15] mm, the closed-loop stability of the system is lost (Figures 7.10(c) and (d)). The amplitude of

vibration grows as well as the amplitude of control forces. However, if the proposed H_∞ LPV controller is applied, the closed-loop stability is preserved (Figures 7.10 (e) and (f)).

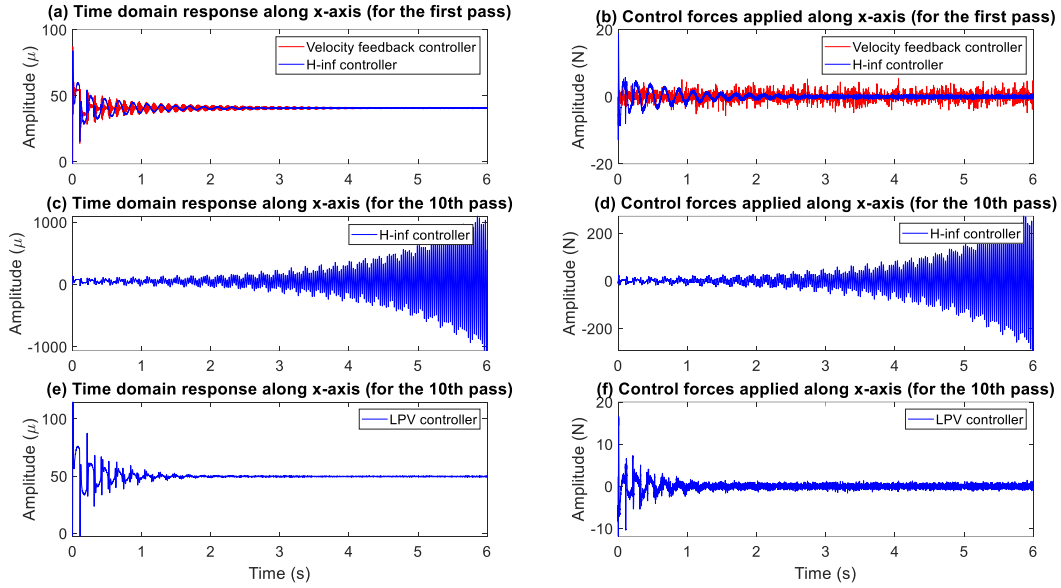

Figure 7.10 Time-domain performance of the perturbed system (the 10th pass of the tool) with the nominal H-inf and LPV controller

In this work, the EA is proposed for the generation of control forces. Eddy current probe is used for measuring displacements of the workpiece from the equilibrium position. Section 7.2 is devoted to actuator dynamics. With parameters shown in Table 7.1, the dynamics of the actuator is developed. An AC voltage amplifier is used for increasing the amplitude of control voltage generated by the controller (computer). Figure 7.11 shows the amplitude of control voltages for the ACC implementation. A feed rate of 100 microns/revolution is maintained during this experiment. Afterwards, the feed rate is then enhanced to 400 microns/revolution and the experiment is repeated. Due to the high feed rate, the steady-state deflection of the workpiece is increased. Figure 7.12 shows the response of the system along the x-axis and the applied control voltage along the x-axis. To suppress the initial transient vibrations, high control forces are required which can be seen in the high control voltage applied to the actuator.

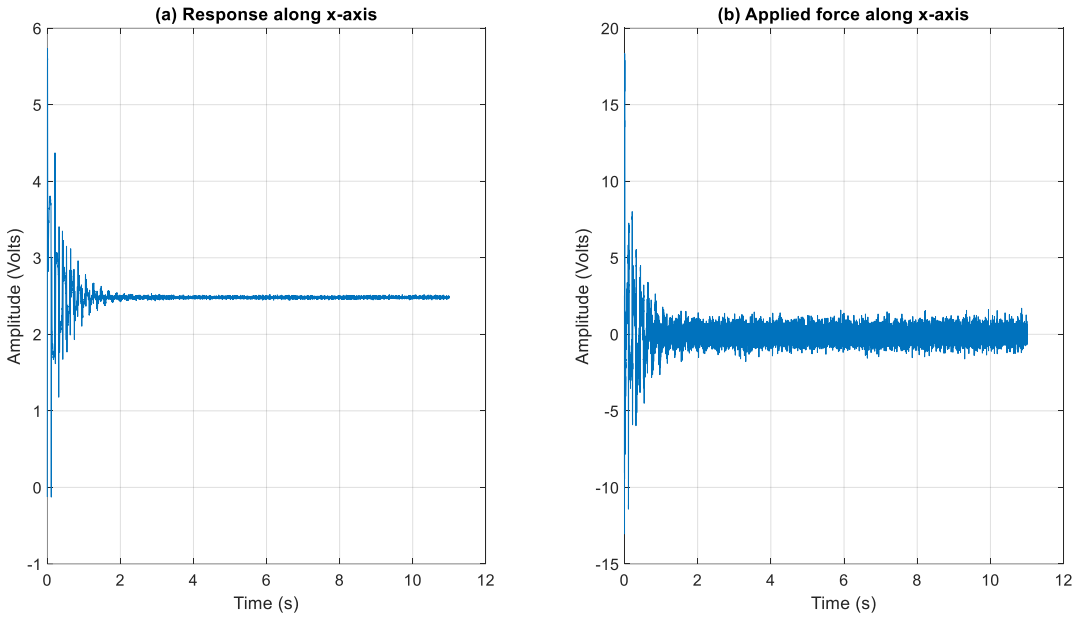

Figure 7.11 Performance of the perturbed system with a gain scheduled/LPV controller with sensor and actuator in the loop

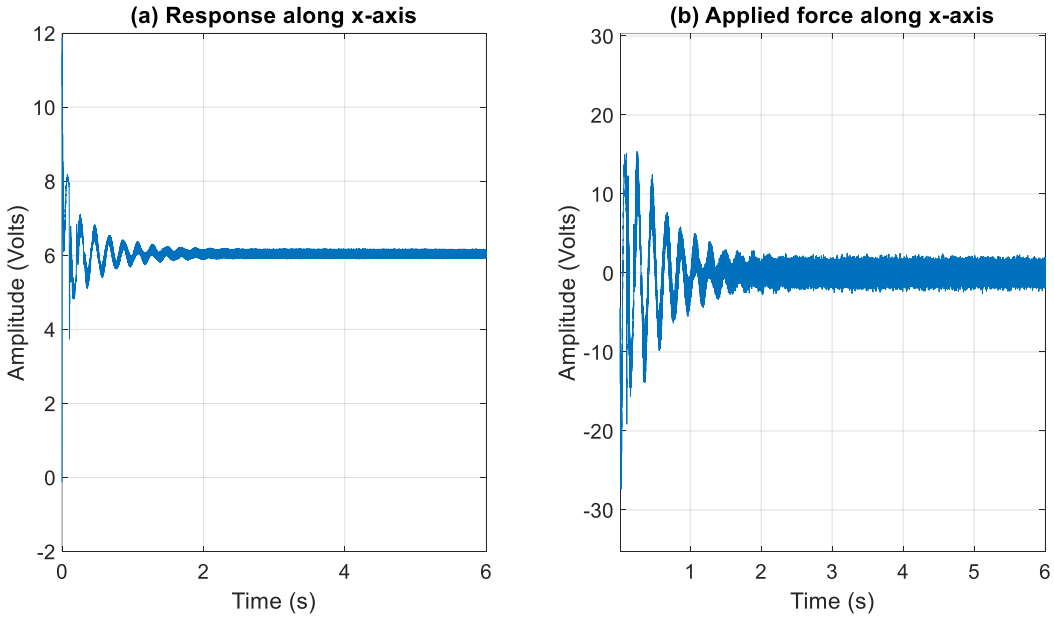

Figure 7.12 Performance of the perturbed system with a gain-scheduled/LPV controller with sensor and actuator in the loop (feedrate 400 microns/second)

It is observed that to maintain stability and avoid the chatter, control forces need to be applied along x-direction only. However, transient vibrations along the y-axis can be quenched quickly by

the application of control forces along the y-direction. The stiffness of the cutting tool is taken sufficiently high to avoid any control force requirement for quenching vibrations along the z-direction.

7.6. Concluding remarks

Following conclusions are drawn from the work presented in this chapter

- Due to the limited flexibility of long shafts, the chatter cannot be prevented even if the cutting tool is rigid. On the other hand, the flexibility of the stepped shaft depends on the tool location. With subsequent cutting passes, the material is lost and natural frequencies are subjected to change. Hence the controller designed for one particular tool location and cutting pass losses its stability for the other.
- An LPV controller designed can stabilize the cutting system for the total range. The system stability is ensured for all cutting passes. Much higher cutting rate (250 microns/r) is obtained with the proposed method compared to open loop conditions (72 microns/r), enhancing the overall productivity.

Chapter 8

Active chatter control of boring operations

8.1. Overview

Boring is a machining process to make a precise hole in a workpiece. Figure 8.1 shows two types of boring operations. Part (a) shows a case of the stationary bar (SB) boring operation. In this case, the workpiece is light and is revolving. Part (b) shows the rotating bar (RB) boring case for the heavy workpiece. There is a tremendous difference in dynamic modelling of these two processes.

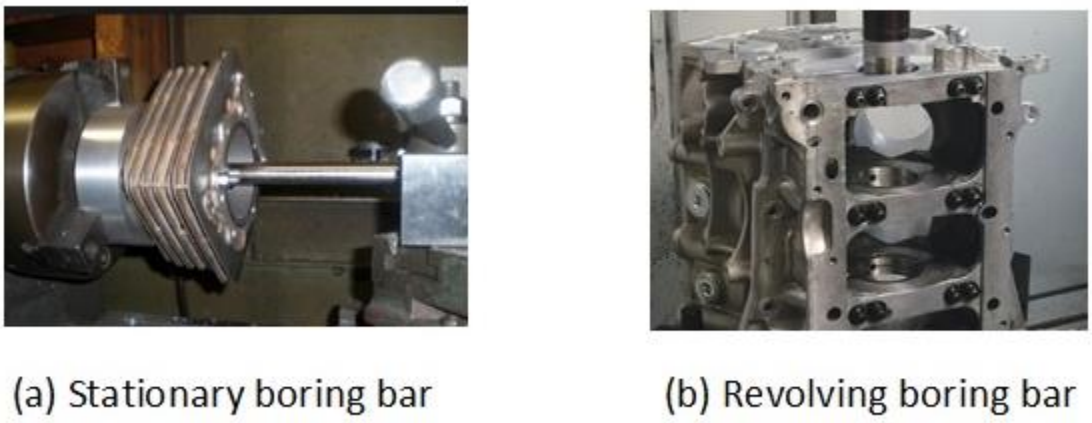

Figure 8.1 Different types of boring operations

Due to the factor of limited rigidity of boring bars, small depths of cutting are normally applied for chatter-free machining. Stability lobe diagrams can truly represent this limit. However, due to the presence of manufacturing inaccuracies like ovality and eccentricity, these limits are considerably changed. Hence, considering these in modelling the cutting process, stability analysis

and controller design is a novel idea, hence implemented in this work. Dynamic modelling of the boring process is presented in detail using a 3-DOF model. Dynamics of such systems is represented using delay differential equations with time-periodic coefficients. The system stability is enhanced with active chatter control (ACC) techniques. The closed-loop system considering fractional-order PD^{λ} in the loop is a nonlinear time-periodic delay differential equation system. Any systematic controller synthesis process for such systems is rarely available in the literature. It is observed that a fractional-order PD^{λ} controller designed by using a combination of pseudo-spectral and response optimization techniques is highly efficient in terms of the requirement of the low amplitude of the peak force and simplicity of implementation. Transient vibrations can also be quenched in a limited period of time by using this controller. Different control techniques available in the literature (H_{∞} Loop shaping and PD control) are tested and compared to the proposed controller for enhancing the material removal rate and surface finish of the workpiece. By using the ACC, the chatter can be efficiently reduced and the material removal rate can be increased. The critical depth of cut is increased from 0.2 mm (open loop) to 0.6 mm (closed-loop) with a limited actuator size in the case study for SB boring machine.

It is also observed in this work that the open loop stable depth of cut for the RB boring process is much more compared to an SB boring process. It is further observed that the RB boring process is not a suitable candidate for ACC because much higher harmonic control forces are required for the minor improvement in the critical depth of cut.

8.2. Mathematical Modelling of stationary bar boring operation

8.2.1. The dynamic model of the boring bar

The transfer function from the input (cutting point) to output (cutting point) locations is given by (Figure 8.2):

$$\frac{y(s)}{F_y(s)} = \frac{x(s)}{F_x(s)} = \frac{(\Psi_1)^2}{s^2 + 2\xi\omega s + \omega^2} \tag{8.1}$$

where Ψ_1 is the mode shape at the cutting point, ω is the resonance frequency and ξ is the damping ratio of the boring bar. The transfer function from the input (electromagnetic actuator) to output (eddy current sensor) is given by:

$$\frac{y_{sensor}(s)}{F_{y_{actuator}}(s)} = \frac{x_{sensor}(s)}{F_{x_{actuator}}(s)} = \frac{(\Psi_3)^2}{s^2 + 2\xi\omega s + \omega^2} \tag{8.2}$$

The transfer function from the input (electromagnetic actuator) to output (cutting point) is given by:

$$\frac{y(s)}{F_{y_{actuator}}(s)} = \frac{x(s)}{F_{x_{actuator}}(s)} = \frac{\Psi_1\Psi_3}{s^2 + 2\xi\omega s + \omega^2} \tag{8.3}$$

Forces on the boring bar are entering via cutting point as well as the electromagnetic actuator. The relation in a transfer matrix form is given as follows (in Y-direction).

$$\begin{bmatrix} y(s) \\ y_{sensor}(s) \end{bmatrix} = \begin{bmatrix} \frac{\Psi_1\Psi_1}{s^2 + 2\xi\omega s + \omega^2} & \frac{\Psi_1\Psi_3}{s^2 + 2\xi\omega s + \omega^2} \\ \frac{\Psi_3\Psi_1}{s^2 + 2\xi\omega s + \omega^2} & \frac{\Psi_3\Psi_3}{s^2 + 2\xi\omega s + \omega^2} \end{bmatrix} \begin{bmatrix} F_y(s) \\ F_{y_{actuator}}(s) \end{bmatrix} \tag{8.4}$$

Similarly, in X-direction, the transfer matrix is given as:

$$\begin{bmatrix} x(s) \\ x_{sensor}(s) \end{bmatrix} = \begin{bmatrix} \frac{\Psi_1\Psi_1}{s^2 + 2\xi\omega s + \omega^2} & \frac{\Psi_1\Psi_3}{s^2 + 2\xi\omega s + \omega^2} \\ \frac{\Psi_3\Psi_1}{s^2 + 2\xi\omega s + \omega^2} & \frac{\Psi_3\Psi_3}{s^2 + 2\xi\omega s + \omega^2} \end{bmatrix} \begin{bmatrix} F_x(s) \\ F_{x_{actuator}}(s) \end{bmatrix} \tag{8.5}$$

This model can be used to simulate the dynamics of boring operations. It actually forms a multi-input and multi-output system, where cutting forces act as disturbing forces and forces applied at actuators are controlling forces. Cutting forces to be used in Equations (8.1-8.5) are given by equations (7.20-7.22) in Chapter 7. By considering the cutting forces, system dynamics can be represented by delay differential equations.

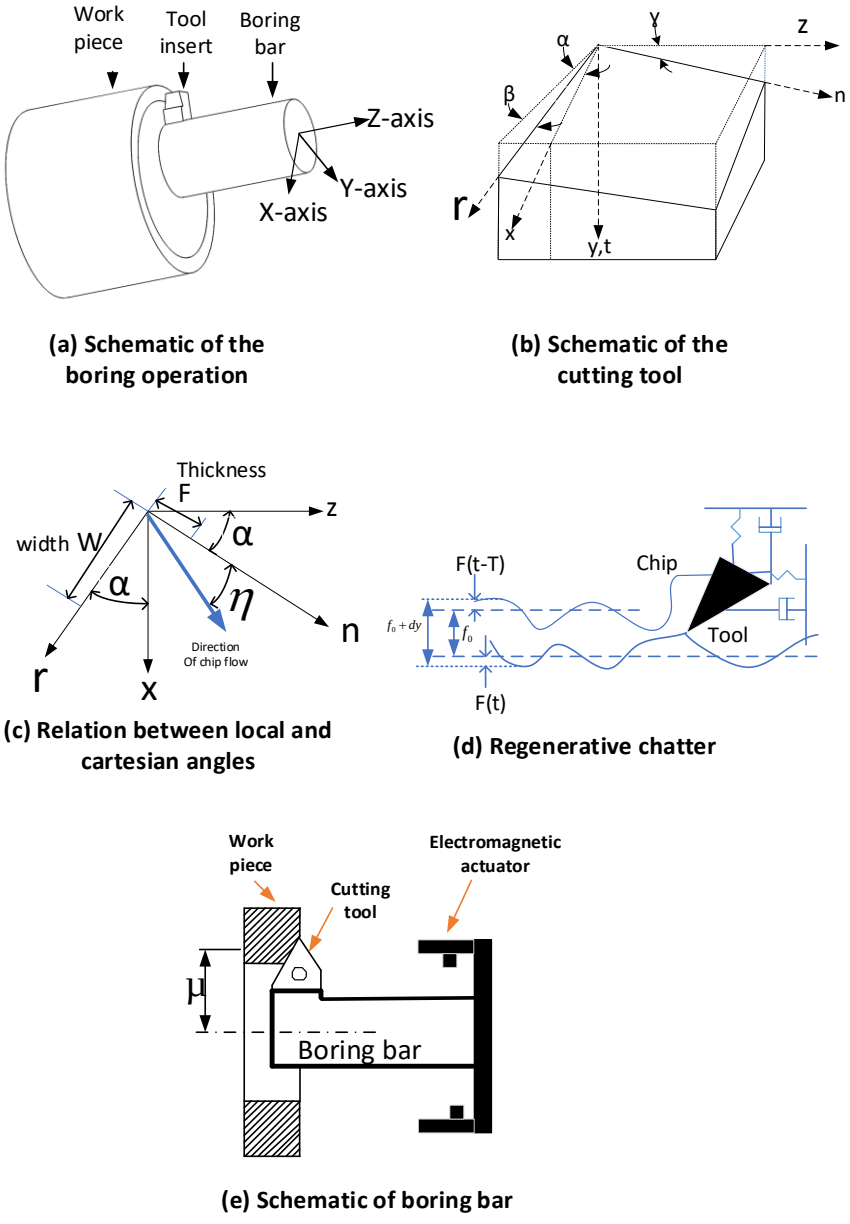

Figure 8.2 Schematic of the overall boring operation

8.2.2. Consideration of Ovality

It is assumed that there is ovality in the inside diameter of the workpiece as shown in Figure 8.3 (a). The maximum radius of the inside portion is a_x and minimum radius is b_y. The equation of the oval system is given by:

$$\frac{x^2}{a_x^2}+\frac{y^2}{b_y^2}=1 \tag{8.6}$$

where x and y are coordinates of a point moving on the ellipse. At an angle χt, the ratio of different coordinates is as follows.

$$\tan\left(\chi t\right)=\frac{y}{x} \tag{8.7}$$

Solving the above equations for x and y and substituting in R i.e. instantaneous radius.

$R=\sqrt{x^2+y^2}$, we get

$$R=\sqrt{\frac{a_x^2\ b_y^2\ \sec^2(\chi \mathrm{t})}{a_x^2\ \tan^2(\chi \mathrm{t})+b_y^2}} \tag{8.8}$$

If R_{max} is the maximum radius, the time varying depth of cut is given as:

$$b(t)=R_{\max}-\sqrt{\frac{a_x^2\ b_y^2\ \sec^2(\chi \mathrm{t})}{a_x^2\ \tan^2(\chi \mathrm{t})+b_y^2}} \tag{8.9}$$

where the varying depth or width of cut b(t) keeps on changing as the workpiece revolves i.e. the width of cut changes periodically. The term periodically means that the width of cut b(t) at a particular time is same as its value at T time ago, where T is the time period to complete one revolution.

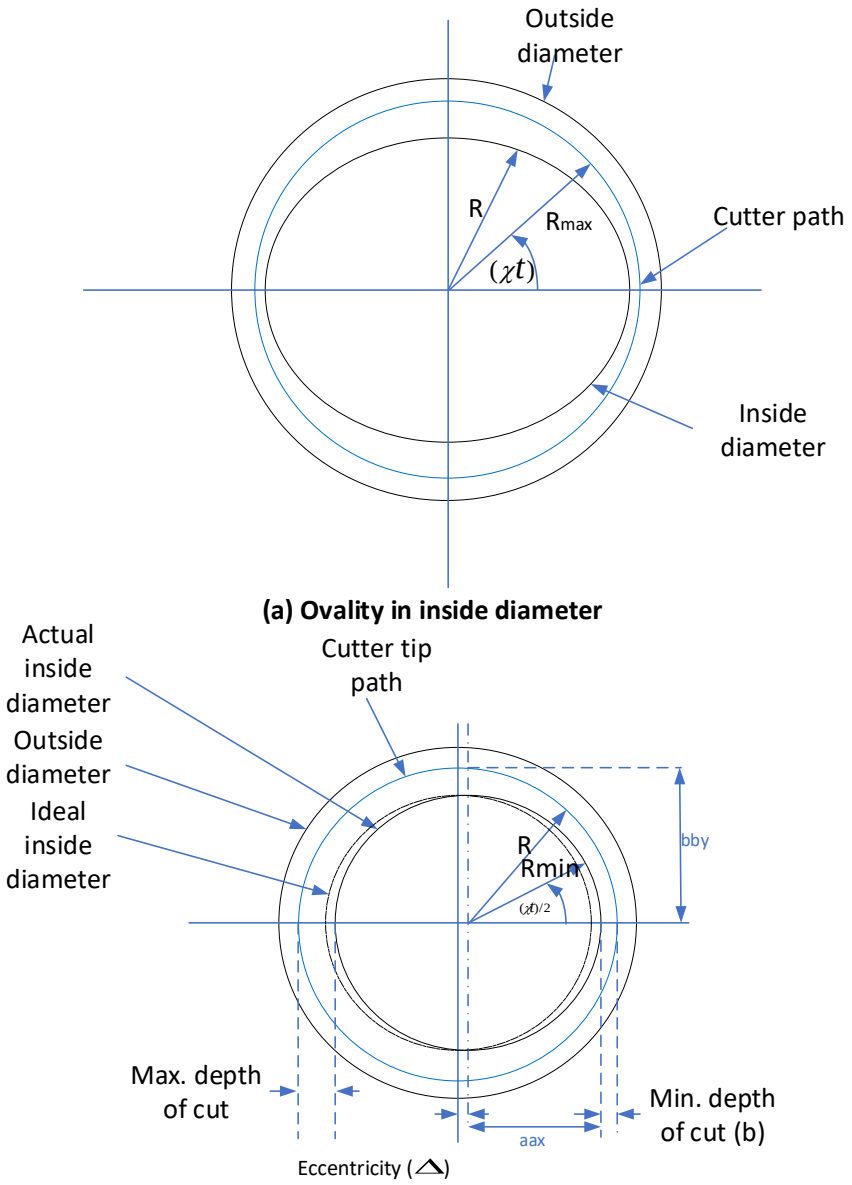

Figure 8.3 Analysis of ovality and eccentricity

8.2.3. Consideration of Eccentricity

Another most common problem during metal cutting is eccentricity. The workpiece may not be mounted in the lathe chuck properly, causing overall eccentricity. It is assumed that there is eccentricity at the inside diameter of the workpiece as shown in Figure 8.3 (b). The minimum radius of the inside portion is aa_x and maximum radius is bb_y. The equation of the oval system is:

$$\frac{x^2}{\left(aa_x\right)^2}+\frac{y^2}{\left(bb_y\right)^2}=1 \tag{8.10}$$

At an angle χt, the ratio of different coordinates is as follows.

$$\tan\left(\chi t\right)=\frac{y}{x} \tag{8.11}$$

Solving the above equations for x and y and substituting in R i.e. instantaneous radius.

$R=\sqrt{x^2+y^2}$, we get

$$R=\sqrt{\frac{\left(aa_x\right)^2\left(bb_y\right)^2\sec^2\left(\chi t/2\right)}{\left(aa_x\right)^2\tan^2\left(\chi t/2\right)+\left(bb_y\right)^2}} \tag{8.12}$$

If R_{min} is the minimum radius of the cavity, the time-varying depth of cut is given as:

$$b(t)=\sqrt{\frac{\left(aa_x\right)^2\left(bb_y\right)^2\sec^2\left(\chi t/2\right)}{\left(aa_x\right)^2\tan^2\left(\chi t/2\right)+\left(bb_y\right)^2}}-R_{\min} \tag{8.13}$$

Putting $aa_x=R_{\min}+b$ and $bb_y=R_{\min}+b+2\Delta$, where b is the minimum width of cut, R_{min} is the inside radius of the cavity and Δ is the eccentricity in the horizontal direction as shown in Figure 8.3, part (b).

$$b\left(t\right)=\sqrt{\frac{\left(R_{\min}+b\right)^2\left(R_{\min}+b+2\Delta\right)^2\sec^2\left(\chi t/2\right)}{\left(R_{\min}+b\right)^2\ \tan^2\left(\chi t/2\right)+\left(R_{\min}+b+2\Delta\right)^2}}-R_{\min} \tag{8.14}$$

One thing worth consideration at this point is that with time-varying width of cut b(t), forces in Equations (7.20-7.22) are periodically time-varying. It is observed that this factor changes the

ordinary delay differential equations (with constant coefficients) into time-periodic delay differential equations (with coefficients changing periodically).

8.3 Mathematical modelling of rotating bar boring operation

In the case of CNC machining centres, the workpiece remains stationary and the tool rotates. It is the case of RB boring operations. In terms of a global coordinate axis, cutting forces are given as follows (Figure 8.4).

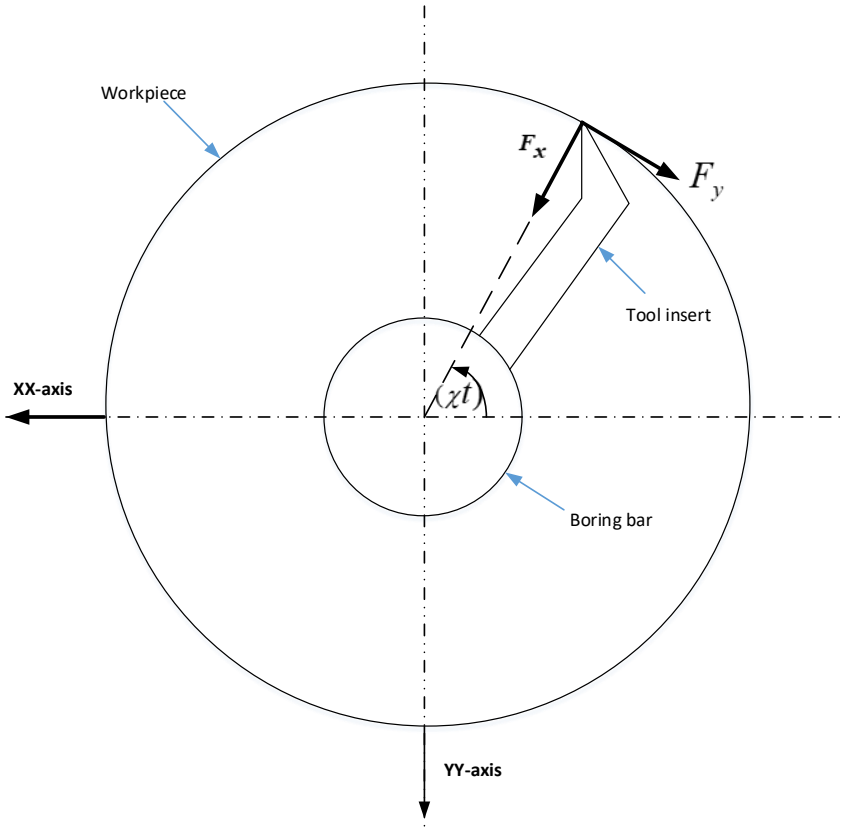

Figure 8.4 Forces during revolving bar boring (not to scale)

$$F_{xx} = F_x \cos(\chi t) - F_y \sin(\chi t) \tag{8.15}$$

$$F_{yy} = F_x \sin(\chi t) + F_y \cos(\chi t) \tag{8.16}$$

In the expanded form it can be written as:

$$F_{xx} = b\begin{pmatrix} f_0\left(\cos(\chi t)\, g_{41} - \sin(\chi t)\right) g_{61} + \left(\sin(\chi t)\, g_{63} - \cos(\chi t)\, g_{43}\right) x(t) \\ +\left(\cos(\chi t)\, g_{43} - \sin(\chi t)\, g_{63}\right) x(t-T) + \mu\left(\sin(\chi t)\, g_{61} - \cos(\chi t)\, g_{41}\right)\theta(t) \\ +\mu\left(\cos(\chi t)\, g_{41} - \sin(\chi t)\, g_{61}\right)\theta(t-T) \end{pmatrix} \quad (8.17)$$

$$F_{yy} = b\begin{pmatrix} f_0\left(\sin(\chi t)\, g_{41} + \cos(\chi t)\right) g_{61} + \left(-\sin(\chi t)\, g_{43} - \cos(\chi t)\, g_{63}\right) x(t) \\ +\left(\sin(\chi t)\, g_{43} + \cos(\chi t)\, g_{63}\right) x(t-T) + \mu\left(-\sin(\chi t)\, g_{41} - \cos(\chi t)\, g_{61}\right)\theta(t) \\ +\mu\left(\sin(\chi t)\, g_{41} + \cos(\chi t)\, g_{61}\right)\theta(t-T) \end{pmatrix} \quad (8.18)$$

By considering Equations (8.17 and 8.18), it is obvious that the resulting system contains time periodic delay terms as well as forced terms. χ represents the angular frequency of rotation i.e. $\chi = 2\pi\left(\frac{1}{T}\right)$ where T is the time delay, or the time required to complete one revolution is in seconds.

8.4. Simulation model and formulation of delay equations

A boring bar of length 0.6 m is considered. The diameter of the bar is 70 mm. The tool insert is attached at the free end. The density and Young's modulus of elasticity are taken as 7800 Kg/m^3 and 210x10^9 N/m^2. The first four natural frequencies are calculated as 141.15 Hz, 884.5 Hz, 2477.3 and 4858 Hz. The damping coefficient for each mode is 0.0318. For simplicity, only one mode is considered for analysis. There are four DOF per element i.e. two at each node. First is the linear displacement and the second is the slope. After solving the eigenvalues, for the first mode, the mass normalised mode shape coefficient ψ_1 for the linear displacement is 0.4712 Kg$^{-1/2}$. The slope mode shape coefficient ψ_2 is 1.08 Kg$^{-1/2}$. The control force is applied near the fixed end at a distance 60 mm from the fixed end. The linear displacement mode shape ψ_3 is 7.9048 x10^{-3} Kg$^{-1/2}$.

For properties of the workpiece material, it is considered as steel with K_m, K_r and K_t as 1544x10^6 N/m^2, 124x10^6 N/m^2 and 2881x10^6 N/m^2 respectively. These values are taken from

reference (Eynian et al., 2009) based on practical results. The values of tool angles α, β and γ are taken as 30^0 each. Due to force acting along the z-direction, the slope of the tool inserts (i.e. tool bit) changes dynamically. Apart from that, there is a dynamic movement along x-axis and y-axis. By considering the first mode only, equations of the motion are as follows.

$$\begin{aligned}
&\ddot{\theta}(t)+2\xi\omega\dot{\theta}(t)+\omega^2\theta(t)=\left(\Psi_2\right)^2\mu \mathrm{F}_z(t)\\
&\ddot{x}(t)+2\xi\omega\dot{x}(t)+\omega^2 x(t)=\left(\Psi_1\right)^2 \mathrm{F}_x(t)\\
&\ddot{y}(t)+2\xi\omega\dot{y}(t)+\omega^2 y(t)=\left(\Psi_1\right)^2 \mathrm{F}_y(t)
\end{aligned} \qquad (8.19\text{-}8.21)$$

where $\theta(t)$, $x(t)$ and $y(t)$ represent dynamic slope changes of the cutting tool tip, its displacements in the x-axis and y-axis are in the global coordinate system. In these equations, parameter μ represents the distance of the cutting edge from the central axis of the boring bar (Figure 8.2 e). For stability calculations, equations of the system can be represented in the first-order form as follows.

$$\dot{\mathbf{X}}(t) = \mathbf{A}\ \mathbf{X}(t) + \mathbf{A}_d\ \mathbf{X}(t-T) + \mathbf{B}\ u(t) \qquad (8.22)$$

where

$$A=\begin{bmatrix}
0 & 0 & 0 & 1 & 0 & 0\\
0 & 0 & 0 & 0 & 1 & 0\\
0 & 0 & 0 & 0 & 0 & 1\\
-\omega^2 - g_{21}b\mu^2\psi_2^2 & -g_{23}b\mu\psi_2^2 & 0 & -2\xi\omega & 0 & 0\\
-g_{41}b\mu\psi_1^2 & -\omega^2 - g_{43}b\psi_1^2 & 0 & 0 & -2\xi\omega & 0\\
-g_{61}b\mu\psi_1^2 & -g_{63}b\psi_1^2 & -\omega^2 & 0 & 0 & -2\xi\omega
\end{bmatrix} \qquad (8.23)$$

with $\mathbf{X}(t)=\begin{bmatrix}\theta(t) & x(t) & y(t) & \dot{\theta}(t) & \dot{x}(t) & \dot{y}(t)\end{bmatrix}^T$

$$\boldsymbol{A_d} = \begin{bmatrix} 0 & 0 & 0 & 0 & 0 & 0 \\ 0 & 0 & 0 & 0 & 0 & 0 \\ 0 & 0 & 0 & 0 & 0 & 0 \\ g_{21}b\mu^2\psi_2^2 & g_{23}b\mu\psi_2^2 & 0 & 0 & 0 & 0 \\ g_{41}b\mu\psi_1^2 & g_{43}b\psi_1^2 & 0 & 0 & 0 & 0 \\ g_{61}b\mu\psi_1^2 & g_{63}b\psi_1^2 & 0 & 0 & 0 & 0 \end{bmatrix} \tag{8.24}$$

with $\mathbf{X}(\mathrm{t}-\mathrm{T}) = \begin{bmatrix} \theta(t-T) & x(t-T) & y(t-T) & \dot{\theta}(t-T) & \dot{x}(t-T) & \dot{y}(t-T) \end{bmatrix}^T$

and

$$\boldsymbol{B} = \begin{bmatrix} 0 \\ 0 \\ 0 \\ 0 \\ \psi_1\psi_3 \\ 0 \end{bmatrix} \tag{8.25}$$

In case of ovality and eccentricity, Equation (8.22) changes to:

$$\dot{\mathbf{X}}(\mathrm{t}) = \mathbf{A}(\mathrm{t})\ \mathbf{X}(\mathrm{t}) + \mathbf{A}_d(\mathrm{t})\ \mathbf{X}(t-T) + \mathbf{B}\ \mathrm{u}(\mathrm{t}) \tag{8.26}$$

where

$$\boldsymbol{A}(t) = \begin{bmatrix} 0 & 0 & 0 & 1 & 0 & 0 \\ 0 & 0 & 0 & 0 & 1 & 0 \\ 0 & 0 & 0 & 0 & 0 & 1 \\ -\omega^2 - g_{21}b(t)\mu^2\psi_2^2 & -g_{23}b(t)\mu\psi_2^2 & 0 & -2\xi\omega & 0 & 0 \\ -g_{41}b(t)\mu\psi_1^2 & -\omega^2 - g_{43}b(t)\psi_1^2 & 0 & 0 & -2\xi\omega & 0 \\ -g_{61}b(t)\mu\psi_1^2 & -g_{63}b(t)\psi_1^2 & -\omega^2 & 0 & 0 & -2\xi\omega \end{bmatrix} \tag{8.27}$$

$$\boldsymbol{A_d}(t) = \begin{bmatrix} 0 & 0 & 0 & 0 & 0 & 0 \\ 0 & 0 & 0 & 0 & 0 & 0 \\ 0 & 0 & 0 & 0 & 0 & 0 \\ g_{21}b(t)\mu^2\psi_2^2 & g_{23}b(t)\mu\psi_2^2 & 0 & 0 & 0 & 0 \\ g_{41}b(t)\mu\psi_1^2 & g_{43}b(t)\psi_1^2 & 0 & 0 & 0 & 0 \\ g_{61}b(t)\mu\psi_1^2 & g_{63}b(t)\psi_1^2 & 0 & 0 & 0 & 0 \end{bmatrix} \tag{8.28}$$

8.5. Active chatter control of stationary bar boring operation

The virtual stiffness and damping of the boring bar can be enhanced using active control techniques. It is a form of the closed-loop system. An electromagnetic actuator can be applied near the fixed end. Figure 8.5 shows the physical schematic of the system.

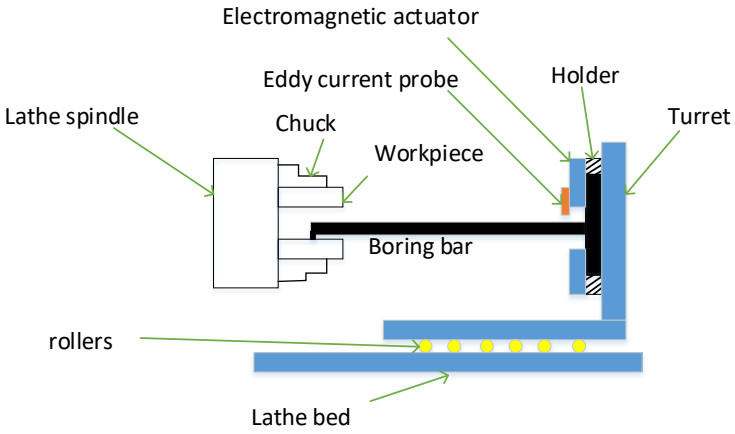

(a) Setup for boring machine

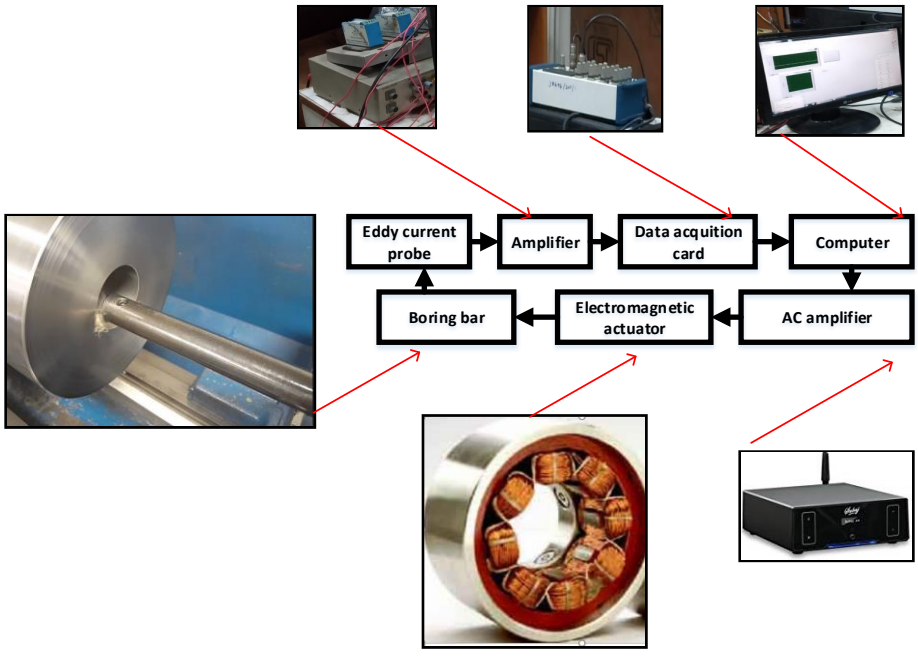

(b) Experimental setup

Figure 8.5 Physical schematic for active chatter control

8.5.1. Experimental setup for active chatter control

Components of the experimental setup can be found in Chapters 5, 6 and 7. The physical parameters of the electromagnetic actuator are shown in Table 8.1.

Table 8.1 Physical Parameters of Electromagnetic actuator

No.	Parameter	Notation	Value
1	Permeability of air	μ_0	1.256×10^{-6} N/A^2
2	Area of iron core	A	40 mm x 40mm
3	Number of winding turns	n	500
4	Nominal air gap	gap	1 mm
5	Bias current	i_0	3 A

8.5.2. Experimental system identification of boring bar dynamics

The transfer function of the boring bar system in the finite element method is verified experimentally. For estimating the transfer function at the cutting location, a piezoelectric impact hammer with the force sensor is used. From input/output data, the frequency response function of the system is calculated using the MATLAB command ‘tfestimate’. However, to estimate the transfer function at the actuator location, an excitation signal is applied at the electromagnetic actuator location. Eddy current probes are used to measure the deflection of the boring bar. From the frequency response functions, the natural frequency, damping ratio and mode shape are calculated. Table 8.2 shows the comparison of theoretical and experimental values.

Table 8.2 Comparison of theoretical and experimental results

Parameter	Theoretical value	Experimental value	% Error
ω (First natural frequency)	141.15 (Hz)	147.1 (Hz)	04.04
ξ (Damping ratio)	-	0.0318	-
ψ_1 (Mode shape at cutting location)	0.4712 $Kg^{-1/2}$	0.5020 $Kg^{-1/2}$	06.1
ψ_2 (Mode shape at cutting location (slope))	1.08 $Kg^{-1/2}$	1.20 $Kg^{-1/2}$	10.0
ψ_3 (Mode shape at actuator location)	8 x10^{-3} $Kg^{-1/2}$	9.3 x10^{-3} $Kg^{-1/2}$	13.9

8.5.3. Controller design

a). Loop Shaping Design Procedure controller

For designing the loop shaping design procedure (LSDP) controller, original delay differential equations are converted into ordinary differential equations by using the 5th order Pade's approximation. The order of the approximate system is 11. Figure 8.6 (a) shows the comparison of the original and approximated systems.

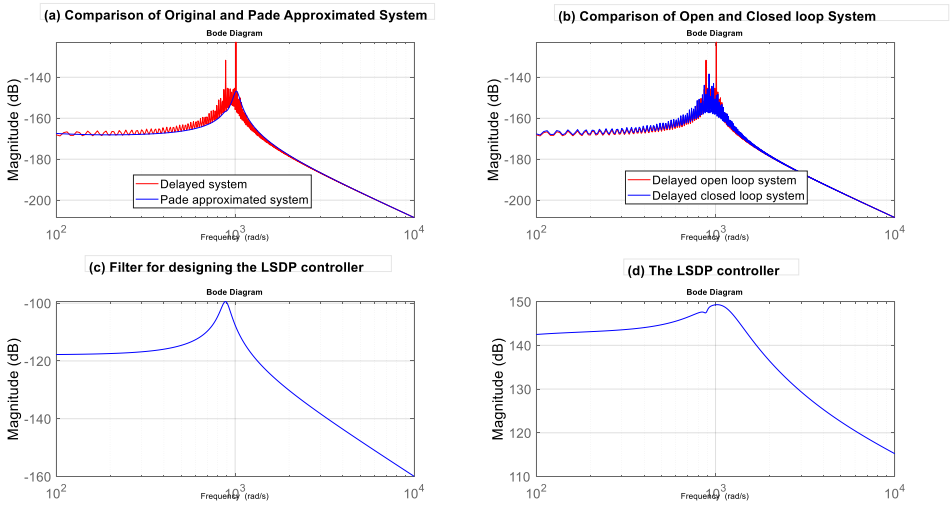

Figure 8.6 Design parameters and frequency response of the loop shaping design procedure controller

The LSDP controller is designed using the method in reference (Gu et al., 2015). The comparison of the open and closed-loop systems is shown in Figure 8.6 (b). The plot of the controller is shown in Figure 8.6 (d).

b). Proportional Derivative controller

By considering the ovality in the workpiece, delay differential equations are converted into time-periodic delay differential equations i.e. delay differential equations with periodically varying coefficients. Pade's approximation of these types of systems is not possible and hence the robust control synthesis. Systematic controller design procedures for such systems are scant in literature. Methods for the stability analysis are used to design the controller. Proportional derivative (PD) controllers can be successfully designed base on this technique. The system of time periodic delay differential equations can be represented as:

$$\dot{\mathbf{X}}(t) = \mathbf{A}(t)\ \mathbf{X}(t) + \mathbf{A}_d(t)\ \mathbf{X}(t-T) + \mathbf{B}\ u(t) \tag{8.29}$$

The integral controller is not useful for the active chatter reduction due to the presence of steady deflection of the tool resulting actuator saturation. The PD controller is quite suitable. By choosing $u(t) = -K_P\, x(t) - K_D \dot{x}(t)$, the above equation is modified with the following matrix.

$$\boldsymbol{A}(t) = \begin{bmatrix} 0 & 0 & 0 & 1 & 0 & 0 \\ 0 & 0 & 0 & 0 & 1 & 0 \\ 0 & 0 & 0 & 0 & 0 & 1 \\ -\omega^2 - g_{21} b(t) \mu^2 \psi_2^2 & -g_{23} b(t) \mu \psi_2^2 & 0 & -2\xi\omega & 0 & 0 \\ -g_{41} b(t) \mu \psi_1^2 & -\omega^2 - g_{43} b(t) \psi_1^2 - (K_P)\psi_1\psi_3 & 0 & 0 & -2\xi\omega - (K_D)\psi_1\psi_3 & 0 \\ -g_{61} b(t) \mu \psi_1^2 & -g_{63} b(t) \psi_1^2 & -\omega^2 & 0 & 0 & -2\xi\omega \end{bmatrix} \tag{8.30}$$

Parameters of the controller can be chosen based on the stability of the overall closed-loop system. In the section of results, it is described that the derivative controller (i.e. velocity feedback)

is more suitable in terms of lower peak force requirements than a proportional controller (i.e. position feedback). More details will be followed in the result section.

c). Fractional order Proportional Derivative controller

Fractional order proportional derivative (FOPD) controller can be realised by using the proportional and fractional-order derivative of output error e(t). In active chatter control applications, the output error is given as -x(t). The control force applied to the boring bar can be represented as follows.

$$u(t)=K_p e(t)+K_d D^{\lambda} e(t) \tag{8.31}$$

where K_p and K_d are the proportional and derivative gains, respectively. D^{λ} denotes the fractional-order derivative controller and is represented as:

$$D^{\lambda} e(t)=\lim_{h\to 0} \frac{1}{h^{\lambda}}\left[e(t)+\sum_{j=1}^{\frac{t}{h}} w_j^{(\lambda)} e\left(t-jh\right) \right] \tag{8.32}$$

with

$$w_0^{(\lambda)}=1 \quad \text{and} \quad w_j^{(\lambda)}=\left[1-\frac{\lambda+1}{j}\right] w_{j-1}^{(\lambda)} \tag{8.33}$$

The value of λ ranges generally from 0 to 2. In this work, $0<\lambda<1$ is considered. If the value of λ is taken as 1, it will represent a conventional PD controller. For designing the FOPD controller (rough estimation), the following algorithm (Figure 8.8) is applied based on the pseudo-spectral method (Breda et al., 2012, Breda et al., 2014).

Values of K_p for the FOPD controller remain the same as for ordinary PD controllers. However, K_d for FOPD (with λ=0.5) is given as $\sqrt{K_d}$ for ordinary PD controllers. K_d obtained using the above method is approximate. It acts as a starting point for determining actual values by response optimization techniques. Figure 8.7 shows the Simulink model of the system.

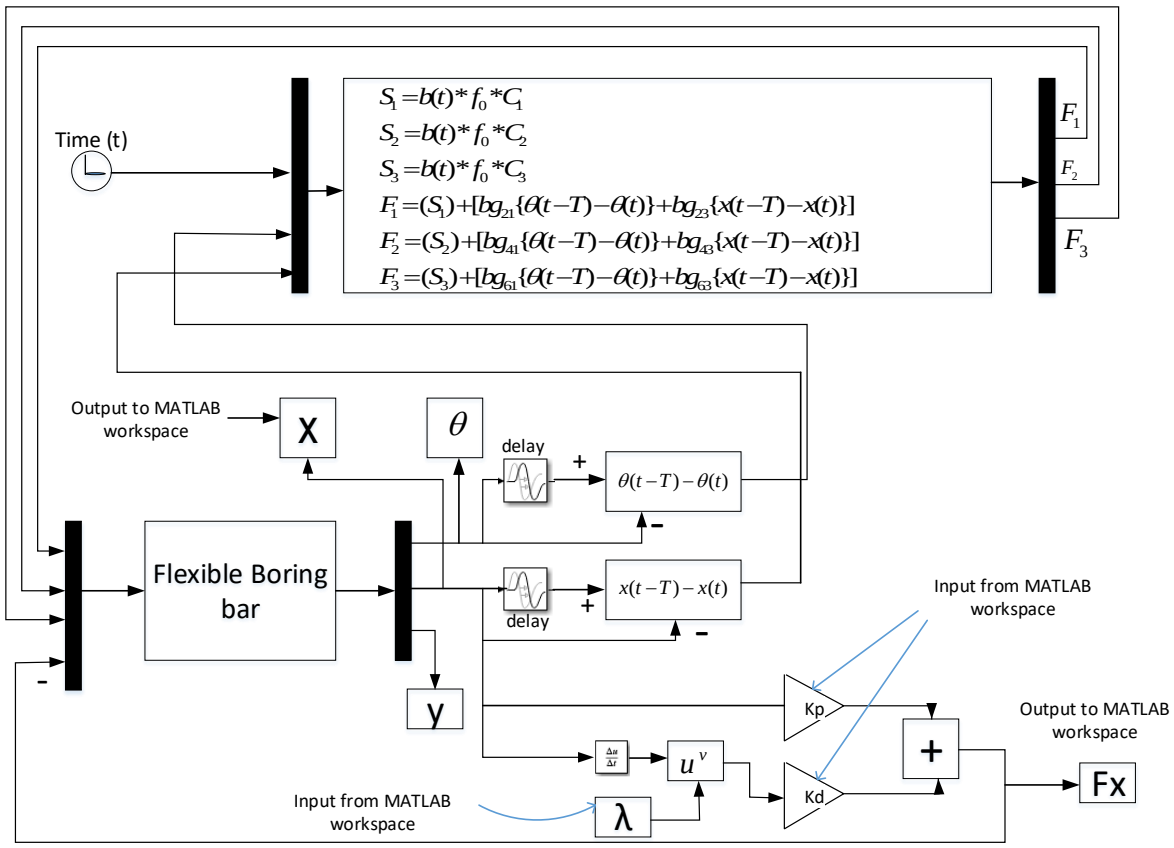

Figure 8.7 Simulink presentation of the control system

with

$$S_1 = b(t) * f_0 * C_1$$
$$S_2 = b(t) * f_0 * C_2 \quad (8.34)$$
$$S_3 = b(t) * f_0 * C_3$$

and

$$C_1 = \mu\left(\cos(\alpha)\right)^2 X_1$$
$$C_2 = \left(\cos(\alpha)\right)^2 X_2 \quad (8.35)$$
$$C_3 = \left(\cos(\alpha)\right)^2 X_3$$

Values of constants X_1, X_2 and X_3 are dependent on material parameters (Eynian et al., 2009). A flowchart of designing the FOPD controller (exact parameters) is shown in Figure 8.8. The combination of Pseudospectral (PS) and response optimization technique is then used.

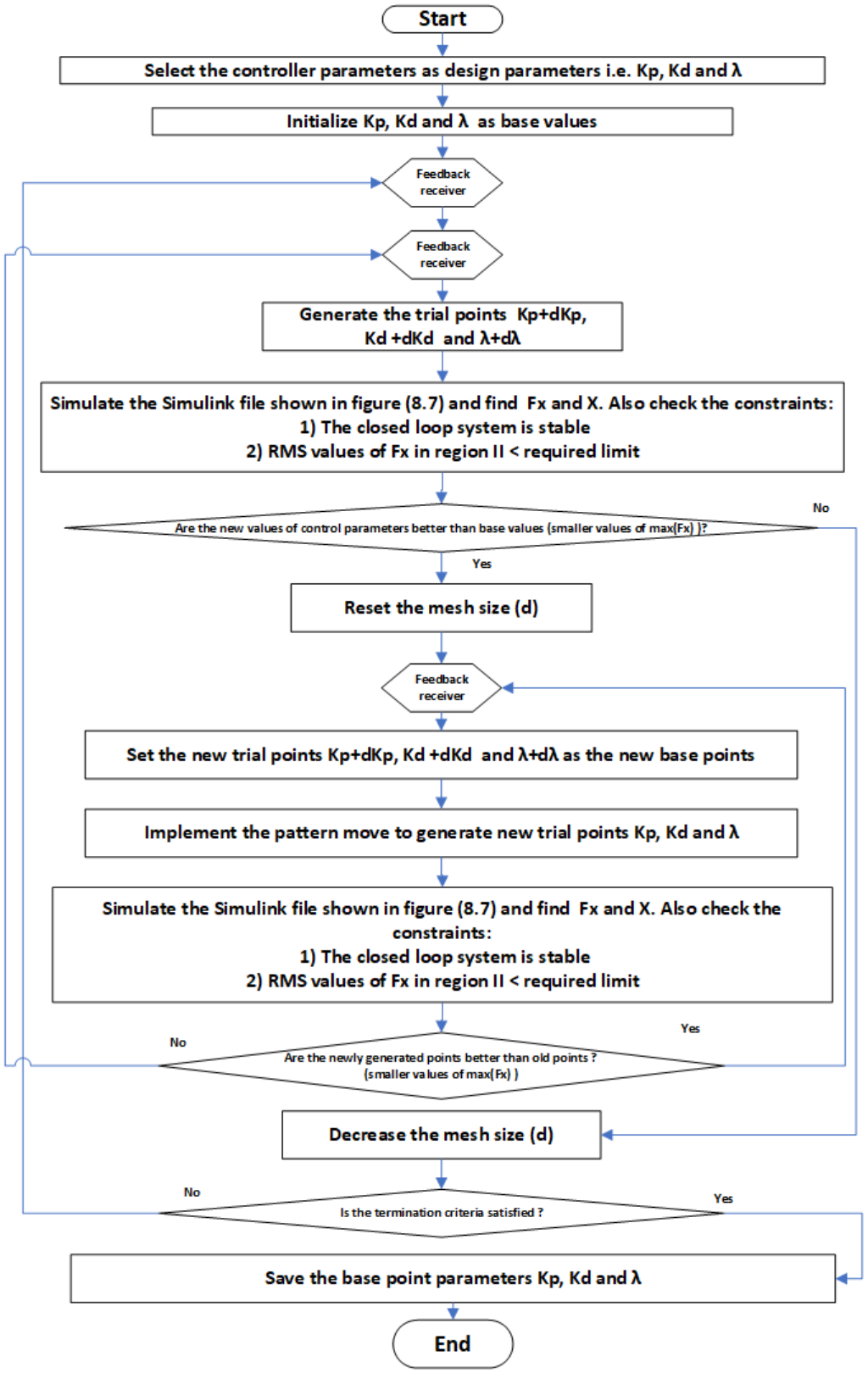

Figure 8.8 Flowchart for fractional order PD$^{\lambda}$ control system synthesis

A pattern search optimization technique is applied for optimization. The Simulink file shown in Figure 8.7 is executed along with constraints of the closed loop stability and the root mean square of control signal below a certain critical value.

As per the flow chart, parameters K_p, K_d and λ are optimised to find such parameters with the minimum value of amplitude of control forces along with preserving the closed loop stability. Parameter λ plays an important role. Figure 8.9 shows the response of the system corresponding to λ =0.2. It is obvious that much lower values result in control signal fluctuations in region II as shown in Figure 8.9 (d). There is fluctuation in control forces although the transient vibrations are over. This is not desirable.

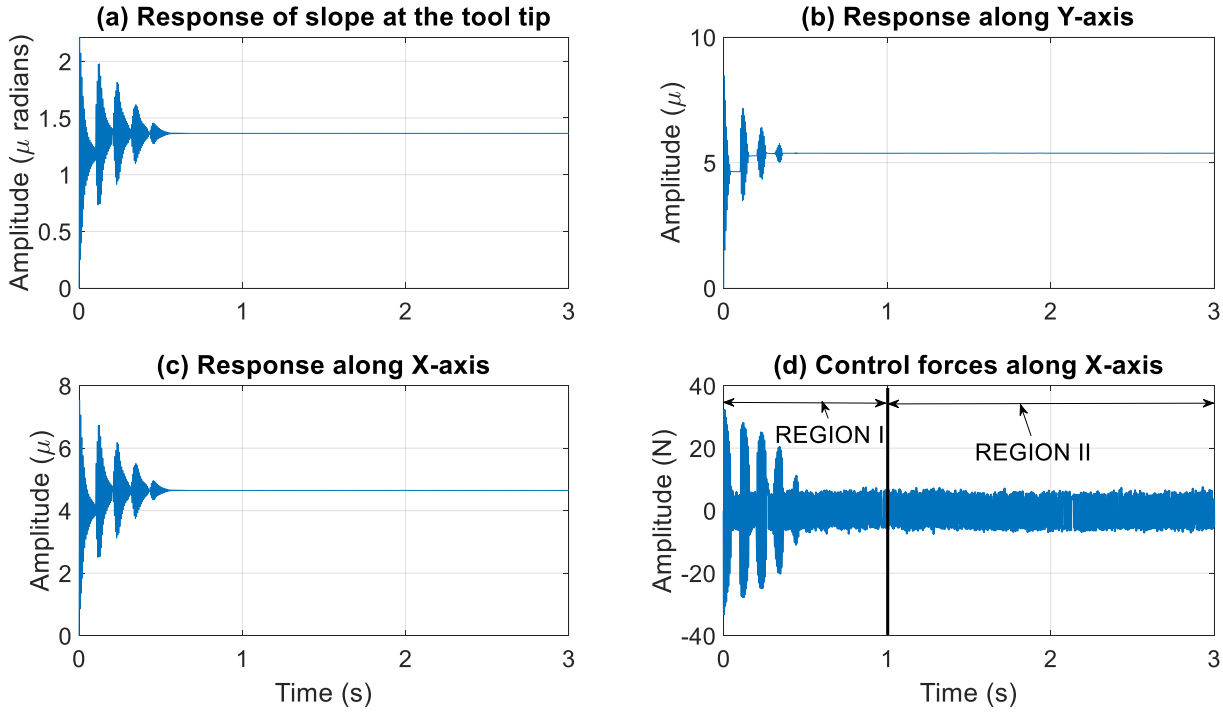

Figure 8.9 Closed loop response of the boring process with fractional order PD controller (λ=0.2) (simulations)

8.5.4. Simulation and experimental results

a). Open loop stability analysis

Figure 8.10 shows the stability lobe diagram for the boring operation in open loop conditions. The semi-discretization method (Insperger et al., 2004) and PS method are compared. The first column shows results by the PS method. The second column shows results by the semi-discretization method. It is obvious that PS methods give more accurate results at lower spinning rates. Figure 8.11 shows the stability lobe diagram for the open loop system with and without ovality. The figure shows the comparison of the minimum critical width or depth of cut as a function of spinning speed. The spinning speed from 400 Hz – 1200 Hz is considered. This is the practical limit for most boring operations. In all these figures, the area below the curve is the stable zone (chatter free) and area above the curve is unstable region (with chatter) (Breda et al., 2012, Breda et al. 2014).

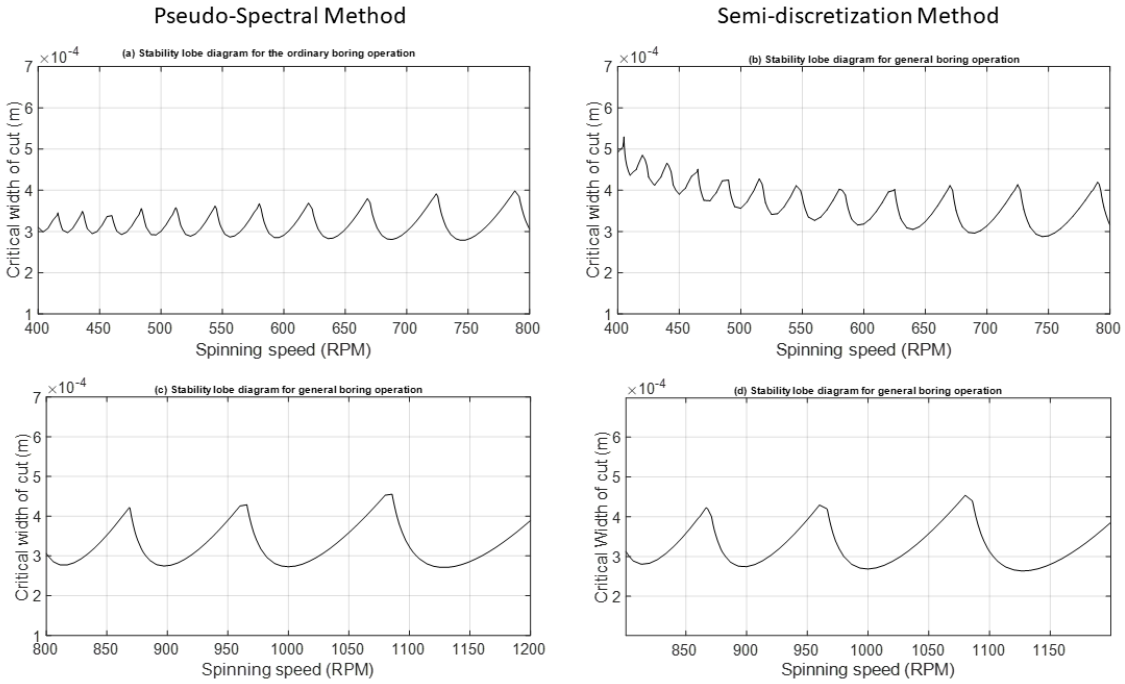

Figure 8.10 Comparison of the semi-discretization approach and Pseudo spectral approach

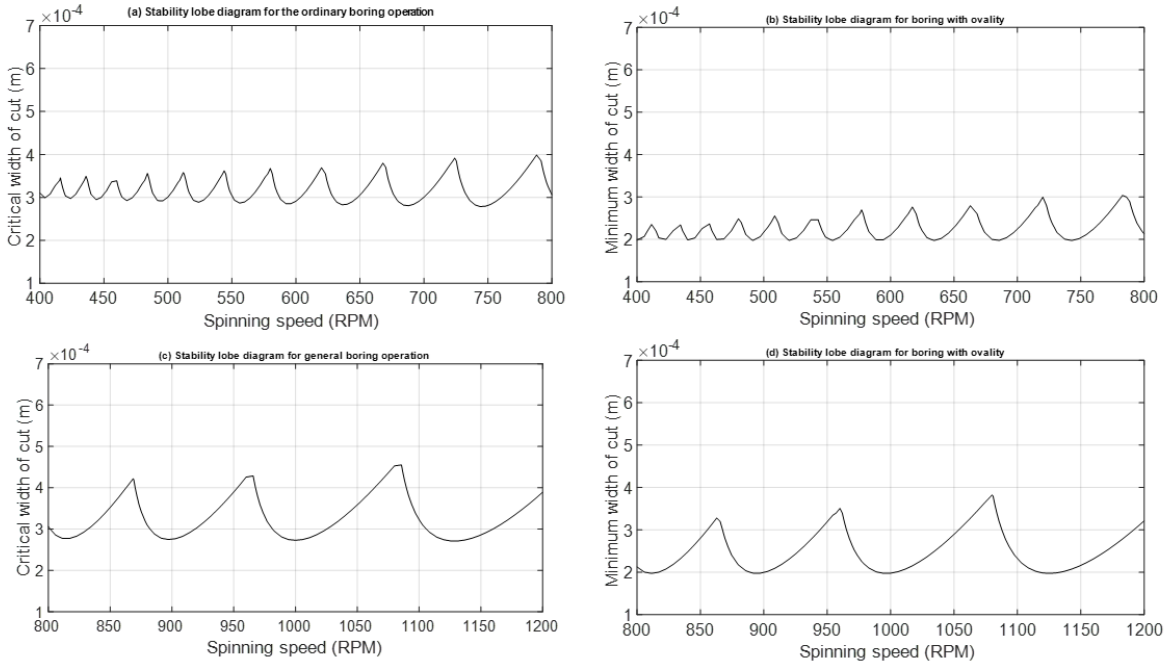

Figure 8.11 Open-loop Stability lobe diagram for boring without and with ovality

In case of the workpiece without ovality, the critical depth of cut is 0.28 mm. To analyse the effect of ovality, a particular case is used with the cavity radius 100 mm (major radius) and 99.9 mm (minor radius). The minimum depth of cut is settled as 0.2 mm. With these parameters, the depth of cut varies from 0.2 mm to 0.3 mm periodically. Figures 8.11 (b) and (d) show the stability lobe diagram for boring operations with ovality. From the figure, it is obvious that as the spinning speed increases there are bigger regions of stability. If there is an eccentricity of 0.05 mm, the actual width or depth of cut varies from 0.2 mm to 0.3 mm periodically. The stability lob diagram is the same as shown in Figure 8.11 (with very minute differences, hence not shown).

b). Performance with active control

For the chatter stability with active damping, control forces are applied along the x-axis only. This ensures the overall stability of a closed-loop system. There is no need to apply forces in z-axis and y-axis. The feedback rate of 20 microns/revolution with the depth of cut 0.6 mm is applied.

The closed-loop system with a stabilizing LSDP controller produces a control force of 120 Newton (when the tool engages with workpiece). If higher feed rates are applied, the amplitude of control forces increases to higher values. Experiments are also conducted with this controller and the pattern of results is quite matching.

The control system should be applied from the start so that the amplitude of control forces does not go to very high values. Without a Band – Pass filter, the LSDP controller has integral action. To remove the steady-state deflection of the cutting tool, the control action is applied in a single direction. This will cause the actuator saturation. This difficulty is removed by using a Band Pass filter of appropriate configuration.

With a stabilizing PD controller, the amplitude of control force decreases to 85 Newton. The PD controller increases the virtual damping of the system. The LSDP controller increases both the dynamic stiffness and virtual damping of the boring bar. There is a requirement of the high control force for the LS controller compared to the PD controller.

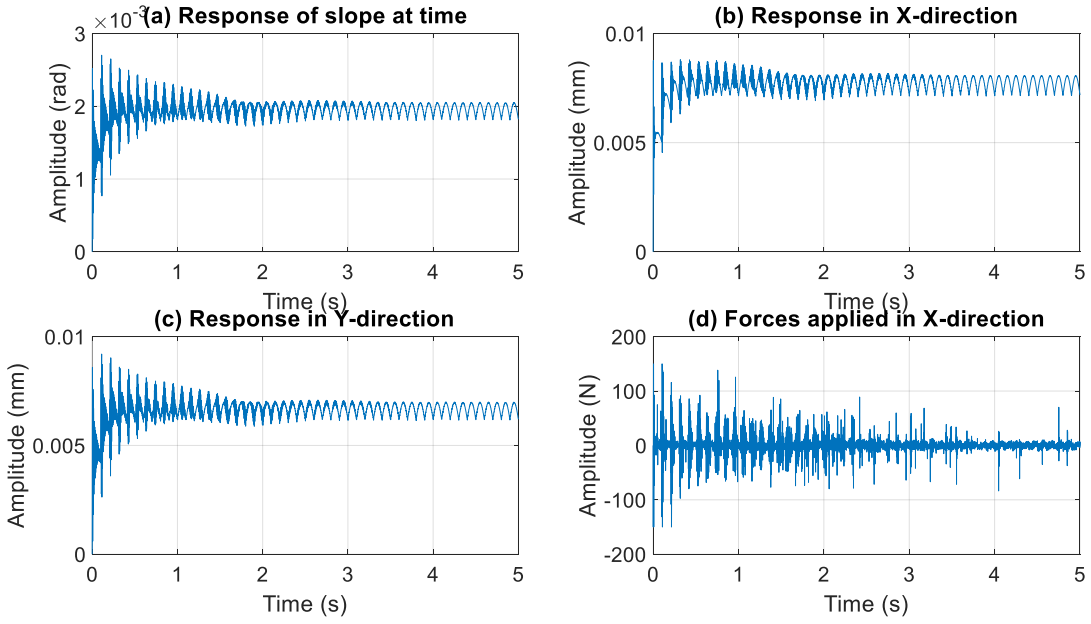

Figure 8.12 Closed loop response the boring process with eccentricity using PD controller (experimental)

In simulations, it is assumed that there is no ovality and eccentricity in the boring operation. However, it is difficult to avoid these faults in real life. The presence of eccentricity makes the response of the system in x-direction and y-direction sinusoidal even if the transients have died. The magnitude of eccentricity is the same as used to construct the stability lobe diagrams. Figure 8.12 shows experimentally measured responses of the boring bar in various directions.

Figure 8.13 shows experimental results for the FOPD controller with 20 microns/revolution feed rate. The response of vibrations in various directions is not sinusoidal after transients are over. This is due to the reason that eccentricity and ovality were completely eliminated in this experimental set. The steady-state deflection approaches a constant value here. The applied force reaches to a virtual zero value (due to the presence of a bandpass filter in the circuit) after dying out of the transients. The sensor/actuator results are converted into microns/Newtons respectively for comparison with simulation results. From the simulated and experimental results, it is obvious that the FOPD controller requires much less amplitude of the control force (35 N). Also, transients are quenched out much quickly with this controller compared to PD and LSDP controllers. For detail the reference (Vashisht et al., 2020) can be referred.

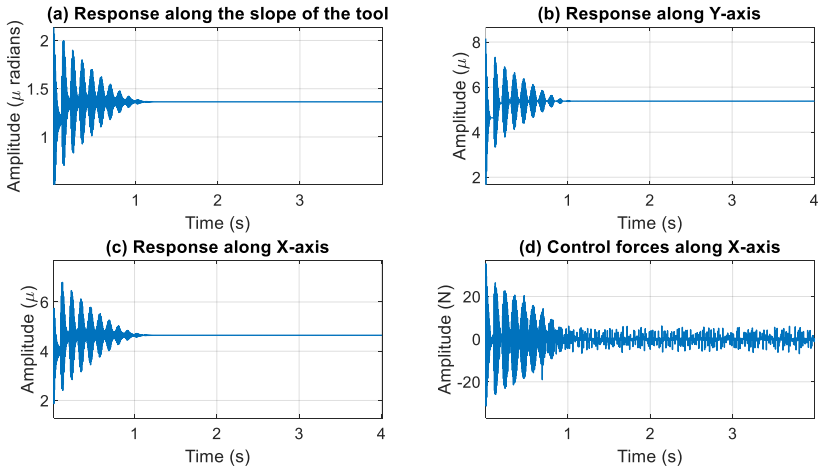

Figure 8.13 Performance of Fractional order PD$^{\lambda}$ controller at 20 microns/rev feed rate (experimental)

8.6. Active chatter control for rotating bar boring operation

8.6.1. Controller design

Similarly, the dynamics of the revolving bar boring operation (in the presence of active feedback control) equation (8.26) can be represented by:

$$\dot{\boldsymbol{X}}(t) = \boldsymbol{A}(t)\,\boldsymbol{X}(t) + \boldsymbol{A_d}(t)\boldsymbol{X}(t-T) \tag{8.36}$$

With matrix in Equation (8.27) converted into the following matrix (using PD control).

$$\boldsymbol{A}(t) = \begin{bmatrix} 0 & 0 & 0 & 1 & 0 & 0 \\ 0 & 0 & 0 & 0 & 1 & 0 \\ 0 & 0 & 0 & 0 & 0 & 1 \\ -\omega^2 - g_{21} b\mu^2\psi_2^2 & -g_{23} b\mu\psi_2^2 & 0 & -2\xi\omega & 0 & 0 \\ -(g_{41}\cos(\chi t) - g_{61}\sin(\chi t))b\mu\psi_1^2 & -\omega^2 - (g_{43}\cos(\chi t) - g_{63}\sin(\chi t))b\psi_1^2 - (K_P)\psi_1\psi_3 & 0 & 0 & -2\xi\omega - (K_D)\psi_1\psi_3 & 0 \\ -(g_{61}\cos(\chi t) + g_{41}\sin(\chi t))b\mu\psi_1^2 & -(g_{63}\cos(\chi t) + g_{43}\sin(\chi t))b\psi_1^2 & -\omega^2 & 0 & 0 & -2\xi\omega \end{bmatrix}$$

(8.37)

In a similar way, PD^{λ} controller can be designed for this system as per section 8.5.3.

8.6.2. Simulation results

a). Open-loop stability analysis

For RB boring operations, the critical depth of cut increases to 1.4 mm (at 600 rpm) under open-loop conditions (Figure 8.14). It is obvious that there is 418% increase (at 600 rpm) in the critical depth of cut. Hence, it is safe to conclude that, stability margins for RB boring operations are much higher than SB boring operations. The simplest method to increase the stable depth of cut is to make the workpiece stationary and boring bar revolving.

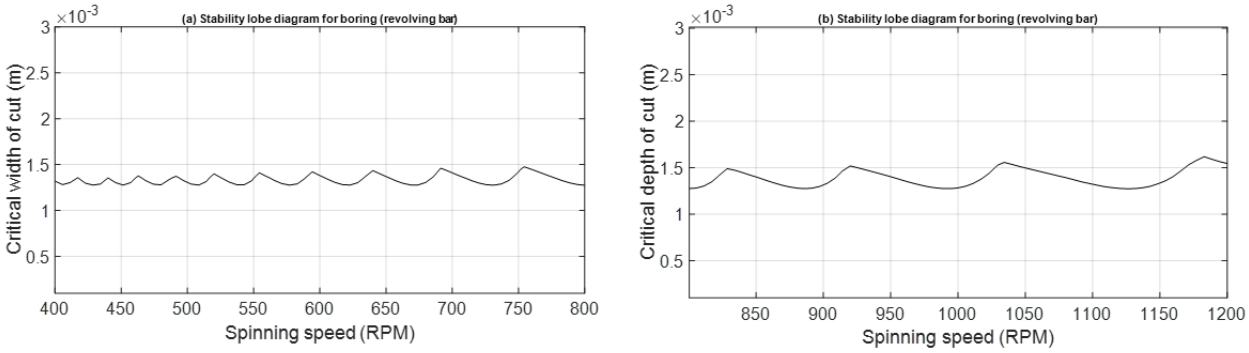

Figure 8.14 Open-loop Stability lobe diagram for boring with revolving bar

b). Performance with active control

The spinning speed of the rotor is taken as 600 rpm and width of the cut as 1.4 mm. There are steady-state vibrations in both horizontal and vertical directions (Figure 8.15). However, the system is stable. Afterwards, the depth of cut is enhanced to 1.6 mm (i.e. in the chatter zone with 14% increase in depth of cut). The feed rate of 5 microns/revolution is fixed. The controller designed in Section 8.6.1 is applied. A control force with an amplitude of 290 Newton is applied by using this stabilizing controller (Figure 8.15, Part (c)). Even for such a low value of feed rate, much higher control forces are required to prevent chatter. Part (d) of Figure 8.15 shows the zoomed view of the control forces applied along the x-axis.

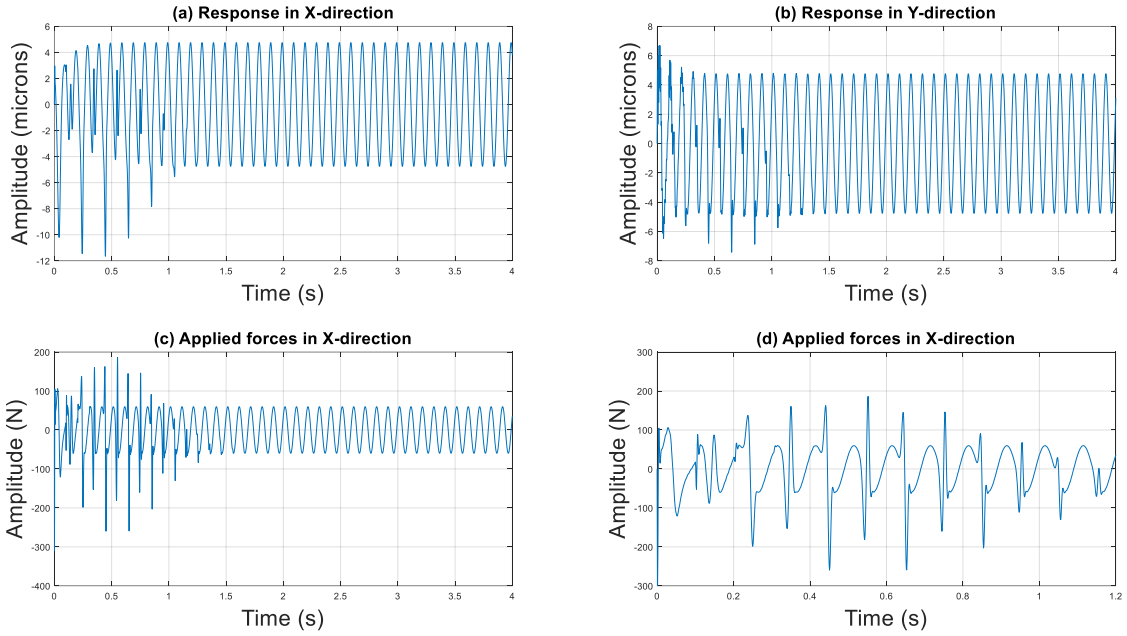

Figure 8.15 Closed loop response of the boring operation (with revolving bar) using PD control

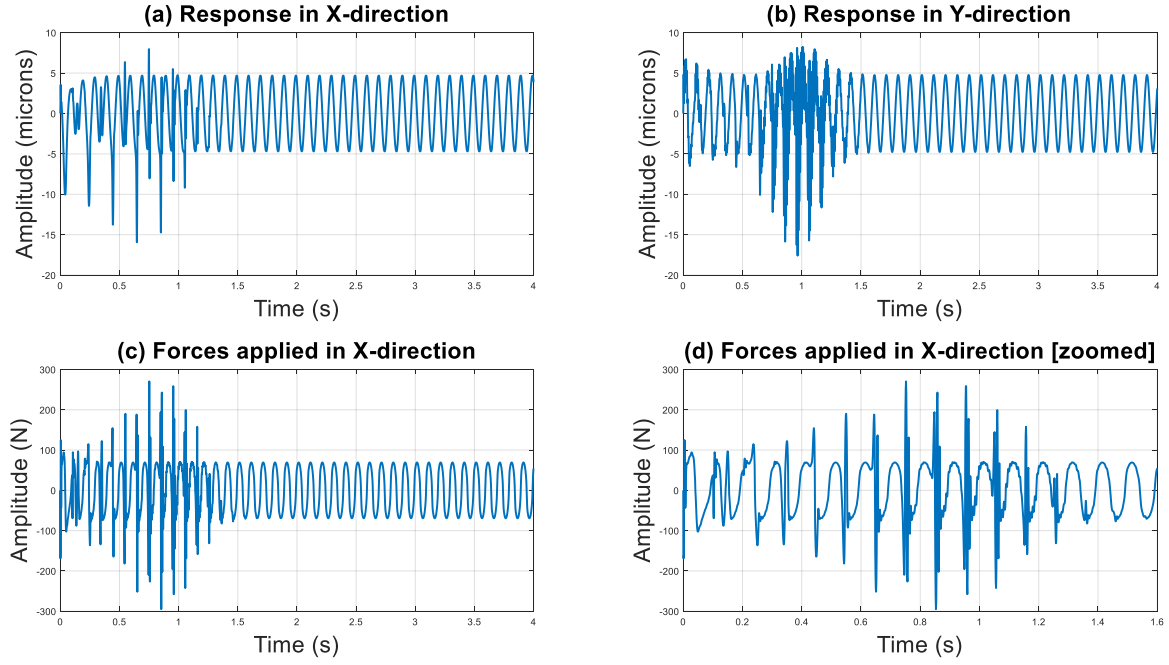

Figure 8.16 Closed loop response of the boring operation (with revolving bar) using PD$^{\lambda}$ controller

Afterwards, fractional-order PD$^{\lambda}$ controller is applied (Figure 8.16). There is no change in the magnitude of control forces required for the stabilization purpose. Also, after the transients are over (nearly after 1.5 seconds), the harmonic component of force (nearly 60 N) remains active.

However, this force can be reduced by switching the PD or PD$^{\lambda}$ controller gains to lower values (Figure 8.17) (i.e. after 2s). The feed rate is slowly increased from 5 microns/r to 20 microns/r (from 4s-7s) (Figure 8.17). With this, the steady-state vibration amplitude keeps on increasing along with the applied control forces. A harmonic force of 100 N is applied to maintain stability and avoid chatter. Obviously, the ACC for RB boring operations above the critical depth is not a good candidate for the active damping treatment. For detail the reference (Vashisht et al., 2020a) can be referred.

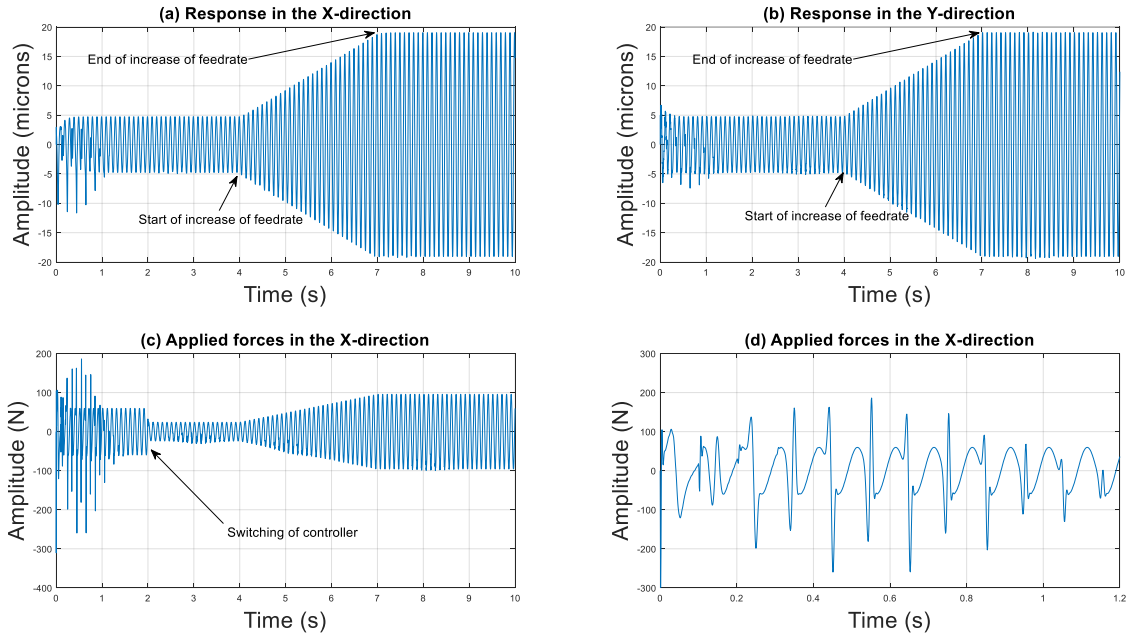

Figure 8.17 Closed-loop response of the boring operation using switching control and time-varying feedback (with revolving bar)

8.7. Concluding remarks

- PS techniques are more efficient in terms of the stability analysis compared to semi-discretization techniques.
- PD controllers are efficient in terms of low peak force requirements. Their efficiency is better than the LSDP type of robust controllers. However, FOPD controllers are most efficient in terms of peak force requirements. The transient response with this controller is superior to other controllers. Hence, small size actuators are required to implement active chatter control using FOPD control techniques.
- The presence of ovality and eccentricity converts the boring operation dynamics from ordinary time-delay equations to time-periodic delay differential equations. PS techniques can be successfully applied for the stability analysis and approximate FOPD controller design for such systems. Using response optimization techniques, the exact parameters of this controller can be obtained.
- The open-loop critical depth of cut for the revolving bar boring operation is much higher than the stationary bar boring operation. The easiest way to increase the critical depth of cut and hence the material removal rate is to make the workpiece stationary and revolve the boring bar.
- However, to further increase the depth of cut, high amplitude sinusoidal forces are required. This makes it an unsuitable candidate for the active damping treatment.
- ACC is quite suitable for SB boring operations but not for RB boring operations. Even by using fractional order PD^{λ} controller no significant improvement is observed.

Chapter 9

Chatter detection in milling operations using Neural Networks

9.1. Overview

In this chapter, three chatter indicators for milling operation are provided based on Hilbert Huang Transformations, short-time Fourier transform and locus of the milling cutter at sampling frequency synchronous to per revolution frequency. Convolutional neural network (CNN) system based on machine/deep learning is proposed for the chatter detection based on these indicators. It is observed that even in the chatter-free zones, the amplitude of vibrations of the cutting tool varies a lot and depends on the spinning speed of milling tools. For a better surface finish of the workpiece, this amplitude should be kept at the minimum level. Theoretically, during chatter, due to the regenerative effect, the amplitude of vibrations increases infinitely. However, practically, due to the disengagement of the cutting tool and workpiece, the amplitude of vibrations remains finite. Certain modifications are presented in the dynamic equations of motion of the milling operation, which can be used to find the amplitude of vibrations during chatter conditions. The simulated data generated in this way is used to train a CNN. The trained CNN is then used to detect chatter in an online manner. The results show the maximum 99.8% accuracy even in the presence of the measurement noise with a signal-to-noise ratio of 20 dB.

9.2. Dynamic modelling of milling operations

The dynamic model of the milling process can be represented by the following equation (Insperger et al., 2004).

$$\begin{bmatrix}\ddot{x}(t)\\ \ddot{y}(t)\end{bmatrix}+\begin{bmatrix}2\xi\omega & 0\\ 0 & 2\xi\omega\end{bmatrix}\begin{bmatrix}\dot{x}(t)\\ \dot{y}(t)\end{bmatrix}+\begin{bmatrix}\omega^2 & 0\\ 0 & \omega^2\end{bmatrix}\begin{bmatrix}x(t)\\ y(t)\end{bmatrix}=\left(\frac{1}{m}\right)w\begin{bmatrix}h_{xx}(t) & h_{xy}(t)\\ h_{yx}(t) & h_{yy}(t)\end{bmatrix}\begin{bmatrix}a_0+x(t-\tau)-x(t)\\ y(t-\tau)-y(t)\end{bmatrix} \tag{9.1}$$

where $x(t), \dot{x}(t)$ and $\ddot{x}(t)$ represent the displacement, velocity and acceleration respectively of the tool in the feed direction. Similarly, ys represents corresponding quantities in the direction perpendicular to the feed direction. ξ is the damping ratio and ω represents the natural frequency of the milling cutter (tool). w is the axial width of cut and m is the modal mass. a_0 is the feed rate (in meters/tooth pass) of the cutting tool. $x(t-\tau)$ and $y(t-\tau)$ are displacements of the cutting tool in the appropriate directions τ time ago in which:

$$\tau=\frac{60}{N\Omega} \tag{9.2}$$

where N is the number of teeth in the cutter and Ω is the spinning speed of the cutter in revolutions per minute. The other quantities are given below (Insperger et al. 2004).

$$\begin{aligned}
h_{xx}(t)&=\sum_{j=1}^{N} g[\phi_j(t)]\sin\left(\phi_j(t)\right)\left(K_t\cos\left(\phi_j(t)\right)+K_n\sin\left(\phi_j(t)\right)\right)\\
h_{xy}(t)&=\sum_{j=1}^{N} g[\phi_j(t)]\cos\left(\phi_j(t)\right)\left(K_t\cos\left(\phi_j(t)\right)+K_n\sin\left(\phi_j(t)\right)\right)\\
h_{yx}(t)&=\sum_{j=1}^{N} g[\phi_j(t)]\sin\left(\phi_j(t)\right)\left(-K_t\sin\left(\phi_j(t)\right)+K_n\cos\left(\phi_j(t)\right)\right)\\
h_{yy}(t)&=\sum_{j=1}^{N} g[\phi_j(t)]\cos\left(\phi_j(t)\right)\left(-K_t\sin\left(\phi_j(t)\right)+K_n\cos\left(\phi_j(t)\right)\right)
\end{aligned} \tag{9.3}$$

With

$$\phi_j(t)=\left(\frac{2\pi\Omega}{60}\right)t+j\frac{2\pi}{N} \tag{9.4}$$

$$g[\phi_j(t)]=\begin{cases}1 & \text{if } \phi_{st}<\phi_j(t)<\phi_{ex}\\ 0 & \text{otherwise}\end{cases} \tag{9.5}$$

where ϕ_{st} and ϕ_{ex} are start and exit immersion angles respectively. For up milling (present case) $\phi_{st} = 0$ and $\phi_{ex} = \arccos\left(1 - 2\frac{a}{D}\right)$. Here $\frac{a}{D}$ is the radial depth of cut ratio (Figure 9.1).

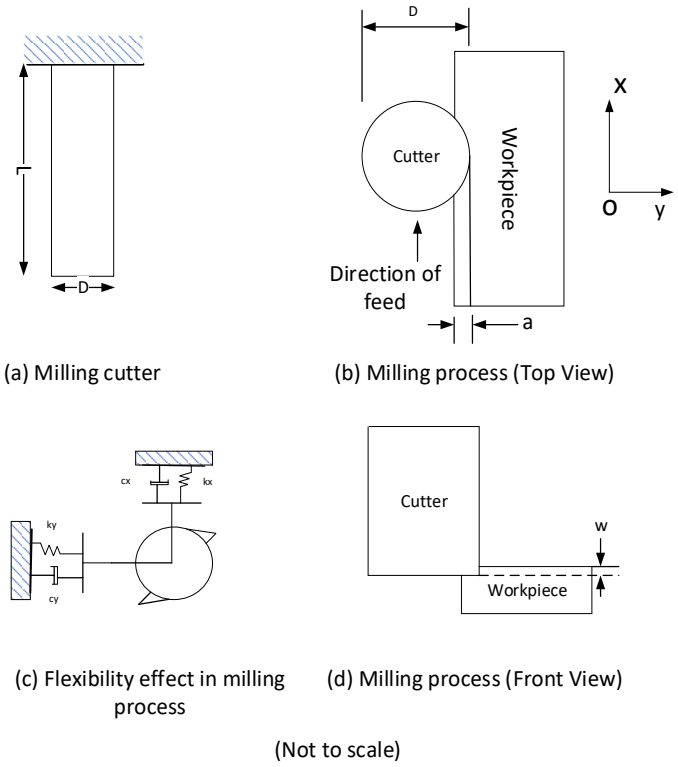

Figure 9.1 Geometric parameter representation of the milling tool

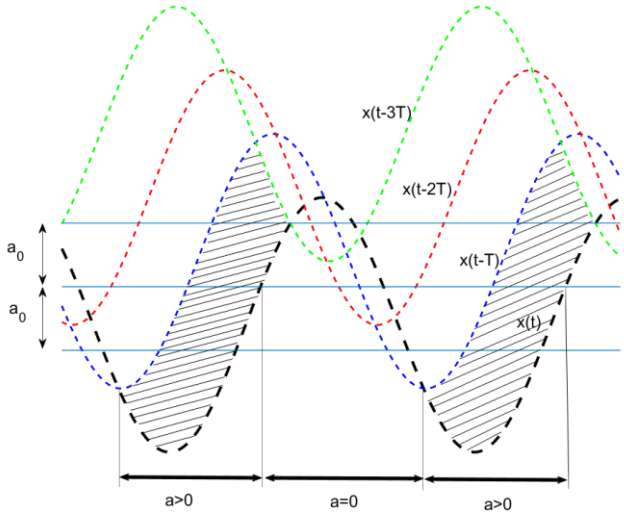

Figure 9.2 Geometric parameters of the cutting surface when the tool leaves the workpiece

When simulations are carried out using Equation 9.1, the tool displacement from the equilibrium position along the feed direction as well as perpendicular to the feed direction can be calculated. Due to the presence of delay in these equations, the simulation system becomes unstable for certain combinations of axial width of cut and spinning speed of the milling tool. Theoretically, the amplitude of vibration becomes infinite under these unstable conditions. However, under practical conditions, the amplitude of vibration remains finite. This happens because the tool leaves the workpiece during the certain portion of the cutting period and the amplitude of applied forces remains finite. This is called a flyover effect. By writing Equation (9.1) in the following form.

$$\begin{bmatrix} \ddot{x}(t) \\ \ddot{y}(t) \end{bmatrix} + \begin{bmatrix} 2\xi\omega & 0 \\ 0 & 2\xi\omega \end{bmatrix} \begin{bmatrix} \dot{x}(t) \\ \dot{y}(t) \end{bmatrix} + \begin{bmatrix} \omega^2 & 0 \\ 0 & \omega^2 \end{bmatrix} \begin{bmatrix} x(t) \\ y(t) \end{bmatrix} = \left(\frac{1}{m}\right) \begin{bmatrix} F_x(t) \\ F_y(t) \end{bmatrix} \tag{9.6}$$

with

$$\begin{bmatrix} F_x(t) \\ F_y(t) \end{bmatrix} = \begin{bmatrix} wh_{xx}(t) & wh_{xy}(t) \\ wh_{yx}(t) & wh_{yy}(t) \end{bmatrix} \begin{bmatrix} a_0 + x_T - x(t) \\ y_T - y(t) \end{bmatrix} \tag{9.7}$$

where F_x (t) and F_y (t) are the cutting forces in the feed and perpendicular to feed direction, respectively. Time delay terms are important and hence we are writing x_T=x(t-τ) and y_T=y(t-τ) in these equations. More precise values for x_T and y_T should be considered to model the flyover effect. That means more than one proceeding milling tool revolution must be considered in the analysis (Figure 9.2). In that case (Jemielniak et al., 1989):

x_T= minimum [x(t), a_0 +x(t-2τ), 2a_0+x(t-3τ), ……, n a_0 +x(t-(n+1)τ)] (9.8)

and

y_T= minimum [y(t), y(t-2τ), y(t-3τ), ……, y(t-(n+1)τ)] (9.9)

Following relations are used to calculate cutting forces.

$$F_x(t) = \begin{cases} wh_{xx}(t)x^* + wh_{xy}(t)y^* & if\ x^* > 0 \text{ and } y^* > 0 \\ wh_{xx}(t)x^* & if\ x^* > 0 \text{ and } y^* < 0 \\ wh_{xy}(t)y^* & if\ x^* < 0 \text{ and } y^* > 0 \\ 0 & if\ x^* < 0 \text{ and } y^* < 0 \end{cases}$$

and (9.10, 9.11)

$$F_y(t) = \begin{cases} wh_{yx}(t)x^* + wh_{yy}(t)y^* & if\ x^* > 0 \text{ and } y^* > 0 \\ wh_{yx}(t)x^* & if\ x^* > 0 \text{ and } y^* < 0 \\ wh_{yy}(t)y^* & if\ x^* < 0 \text{ and } y^* > 0 \\ 0 & if\ x^* < 0 \text{ and } y^* < 0 \end{cases}$$

with

$$x^* = a_0 + x_T - x(t) \tag{9.12}$$

and

$$y^* = y_T - y(t) \tag{9.13}$$

Figure 9.2 shows the graphical representation of selecting a delay term in the feed direction. In a similar way, the delay terms in the perpendicular to feed direction can be calculated. Choosing the cutting forces in this way, simulation results can effectively take into account the flyover effect. With this arrangement, through simulations, we can effectively predict the behaviour of the system during chatter conditions. Jemielniak et al. (1989) suggested that this effect must be taken into consideration for effectively designing any chatter detection strategy. The milling tool behaviour can be better understood using these sets of equations. The pattern of cutting forces predicted by this method gives new understanding to chatter phenomena.

9.3. Comparison of simulation results with literature and experimental results

To validate the simulation results, the experiment is conducted. Results are also compared with solutions in the literature (Mann, 2003, Insperger et al. 2003).

9.3.1. Simulation model

A carbide end mill with a diameter 19.05 mm (3/4 inch) with a single flute is used (the second flute is grounded to avoid any contribution of asymmetry or runout). A radial immersion of a=4.515 mm is fixed so that the radial immersion ratio of $\frac{a}{D}$=0.237 is used. The up-milling is conducted for aluminium (i.e. 7075-T6). The cutting coefficients in the tangential and normal direction are calculated by using Kistler rigid dynamometer. Estimated values of these coefficients are $K_n=2.1x10^8$ N/m^2 and $K_t=5.6x10^8$ N/m^2. These values are similar to those in references (Mann 2003, Insperger et al. 2003). Modal parameters of the cutting tool (i.e. milling cutter) are in good agreement with these references. These values are intentionally chosen to verify the respective results with the previously available results. Impact testing using an impact hammer is used to experimentally estimate the modal parameters of the milling tool. The first modal frequency is estimated to be 146 Hz with modal damping ratio 0.003. The estimated modal mass is 2.6 Kg. The tool feed per revolution is fixed at 0.1 mm.

9.3.2. Experimental setup

The schematic of the experimental setup is shown in Figure 9.3. Components of the experimental setup can be found in previous chapters.

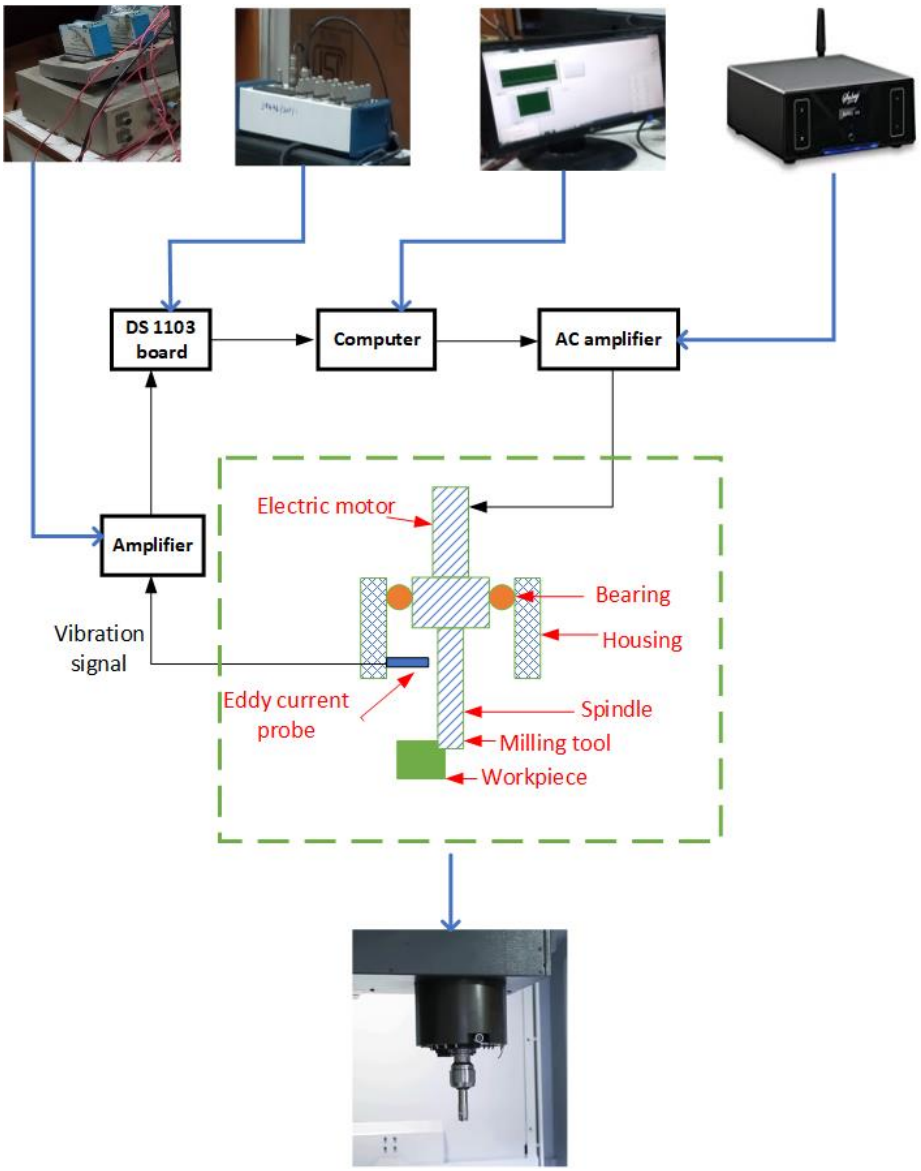

Figure 9.3 Schematic of the milling process with corresponding sensors

9.3.3. Stability lobe diagrams

The regenerative process in metal cutting processes is the main source of instability. In literature, single and two-degree-of-freedom models of the milling tool had been used for analysis. In this research, a two-degree-of-freedom model is built with the flexibility of the tool in feed and perpendicular to the feed direction. Equation (9.1) can be written in the first-order form in a state-space form as follows.

$$\dot{\boldsymbol{X}}(t) = \boldsymbol{A}(t)\boldsymbol{X}(t) + \boldsymbol{A}_d(t)\boldsymbol{X}(t-\tau) \tag{9.14}$$

with

$$\boldsymbol{A}(t) = \begin{bmatrix} 0 & 0 & 1 & 0 \\ 0 & 0 & 0 & 1 \\ -\omega^2 - \frac{wh_{xx}(t)}{m} & -\frac{wh_{xy}(t)}{m} & -2\xi\omega & 0 \\ -\frac{wh_{yx}(t)}{m} & -\omega^2 - \frac{wh_{yy}(t)}{m} & 0 & -2\xi\omega \end{bmatrix}$$

$$\boldsymbol{A}_d(t) = \begin{bmatrix} 0 & 0 & 0 & 0 \\ 0 & 0 & 0 & 0 \\ \frac{wh_{xx}(t)}{m} & \frac{wh_{xy}(t)}{m} & 0 & 0 \\ \frac{wh_{yx}(t)}{m} & \frac{wh_{yy}(t)}{m} & 0 & 0 \end{bmatrix}$$

Such that

$$\boldsymbol{X}(t) = \begin{bmatrix} x(t) \\ y(t) \\ \dot{x}(t) \\ \dot{y}(t) \end{bmatrix} \text{ and } \boldsymbol{X}(t-\tau) = \begin{bmatrix} x(t-\tau) \\ y(t-\tau) \\ \dot{x}(t-\tau) \\ \dot{y}(t-\tau) \end{bmatrix} \tag{9.15a, 9.15b, 9.15c, 9.15d}$$

The simulation model discussed in Section 9.3.1 is used for constructing stability lobe diagrams. The spinning speed ranging from 2900 r.p.m. to 3800 r.p.m. is considered. Same parameters in references (Mann 2003, Insperger et al. 2003) are taken so that a valid comparison can be made between simulations, our experimental results and in these references. The semi-discretization method discussed in reference (Insperger et al., 2004) is used to construct the stability lobe diagram based on Equation (9.14-9.15). Two specific points at 3300 rpm and 3650 rpm. are taken in the chatter zone (dark area) to observe the behaviour during chatter conditions. Figure 9.4 shows the corresponding stability lobe diagram.

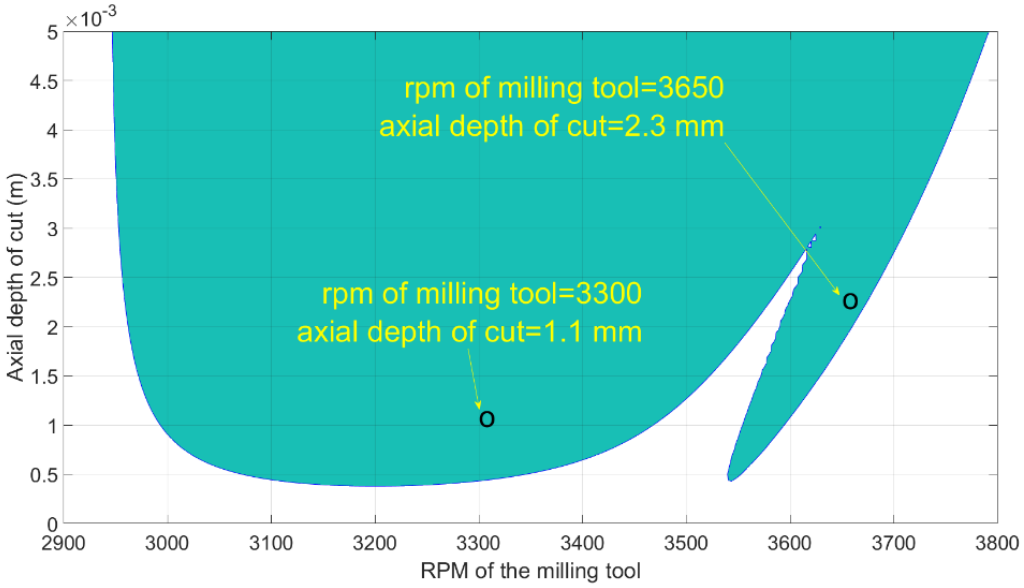

Figure 9.4 Stability lobe diagram for a specified range

9.3.4. Simulation vs experimental results

For comparing simulation results with our experimental results and those in literature (Mann 2003, Insperger et al. 2003), Figures 9.5 and 9.6 are generated.

(a) Simulation time response for 3300 rpm

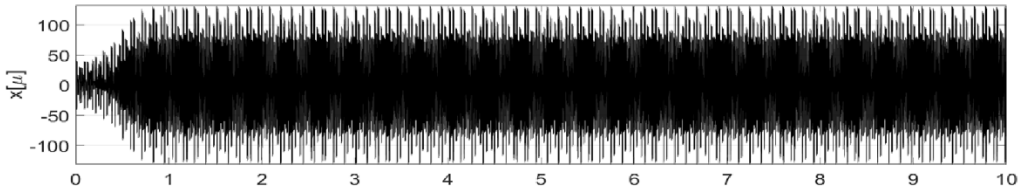

(b) Simulation per revolution time response for 3300 rpm

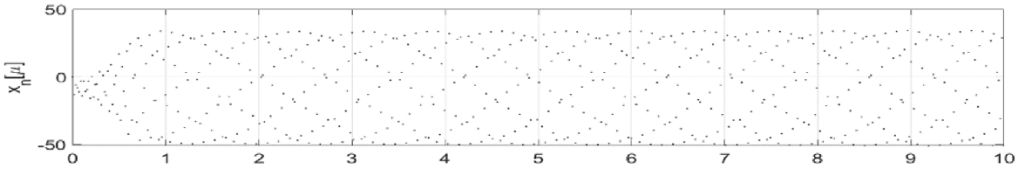

(c) Practical time response for 3300 rpm

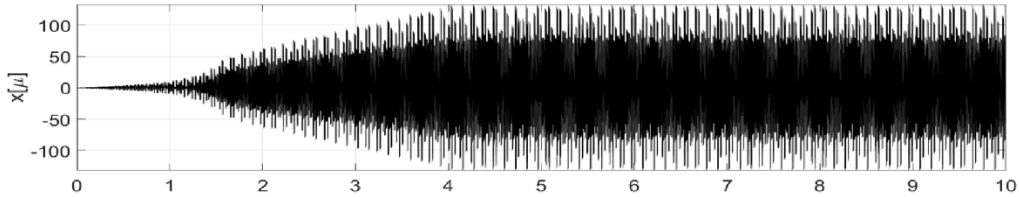

(d) Practical per revolution time response for 3300 rpm

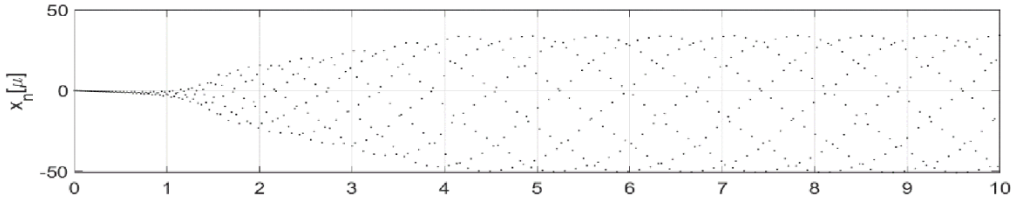

(e) Mann (2003) and Insperger et al. (2003) based time response for 3300 rpm

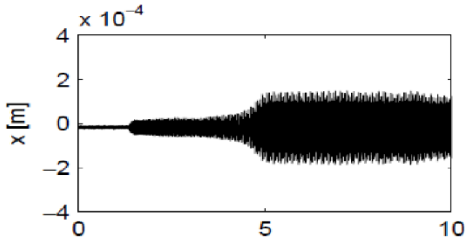

(f) Mann (2003) and Insperger et al. (2003) based per revolution time response for 3300 rpm

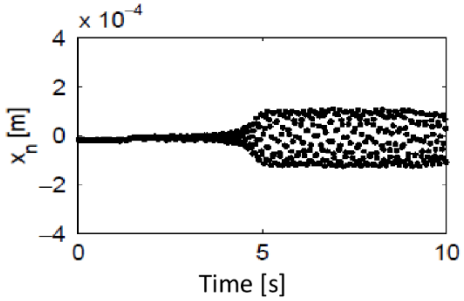

Figure 9.5 Comparison of simulation results with experimental results at 3300 rpm

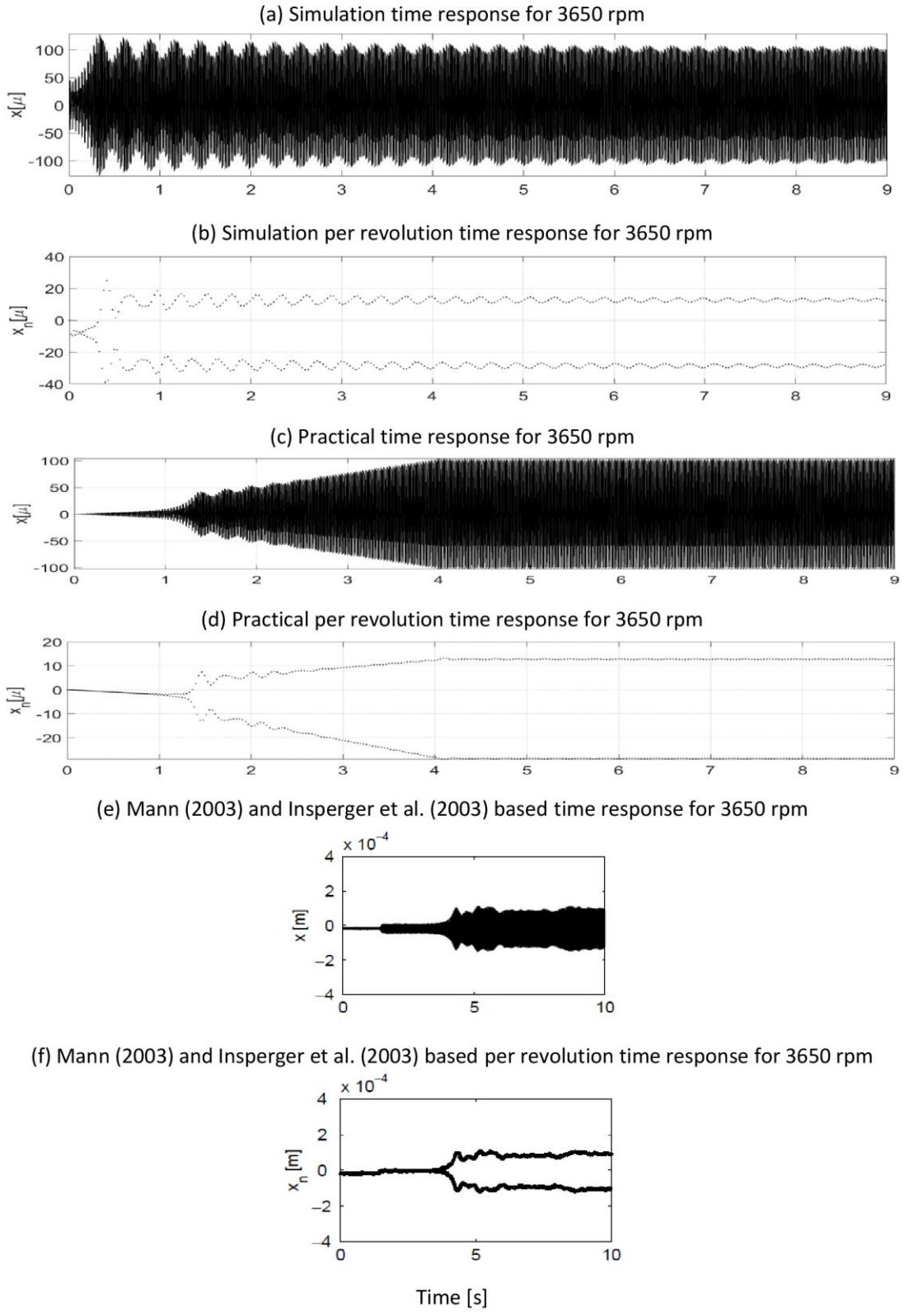

Figure 9.6 Comparison of simulation results with experimental results at 3650 rpm.

First of all, results are compared at 3300 rpm. Two different sampling frequencies are used in the data collection. Firstly, the sampling frequency is taken as 2kHz. Parts (a), (c) and (e) of Figure 9.5 represent the signal in the feed direction. Secondly, per revolution sampling frequency is taken (3300/60=55 Hz). Since the second tooth of the milling tool is grounded, it also corresponds to the tooth pass frequency. Parts (b), (d) and (f) represent the signal corresponding to this frequency. During experimentation, the feed rate is progressively increased so that the feed rate of 0.1 mm/r is obtained in 4 seconds starting from zero. After the steady-state, the simulated amplitude of vibration matches well with experimental results as well as results from the literature. Similar is the case with 3650 rpm, spinning speed. Period double vibrations are obvious in Figure 9.6. With these comparisons, it is obvious that our simulation technique is correct and can be used to design a suitable chatter detection strategy using simulation assisted data.

9.4 The amplitude of tool vibrations and tool forces during chatter

It is a common myth that chatter corresponds to high amplitude vibrations only. To investigate it thoroughly, the situation at points marked in a stability lobe diagram shown in Figure 9.7 is considered.

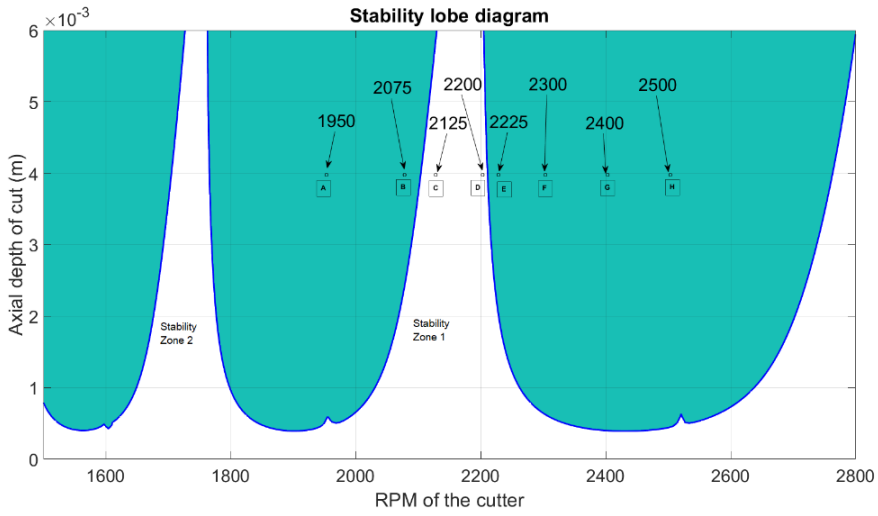

Figure 9.7 Stability lobe diagram for the system under analysis

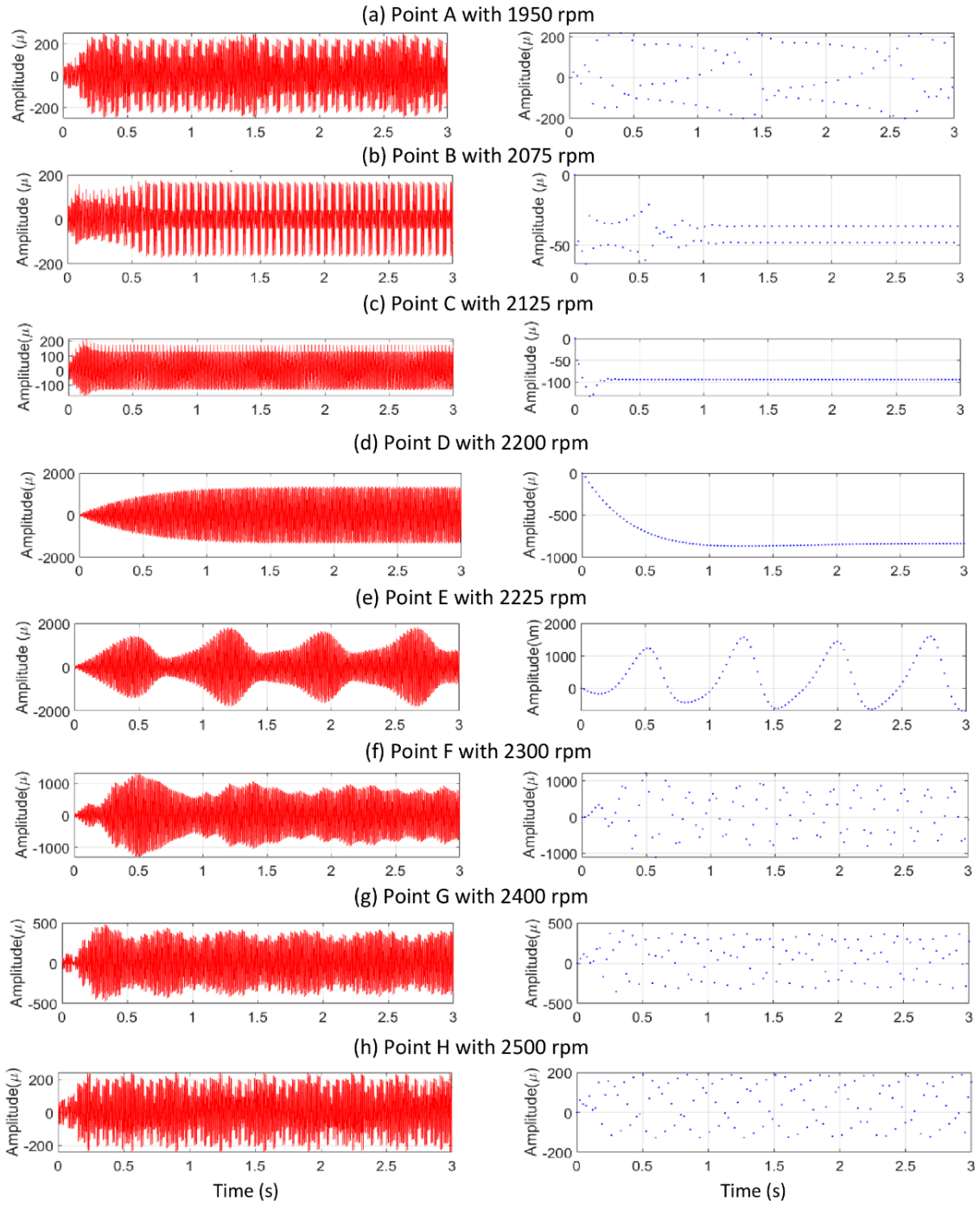

Figure 9.8 Amplitude of vibration (in x-direction i.e. feed direction) at a different spinning speed of milling tool

Two stability lobes are considered in this figure. Dark areas represent the unstable zone. Only points in the range 2125 -2200 rpm are stable (corresponding to 4 mm axial depth of cut).

This stability zone is termed as number 1. The other stability zone is termed as number 2. Another stability zone is in the range of 1700-1750 rpm. At other depth of cuts, there is some variation in spinning speed. The interest is to work in this narrow range so that that maximum axial depth of cut can be obtained corresponding to that spinning rate. The unstable points are considered towards the left and right of stability zone 1. Point B with 2075 rpm is under chatter conditions (Figure 9.8). The amplitude of vibrations is nearly 200 microns. Similarly, at point E with 2225 rpm. the amplitude of vibration of the milling tool in the feed direction is near 1800 microns. The amplitude of vibrations is minimum at point C with 2125 rpm (stable point). However, point D with 2200 rpm is also stable with an amplitude of vibration near 1600 microns. Hence, the amplitude of vibration is not the criterion for chatter. As towards the right, the amplitude of vibration decreases. The second column of this figure shows the response at per revolution sampling rate (also known as tooth pass frequency). The scattering of response is a better indicator of chatter.

9.5. Presence of multiple chatter frequencies

The displacement of the cutting tool in the feed direction is simplified as follows.

$$\ddot{x}(t) + 2\xi\omega\dot{x}(t) + \omega^2 x(t) = -\frac{w}{m} h_{xx}(t)\left[a_0 + x(t) - x(t-\tau)\right] \tag{9.16}$$

Response x(t) is composed of the following components.

$$x(t) = a_0 + x_p(t) + \eta(t) \tag{9.17}$$

where a_0 is the feed per tooth pass, $x_p(t)$ is the forced periodic response of the system when no self-excited vibrations are present. For $x_p(t) = x_p(t+\tau)$, $\eta(t)$ is the response due to self-excited vibrations at chatter frequencies. During chatter, this response component is as follows (Insperger et al. 2003).

$$\ddot{\eta}(t) + 2\xi\omega\dot{\eta}(t) + \omega^2\eta(t) = -\frac{w}{m} h_{xx}(t)\left[\eta(t) - \eta(t-\tau)\right] \tag{9.18}$$

Stability properties of this equation can be determined by the infinite number of characteristic multipliers. Floquet theory for delay differential equations can be applied to determine the stability. If $\mu = e^{\lambda\tau}$ is a characteristic multiplier, there exists a solution of Equation (9.18) in the following form.

$$\eta(t) = p(t)e^{\lambda t} + \bar{p}(t)e^{\bar{\lambda} t} \tag{9.19}$$

where $p(t) = p(t+\tau)$ is a periodic function, λ is a so-called characteristic exponent and the bar denotes the complex conjugates. This equation is stable if all the characteristic multipliers have the modulus less than 1. The characteristic multipliers of Equation (9.14) can be located in the following ways.

1. In case 1, These can be located on the unit circle as complex pairs (i.e. $|\mu| = |\bar{\mu}| = 1,$). This is equivalent to Hopf Bifurcations of autonomous systems.
2. In case 2, $\mu = 1,$ these are equivalent to saddle-node bifurcations of autonomous systems.
3. In case 3, $\mu = -1,$ these are called period two, flip bifurcations.

As suggested by Insperger et al. (2003), case 2, $\mu = 1,$ can not arise in Equation (9.18). First of all, for case 1, $|\mu| = |\bar{\mu}| = 1$. In this case, $\lambda = i\omega$ is pure imaginary where $\omega = \dfrac{\ln(\mu)}{\tau}$. Since the complex function is periodic, the logarithmic function is not unique in the complex plane. Hence, multiple chatter frequencies exist in the solution. This shows that frequencies arising in Equation (9.18) for the signal $\eta(t)$ are as follows (Insperger et al. 2003).

$$f_H = \left[\pm\omega + n\frac{2\pi}{\tau} \right] [rad/s] \tag{9.20}$$

In the above expression, the index f_H is for secondary Hopf bifurcations. For period-doubling bifurcations where $\mu = -1$ (case 3), the characteristic exponent is given $\lambda = \frac{\ln(-1)}{\tau}$. Frequencies, in that case, are as follows (Insperger et al. 2003).

$$f_{PD} = \left[\frac{\pi}{\tau} + n\frac{2\pi}{\tau}\right][rad/s] \tag{9.21}$$

where index f_{PD} is for period-doubling bifurcations. Based on the above discussion, Figure 9.9 is constructed for spinning speeds of the milling cutter in the range 2200 to 2500 rpm.

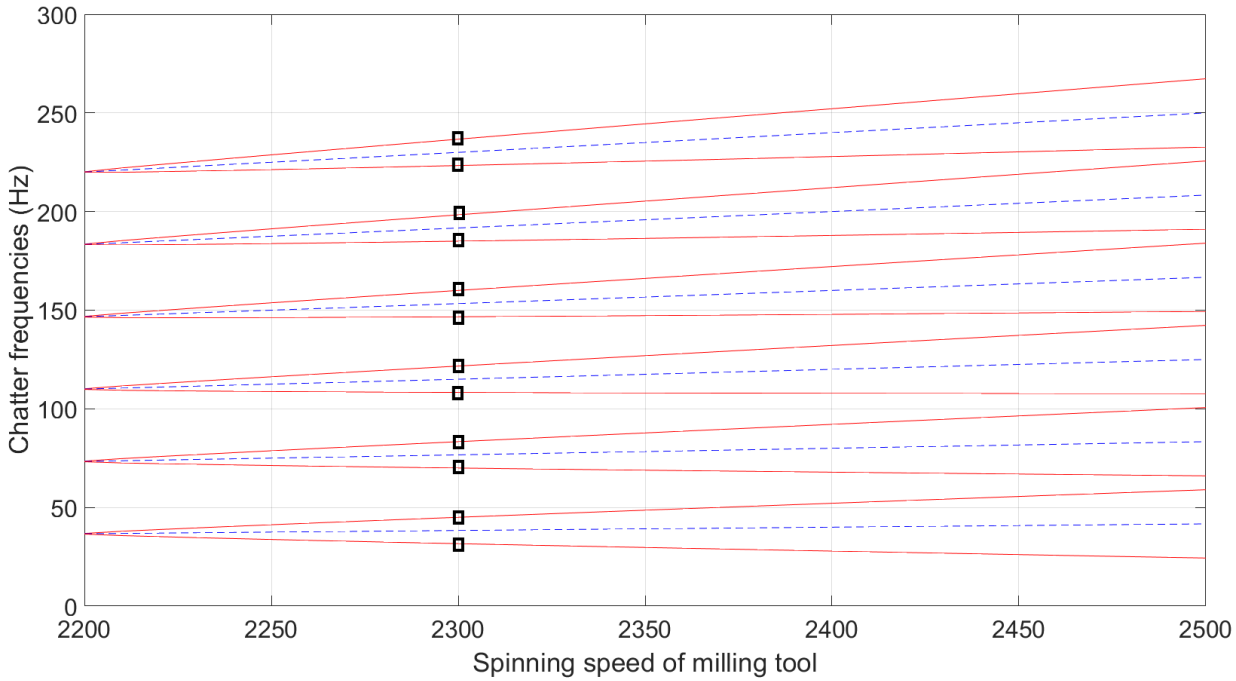

Figure 9.9 Chatter frequencies as a function of spinning speed of milling cutter

9.6. Chatter indicators

Based on simulated data, using various signal processing techniques, different characteristics are observed that can be used to indicate the presence of chatter in the machining processes. First, a brief introduction of these techniques is as follows.

9.6.1. Hilbert Huang Transformations based indicators

Using Equations 9.1-9.13, for simulation purposes, the displacement of the milling tool in the feed direction is calculated. Using Hilbert Huang Transformations (HHT), the instantaneous frequency of the signal as a function of time is calculated at various spinning speeds of the milling cutter. Figure 9.10 shows that plot. Following spinning speeds are considered: 1950, 2075, 2125, 2200, 2225, 2300, 2400 and 2500 rpm. Under noise-free simulations, instantaneous frequencies as a function of time are shown in this figure. As the spinning rate of the milling cutter changes, there are unique instantaneous frequency patterns associated with each spinning rate. This feature can be used as the chatter indicator. At 2125 rpm. the instantaneous frequency ranges from 120-150 Hz. It is a chatter-free case. The amplitude of vibrations is also minimum at this spinning rate. Although 2200 rpm case is also chatter-free, the amplitude of vibrations is much higher (1350 microns compared to 175 microns) at this spinning rate (Figure 9.8). From Figure 9.10, it is obvious that this pattern is independent of the displacement amplitude of the milling tool. The advantage of this technique is that the instantaneous frequency range can easily be calculated.

However, there are certain limitations to this approach. The sensitivity of this approach is highly dependent on the noise present in the data. Figure 9.11 shows the effect of noise on the HHT at different spinning rates. Spinning rate of 2175 rpm. (chatter-free case) and 2225 rpm. (with chatter) are considered in this figure. It is observed that as the Signal-to-Noise-Ratio (SNR) approaches 20 dB, it becomes difficult to distinguish between the chatter-free and with chatter case. Discrete wavelet transformations (DWT) as well as HHT (by selectively choosing the Intrinsic Mode Functions) can be used to denoise the signal. However, limited success is achieved using these techniques.

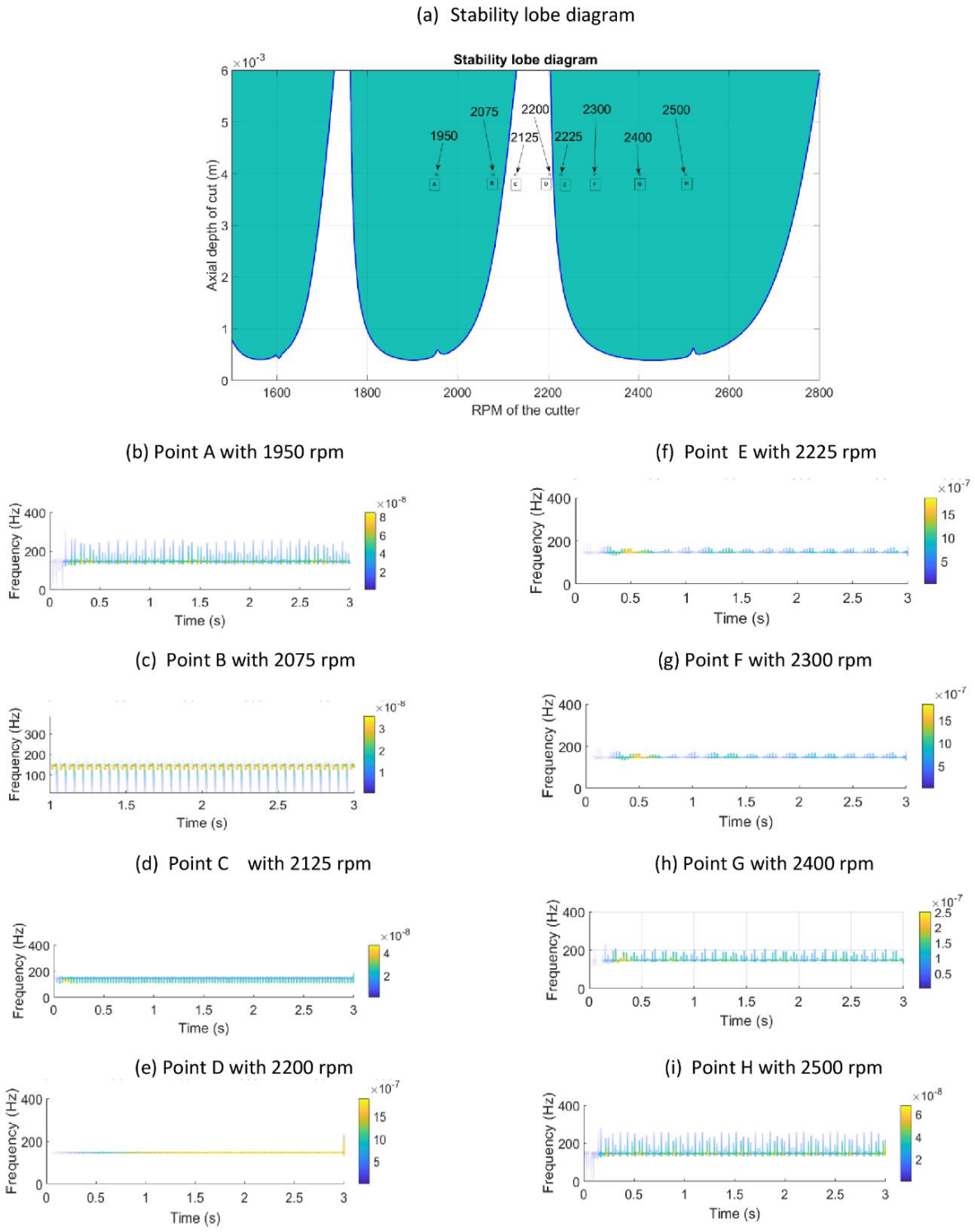

Figure 9.10 Instantaneous frequencies as a function spinning speed of milling tool (axial depth of cut is 4 mm)

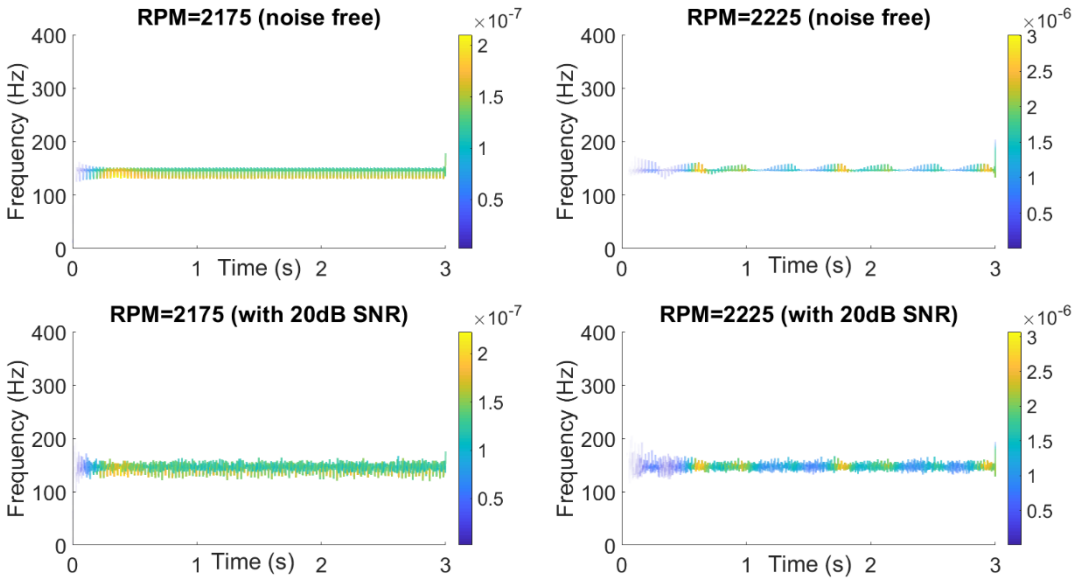

Figure 9.11 Effect of noise on instantaneous frequencies

9.6.2. Short time Fourier Transformation based indicators

Short time Fourier Transformation (STFT) of the displacement of the milling tool is generated. A sampling frequency of 2000 Hz is used to collect the signal as shown in Figure 9.12. Power Spectral Densities, as well as Spectrograms, are shown in this figure. Spinning speed from 1950 to 2500 rpm is used in this analysis. In the spinning rate 1950-2075 rpm and 2225-2500 rpm chatter conditions prevail in the system. Multiple chatter frequencies are also present in the signal. Figure 9.9 shows the chatter frequencies in the range 2200 to 2500 rpm. As discussed in the next section, convolutional neural networks can be used to classify images. A properly trained neural network can distinguish the chatter and chatter-free conditions.

However, the measurement noise is inevitable. In the noise presence, the difference in spectrogram characteristics (with and without chatter) drastically reduces. Figure 9.13 represents a particular case showing the effect of noise on the power spectral density. Spinning speeds of 2175 rpm (chatter-free case) and 2225 rpm (chatter conditions) are considered in the analysis.

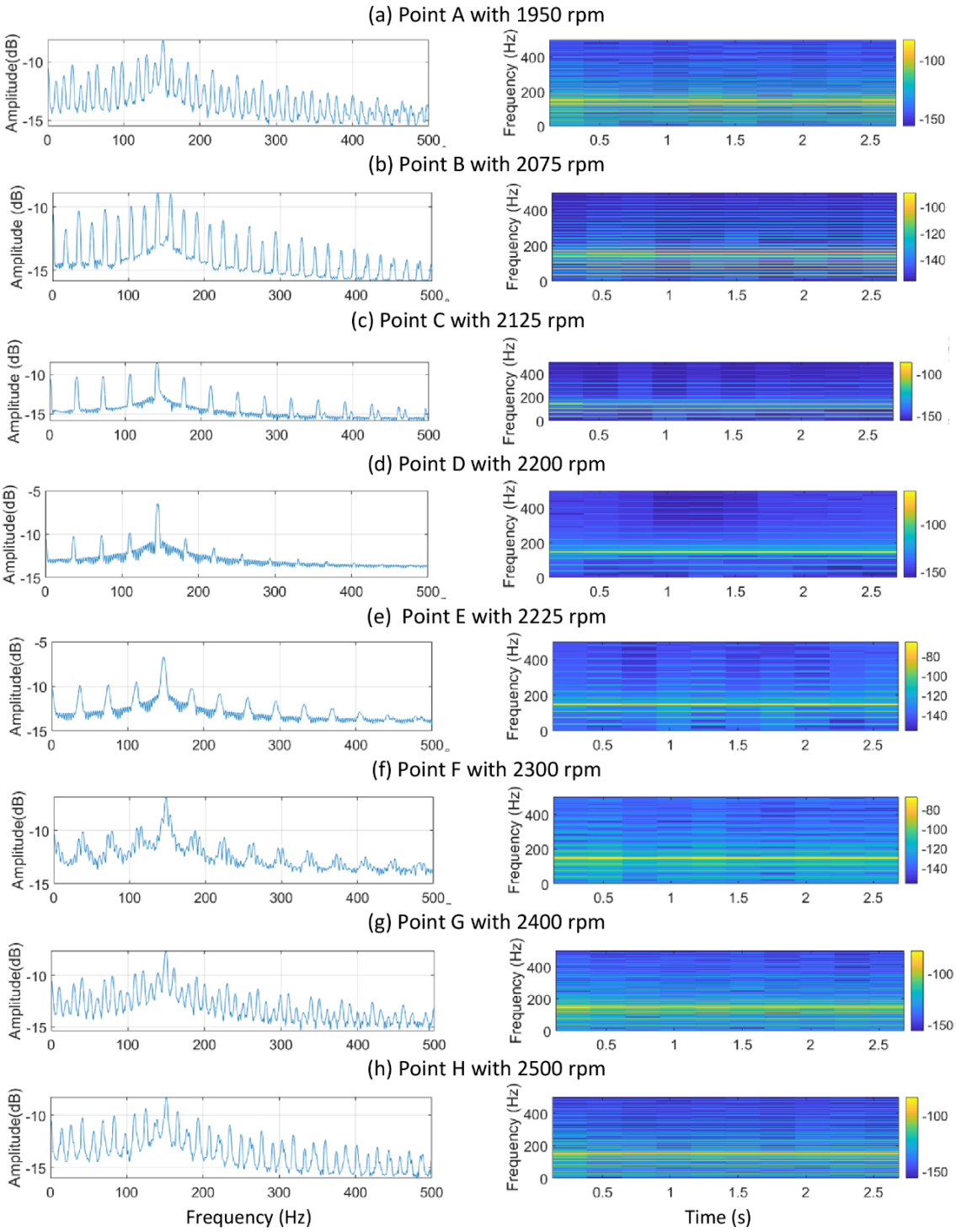

Figure 9.12 STFT as a function of spinning speed of milling tool (at 4 mm axial depth of cut)

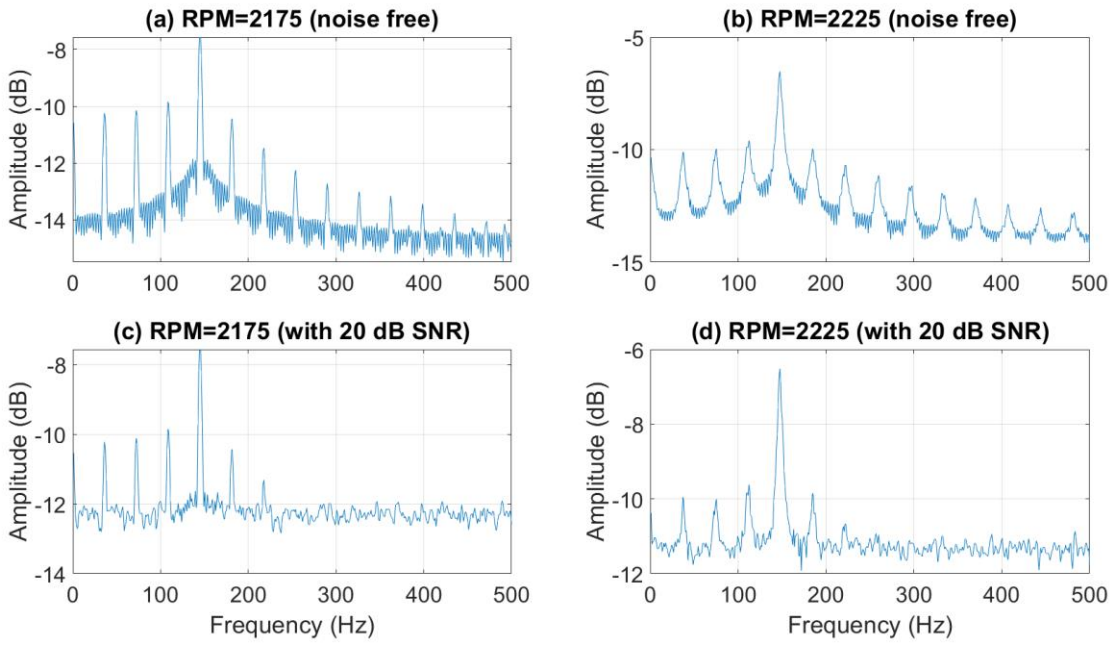

Figure 9.13 Effect of noise on power spectral density

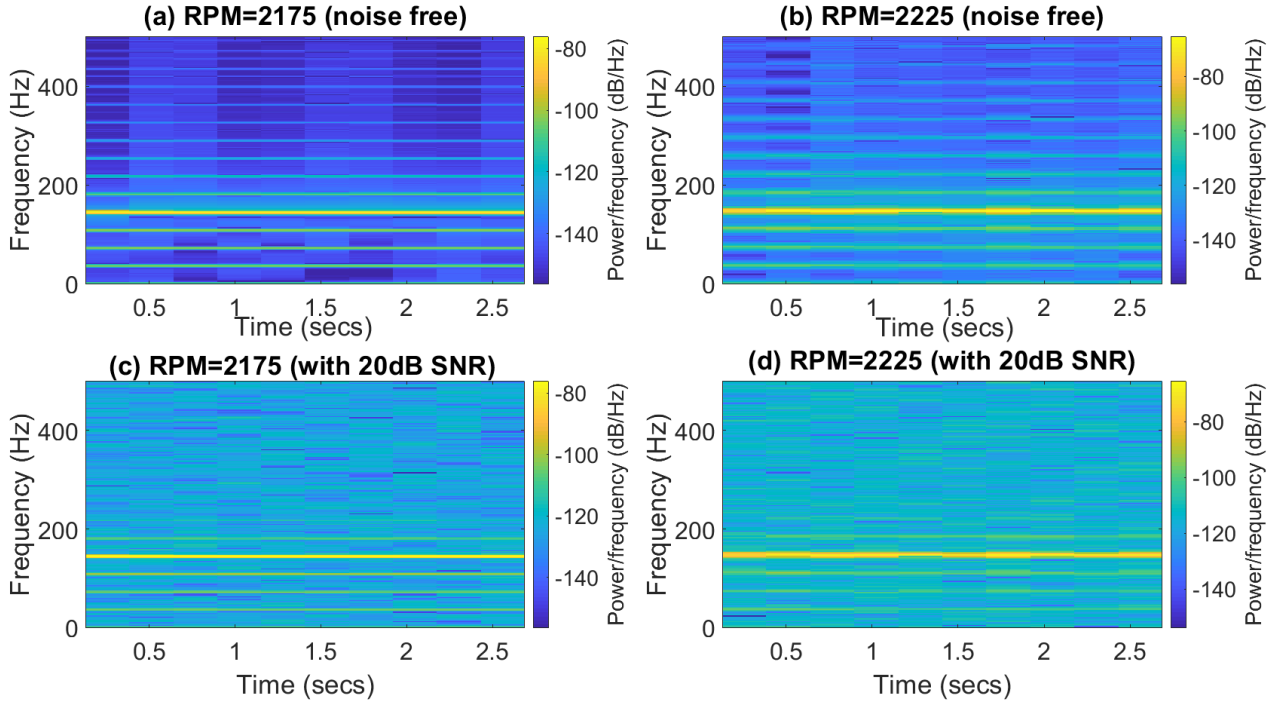

Figure 9.14 Effect of noise on Spectrogram

A signal with 20 dB SNR is distinguished from the noise-free case. Figure 9.14 shows the Spectrograms of the signal under the noisy condition and noise-free case. Obviously, it is comparatively difficult to distinguish between chatter and chatter-free cases even with trained convolutional neural networks. On the other hand, when the spinning rate gap between chatter and non-chatter conditions increases, chatter becomes easy to detect even at lower SNR values.

9.6.3. Locus of milling tool (at synchronous per revolution frequency)-based indicators

Chatter indicators indicated in the above two sub-sections require only one sensor measuring the tool displacement (in the feed direction). Due to the problem of measurement noise, their efficiency is not up to the mark. In this section, we discuss a two-sensor approach (one along feed direction and the other perpendicular to feed direction) collecting data at sampling frequency synchronous to tooth pass frequency. In this work, due to the presence of only one tooth for cutting, tooth pass frequency is equal to the milling tool spinning frequency. For example, at 2075 rpm the sampling frequency should be integer multiple of 2075/60 Hz. The integer is chosen as 100, so the sampling frequency is $\frac{2075}{60}\text{x}100 = 3458.3\ Hz$. The collected data in x and y-direction are used to plot the locus of the milling tool. Figure 9.15 shows loci/paths at 2075 (chatter), 2125 (chatter-free), 2175(chatter-free) and 2225 rpm (chatter).

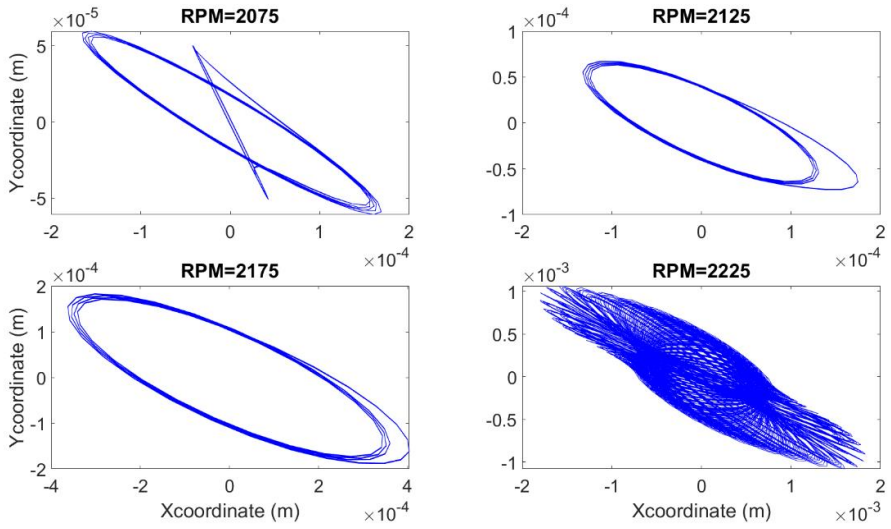

Figure 9.15 Milling tool locus as a function spinning speed of milling tool (noise free cases)

At 2075 rpm the response of the system is equivalent to period two bifurcations. At 2225 rpm, the response is equivalent to Hopf Bifurcations. During other chatter-free conditions (2125 and 2175 rpm), the response is a hollow tilted circle. Fortunately, the response pattern in the presence of measurement noise does not change. Figure 9.16 shows the locus of the cutting tool in the presence of measurement noise (i.e. 20 dB SNR).

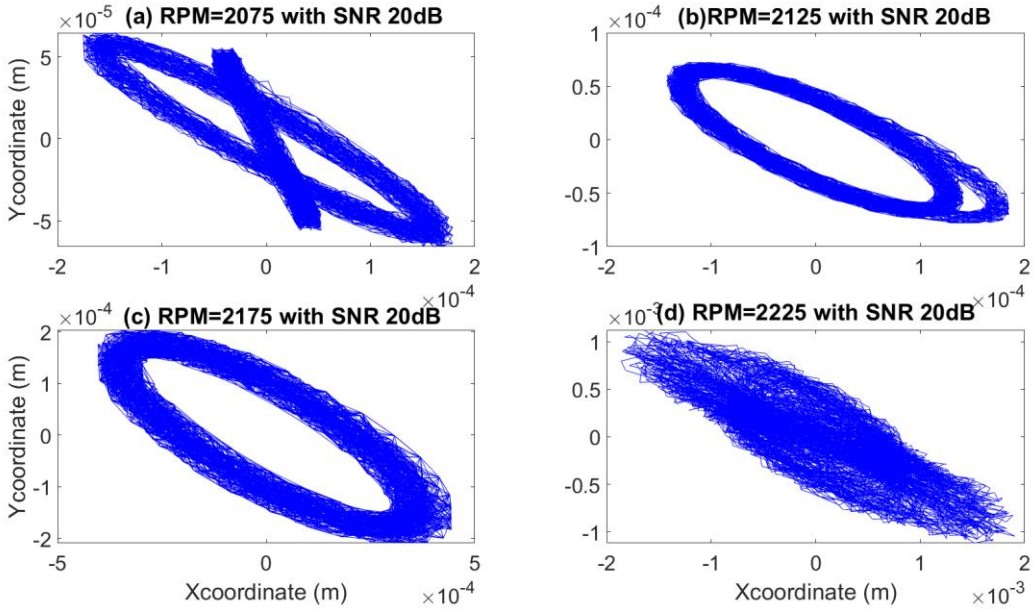

Figure 9.16 Effect of noise on locus of milling tool at different spinning speeds

In this case, neural networks can be used to classify the response of the system.

9.7. Online chatter identification based on Convolutional Neural Networks

Convolutional Neural Networks as shown in Figure 9.17 are used for image classification. It contains convolutional layer, pooling layer, fully connected layer and classification layer (Zhao et al., 2019).

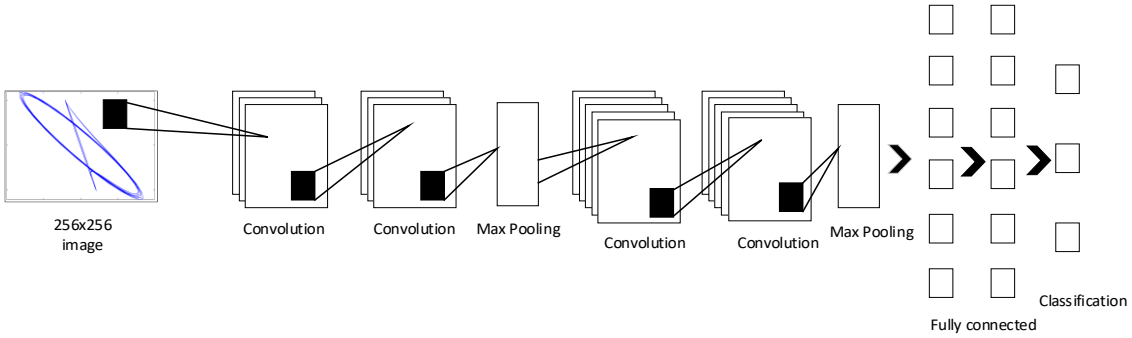

Figure 9.17 Architecture of convolutional Neural Networks

For training of CNN, simulation-based data are used to reduce the cost of experimental data. Based on the quality of the machine, the response of the system at higher spinning rates can be predicted. In this work, the rpm of the milling cutter is assumed to vary between 1500-2800. The axial depth of cut is fixed in the range 0.5-4 mm. From the stability lobe diagram (Figure 9.18), the cutting space is divided into 12 (A to L) x 20 =240 points. All depths of cuts as well as spinning speeds are covered in the required range. Using a computer program, the tool displacement data in the feed as well as perpendicular to feed direction are calculated for a certain period of time. It is observed that for the first 0.6 seconds, the initial transients are over and the steady-state response is achieved. Hence simulation data are created for the first 2 seconds. The images of the milling tool locus are made with a pixel density (227x227). For training of the CNN, 3 categories are considered. The first category contains type I chatter (corresponding to period-doubling bifurcations), the second category contains type II chatter (corresponding to Hopf Bifurcations)

and the third category is chatter-free vibrations. The neural network is trained on Intel core i7-8550 CPU based laptop with 8GB RAM.

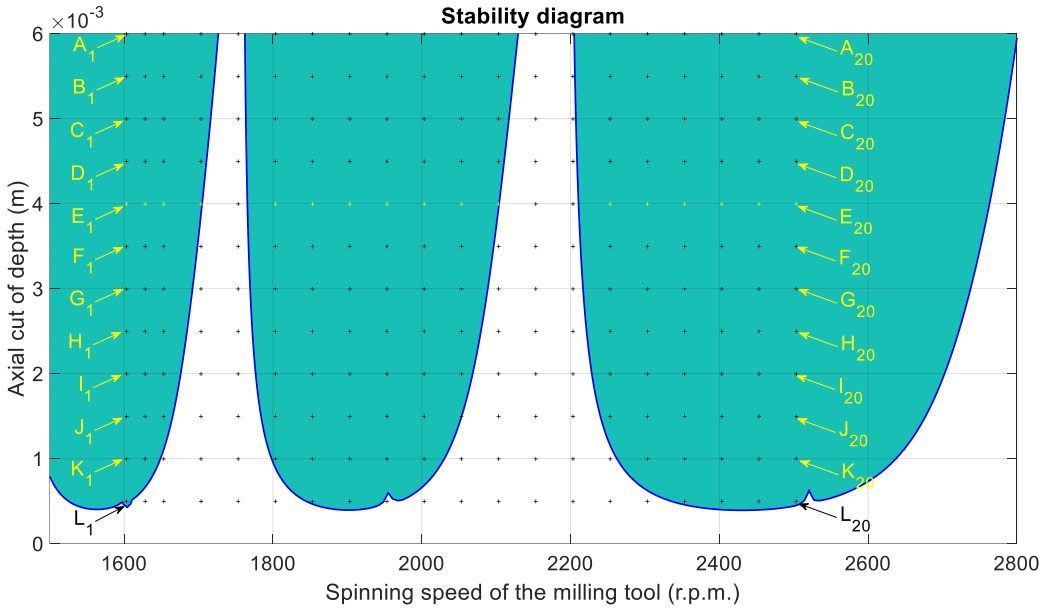

Figure 9.18 Training points for simulation assisted deep learning

9.7.1. CNN for Short Time Fourier Transformation based chatter detection

All the 240 images are classified into these three categories. All the images are infected with 20 dB SNR noise. It is observed that after 400 iterations, there is no significant improvement in results. It takes almost 30 minutes to complete these iterations. The configuration of the CNN in the MATLAB toolbox for Deep Learning is used (after certain hit and trials) as follows.

Input [227x227]-64Convolution [3x3]-64Pooling[3x3]-BatchNormalization-ReLU-128Convolution[3x3]-128Pooling[3x3] -BatchNormalization-ReLU-256Convolution[3x3]-256Pooling[3x3] -BatchNormalization-ReLU-320Convolution[3x3]-320Pooling[3x3] -BatchNormalization-ReLU-384Convolution[3x3]-384Pooling[3x3] -BatchNormalization-ReLU-FullyConnected-FullyConnected-Softmax-Classification.

An accuracy of 80% is obtained with an SNR of 20 dB after training the network. It is also observed that it is easy to distinguish between type I chatter and chatter-free conditions (than with type II chatter and chatter-free conditions) with STFT based images. This is due to a large number of additional chatter frequencies in the spectrogram. Unfortunately, type II chatter is more dangerous which is difficult to detect with this method. The confusion matrix for this system (STFT-based detection) is given as Table 9.1. Class 1 represents no chatter, class 2 represents type I chatter and class 3 represents type II chatter.

Table 9.1 Confusion matrix for STFT based detection

		Truth data				
		Class 1	Class 2	Class 3	Classification overall	Producer Accuracy (Precision)
Classifier results	Class 1	80	2	8	90	88.889%
	Class 2	12	82	14	108	75.926%
	Class 3	8	16	78	102	76.471%
	Truth overall	100	100	100	300	
	User Accuracy (Recall)	80%	82%	78%		

Overall accuracy (OA):	80%

9.7.2. CNN for Tool locus-based chatter detection

In tool locus-based chatter detection, 240 images are infected with white Gaussian noise corresponding to the 20 dB SNR. After 500 iterations, CNN is converged to an accuracy of 99.8%. It takes an average time of 35 minutes to complete the task. All the 240 images are classified into these three categories. The configuration of the CNN in the MATLAB toolbox for Deep Learning is used (after certain hit and trials) as follows.

Input [227x227]-64Convolution [3x3]-64Pooling[3x3]-BatchNormalization-ReLU-128Convolution[3x3]-128Pooling[3x3] -BatchNormalization-ReLU-256Convolution[3x3]-256Pooling[3x3] -BatchNormalization-ReLU-384Convolution[3x3]-384Pooling[3x3] -BatchNormalization-ReLU-FullyConnected-FullyConnected-Softmax-Classification.

The biggest advantage of tool locus-based chatter detection is that it is easy to detect type II chatter which is more dangerous. The confusion matrix for this system (tool locus-based detection) is given as Table 9.2. Class 1 represents no chatter, class 2 represents type I chatter and class 3 represents type II chatter.

Table 9.2 Confusion matrix for tool locus-based detection

		Truth data				
		Class 1	Class 2	Class 3	Classification overall	Producer Accuracy (Precision)
Classifier results	Class 1	99	1	0	100	99%
	Class 2	1	98	1	100	98%
	Class 3	1	1	99	101	98.02%
	Truth overall	101	100	100	301	
	User Accuracy (Recall)	98.02%	98%	99%		

Overall accuracy (OA): 98.339%

9.8. Concluding remarks

In this work, CNN based algorithms are proposed for online chatter detection. A CNN is trained using images formed by simulation based on the locus of the milling cutter. This trained CNN is then used to detect chatter on an online basis. Various chatter indicators are introduced for chatter detections. Following conclusions are drawn from this work.

- Mathematical techniques to model the flyover effect can predict the amplitude of vibrations during chatter conditions with sufficient accuracy hence are useful to create simulated data. Generated simulated data can be used to train the CNN.
- The amplitude of vibrations is not always high during chatter conditions. At certain spinning rates, the amplitude of vibrations during chatter-free conditions is several times higher than under chatter conditions.
- Type II chatter is much dangerous than type I. But, fortunately, it is easy to detect type II chatter using a tool locus method. The reverse is also true for the STFT based method.
- HHT and STFT based chatter detection requires only one sensor but efficiency is prone to measurement noise. CNN for detecting chatter is less accurate using the image based on STFT. The second method based on tool locus at synchronous per revolution sampling frequencies requires two sensors but is quite tolerant to measurement noise.
- CNN has remarkable accuracy in terms of the image classification and is quite useful to detect chatters during milling process on the real-time basis using tool locus method, however, short-time Fourier transformation-based methods provide average chatter detection results.

Chapter 10

Research conclusions, contributions and future recommendations

10.1. Conclusions

Mathematical modelling, fault detection and active vibration control of rotor dynamic systems with applications in machine tools have been discussed in this dissertation. First of all, the mathematical modelling of the cracked rotor is presented. Based on simulation results, it shows that different components of the rotor system like ball bearings transform the linear dynamics of the rotor system to nonlinear dynamics. It is observed that the different crack detection techniques based on the steady-state vibration response start losing their effectiveness in the presence of nonlinearities caused by ball bearings. The transient vibration response-based techniques are better suitable under these conditions. Switching control strategy can enhance the dynamic characteristics related to the transverse crack. Short-time Fourier transform techniques can be effectively used for detecting the interesting characteristics hidden in a frequency varying signal during the run-up of the rotor. However, there are certain limitations in the proposed technique (based on switching control). In the presence of other faults like coupling misalignment and rotor/stator rub (in certain specific circumstances), similar results are obtained. Under these circumstances, it is difficult to pinpoint the type of fault.

Rotor/stator rubbing phenomena are modelled mathematically. The phenomena of the dry whip, partial forward whirl and partial backward whirl are easily observed in case of vertical rotors under the absence of gravity. However, for horizontal rotors (under the influence of gravity), it is very difficult to observe these phenomena. For horizontal rotors, multiple harmonics are generated

when the rotor is running at a constant spinning speed. This aspect can be used as a rubbing detection indicator. However, a similar response is observed in the case of cracked flexible rotors. Hence, it is concluded that it is difficult to pinpoint the type of fault based on steady-state vibration response. On the other hand, transient vibration responses during run-up can easily differentiate between rotor crack and rubbing action using the short-time Fourier transform.

A hybrid controller, made by combining Mu-synthesis based feedback controller and adaptive feedforward cancellation controller, is used to quench the steady-state as well as transient vibrations of the flexible rotor system. Due to the external frequency estimator, the controller is effective when the spinning speed of the rotor is changed to a large extent. The single input, single output and multi-input, multi-output control architecture is investigated theoretically as well as experimentally. Excellent experimental results are obtained. The biggest advantage of the proposed controller is that multiple harmonics can be quenched efficiently. This aspect can be used to detect the presence of rotor crack and coupling misalignment from the Fourier transform of the control signal. However, this technique has one shortcoming also i.e. it cannot pinpoint the type of fault. We may not be able to distinguish whether the fault is coupling misalignment or rotor crack.

The precise control of ball screw drives used in CNC machines has been carried out. Due to the axial flexibility of the rotating screw, the resonance modes are excited. For better command tracking efficiency, the active vibration control of these resonant modes is necessary. In the absence of pre-loading, there is a drastic change in the dynamics of the ball screw drive as the table/carriage moves from one extreme end to the other. The conventional robust control design techniques cannot maintain stability under these conditions. PPI controllers are normally used in industry for the large variation in system parameters. However, they have limited command

tracking efficiency. A hybrid controller made by combining conventional PPI controller and linear parameter varying controller is investigated theoretically as well as experimentally. The resulting controller is high in bandwidth and efficient in closed-loop command tracking. It is observed that gains of linear parameter varying controllers cannot be increased arbitrarily.

For the active chatter control of turning operations in flexible shafts. Improved depth of cuts and hence productivity is obtained using active chatter control applications. The main difficulty in active chatter control of these systems is that there is a large variation in dynamic parameters as the material is removed. Linear parameter varying controllers designed with H-infinity optimization and interpolation techniques provide robust stability and performance under these conditions. Experimental implementation of the proposed controller confirms its efficiency.

For the feasibility analysis of active chatter control for boring operations, stationary and revolving bar boring operations are analysed in detail. Mathematical modelling of both types of boring operations is discussed in detail. The fractional-order PD controllers are tested for active chatter control applications. The experimental implementation of these controllers confirms their efficiency. The effect of workpiece ovality and eccentricity on the stability of the system has been investigated theoretically and experimentally. It is observed that small size electromagnetic actuators are required for maintaining the closed-loop stability during active chatter controls using these controllers. It is observed that although the rotating bar boring operation is more stable in open-loop conditions, it is not a suitable candidate for active chatter controls.

Convolutional neural networks are applied for online chatter detections in milling operations. Various chatter indicators have been suggested for online implementations. It is observed that the milling tool locus is a better chatter indicator efficiently to distinguish chatter from non-chatter conditions in an online manner. On the other hand, the spectrogram of the milling tool deflection

is not that much efficient for distinguishing chatter conditions from stable machining conditions in the presence of measurement noise. Apart from that, it is observed that by using certain modifications in dynamic equations of milling operations, the system behaviour during chatter conditions can be predicted to a reasonable accuracy. Experimental results confirm the accuracy of simulation equations. They are successfully used to train the convolutional neural networks for the system classification.

10.2 Research contributions

Contributions of this thesis work are as follows.

- Efficiency of the state-of-the-art crack detection techniques is verified in the presence of ball bearings in rotor systems.
- Transient response-based crack detection strategies using the combination of short-time Fourier transform and switched control are proposed and tested.
- The effect of gravity and rotor configurations on the dynamic behaviour of the rotor system in the presence of rotor/stator rubbing action is investigated.
- Short Time Fourier transformation-based strategy is proposed to distinguish different faults such as transverse crack and rotor/stator rubbing action for a two-degree-of-freedom rotor system.
- Model-based determination of size and location of a crack in a rotor system is proposed using wavelet transformations and pattern search optimization techniques.
- Active vibration control of rotor systems in the presence of rotor crack and coupling misalignment is developed theoretically as well as experimentally. A hybrid controller made by joining feedback and adaptive feedforward cancellation control is implemented to reduce the transient and steady-state vibrations.

- A hybrid controller made by joining the PPI and Linear Parameter Varying controller is developed theoretically and experimentally to improve the command tracking efficiency of the ball screw drive used in CNC machines. Better performance is achieved using the proposed technique for the BSD system during the metal cutting process.
- A Linear Parameter Varying (LPV) controller based on H-infinity optimization and interpolation techniques is developed theoretically and practically for active chatter controls in turning operations.
- A fractional-order proportional derivative (PD^{λ}) controller is evaluated theoretically and experimentally for active chatter controls of the boring process. It is observed that using the proposed control strategy, small size electromagnetic actuators can be used in robust controllers. Feasibility of active chatter control for revolving bar boring operation is investigated.
- Online chatter detection techniques for milling operations using convolutional neural networks are developed theoretically as well as experimentally. An algorithm is implemented to automatically adjust the spindle speed so that the system moves from chatter zone to chatter-free conditions.

10.3 Further recommendations

Follows are recommendations of the further work.

- The experimental verification of the proposed crack detection techniques in rotor dynamic systems is recommended as a future research direction. Further work is also needed to differentiate different types of fault present in the rotor system.
- The experimental verification of theoretical facts for rotor/stator rubbing actions is recommended as a future research direction.

- It is needed for developing control strategies to not only quench the steady-state and transient vibration but pinpoint the type of fault in the rotor system also. Using fractional calculus, certain controllers can be developed to quench the rotor vibrations with the minimum control energy utilization. Development and experimental implementation of such controllers are recommended as future work.
- There is a need to develop controllers that are high in bandwidth and do not produce large variations in torque applied at the motor when the ball screw drive is used for metal cutting operations.
- One of the limitations of LPV controllers is that they require high-cost hardware (like DSPACE boards) for experimental implementation. It is needed for the implementation of these controllers using low-cost data acquisition boards.
- There are certain limitations in the proposed fractional-order controllers for active chatter control in boring operations. These controllers are low in bandwidth. Hence, there is a clear need for improving the bandwidth of these controllers in future so that experimental implementation poses fewer problems.
- It is recommended for the online prediction of chatter using Long Short-Term Memory networks. These neural networks can efficiently classify the pattern/sequence of signals and hence can be used in combination with the current signal from ball screw drives for online chatter detection.

Papers published/submitted from dissertation

Journal papers published

1. Vashisht, R. K., Peng, Q., 2018. Crack detection in the rotor ball bearing system using switching control strategy and Short Time Fourier Transform. Elsevier Publication, Journal of Sound and Vibration 432, 502-529
2. Vashisht, R. K., Peng, Q., 2018. Nonlinear dynamic modelling of the cracked rotor ball bearing system with emphasis on damage detection capabilities. ASME Publication, Journal of Vibration and Acoustics, 140, pp 041018-10
3. Vashisht, R. K., Peng, Q., 2019. Adaptive hybrid control of unbalanced vibrations of a rotor/active magnetic bearing system with coupling misalignment using low cost instrumentation. Sage Publication, Journal of Vibration and Control. 25(15), pp. 1-24.
4. Vashisht, R. K., Peng, Q., 2019. Improving the cutting rate in turning operations of flexible stepped shafts with a linear parameter varying controller using the electromagnetic actuator. Springer Publication, International Journal of Advanced Manufacturing Technology, 104, pp. 1-16.
5. Vashisht, R. K., Peng, Q., 2020. Efficient active chatter mitigation for boring operation by electromagnetic actuator using optimal fractional order PD-λ controller. Elsevier publication, Journal of Material Processing Technology, 276, 116423.
6. Vashisht, R. K., Peng, Q., 2020, Feasibility analysis of active chatter control for stationary and revolving bar boring operations based on magnitude of control forces using Fractional order PD-λ controller. Springer Publication, International journal of Advanced Manufacturing Technology, 106, pp. 3957–3974.
7. Rajiv Kumar Vashisht, Qingjin Peng., 2020. Simultaneous fault detection and multivariable adaptive hybrid control of unbalanced vibrations of a cracked flexible rotor system using low-cost instrumentation. ASME Publication, Journal of Dynamic Systems, Measurement and Control, 142 pp. 121001-3
8. Rajiv Kumar Vashisht, Qingjin Peng., 2021, Fractional calculus-based energy-efficient active chatter control of milling process using small size electromagnetic actuators. ASME Journal of Vibration and Acoustics, 143 / pp. 011005-1
9. Rajiv Kumar Vashisht, Qingjin Peng. Online chatter detection for milling operations using neural networks assisted by motor current signals of ball screw drives. ASME journal of Manufacturing Science and Engineering. Published online with DOI : 10.1115/1.4048001

Journal papers submitted/accepted papers

10. Rajiv Kumar Vashisht, Qingjin Peng. 2020, Linear parameter varying modelling and evaluation of a hybrid controller for machine tool ball screw drives. Mechanical Systems and Signal Processing. Submitted in Feb. 2020
11. Rajiv Kumar Vashisht, Qingjin Peng., 2020, Online chatter detection and spindle speed regulation for milling operations using simulation assisted 2D convolutional neural networks. Elsevier publication, Journal of Intelligent Manufacturing. Accepted

Conference papers published

12. Vashisht, R. K., 2019. Model based determination of size and location of a crack in a rotor system using wavelet transformation and pattern search optimization. ASME 2019 International Design Engineering Technical Conferences and Computers and Information in Engineering Conference, IDETC2019-97072.
13. Vashisht, R. K., Peng, Q., 2019. Dynamic modelling and diagnosis of transverse crack and rotor/stator rub in a flexible rotor system. ASME 2019 International Design Engineering Technical Conferences and Computers and Information in Engineering Conference, DETC2019-97047.
14. Vashisht, R. K., 2019. The effect of gravity and rotor configuration on dry friction whip and safe rotor/stator clearance. ASME 2019 International Design Engineering Technical Conferences and Computers and Information in Engineering Conference, DETC2019-97048.

Bibliography

Abrahamsson, J., Hedlund, M., Kamf, T., Bernhoff, H., 2014. High-Speed Kinetic Energy Buffer: Optimization of Composite Shell and Magnetic Bearings. IEEE Transactions on Industrial Electronics 61, 3012-3021.

Altintas, Y., Verl, A., Brecher, C., Uriarte, L., Pritschow, G., 2011. Machine tool feed drives. CIRP Annals 60, 779-796.

Andrén, L., Häkansson, L., Claesson, I., 2003. Active control of machine tool vibrations in external turning operations. Proceedings of the Institution of Mechanical Engineers, Part B: Journal of Engineering Manufacture 217, 869-872.

Aslan, D., Altintas, Y., 2018. On-line chatter detection in milling using drive motor current commands extracted from CNC. International Journal of Machine Tools and Manufacture 132, 64-80.

Babu, Ramesh., Srikanth, S., Sekhar, A.S., 2008. Hilbert–Huang transform for detection and monitoring of crack in a transient rotor. Mechanical Systems and Signal Processing 22, 905-914.

Behzad, M., Alvandi, M., Mba, D., Jamali, J., 2013. A finite element-based algorithm for rubbing induced vibration prediction in rotors. Journal of Sound and Vibration 332, 5523-5542.

Bozorg, O., Solgi, M., Loáiciga, H., 2017, Meta-Heuristic and Evolutionary Algorithms for Engineering Optimization,Wiley, New York.

Breda, D., Maset, S., Vermiglio, R., 2012. Approximation of Eigenvalues of Evolution Operators for Linear Retarded Functional Differential Equations.

Breda, D., Maset, S., Vermiglio, R., 2014. Pseudospectral methods for stability analysis of delayed dynamical systems. International Journal of Dynamics and Control 2, 143-153.

Cao, H., Lei, Y., He, Z., 2013. Chatter identification in end milling process using wavelet packets and Hilbert–Huang transform. International Journal of Machine Tools and Manufacture 69, 11-19.

Chen, C.-S., Fan, Y.-H., Tseng, S.P., 2006. Position command shaping control in a retrofitted milling machine. International Journal of Machine Tools and Manufacture 46, 293-303.

Chen, C., Dai, L., Fu, Y., 2007. Nonlinear response and dynamic stability of a cracked rotor. Communications in Nonlinear Science and Numerical Simulation 12, 1023-1037.

Chen, F., Lu, X., Altintas, Y., 2014. A novel magnetic actuator design for active damping of machining tools. International Journal of Machine Tools and Manufacture 85, 58-69.

Chen, G., 2009. Study on Nonlinear Dynamic Response of an Unbalanced Rotor Supported on Ball Bearing. Journal of Vibration and Acoustics 131.

Chen, Q., Liu, G., Zheng, S., 2015. Suppression of imbalance vibration for AMBs controlled driveline system using double-loop structure. Journal of Sound and Vibration 337, 1-13.

Chen, Y.S., Zhang, H.B., 2011. Review and prospect on the research of dynamics of complete aero-engine systems. Hangkong Xuebao/Acta Aeronautica et Astronautica Sinica 32, 1371-1391.

Chen, Z., Zhang, H.-T., Zhang, X., Ding, H., 2013. Adaptive Active Chatter Control in Milling Processes. Journal of Dynamic Systems, Measurement, and Control 136, 021007-021007-021007.

Cheng, L., Li, N., Chen, X.-F., He, Z.-J., 2011. The influence of crack breathing and imbalance orientation angle on the characteristics of the critical speed of a cracked rotor. Journal of Sound and Vibration 330,

Choi, T., Shin, Y.C., 2003. On-Line Chatter Detection Using Wavelet-Based Parameter Estimation. Journal of Manufacturing Science and Engineering 125, 21-28.

Chu, Z., Ding, M., Du, S., Feng, X., 2011. Exponential Stability, Semistability, and Boundedness of a Multi-ANF System. IEEE Transactions on Circuits and Systems I: Regular Papers 58, 326-335.

Collins, K.R., Plaut, R.H., Wauer, J., 1991. Detection of Cracks in Rotating Timoshenko Shafts Using Axial Impulses. Journal of Vibration and Acoustics 113, 74-78.

Cong, F., Chen, J., Dong, G., Huang, K., 2011. Experimental validation of impact energy model for the rub–impact assessment in a rotor system. Mechanical Systems and Signal Processing 25, 2549-2558.
Darpe, A.K., Gupta, K., Chawla, A., 2004a. Coupled bending, longitudinal and torsional vibrations of a cracked rotor. Journal of Sound and Vibration 269, 33-60.
Darpe, A.K., Gupta, K., Chawla, A., 2004b. Transient response and breathing behaviour of a cracked Jeffcott rotor. Journal of Sound and Vibration 272, 207-243.
Delio, T., Tlusty, J., Smith, S., 1992. Use of Audio Signals for Chatter Detection and Control. Journal of Engineering for Industry 114, 146-157.
Dimarogonas, A.D., 1996. Vibration of cracked structures: A state of the art review. Engineering Fracture Mechanics 55, 831-857.
Djurovic, I., 2007. Estimation of the Sinusoidal Signal Frequency Based on the Marginal Median DFT. IEEE Transactions on Signal Processing 55, 2043-2051.
Doppenberg, E.J.J., Faassen, R.P.H., Van de Wouw, N., Oosterling, J.A.J. 2006, CIRP (Eds.), Active in-process chatter control, 12–13, Vancouver, British Columbia, Canada.
Duan, M., Yoon, D., Okwudire, C.E., 2018. A limited-preview filtered B-spline approach to tracking control – With application to vibration-induced error compensation of a 3D printer. Mechatronics 56, 287-296.
Dumanli, A., Sencer, B., 2018. Optimal high-bandwidth control of ball-screw drives with acceleration and jerk feedback. Precision Engineering 54, 254-268.
Eppel, A., Enikov, E.T., Insperger, T., Gabor, S., 2010. Feasibility Study of Optical Detection of Chatter Vibration During Milling. International Journal of Optomechatronics 4, 195-214.
Erkorkmaz, K., Altintas, Y., 2001. High speed CNC system design. Part III: high speed tracking and contouring control of feed drives. International Journal of Machine Tools and Manufacture 41, 1637-1658.
Eynian, M., Altintas, Y., 2009. Chatter Stability of General Turning Operations With Process Damping. Journal of Manufacturing Science and Engineering 131, 041005-041005-041010.
Fang, J., Xu, X., Tang, J., Liu, H., 2013a. Adaptive complete suppression of imbalance vibration in AMB systems using gain phase modifier. Journal of Sound and Vibration 332, 6203-6215.
Fang, J., Zhou, X., Liu, G., 2013b. Precise Accelerated Torque Control for Small Inductance Brushless DC Motor. IEEE Transactions on Power Electronics 28, 1400-1412.
Faassen, R.P.H., Doppenberg, E.J.J., VandeWouw, N., Oosterling, J.A.J., Nijmeijer, H., 2006 CIRP(Eds.),Online detection of the onset and occurrence of machine tool chatter in the milling process, 12–13, Vancouver, British Columbia, Canada
Ganguli, A., Deraemaeker, A., Horodinca, M., Preumont, A., 2005. Active Damping of Chatter in Machine Tools - Demonstration with a 'Hardware-in-the-Loop' Simulator. Proceedings of the Institution of Mechanical Engineers, Part I: Journal of Systems and Control Engineering 219, 359-369.
Ganguli, A., Deraemaeker, A., Preumont, A., 2007. Regenerative chatter reduction by active damping control. Journal of Sound and Vibration 300, 847-862.
Gasch, R., 1993a. A Survey Of The Dynamic Behaviour Of A Simple Rotating Shaft With A Transverse Crack. Journal of Sound and Vibration 160, 313-332.
Gasch, R., 1993b. A Survey Of The Dynamic Behaviour Of A Simple Rotating Shaft With A Transverse Crack.
Gordon, D.J., Erkorkmaz, K., 2013. Accurate control of ball screw drives using pole-placement vibration damping and a novel trajectory prefilter. Precision Engineering 37, 308-322.
Gu, D. W., Petkov, P. H., and Konstantinov, M. M., 2005, Robust Control Design With MATLAB, Springer, London
Han, Q., Chu, F., 2012. Parametric instability of a rotor-bearing system with two breathing transverse cracks. European Journal of Mechanics - A/Solids 36, 180-190.

Hanifzadegan, M., Nagamune, R., 2015. Tracking and Structural Vibration Control of Flexible Ball–Screw Drives With Dynamic Variations. IEEE/ASME Transactions on Mechatronics 20, 133-142.
Harsha, S.P., Sandeep, K., Prakash, R., 2004. Non-linear dynamic behaviors of rolling element bearings due to surface waviness. Journal of Sound and Vibration 272, 557-580.
Hoang, D.-T., Kang, H.-J., 2019. A survey on Deep Learning based bearing fault diagnosis. Neurocomputing 335, 327-335.
Hou, L., Chen, Y., Cao, Q., Lu, Z., 2016. Nonlinear vibration analysis of a cracked rotor-ball bearing system during flight maneuvers. Mechanism and Machine Theory 105, 515-528.
Insperger, T., Stépán, G., 2004. Updated semi-discretization method for periodic delay-differential equations with discrete delay. International Journal for Numerical Methods in Engineering 61, 117-141.
Insperger, T., Stépán, G., Bayly, P.V., Mann, B.P., 2003. Multiple chatter frequencies in milling processes. Journal of Sound and Vibration 262, 333-345.
Ishida, Y., Ikeda, T., Yamamoto, T., 1990. Nonlinear Forced Oscillations Caused by Quartic Nonlinearity in a Rotating Shaft System. Journal of Vibration and Acoustics 112, 288-297.
Ismail, F., Ziaei, R., 2002. Chatter suppression in five-axis machining of flexible parts. International Journal of Machine Tools and Manufacture 42, 115-122.
Jacquet-Richardet, G., Torkhani, M., Cartraud, P., Thouverez, F., Nouri Baranger, T., Herran, M., Gibert, C., Baguet, S., Almeida, P., Peletan, L., 2013. Rotor to stator contacts in turbomachines. Review and application. Mechanical Systems and Signal Processing 40, 401-420.
Jalan, A. K., Mohanty A. R., 2009, Model based fault diagnosis of rotor bearing system for misalignment and imbalance under steady state conditions, Journal of Sound and Vibration 327, 604-622.
Jastrzębski, R.P., Pöllänen, R., 2009. Centralized optimal position control for active magnetic bearings: comparison with decentralized control. Electrical Engineering 91, 101-114.
Jemielniak, K., Widota, A., 1989. Numerical simulation of non-linear chatter vibration in turning. International Journal of Machine Tools and Manufacture 29, 239-247.
Jen, M.U., Magrab, E.B., 1996. The Dynamic Interaction of the Cutting Process, Workpiece, and Lathe's Structure in Facing. Journal of Manufacturing Science and Engineering 118, 348-358.
Ji, Z., Zu, J.W., 1998. Method of multiple scales for vibration analysis of rotor shaft systems with non-linear bearing pedestal model. Journal of Sound and Vibration 218, 293-305.
Jiang, J., Ulbrich, H., 2004. The Physical Reason and the Analytical Condition for the Onset of Dry Whip in Rotor-to-Stator Contact Systems. Journal of Vibration and Acoustics 127, 594-603.
Jun, O.S., Eun, H.J., Earmme, Y.Y., Lee, C.W., 1992. Modelling and vibration analysis of a simple rotor with a breathing crack. Journal of Sound and Vibration 155, 273-290.
Kakinuma, Y., Sudo, Y., Aoyama, T., 2011. Detection of chatter vibration in end milling applying disturbance observer. CIRP Annals 60, 109-112.
Kamalzadeh, A., Erkorkmaz, K., 2007. Compensation of Axial Vibrations in Ball Screw Drives. CIRP Annals 56, 373-378.
Kato, S., Marui, E., 1974. On the Cause of Regenerative Chatter Due to Workpiece Deflection. Journal of Engineering for Industry 96, 179-186.
Klein, R.G., Nachtigal, C.L., 1975. A Theoretical Basis for the Active Control of a Boring Bar Operation. Journal of Dynamic Systems, Measurement, and Control 97, 172-178.
Kulesza, Z., 2014. Dynamic behavior of cracked rotor subjected to multisine excitation. Journal of Sound and Vibration 333, 1369-1378.
Kulesza, Z., Sawicki, J., 2011. Auxiliary state variables for rotor crack detection. Journal of Vibration and Control 17, 857-872.
Kuljanic, E., Sortino, M., Totis, G., 2008. Multisensor approaches for chatter detection in milling. Journal of Sound and Vibration 312, 672-693.
Kuljanic, E., Totis, G., Sortino, M., 2009. Development of an intelligent multisensor chatter detection system in milling. Mechanical Systems and Signal Processing 23, 1704-1718.

Lalanne, M., Ferraris, G., Rotordynamics 1990, Prediction in Engineering, Wiley, New York.

Lee, C.W., Han, Y.S., 1998. The directional wigner distribution and its applications. Journal of Sound and Vibration 216, 585-600.

Li, D., Cao, H., Zhang, X., Chen, X., Yan, R., 2019. Model predictive control based active chatter control in milling process. Mechanical Systems and Signal Processing 128, 266-281.

Li, F., Jiang, Y., Li, T., Ehmann, K.F., 2018. Compensation of dynamic mechanical tracking errors in ball screw drives. Mechatronics 55, 27-37.

Li, S., Qun Li, Z., Zheng, M., 2012. Chatter Stability Modeling and Simulation for Long Slender Shaft Turning Operation.

Liao, Y.S., Young, Y.C., 1996. A new on-line spindle speed regulation strategy for chatter control. International Journal of Machine Tools and Manufacture 36, 651-660.

Liu, C., Zhu, L., Ni, C., 2018. Chatter detection in milling process based on VMD and energy entropy. Mechanical Systems and Signal Processing 105, 169-182.

Liu, H., Zhang, J., Zhao, W., 2017a. An Intelligent Non-Collocated Control Strategy for Ball-Screw Feed Drives with Dynamic Variations. Engineering 3, 641-647.

Liu, J., Yang, L., Yang, L., Zhang, X., Chen, X., 2017b. Multiple-harmonic amplitude and phase control method for active noise and vibration reshaping. Journal of Vibration and Control 24, 3173-3193.

Lu, K., Lian, Z., Gu, F., Liu, H., 2018. Model-based chatter stability prediction and detection for the turning of a flexible workpiece. Mechanical Systems and Signal Processing 100, 814-826.

Lu, X., Chen, F., Altintas, Y., 2014. Magnetic actuator for active damping of boring bars. CIRP Annals 63, 369-372.

Ma, H., Shi, C., Han, Q., Wen, B., 2013. Fixed-point rubbing fault characteristic analysis of a rotor system based on contact theory. Mechanical Systems and Signal Processing 38, 137-153.

Ma, H., Wu, J., Yang, L., Xiong, Z., 2017. Active chatter suppression with displacement-only measurement in turning process. Journal of Sound and Vibration 401, 255-267.

Ma, H., Wu, Z., Tai, X., Wen, B., 2014. Dynamic characteristics analysis of a rotor system with two types of limiters. International Journal of Mechanical Sciences 88, 192-201.

Ma, H., Zhao, Q., Zhao, X., Han, Q., Wen, B., 2015. Dynamic characteristics analysis of a rotor–stator system under different rubbing forms. Applied Mathematical Modelling 39, 2392-2408.

Mann, B.P., Insperger, T., Bayly, P.V., Stépán, G., 2003. Stability of up-milling and down-milling, part 2: experimental verification. International Journal of Machine Tools and Manufacture 43, 35-40.

Manngård, M., Böling, J.M., 2017. Online frequency estimation with applications to engine and generator sets. Mechanical Systems and Signal Processing 91, 233-249.

Markert, R., Platz, R., Seidler, M., 2001. Model Based Fault Identification in Rotor Systems by Least Squares Fitting. International Journal of Rotating Machinery 7.

Marui, E., Ema, S., Kato, S., 1983. Chatter Vibration of Lathe Tools. Part 1: General Characteristics of Chatter Vibration. Journal of Engineering for Industry 105, 100-106.

Mayes, I.W., Davies, W.G.R., 1984. Analysis of the Response of a Multi-Rotor-Bearing System Containing a Transverse Crack in a Rotor. Journal of Vibration, Acoustics, Stress, and Reliability in Design 106, 139-145.

McCormack, A.S., Godfrey, K.R., Flower, J.O., 1994. The detection of and compensation for nonlinear effects using periodic input signals, 1994 International Conference on Control - Control '94., pp. 297-302 vol.291.

Mei, C., Cherng, J.G., Wang, Y., 2005. Active Control of Regenerative Chatter During Metal Cutting Process. Journal of Manufacturing Science and Engineering 128, 346-349.

Mei, D., Kong, T., Shih, A.J., Chen, Z., 2009. Magnetorheological fluid-controlled boring bar for chatter suppression. Journal of Materials Processing Technology 209, 1861-1870.

Meng, H., Kang, Y., Chen, Z., Zhao, Y., Liu, G., 2015. Stability Analysis and Stabilization of a Class of Cutting Systems With Chatter Suppression. IEEE/ASME Transactions on Mechatronics 20, 991-996.

Merritt, H.E., 1965. Theory of Self-Excited Machine-Tool Chatter: Contribution to Machine-Tool Chatter Research—. Journal of Engineering for Industry 87, 447-454.
Mojiri, M., Bakhshai, A.R., 2004. An adaptive notch filter for frequency estimation of a periodic signal. IEEE Transactions on Automatic Control 49, 314-318.
Monnin, J., Kuster, F., Wegener, K., 2014a. Optimal control for chatter mitigation in milling—Part 1: Modeling and control design. Control Engineering Practice 24, 156-166.
Monnin, J., Kuster, F., Wegener, K., 2014b. Optimal control for chatter mitigation in milling—Part 2: Experimental validation. Control Engineering Practice 24, 167-175.
Mushi, S.E., Lin, Z., Allaire, P.E., 2012. Design, Construction, and Modeling of a Flexible Rotor Active Magnetic Bearing Test Rig. IEEE/ASME Transactions on Mechatronics 17, 1170-1182.
OKUMA.MachiningNavi,MacNavi.Available at: http://www.okuma.co.jp/english/onlyone/process/index.html.
Oleaga, I., Pardo, C., Zulaika, J.J., Bustillo, A., 2018. A machine-learning based solution for chatter prediction in heavy-duty milling machines. Measurement 128, 34-44.
Otto, A., Khasawneh, F.A., Radons, G., 2015. Position-dependent stability analysis of turning with tool and workpiece compliance. The International Journal of Advanced Manufacturing Technology 79, 1453-1463.
Park, Y., 2014. Design and implementation of an electromagnetic levitation system for active magnetic bearing wheels. IET Control Theory & Applications 8, 139-148.
Patel, T.H., Darpe, A.K., 2008a. Influence of crack breathing model on nonlinear dynamics of a cracked rotor. Journal of Sound and Vibration 311, 953-972.
Patel, T.H., Darpe, A.K., 2008b. Vibration response of a cracked rotor in presence of rotor–stator rub. Journal of Sound and Vibration 317, 841-865.
Patel, T.H., Darpe, A.K., 2009. Study of coast-up vibration response for rub detection. Mechanism and Machine Theory 44, 1570-1579.
Pratt, J., Nayfeh, A., 2001. Chatter control and stability analysis of a cantilever boring bar under regenerative cutting conditions.
Pritschow, G., Croon, N., 2013. Ball screw drives with enhanced bandwidth by modification of the axial bearing. CIRP Annals 62, 383-386.
Pritschow, G., Eppler, C., Lehner, W.D., 2003. Ferraris Sensor – The Key for advanced dynamic Drives. CIRP Annals 52, 289-292.
Rahman, M., Ito, Y., 1986. Detection of the onset of chatter vibration. Journal of Sound and Vibration 109, 193-205.
Babu, R., T., Srikanth, S., Sekhar, A.S., 2008. Hilbert–Huang transform for detection and monitoring of crack in a transient rotor. Mechanical Systems and Signal Processing 22, 905-914.
Rao, B.C., Shin, Y.C., 1999. A comprehensive dynamic cutting force model for chatter prediction in turning. International Journal of Machine Tools and Manufacture 39, 1631-1654.
Ren, Y., Su, D., Fang, J., 2013. Whirling Modes Stability Criterion for a Magnetically Suspended Flywheel Rotor With Significant Gyroscopic Effects and Bending Modes. IEEE Transactions on Power Electronics 28, 5890-5901.
Rodriguez, P., Luna, A., Candela, I., Mujal, R., Teodorescu, R., Blaabjerg, F., 2011. Multiresonant Frequency-Locked Loop for Grid Synchronization of Power Converters Under Distorted Grid Conditions. IEEE Transactions on Industrial Electronics 58, 127-138.
Sawicki, J.T., Friswell, M.I., Kulesza, Z., Wroblewski, A., Lekki, J.D., 2011a. Detecting cracked rotors using auxiliary harmonic excitation. Journal of Sound and Vibration 330, 1365-1381.
Sawicki, J.T., Storozhev, D.L., Lekki, J.D., 2011b. Exploration of NDE Properties of AMB Supported Rotors for Structural Damage Detection. Journal of Engineering for Gas Turbines and Power 133.
Schmitz, T., 2003. Chatter recognition by a statistical evaluation of the synchronously sampled audio signal. Journal of Sound and Vibration, 262, 721-730.

Schmitz, T.L., Davies, M.A., Medicus, K., Snyder, J., 2001. Improving High-Speed Machining Material Removal Rates by Rapid Dynamic Analysis. CIRP Annals 50, 263-268.
Schmitz, T.L., Medicus, K., Dutterer, B., 2002. Exploring once-per-revolution audio signal variance as a chatter indicator. Machining Science and Technology 6, 215-233.
Schoukens, J., Pintelon, R., Rolain, Y., Dobrowiecki, T., 2001. Frequency response function measurements in the presence of nonlinear distortions. Automatica 37, 939-946.
Sencer, B., Ishizaki, K., Shamoto, E., 2015. High speed cornering strategy with confined contour error and vibration suppression for CNC machine tools. CIRP Annals 64, 369-372.
Sencer, B., Tajima, S., 2016. Frequency Optimal Feed Motion Planning in Computer Numerical Controlled Machine Tools for Vibration Avoidance. Journal of Manufacturing Science and Engineering 139, 011006-011006-011013.
Sepasi, D., Nagamune, R., Sassani, F., 2012. Tracking Control of Flexible Ball Screw Drives With Runout Effect and Mass Variation. IEEE Transactions on Industrial Electronics 59, 1248-1256.
Shang, Z., Jiang, J., Hong, L., 2011. The global responses characteristics of a rotor/stator rubbing system with dry friction effects. Journal of Sound and Vibration 330, 2150-2160.
Shah, P. , Agashe, S., 2016, Review of fractional PID controller, Mechatronics 38, 29–41
Shawky, A.M., Elbestawi, M.A., 1998. Model-Based Predictive Control of Workpiece Accuracy in Bar Turning. Journal of Manufacturing Science and Engineering 120, 57-67.
Shimada, Y., Nishimura, Y., Usagawa, T., Ebata, M., 1999. Active control for periodic noise wih variable fundamental. An extended DXHS algorithm with frequency tracking ability.
Shimoda, T., Fujimoto, H., Kumagai, N., Terada, Y., 2017. External sensorless adaptive chatter avoidance in NC machining by applying disturbance observer using high resolution linear encoder, 2017 IEEE International Conference on Advanced Intelligent Mechatronics (AIM), pp. 879-884.
Shiraishi, M., Yamanaka, K., Fujita, H., 1991. Optimal control of chatter in turning. International Journal of Machine Tools and Manufacture 31, 31-43.
Silani, M., Ziaei-Rad, S., Talebi, H., 2013. Vibration analysis of rotating systems with open and breathing cracks. Applied Mathematical Modelling 37, 9907-9921.
Singhose, W.E., Searing, W.P., Singer, N.C., 1996. Improving repeatability of coordinate measuring machines with shaped command signals. Precision Engineering 18, 138-146.
Sinou, J.-J., 2007. Effects of a crack on the stability of a non-linear rotor system. International Journal of Non-Linear Mechanics 42, 959-972.
Sobie, C., Freitas, C., Nicolai, M., 2018. Simulation-driven machine learning: Bearing fault classification. Mechanical Systems and Signal Processing 99, 403-419.
Stepan, G., Kiss, A.K., Ghalamchi, B., Sopanen, J., Bachrathy, D., 2017. Chatter avoidance in cutting highly flexible workpieces. CIRP Annals 66, 377-380.
Sun, Z., Pritschow, G., Lechler, A., 2016. Enhancement of feed drive dynamics using additional table speed feedback. CIRP Annals 65, 357-360.
Sun, Z., Pritschow, G., Zahn, P., Lechler, A., 2018. A novel cascade control principle for feed drives of machine tools. CIRP Annals 67, 389-392.
Tanaka, H., Obata, F., Matsubara, T., Mizumoto, H., 1994. Active Chatter Suppression of Slender Boring Bar Using Piezoelectric Actuators. JSME international journal. Ser. C, Dynamics, control, robotics, design and manufacturing 37, 601-606.
Tangjitsitcharoen, S., 2009. In-process monitoring and detection of chip formation and chatter for CNC turning. Journal of Materials Processing Technology 209, 4682-4688.
Tangjitsitcharoen, S., Moriwaki, T., 2008. Intelligent monitoring and identification of cutting states of chips and chatter on CNC turning machine. Journal of Manufacturing Processes 10, 40-46.
Tansel, I.N., Li, M., Demetgul, M., Bickraj, K., Kaya, B., Ozcelik, B., 2012. Detecting chatter and estimating wear from the torque of end milling signals by using Index Based Reasoner (IBR). The International Journal of Advanced Manufacturing Technology 58, 109-118.
Tewani, S.G., Rouch, K.E., Walcott, B.L., 1995. A study of cutting process stability of a boring bar with active dynamic absorber. International Journal of Machine Tools and Manufacture 35, 91-108.

Tiwari, M., Gupta, K., Prakash, O., 2000. Effect of radial internal clearance of a ball bearing on the dynamics of a balanced horizontal rotor. Journal of Sound and Vibration 238, 723-756.
Tomizuka, M., 1987. Zero Phase Error Tracking Algorithm for Digital Control. Journal of Dynamic Systems, Measurement, and Control 109, 65-68.
Torkhani, M., May, L., Voinis, P., 2012. Light, medium and heavy partial rubs during speed transients of rotating machines: Numerical simulation and experimental observation. Mechanical Systems and Signal Processing 29, 45-66.
Tsai, N.-C., Chen, D.-C., Lee, R.-M., 2010. Chatter prevention for milling process by acoustic signal feedback. The International Journal of Advanced Manufacturing Technology 47, 1013-1021.
Tsai, N.C., Chen, D.C., Lee, R.M., 2009. Chatter prevention and improved finish of workpiece for a milling process. Proceedings of the Institution of Mechanical Engineers, Part B: Journal of Engineering Manufacture 224, 579-588.
Uchiyama, N., 2008. Adaptive two-degree-of-freedom control of feed drive systems, International Journal of Machine Tools and Manufacture 48(3-4):437-445.
van de Wouw, N., Dijk, N., Schiffler, A., Nijmeijer, H., Abele, E., 2017. Experimental Validation of Robust Chatter Control for High-Speed Milling Processes, pp. 315-331.
Varanasi, K.K., Nayfeh, S.A., 2004. The Dynamics of Lead-Screw Drives: Low-Order Modeling and Experiments. Journal of Dynamic Systems, Measurement, and Control 126, 388-396.
Varney, P., Green, I., 2015. Nonlinear phenomena, bifurcations, and routes to chaos in an asymmetrically supported rotor–stator contact system. Journal of Sound and Vibration 336, 207-226.
Vashisht, R. K., Peng, Q., 2018. Crack detection in the rotor ball bearing system using switching control strategy and Short Time Fourier Transform. Elsevier Publication, Journal of Sound and Vibration 432, 502-529
Vashisht, R. K., Peng, Q., 2018a. Nonlinear dynamic modelling of the cracked rotor ball bearing system with emphasis on damage detection capabilities. ASME Publication, Journal of Vibration and Acoustics, 140, pp 041018-10
Vashisht, R. K., 2019. Model based determination of size and location of a crack in a rotor system using wavelet transformation and pattern search optimization. ASME 2019 International Design Engineering Technical Conferences and Computers and Information in Engineering Conference, IDETC2019-97072
Vashisht, R. K., Peng, Q., 2019a. Dynamic modelling and diagnosis of transverse crack and rotor/stator rub in a flexible rotor system. ASME 2019 International Design Engineering Technical Conferences and Computers and Information in Engineering Conference, DETC2019-97047
Vashisht, R. K., 2019b. The effect of gravity and rotor configuration on dry friction whip and safe rotor/stator clearance. ASME 2019 International Design Engineering Technical Conferences and Computers and Information in Engineering Conference, DETC2019-97048
Vashisht, R. K., Peng, Q., 2019c. Adaptive hybrid control of unbalanced vibrations of a rotor/active magnetic bearing system with coupling misalignment using low cost instrumentation. Sage Publication, Journal of Vibration and Control. 25(15), pp. 1-24.
Vashisht, R. K., Peng, Q., 2019d. Improving the cutting rate in turning operations of flexible stepped shafts with a linear parameter varying controller using the electromagnetic actuator. Springer Publication, International Journal of Advanced Manufacturing Technology, 104, pp. 1-16.
Vashisht, R. K., Peng, Q., 2020. Efficient active chatter mitigation for boring operation by electromagnetic actuator using optimal fractional order PD-λ controller. Elsevier publication, Journal of Material Processing Technology, 276, 116423
Vashisht, R. K., Peng, Q., 2020a, Feasibility analysis of active chatter control for stationary and revolving bar boring operations based on magnitude of control forces using Fractional order PD-λ controller. Springer Publication, International journal of Advanced Manufacturing Technology, 106, pp. 3957–3974

Vela-Martínez, L., Carlos Jauregui-Correa, J., Rodriguez, E., Alvarez-Ramirez, J., 2010. Using detrended fluctuation analysis to monitor chattering in cutter tool machines. International Journal of Machine Tools and Manufacture 50, 651-657.
Verl, A., Frey, S., 2012. Improvement of feed drive dynamics by means of semi-active damping. CIRP Annals 61, 351-354.
Villa, C., Sinou, J.J., Thouverez, F., 2008. Stability and vibration analysis of a complex flexible rotor bearing system. Communications in Nonlinear Science and Numerical Simulation 13, 804-821.
Wang, M., Fei, R., 2001. On-line chatter detection and control in boring based on an electrorheological fluid. Mechatronics 11, 779-792.
Wang, Z.C., Cleghorn, W.L., 2002. Stability analysis of spinning stepped-shaft workpieces in a turning process.
Wang, L., Liang, M., 2009. Chatter detection based on probability distribution of wavelet modulus maxima. Robotics and Computer-Integrated Manufacturing 25, 989-998.
Wauer, J.r., 1990. On the Dynamics of Cracked Rotors: A Literature Survey. Applied Mechanics Reviews 43, 13-17.
Wei, C., Söffker, D., 2016. Optimization Strategy for PID-Controller Design of AMB Rotor Systems. IEEE Transactions on Control Systems Technology 24, 788-803.
Weingaertner, W.L., Schroeter, R.B., Polli, M.L., de Oliveira Gomes, J., 2006. Evaluation of high-speed end-milling dynamic stability through audio signal measurements. Journal of Materials Processing Technology 179, 133-138.
Xie, C., Wu, Y., Liu, Z., 2018, Modeling and active vibration control of lattice grid beam with piezoelectric fiber composite using fractional order PD-μ algorithm, Composite Structures 198, 126–134
Yang, Y., Chen, H., Jiang, T., 2015. Nonlinear response prediction of cracked rotor based on EMD. Journal of the Franklin Institute 352, 3378-3393.
Yao, Z., Mei, D., Chen, Z., 2010. On-line chatter detection and identification based on wavelet and support vector machine. Journal of Materials Processing Technology 210, 713-719.
Yazdani, D., Mojiri, M., Bakhshai, A., JoÓs, G., 2009. A Fast and Accurate Synchronization Technique for Extraction of Symmetrical Components. IEEE Transactions on Power Electronics 24, 674-684.
Yi-Hua, F., Yan-Che, J., Rong-Jhe, C., Ying-Tsun, L., Tzu-Wei, W., 2008. Adaptive variable structure controller design of turbomolecular pump with active magnetic bearings, 2008 3rd IEEE Conference on Industrial Electronics and Applications, pp. 1060-1065.
Yoon, J.-M., Bahn, W., Kim, T.-I., Han, J.-S., Lee, S.-H., Cho, D.-i.D., 2017. Discrete derivative method for adaptive notch filter-based frequency estimators. International Journal of Control, Automation and Systems 15, 668-679.
Yoon, M.C., Chin, D.H., 2005. Cutting force monitoring in the endmilling operation for chatter detection. Proceedings of the Institution of Mechanical Engineers, Part B: Journal of Engineering Manufacture
Zhang, C.L., Yue, X., Jiang, Y.T., Zheng, W., 2010. A Hybrid Approach of ANN and HMM for Cutting Chatter Monitoring. Advanced Materials Research 97-101, 3225-3232.
Zhao, R., Yan, R., Chen, Z., Mao, K., Wang, P., Gao, R.X., 2019. Deep learning and its applications to machine health monitoring. Mechanical Systems and Signal Processing 115, 213-237.
Zhao, X., Patel, T.H., Zuo, M.J., 2012. Multivariate EMD and full spectrum based condition monitoring for rotating machinery. Mechanical Systems and Signal Processing 27, 712-728.
Zheng, S., Feng, R., 2016. Feedforward compensation control of rotor imbalance for high-speed magnetically suspended centrifugal compressors using a novel adaptive notch filter. Journal of Sound and Vibration 366, 1-14.

Appendix A

By using certain excitation signals externally and observing the produced response, various conceptual conclusions can be drawn.

A.1. Auxiliary Harmonic and Multi-Sine Signals

Suppose the shaft is additionally excited by Active magnetic bearing (AMB), the dynamics of the overall system can be represented as follows. First of all, the auxiliary harmonic excitation technique will be explained in brief. If ω_i is the critical or resonance frequency of the rotor, Ω_{rotor} is the rotor spin frequency or rotor velocity, the auxiliary harmonic excitation frequencies Ω_2 can be obtained by the following relation (Sawicki et al., 2011 a, b)

$$\Omega_2 = \left| n\Omega_{rotor} - \omega_i \right|,\ n = \pm 1, \pm 2, \ldots \tag{A.1}$$

Based on the excitation frequency (at the AMB) and the rotational speed of the rotor, the frequency spectrum of the rotor vibration response will include different frequency components given as below (Sawicki et al., 2011a, b)

$$\omega_c = r\Omega_{rotor} + s\Omega_2 \tag{A.2}$$

The simple sine test can verify the nonlinear behaviour of the system based on the presence of high-frequency components in a vibration spectrum. There are other methods like the correlation coefficient-based method, coherence function method, complex stiffness method and Hilbert transform method, which can also be used to measure the effect of nonlinearities in a given system. However, in the present research, the vibration response of the rotor ball bearing system with a sinusoidal excitation signal will be studied. The concept behind the multi-sine excitation method is to use specially designed periodic excitations (also called multi-sine excitations) given as follows (Kulesza, 2014)

$$Q_{AMB}(t) = \sum_{k=1}^{n_h} Q(k)\cos(\omega(k)t + \phi(k)) \quad \text{(A.3)}$$

with Q is the vector of the amplitude of forces, ω is the vector of their harmonic components, ϕ is the vector of their phases, and n_h is the number of frequency components. The signal is called even multi-sine if it is composed of even numbers. Similarly, the odd-multi-sine signal can be presented. The harmonic vector in which every other odd harmonic is left can be shown as follows (Kulesza, 2014)

r = [1, 5, 9, 13, 17, 21….] (A.4)

When a linear system is excited by the above multi-sine excitations, the response will be available at the input frequencies only. However, multiple frequencies will appear in the response spectrum for a nonlinear system. In this work, two different odd signals are utilized. One was developed by McCormack et al., (1994) and contains the following harmonics.

r = [1, 3, 7, 11, 15, 19….] (A.5)

and the other was developed by Schoukens et al., (2001) and contain the following harmonics:

r = [1, 3, 9, 11, 17, 19….] (A.6)

The dynamic response of the system with the above mentioned is studied in the present work. The crack induced nonlinearity in the overall system can be detected by analyzing the dynamic response of the system.

A.2. Application of Auxiliary Harmonic Excitation

Sawicki et al., (2011a, 2011b) introduced the above-mentioned technique for crack detection in rotors. For a healthy rotor, the Fourier Transform of the dynamic response will show a single peak corresponding to rotor spin frequency. In case of a cracked rotor, multiple frequencies (i.e. nX, where n is an integer and X is the frequency of the revolving rotor) observed in the Fourier Transform of the dynamic response (Figure A.1). The nonlinearity caused by parametric excitation

(i.e. time-varying stiffness of the cracked rotor) is responsible for this amazing behaviour. However, in reference (Sawicki et al., 2011a, Figure 20), similar results were reported for a healthy rotor also. Experimental results are given in that figure. Nothing has been mentioned in that reference regarding the reason for this behaviour. Our results indicate that ball bearing nonlinearities are the primary cause of this behaviour. This behaviour may be due to rotor/stator rubbing action also. However, our model predicts this type of behaviour even in the absence of a crack in the rotor. This type of behaviour has been resulted due to bearing nonlinearities. Figure (A.1 b) depicts this behaviour. In this figure (i.e. Figure A.1, parts a-d), the bearing supports are kept flexible. It has been observed that flexibility of bearing supports influences the system dynamics to a large extent (Figure A.1, parts e-h).

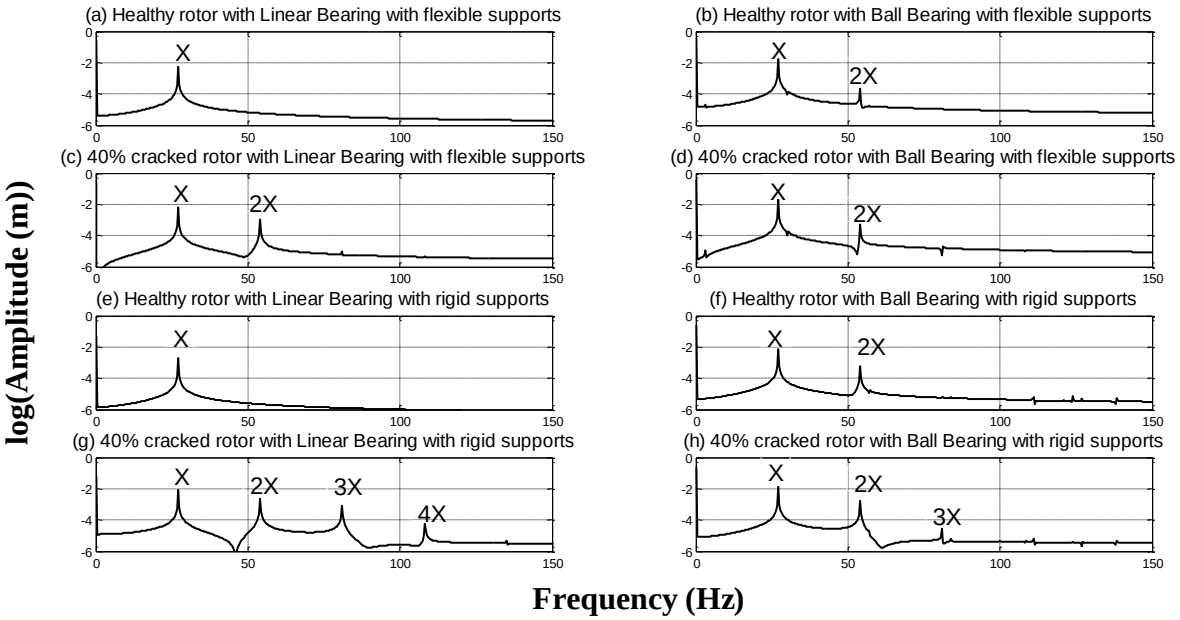

Figure A.1: Vertical response of the system at 27 Hz rotor spin frequency for different system conditions

The bearing supports are considered as rigid as well as flexible (depending on requirement). By this act, the system behaves like two Jeffcott rotors (mounted on flexible bearing supports) connected together side by side (however, not exactly). In this situation, for a 40% cracked rotor

with linear bearing characteristics (with flexible bearing supports) only first two harmonics are generated, the higher harmonics excited reach up to 4 i.e. 1X to 4X in presence of rigid bearing supports. For a healthy rotor (using flexible bearing supports) in the presence of ball bearings, only first 2 harmonics are generated. Similar is the case of a 40% cracked rotor. However, for the cracked rotor mounted on rigid bearing supports, in the presence of ball bearings, 3 harmonics are generated. Figure A.1 is self-explanatory in this regard. The overall effect of the ball bearing is to reduce the number and amplitude of excited harmonics.

To extensively observe these characteristics, the procedure discussed in ref. Sawicki et al., (2011) was followed. For n=2, 3 and 4, in Equation (A.1), auxiliary harmonic excitation frequencies (Ω_2) at 18 Hz, 45 Hz, and 72 Hz were applied one by one. In the ideal case, for a system having nonlinearities, the following frequencies should appear in the spectrum as per Equation (A.2)

[9, 18, 27, 36, 45, 54, 63, 72, 81, 90, 99, 108, 117, 126, 135, and 144 Hz]

Figure A.2 shows multiple response frequencies. The rotor spin frequency was held at X=27 Hz. Auxiliary excitation frequency was fixed at 18 Hz. In this figure, the abbreviation LB represents the linear bearing (i.e. bearings with linear restoring forces) and BB represents the ball bearing (i.e. bearings with nonlinear restoring forces). The AMB is located at disk1. For a 40% cracked rotor using a linear bearing with flexible bearing supports, the response is shown in part (a). It contains 45 Hz harmonics only apart from input frequencies and nX harmonics. In further discussion for the purpose of simplicity, we will write Y as a summation of input frequencies and nX harmonics. The healthy rotor system mounted on ball bearings contained frequencies 9 Hz, 36 Hz, 45 Hz apart from Y (Part b). No other frequencies were observed. The ball bearing nonlinearities are the basic cause of this behaviour. Part (c) represents the response of the system for a 40% cracked rotor in the presence of a ball bearing. The corresponding values of the magnitude with and without cracks

are shown in the same Figure. It is obvious that there is a marginal difference in response amplitudes with such a high crack percentage. This fact reduces the significance of AHE as a crack diagnostic technique.

Rigid bearing supports are considered for the next case (parts d, e, and f in Figure A.2). A number of nX harmonics were generated (part d). However, in the presence of ball bearings, these harmonics are reduced. Parts (e and f) show the response of the system with healthy and a 40% cracked rotor respectively in the presence of ball bearings. Only 36 Hz and 45 Hz harmonics were generated apart from Y. No other frequencies at 9, 18, 36, 45, 54, 63, 72, 81, 90, 99, 117 Hz were observed.

To further investigate the discrepancy, the AHE at disk 2 was applied instead of disk 1. The reason for doing that lies in the fact that the crack is assumed to be lying near disk 2. It cannot be done practically as AMB is located at disk 1. However, for theoretical investigation, excitation was applied at Disk 2. With this act (i.e. applying excitation at disk 2), the response spectrum contains frequencies at 9, 45, 72, 99 Hz apart from Y (Part g of Figure A.2) for a rotor with the linear bearing. For a healthy rotor with ball bearing, the dynamic response contains frequencies at 9Hz and 45 Hz apart from Y. Parts (h and i) show that there is very less difference in magnitude at these frequencies when healthy and cracked rotors mounted on ball bearing are compared. Hence, it is clear that the effectiveness of the technique under consideration is limited.

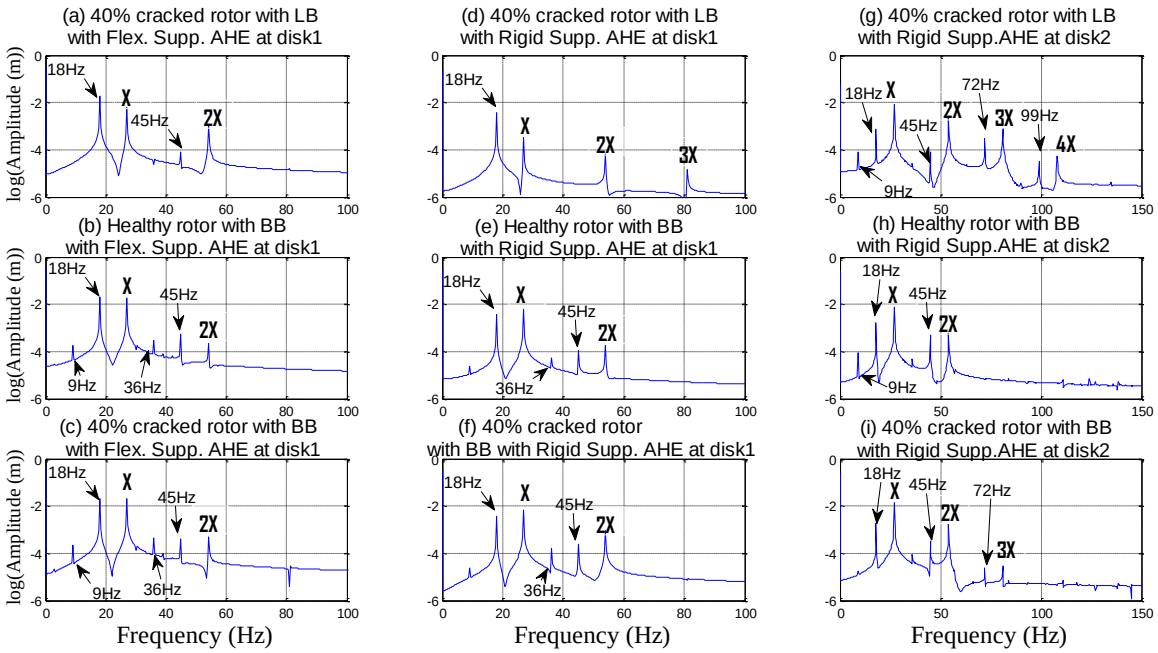

Figure A.2: Vertical responses of the system at 27 Hz rotor spin frequency and 18 Hz auxiliary harmonic excitation frequency

Figure A.3 shows the response of the system with AHE frequencies of 45 Hz and 72 Hz. At 45 Hz AHE, the rotor mounted on the linear bearing (Parts a), the observed frequencies were 18 Hz, 36 Hz, and 72 Hz apart from Y for the 40% cracked rotor. However, for the healthy rotor with a ball bearing (part b), the response contained 18 Hz harmonics apart from Y. Part (c) contains the response of the 40% cracked rotor supported on the ball bearing. 18 Hz and 72 Hz frequency components were seen in the response apart from Y. However, the magnitude is negligible. With the small amount of measurement noise, this is unobservable.

Figure A.3 (parts d, e, and f) shows the response of the system with 72 Hz AHE. For the rotor with the linear bearing (Parts d), the observed frequency was 45 Hz apart from Y for the 40% cracked rotor. However, for the healthy rotor with a ball bearing, the response contains no frequency components apart from Y. Similar is the case for the 40% cracked rotor on ball bearings. It can be safely concluded that this technique has limited practical utility for the real rotor system with multiple ball bearings (i.e. having nonlinearities) and flexible bearing supports.

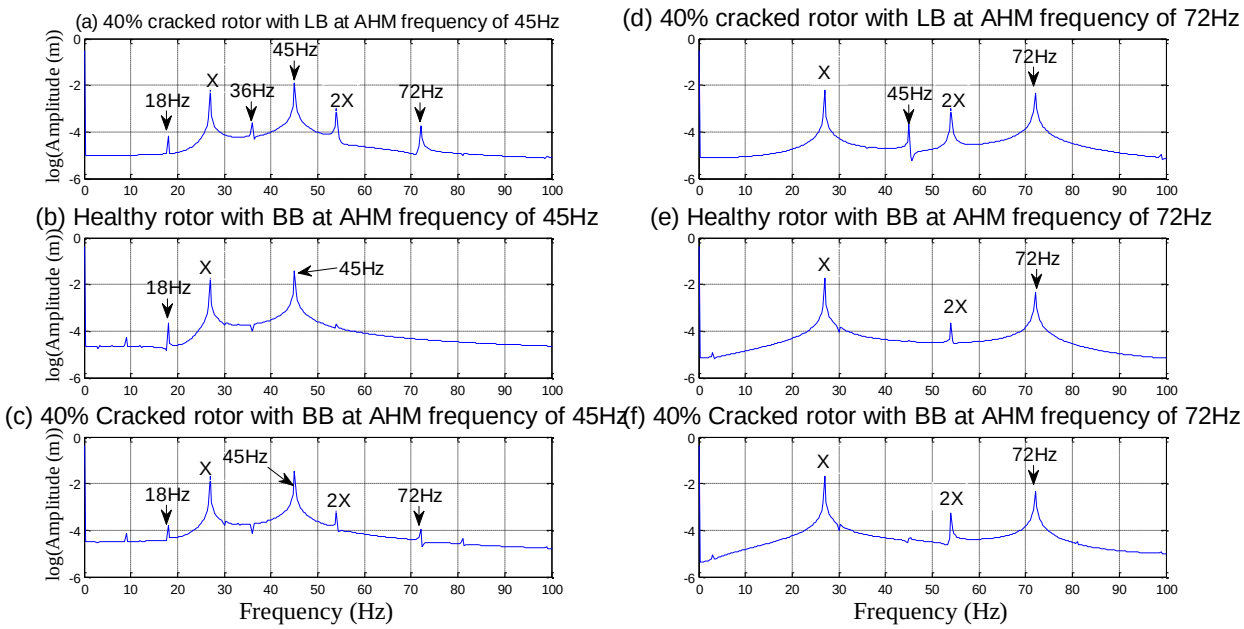

Figure A.3: Vertical responses of the system at disk 1 at 27 Hz rotor spin frequency and 45 Hz and 72 Hz auxiliary harmonic excitation frequency

A.3. Application of Multi-Sine Excitation (MSE)

In this method, the excitation signal contains more than one sinusoid. However, the properly designed signal should contain a sinusoid equal to rotor spin frequency Ω. The numerical analysis has been performed for the following two constant spin speeds i.e. Ω =27 Hz and Ω =30 Hz

For Ω =27 Hz and ω = [3, 15, 27, 39] Hz. Phase shifts of the harmonics are selected as follows: ϕ (1) =0^o, ϕ (2) = 90^o, ϕ (3) =180^o, and ϕ (4) =270^o (Kulesza, 2014).

For Ω=30 Hz and ω= [2, 6, 14, 22, 30] Hz. Phase shifts of the subsequent harmonics is selected in a similar way, i.e. ϕ (1) =0^o, ϕ (2) =90, ϕ (3) =180^o, ϕ (4) =270^o, ϕ (5) =360^o (Kulesza, 2014).

Figure A.4 (a, b and c) shows vertical vibration responses of the rotor for the first multi-sine frequency series, i.e. for ω = [3, 15, 27, 39] Hz. In this figure, LL represents the linear bearing and BB represents the ball bearing. The rotor spin frequency is 27 Hz. The excitation was applied at Disk 1. In the ideal case, the response spectrum should contain 12 Hz, 24 Hz, 42 Hz, 54 Hz, 66 Hz, 78 Hz and 90 Hz frequencies under the influence of crack (Kulesza, 2014). However, the rotor

with linear bearing characteristics contains 12 Hz and 66 Hz as well as Y frequencies only in the spectrum. This happens due to the effect of flexible bearing supports. Under the influence of ball bearing nonlinearities, 24 Hz and 78 Hz frequencies are emerged in the spectrum apart from Y (Figure A.4 b) for rotor under healthy conditions. Part (c) shows that for a 40% cracked rotor only 12 Hz, 24 Hz, 66 Hz and 78 Hz frequencies appear in the spectrum apart from Y. However, the amplitude at 12 Hz and 66 Hz is considerable. In case of healthy rotor, these frequencies were not available in the spectrum. But to justify the presence of crack based on these two frequencies is not logical.

Figure A.4 (d, e, f) shows the response of the system for second multi-sine series i.e. ω = [2, 6, 14, 22, 30] Hz. The rotor spin frequency of 30 Hz was fixed in this case. In case of a 40% cracked rotor, mounted on linear bearings no specific frequency components apart from Y were available in the spectrum. However, 8 Hz, 16 Hz, 32 Hz, 44 Hz, 52 Hz frequencies appear in the spectrum apart from Y for both healthy and cracked rotor mounted on ball bearings. Unfortunately, the magnitude of vibration at these frequencies is practically same for the healthy and cracked rotor. Hence this series of MSE has extremely limited efficacy.

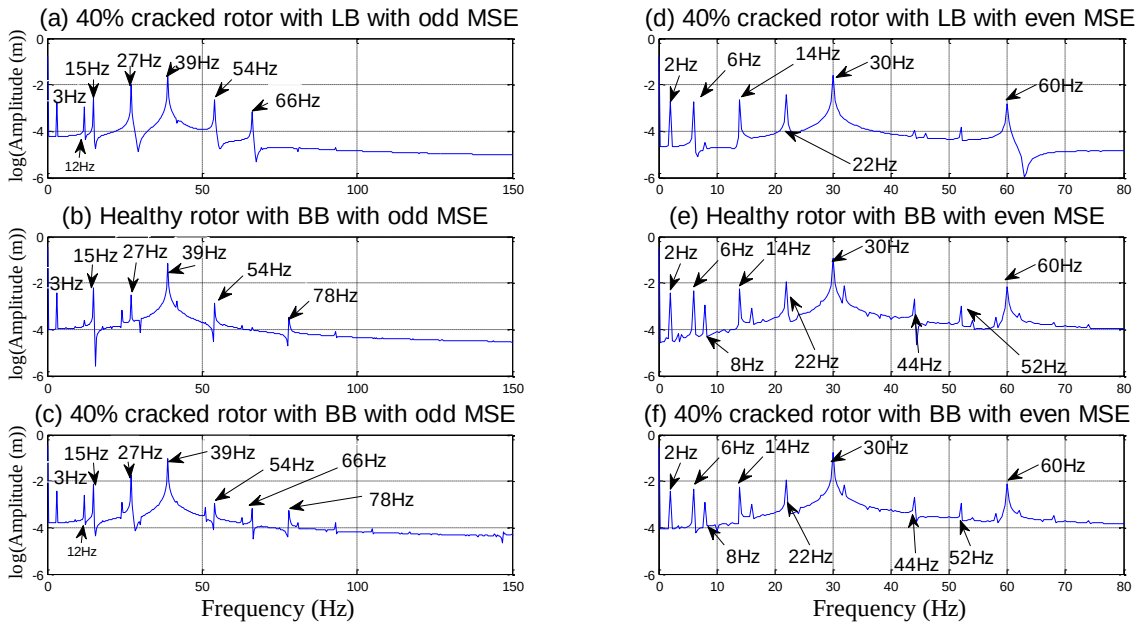

Figure A.4: Vertical responses of the system at disk 1 at different rotor spin frequencies and multi-sine excitation